



HAL
open science

Exploring nonlinear dynamics and amplitude squeezing of quantum dot lasers

Shihao Ding

► **To cite this version:**

Shihao Ding. Exploring nonlinear dynamics and amplitude squeezing of quantum dot lasers. Optics / Photonic. Institut Polytechnique de Paris, 2024. English. NNT : 2024IPPAT008 . tel-04861136

HAL Id: tel-04861136

<https://theses.hal.science/tel-04861136v1>

Submitted on 2 Jan 2025

HAL is a multi-disciplinary open access archive for the deposit and dissemination of scientific research documents, whether they are published or not. The documents may come from teaching and research institutions in France or abroad, or from public or private research centers.

L'archive ouverte pluridisciplinaire **HAL**, est destinée au dépôt et à la diffusion de documents scientifiques de niveau recherche, publiés ou non, émanant des établissements d'enseignement et de recherche français ou étrangers, des laboratoires publics ou privés.



INSTITUT
POLYTECHNIQUE
DE PARIS

NNT : 2024IPPAT008

Thèse de doctorat



Exploring the Nonlinear Dynamics and Amplitude-Squeezing of Quantum Dot Lasers

Thèse de doctorat de l'Institut Polytechnique de Paris
préparée à Télécom Paris

École doctorale n°626 École doctorale de l'Institut Polytechnique de Paris (ED IP
Paris)

Spécialité de doctorat : Electronique et optoélectronique

Thèse présentée et soutenue à Palaiseau, le 27/02/2024, par

Shihao Ding

Composition du Jury :

Alexei Baranov Directeur de Recherche, CNRS, Université de Montpellier, France	Président/Examineur
Geert Morthier Professeur, Ghent University, Belgique	Rapporteur
Nelson Sze-Chun Chan Professeur, City University of Hong Kong, Chine	Rapporteur
Nicolas Volet Professeur Associé, Aarhus University, Danemark	Examineur
Yating Wan Professeur Assistant, King Abdullah University of Science and Technology, Arabie Saoudite	Examinatrice
Nadia Belabas Chargé De Recherche, CNRS, Centre de Nanosciences et de Nanotechnologies, France	Examinatrice
Frédéric Grillot Professeur, Télécom Paris, Institut Polytechnique de Paris, France	Directeur de thèse
Heming Huang Ingénieur de Recherche, Télécom Paris, Institut Polytechnique de Paris, France	Co-directeur de thèse
John Bowers Professeur, University of California, Santa Barbara, États-Unis	Invité

Acknowledgements

First and foremost, I would like to express my deepest gratitude to my supervisor, Prof. Frédéric Grillot, whose unwavering support, insightful guidance and knowledge-sharing throughout this process have been invaluable. His open-mindedness allowed me to fully utilize my ideas in my PhD project. I am also very grateful to him for giving me plenty of opportunities to interact, learn, and collaborate with outstanding scientists.

I am grateful to my co-supervisor Dr. Heming Huang, for his invaluable assistance, guidance, and support throughout of my research. His expertise and insights have been instrumental in the direction of my experiments and the development of new methods. Beyond the laboratory, he also fosters a collaborative and enriching work environment.

I am sincerely grateful to Prof. John Bowers (University of California Santa Barbara, USA) and Prof. Luke Lester (Virginia Tech, USA) for providing high-quality lasers for my doctoral project and engaging in discussions regarding the associated results. Their expertise and insights have significantly contributed to the advancement of my research. I would also thank Prof. Wolfgang Elsaesser (Technische Universität Darmstadt, German) Prof. Isabelle Zaquine (Telecom Paris, France), and Dr. Nadia Belabas (Centre de Nanosciences et de Nanotechnologies, France) for providing me with the test setup and their careful guidance, which helped me tremendously to get my project on track.

I would like to extend my sincere gratitude to Dr. Bozhang Dong from University of California Santa Barbara, USA, Prof. Jianan Duan from Harbin Institute of Technology Shenzhen, China, and Prof. Nicolas Fabre from Telecom Paris, France for their valuable contributions to my this thesis. Additionally, I am deeply appreciative of the collaborative support provided by Prof. Vassilios Kovanis from Virginia Tech, USA, Dr. Weng Chow from Sandia National Laboratories, USA, Prof. Cheng Wang from ShanghaiTech University, China, Prof. Daniel J. Herrera from Virginia Tech, USA.

I also want to thank the professors, colleagues, and friends from Telecom Paris, France: Prof. Elie Awwad, Dr. Olivier Spitz, Dr. Shiyuan Zhao, Dr. Jingtian Liu, Dr. Pierre Didier, Thibaut Renaud, Di Cui, Mingzhao Shi, Zhangdi Chen, Hyunah Kim,

Wenlu Wang, Sara Zaminga, Dr. Jannik Ehlert, Dr. Yuan Yao, Yinhao Wang, Xiaolin Wang, Yibo Wang, Ziyu Li, Weichen Tao for their invaluable support in both work and life.

I acknowledge the funding support from China Scholarship Council and Institut Mines-Telecom.

Last but not least, I am deeply grateful to my parents for their unwavering support, understanding, and encouragement throughout this journey. My special thanks to my fiancée Yi Liu for her love and steadfast support.

Contents

Acknowledgements	iii
List of figures	vii
List of tables	xviii
1 Introduction	1
1.1 Needs for photonic integrated circuits	1
1.1.1 Optical communications	2
1.1.2 Optical sensing	5
1.1.3 Optical computing	6
1.1.4 Quantum photonics	8
1.2 QD lasers for monolithic integration	9
1.3 Motivations	11
1.4 Organization of this thesis	14
2 Fundamentals of Quantum Dot Lasers	23
2.1 Electronic structure	23
2.2 Equivalent circuit	25
2.3 Noise characteristics	27
2.3.1 Intensity noise	27
2.3.2 Frequency noise	29
2.3.3 Linewidth enhancement factor	30
2.4 Spectral dependent α_H -factor for QD lasers	34

2.4.1	Introduction of α_H -factor extraction techniques	34
2.4.2	Static characteristics	42
2.4.3	Experimental setup	43
2.4.4	Results for optical phase modulation	45
2.5	Directly modulated QD laser with high optical feedback resistance	48
2.5.1	Experimental setup	48
2.5.2	Transmission results	50
2.6	Summary	53
3	Optoelectronic Feedback with Quantum Dot Lasers	63
3.1	Introduction	63
3.1.1	External control methods	64
3.1.2	Applications	72
3.2	Optoelectronic feedback with epitaxial QD lasers	77
3.2.1	OEF experimental configuration	77
3.2.2	Enhanced nonlinear dynamic under OEF	79
3.2.3	Theoretical analysis and modeling	84
3.3	Summary	90
4	Effects of Injected Carrier Noise on Quantum Dot Lasers	97
4.1	What affects the linewidth enhancement factor?	97
4.1.1	Active medium	97
4.1.2	Pump ratio	99
4.1.3	Carrier fluctuations	100
4.2	Carrier noise of electrical pump	101
4.2.1	Definition of quiet pump	102
4.2.2	Carrier noise measurement	104
4.3	Numerical simulation and experimental analysis	105
4.3.1	Semi-classical rate equations	105
4.3.2	Comparison of numerical and experimental results	113
4.4	Summary	117

5	Amplitude Squeezed States of Quantum Dot Lasers	125
5.1	Introduction	125
5.1.1	Balanced homodyne detection	127
5.1.2	Quantization of the squeezed states	128
5.1.3	Applications of amplitude squeezing	132
5.1.4	Techniques for amplitude squeezed state generation	135
5.2	Amplitude squeezed states experiments	138
5.2.1	Experimental setup	138
5.2.2	Squeezing characteristics	140
5.3	Reflection-insensitive amplitude squeezed states of QD laser	141
5.3.1	Experimental setup	142
5.3.2	Comparison between QD and QW lasers	143
5.3.3	Non-ideal homodyne detection correction	146
5.4	Analysis of second-order correlation function	147
5.4.1	Relationship between the squeezed characteristics and the second-order correlation function	148
5.4.2	Experimental results	150
5.5	Summary	152
6	Conclusions and Perspectives	163
	Appendix A: Publications	168
	Appendix B: Résumé de thèse en français	171

List of Figures

1.1	The number of photonic components integrated on a single waveguide over time for different photonic integration platforms. [Xia+21]	2
1.2	Schematic diagram of a WDM optical communication systems. (a) WDM transmitter utilizing several single-mode lasers of different wavelengths as the light source. (b) WDM transmitter employing a frequency comb source. [HO21]	3
1.3	(a) Global mobile network data traffic over time (Source: Ericsson). (b) The power consumption of data centers for training AI systems (Source: Our world in data).	4
1.4	LiDAR market overview over time (Source: Yole Développement).	5
1.5	(a) Silicon integrated LiDAR chip. Contains TLD: tunable laser diode. SOA: semiconductor optical amplifier. PS: phase shifter. (b) Configuration of the TOF LiDAR. [Li+22]	6
1.6	Neuromorphic photonic processor architecture. [Sha+21b]	7
1.7	Schematic of all-optical reservoir computer. [Dej+14]	7
1.8	Integrated photonic devices based on InP-based and SiN-based quantum key distribution. [Sib+17]	8
1.9	Impact of quantization on the density of states. [ANK19]	10
1.10	(a) Threshold current density of InAs/GaAs QD and QW lasers on silicon. [Nor+18] (b) The power-current curves at different temperatures of QD lasers. [Sha+21a]	10

1.11	RIN spectra at bias currents of 40, 60, and 80 mA of an integrated silicon-based QD laser. [Lia+18]	12
1.12	Progress in linewidth investigation of semiconductor lasers under three different integration methods. [Xia+21]	13
2.1	Electronic schematic of a QD (conductive band).	24
2.2	Equivalent circuit model diagram of a single mode semiconductor laser. It includes three parts: parasitic circuit, electrical circuit, and optical circuit. [Din+22]	26
2.3	Schematic diagram of the ideal and real output power of a semiconductor laser with DC pump.	28
2.4	Frequency noise spectrum showing the contribution of carrier noise and spontaneous emission noise. [CCM12]	29
2.5	The schematic diagrams illustrate that the phase variations is affected by (a) the direct effect of spontaneous emission only and (b) the combined effect of spontaneous emission and phase-amplitude coupling. [Gri+21]	31
2.6	Spectral dependence of the α_H -factor measured by ASE methods for the epitaxial QD laser. The inset shows the α_H -factor values for the QW laser. [Dua+19b]	32
2.7	(a) Optical and (c) RF spectral mappings of the QD laser as a function of the feedback strength; (b) Optical and (d) RF spectral mappings of the QW laser as a function of the feedback strength. [Dua+19a]	33
2.8	The α_H -factor as a function of wavelength for a p-doped QD laser at room temperature. The black dashed line indicates the peak FP gain (1295 nm). The inset indicates the net modal gain spectra for different sub-threshold bias current conditions. [Dua+18a]	35
2.9	The locked and unlocked states separated by the injected boundaries are used for the α_H -factor extraction. [LJC01]	36
2.10	Generalized stability diagram of a semiconductor laser showing the positions of the four main operating states of the injection-locked system (a) strong injection and (b) weak injection. [HKL21]	37

2.11	The optical spectrum of the injection-locked system at different injection levels near the Hopf bifurcation point when detuning is zero. (a) η_{FH} (b) η_{RH} . The bifurcation point is defined as the injection level when the side mode suppression ratio crosses 30 dB. [HKL21]	38
2.12	Experimental setup for determining AM, FM response, and the α_H -factor. The insert illustrates the transfer function of the interferometer. [PG11]	39
2.13	Modulation frequency dependence of the FM/AM ratio (dashes) and the α_H -factor (thick solid line). The horizontal line indicates the lowest level for the regular α_H -factor of the laser. The inset shows the experimental curve of the FM-AM ratio of a QD laser. [Wan+14]	40
2.14	(a) The normalized spectra, i.e., a longitudinal mode and modulation sidebands, were obtained under four different optical delay conditions. (b) The α_H -factor for the longitudinal mode of the FP QW laser. The inset shows the emission spectrum. [Pro+11]	41
2.15	(a) Experimental setup. (b) The phase plotted as a function of $\log(I(t))$ [SR23]	42
2.16	Optical spectrum measured at twice threshold current, and the insert shows power-current characteristics.	43
2.17	Schematic of the experimental setup of the OPM technique. PM: Phase Modulator; ODL: Optical Delay Line; OSA: Optical Spectrum Analyzer; BT: Bias Tee; RFPS: RF Power Splitter (RFPS). The black line is the circuit, the red line is the light path.	44
2.18	(a) Modulated optical spectrum at zero delays with $f_m = 13$ GHz, and (b) Close-up on one longitudinal mode and the modulation sidebands obtained for four different optical delays.	45
2.19	(a) The α_m -factor measured for each comb line for different modulation frequencies and at $\times 2$ threshold current, (b) $\times 4$ threshold current, and (c) $\times 6$ threshold current, (d) the α_H -factor for different pump currents extracted from the optical phase modulation and ASE methods.	46
2.20	Spectral dependent α_H factor of QW (red) and QD (blue) lasers measured at twice the threshold.	47

2.21	(a) Schematic of epitaxial QD laser device structure. (b) Power-current characteristics at 20 °C. The inset is the spectrum of the QD laser at 60 mA.	49
2.22	Schematic of the experimental setup. The black lines show the electrical circuit and the red lines show the light path.	49
2.23	(a) BER plots at 2 Gbps for back-to-back (B2B) and after transmission (2 km) with and without feedback for the QD laser at 20 °C. The pump current is $2 \times I_{th}$. The eye diagrams (b) without feedback and (c) with feedback when back-to-back. The eye diagrams (d) without feedback and (e) with feedback after 2 km transmission.	51
2.24	(a) BER plots at 6 Gbps for back-to-back (B2B) and after transmission (2 km) with and without feedback for the QD laser at 20 °C. The pump current is $2 \times I_{th}$. The eye diagrams (b) without feedback and (c) with feedback when back-to-back. The eye diagrams (d) without feedback and (e) with feedback after 2 km transmission.	52
3.1	Schematic diagram of optical injection setup.	64
3.2	Two-parameter bifurcation diagrams showcasing (a) α_H -factor = 0.9 and (b) α_H -factor = 3.2 are presented. The diagram is color-coded to denote the count of extremal values, that is, the total number of maxima and minima in the photon density. [Pau+12]	65
3.3	Schematic diagram of external optical feedback setup. BKR: back reflector.	66
3.4	Single-parameter bifurcation diagram of the photon number N_{ph} concerning the feedback strength, obtained from direct numerical integration [(a), (b)] and path continuation using delay differential equations [(c), (d)]. The upper figures show the maximum and minimum photon densities $N_{ph}^{\min/\max}$, while the lower figures display only the maximum values N_{ph}^{\max} . The α_H -factor is set to 0.9 for the left column and 3 for the right column. [Glo+12]	67

3.5	Mapping of the dynamic states of the QD laser under different feedback strengths and external cavity lengths at drive currents of (a) 125 mA and (b) 160 mA. [Don+21]	68
3.6	Schematic diagram of injection current modulation. BT: bias tee.	69
3.7	The graph of modulation index versus modulation frequency for the types of modulated laser signals. [AY12]	69
3.8	Experimental setup for Ikeda-like OEF with modulator. [Che+19]	70
3.9	Schematic diagram of the experimental setup for delayed optoelectronic feedback semiconductor laser system. [LL03]	70
3.10	(a) Mapping of dynamic states for the positive OEF and (b) negative OEF. S: Stable state. RP: Regular pulsing. Q2: Bi-frequency quasiperiodic pulsing. Q3: Tri-frequency quasiperiodic pulsing. FL: Frequency-locked pulsing. C: Chaotic pulsing. [LL03]	71
3.11	(a) Variation of the frequency of local minimum period 1 with detuning frequency for different optical injection strengths. (b) Variation of microwave frequency and power with optical injection strength. (c) Trend of the second harmonic distortion (SHD) and sideband rejection ratio with detuning frequency. [Wan+16]	72
3.12	(a) Superimposed electrical spectra of microwave signals generated at different pressures. (b) Measured beat frequency as a function of applied pressure. [Wan+17]	73
3.13	(a) Experimental setup showing transmitter and receiver units. (b) Synchronization case. (c) Counter-synchronization case. (d) Filtered time series during message recovery in the anti-synchronization case. [Spi+21]	74
3.14	Experimental setup of reservoir computing using a semiconductor laser with feedback modulation function. [KHU22]	75
3.15	(a) Experimental schematic of the coherent Ising machine based on OEF. (b) Working principle. (1) In the sampling stage, (i) feedback signal generation, (ii) spin amplitude measurement, (iii) spin states sign determination. (2) In the processing stage, digital processing and matrix multiplication of spins. [BVV19]	76

3.16	The tabletop experiment was used for studying optoelectronic feedback in the silicon-based QD laser (the solid red lines represent the optical path and the solid black lines represent the electrical path).	78
3.17	(a) Optical power-voltage with bias current. (b) The measured voltage applied on the QD laser concerning the OEF strength.	79
3.18	Temperature impact on the dynamics of the QD laser with OEF. Electrical spectra were measured under different OEF strengths at (a) 20 °C and (b) 30 °C respectively. (c) and (d) are the corresponding mappings of the electrical spectra in the 1 GHz range at 20 °C and 30 °C respectively.	80
3.19	Nonlinear dynamics of the epitaxial QD laser with OEF. Experimental time dependent output of the QD laser at (a1)-(a4) 20 °C and (b1)-(b4) 30 °C with different OEF strengths. (a5) and (b5) are partial zoom-in views.	81
3.20	Nonlinear dynamics of the reference QW laser with OEF. (a) Experimental time series of QW laser with the same OEF setup as QD laser at different feedback strengths. (b) Time series of the QW laser after the inclusion of another electrical amplifier with feedback strengths. . .	83
3.21	A block diagram depicting the time-domain representation of the Ikeda-like OEF loop. The variable $x(t)$ undergoes counterclockwise circulation and interacts with the four key components within the loop.	84
3.22	The experimental and numerical nonlinearity transfer functions of QD (purple) and QW (blue) lasers, respectively.	86
3.23	Simulated bifurcation diagrams of (a) QD and (b) QW lasers. (c) Experimental dynamical regions were observed in QD and QW lasers, respectively.	88
3.24	Simulated time series of the (a)-(b) QD and (c)-(d) QW laser.	88
4.1	Schematic of the variation of gain G and refractive index n with carrier density N for QD and QW lasers.	98
4.2	Calculated GS α_H -factor with the bias current (black dots). Red stars are experimental data. [Gri+08]	99

4.3	Linewidth with an increase in the current noise σ_I at 50 mW output power. [AR88]	100
4.4	Schematic diagram of the theoretical model illustrating the relationship between injected carriers and photons in a semiconductor laser driven by (a) a normal pump and (b) a quiet pump.	103
4.5	(a) The noise power and (b) the noise fluctuation of normal and quiet pumps.	104
4.6	Schematic representation of the electronic structure and carrier dynamics in a QD for normal pumping conditions and quiet pumping conditions. The two current sources are distinguished by the fact that the currents are expected to be equal and the quiet pump has a small current variance.	105
4.7	Reservoir model used in the rate equation analysis of the QD laser. Each solid line arrow in the flow chart represents the number of particles flowing per unit of time. The dashed lines represent the relationship to the phase.	109
4.8	Simulated frequency noise spectra of the QD laser with normal pump (red line) and quiet pump (blue line) at different bias currents (a-d). The FN mapping is mapped as a function of normalized bias pump and frequency under (e) normal pump and (f) quiet pump.	115
4.9	Experimental (dotted line) and simulated (solid line) (a) α_H -factor and (b) optical linewidth with bias current under different pumps.	116
4.10	The experimental α_H -factor of QW laser with normal and quiet pumps.	117
5.1	Different states represented in the phasor diagram: (a) vacuum state, (b) coherent state, (c) phase squeezed state, (d) amplitude squeezed state.	126
5.2	Schematic diagram of the balanced homodyne detection [Lvo15]	127
5.3	Anti-squeezing, shot noise, and squeezing curves in the frequency domain. [Ino+23]	128
5.4	Anti-squeezing, shot noise, and squeezing time traces and their corresponding photon statistics. [Ino+23]	129

5.5	Noisy traces (left), quadrature distribution (center), and reconstructed Wigner function for the generated different quantum states (right). [BSM97]	130
5.6	Second-order correlation functions for ideal amplitude squeezed states with different squeezing parameters. [LDC14]	131
5.7	The CV-QKD experimental set-up. The two OPOs each produce a squeezed state. The squeezed states interfere with the BS to form a two-mode squeezed state. The amplitude or phase quadrature of one mode is measured by Alice's homodyne detector. The other mode is carefully phase-locked to a coherently modulated auxiliary mode. [Mad+12] . . .	132
5.8	Quantum light sources for Gaussian boson sampling. (a) Schematic diagram of the experimental setup for generating two-mode squeezed states. (b) The Wigner function of 25 squeezed states. [Zho+20]	133
5.9	Squeezed light in spin noise spectroscopy (a) experimental setup and (b) corresponding noise spectra. [Luc+16]	134
5.10	The diagram of the interferometer layout shows the propagation of the source laser (red solid line) and the squeezed light (burgundy dashed line). [McC+21]	135
5.11	Experimental setup for measuring frequency-dependent squeezed states and for reconstructing squeezed states' Wigner functions. [Jun+22] . . .	136
5.12	Generation of two-mode squeezed quantum microcombs on a chip. [Yan+21]	136
5.13	Photon distributions of nano light emitter diode under (a) normal pump (b) quiet pump. [MY20]	137
5.14	Experimental setup for amplitude squeezed state generation with quiet pump. The inset shows the time series fluctuations of the quiet pump and the voltage is the signal read from oscilloscope.	139
5.15	The measured RF noise power spectral density at 40 mA.	140
5.16	Histogram calculated from the raw data acquired by the oscilloscope.	141
5.17	Experimental setup for amplitude squeezed state generation employing optical feedback. DA: differential amplifier.	142

5.18	Measured classical noise at different feedback strengths for (a) QD laser and (c) QW laser. Squeezing level at different feedback strengths for (b) QD laser and (d) QW laser.	143
5.19	The squeezing level of (a) QD laser and (b) QW laser under different optical feedback strengths at room temperature.	144
5.20	Squeezing level spectrum for (a)-(c) QD laser and (d)-(f) QW laser without or with optical feedback under -67.8 dB, -18.8 dB, and -15.1 dB respectively.	145
5.21	The noise-corrected SL of QD laser under different optical feedback strengths.	147
5.22	The fitted $g^{(2)}(0)$ of QD and QW laser under different optical feedback strengths.	149
5.23	Experimental setup for amplitude squeezed state generation employing optical feedback.	150
5.24	The comparison of fitted and experimental $g^{(2)}(0)$	151
6.1	The Wigner function for (a), (b) the squeezed state and (c),(d) the vacuum state. [Smi+93]	166
6.2	Diagramme schématique du modèle théorique illustrant la relation entre les porteurs injectés et les photons dans un laser à semiconducteurs alimenté par (a) une pompe normale et (b) une pompe silencieuse.	174
6.3	(a) La puissance de bruit et (b) la fluctuation de bruit des pompes normales et silencieuses.	175
6.4	Représentation schématique de la structure électronique et de la dynamique des porteurs dans un QD pour des conditions de pompage normales et des conditions de pompage silencieuses. Les deux sources de courant sont distinguées par le fait que les courants sont censés être égaux et que la pompe silencieuse a une petite variance de courant.	176
6.5	Modèle de réservoir utilisé dans l'analyse des équations de taux du laser à points quantiques. Chaque flèche pleine dans le diagramme de flux représente le nombre de particules qui circulent par unité de temps. Les lignes en pointillés représentent la relation avec la phase.	181

6.6	Spectres simulés du bruit de fréquence du laser à points quantiques avec pompe normale (ligne rouge) et pompe silencieuse (ligne bleue) à différents courants de polarisation (a-d). La cartographie de FN est représentée en fonction de la pompe de polarisation normalisée et de la fréquence sous (e) pompe normale et (f) pompe silencieuse.	184
6.7	Facteur α_H expérimental (ligne en pointillés) et simulé (ligne pleine) (a) et largeur de raie optique (b) en fonction du courant de polarisation sous différentes pompes.	185
6.8	Le facteur α_H expérimental du laser QW avec des pompes normales et silencieuses.	186

List of Tables

- 3.1 Comparison about the dynamics generation between QD and QW lasers 83
- 4.1 Material and optical parameters of InAs/GaAs QD laser [FM07; Kir+96] 108
- 6.1 Paramètres matériels et optiques du laser à points quantiques InAs/GaAs 180

CHAPTER 1

Introduction

The introduction section will outline the research background and motivation of this thesis. Firstly, it combines industrial development to introduce the demand for photonic integrated circuits (PICs) in various applications, including optical communication, optical sensing, optical computing, and quantum photonics. Then, it describes the potential of quantum dot (QD) lasers in the aforementioned applications. For this, the thesis will also introduce the advantages of researching the fundamental characteristics of QD lasers and the potential for optical isolator-free integrated optical communication. Additionally, the unique dynamics and quantum noise characteristics of QD lasers will be discussed. Finally, the overall arrangement of the manuscript will be detailed at the end of this chapter.

1.1 Needs for photonic integrated circuits

In the era of big data and cloud computing, the demand for faster, higher-capacity data transmission continues to soar. The ability of PICs to process and transmit data at high speeds is critical to satisfy these growing bandwidth requirements. They are an integral part of the optical communication field for high-speed networks and efficient data center operations. With efforts to overcome energy conservation and sustainability challenges, PICs offer a more energy-efficient alternative to electronic circuits, as their lower energy consumption is critical to reducing the carbon footprint of data cen-

ters and communication networks. In addition, PICs allow multiple optical functions to be integrated into a single chip, reducing the size and complexity of optical systems. This is particularly beneficial for areas such as optical sensors, LIDAR, and aerospace technology [AC17; Kra+19]. Furthermore, the rapid development of quantum computing and quantum communication technologies has made high-throughput, highly integrated quantum photonics a hot research topic. Fig. 1.1 summarizes the evolution of the number of components integrated on a single waveguide for monolithic InP, monolithic Si, and heterogeneous InP/Si or GaAs/Si platforms. The trends of these integration platforms are predicted for the coming years [Xia+21]. Microchip companies have selected different integration platforms according to their business development.

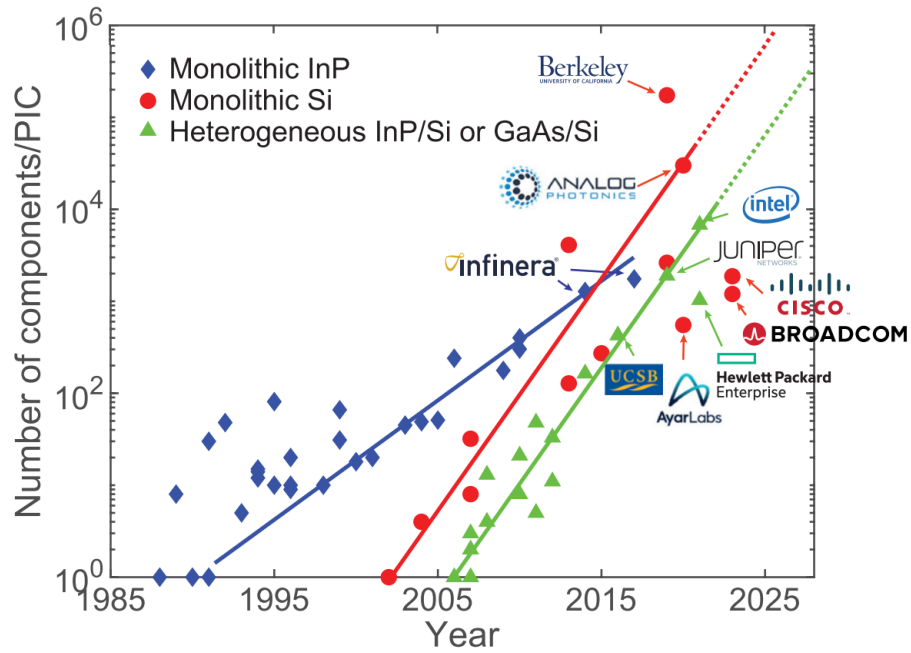


Figure 1.1: The number of photonic components integrated on a single waveguide over time for different photonic integration platforms. [Xia+21]

1.1.1 Optical communications

Optical communication networks, which have been evolving for many years, form the backbone of a global telecom network that operates on three primary scales. The first

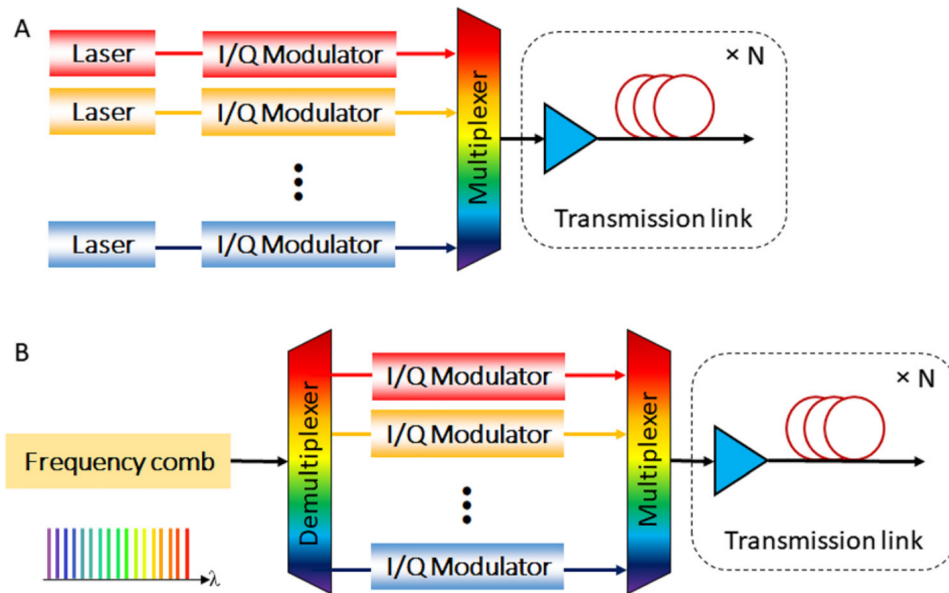


Figure 1.2: Schematic diagram of a WDM optical communication systems. (a) WDM transmitter utilizing several single-mode lasers of different wavelengths as the light source. (b) WDM transmitter employing a frequency comb source. [HO21]

of these is the long-haul networks, designed to connect continents through extensive transpacific and transatlantic submarine cables spanning thousands kilometers. The second scale encompasses metropolitan networks, which link countries and cities over distances of several hundred kilometers. These networks typically employ a ring topology, allowing for efficient connections between regional networks, access networks, and data center interconnects. Finally, the access networks connect individual endpoints to the local exchanges, while the interlinks are usually a few kilometers. In addressing high-capacity transmission, two types of setups have been considered as transmitters as in Fig. 1.2. Individual sources of different wavelengths or a frequency comb containing multiple wavelengths are modulated and transmitted to the next level of receivers [HO21]. To further satisfy the enormous transmission task, it is also necessary to consider the monolithic integration of optical sources, modulators, wavelength-division multiplexers (WDM), and so on. Alternatively, the development of direct modulation on the optical sources can reduce the on-chip components and thus increase the integration density [ABC20; Nis+18].

In recent years, the Internet and personal terminals have been rapidly growing. As shown in Fig. 1.3(a) total global mobile data traffic reaches 93 Ebit per month by the end of 2022 and is expected to grow 3.5 times by 2028, especially with the rapid growth of 5G traffic. Thus, PICs can expand data transmission channels and increase transmission rates, providing a feasible foundation for future more high-speed data transmission technologies. On the other hand, the rapid development of cloud computing and artificial intelligence (AI) technologies has led to a significant increase in power consumption due to the massive data transmission in data centers [DMH23]. As illustrated in Fig. 1.3(b), this is particularly true for advanced models like the GPT-4 AI, which requires computational power up to 10^{25} floating-point operations for training. Therefore, the study of PICs with high data throughput and low power consumption (especially silicon-based PICs compatible with electronic integrated circuits (EIC)) can help solve the issue of high energy consumption and benefit other disciplines and technologies [CGV22; Sha+21b].

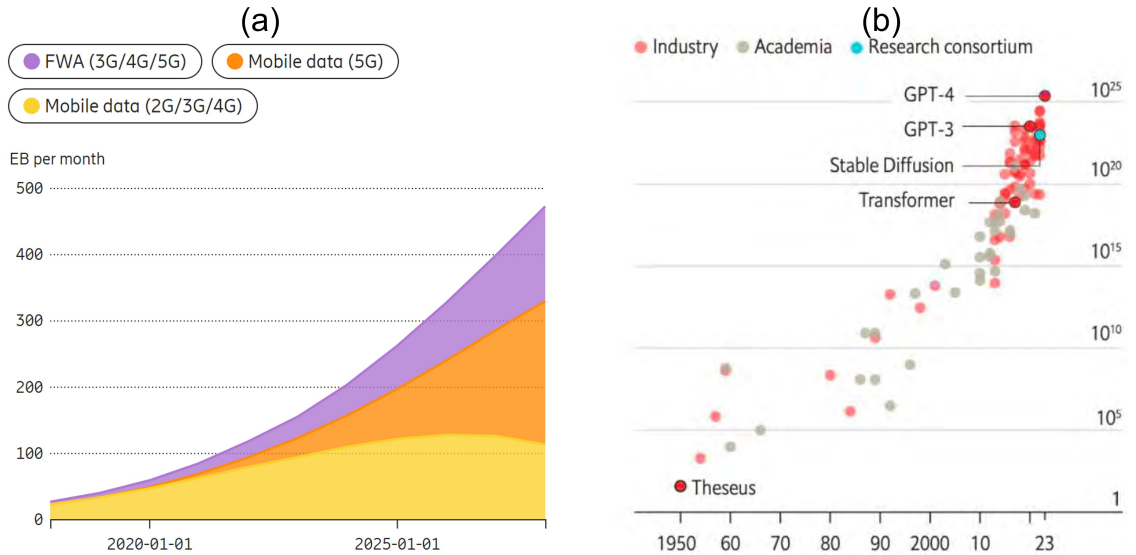


Figure 1.3: (a) Global mobile network data traffic over time (Source: Ericsson). (b) The power consumption of data centers for training AI systems (Source: Our world in data).

1.1.2 Optical sensing

Optical sensors often require the combination of various optical components, such as lasers, modulators, detectors, and waveguides. PICs enable the integration of these components onto a single, compact chip, which brings convenience to LiDAR, wearable technology, biomedical devices, and on-chip sensing systems. Additionally, integrating photonic components on a chip can reduce signal loss and interference, leading to more accurate and reliable measurements. The development of PICs is key to breaking through the limits of optical sensing technology, offering advantages in miniaturization, sensitivity, scalability, versatility, speed, energy efficiency, and reliability [Pas+12]. These advancements enable the creation of more sophisticated, compact, and cost-effective optical sensors for a wide range of applications. As the most widely used optical sensor LiDAR, its market has grown exponentially in recent years. Especially in the era of intelligent development, the market for LiDAR in advanced driver assistance systems (ADAS) has shown explosive growth, as shown in Fig. 1.4.

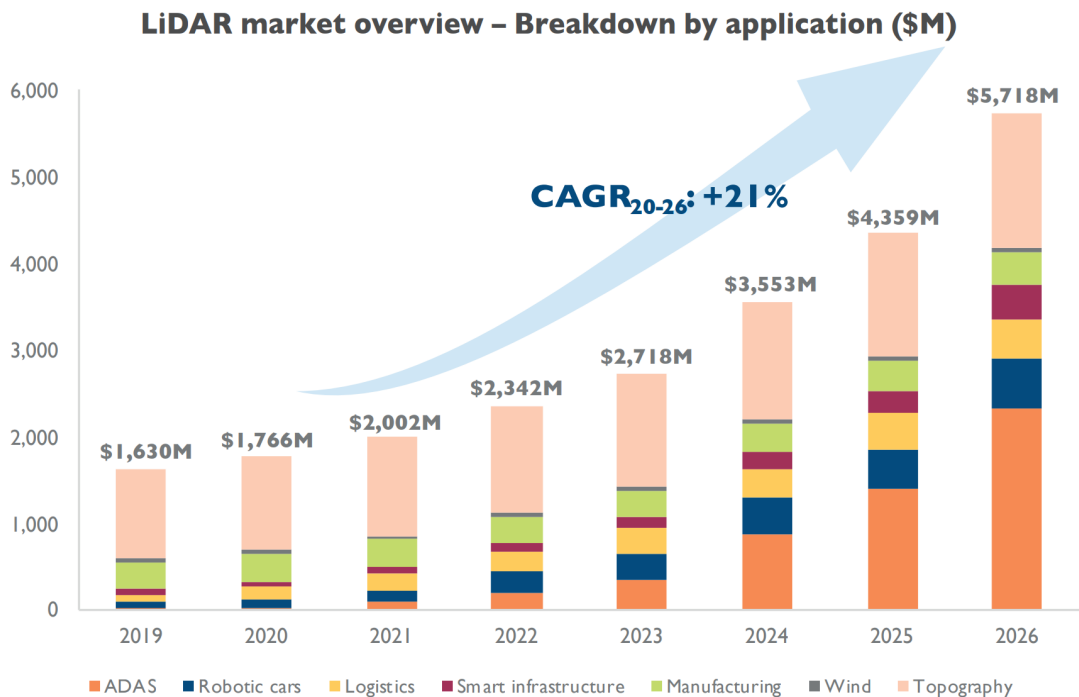


Figure 1.4: LiDAR market overview over time (Source: Yole Développement).

PICs can integrate multiple optoelectronic functions into a single compact chip, as illustrated in Fig. 1.5 with the silicon-based integrated LiDAR chip [Li+22]. This miniaturization in terms of space and weight is particularly beneficial for applications such as autonomous vehicles and drones. Additionally, the energy-saving characteristics of PICs can reduce the power consumption of LiDAR systems, extending the battery life of devices like drones and electric vehicles [Fal+20].

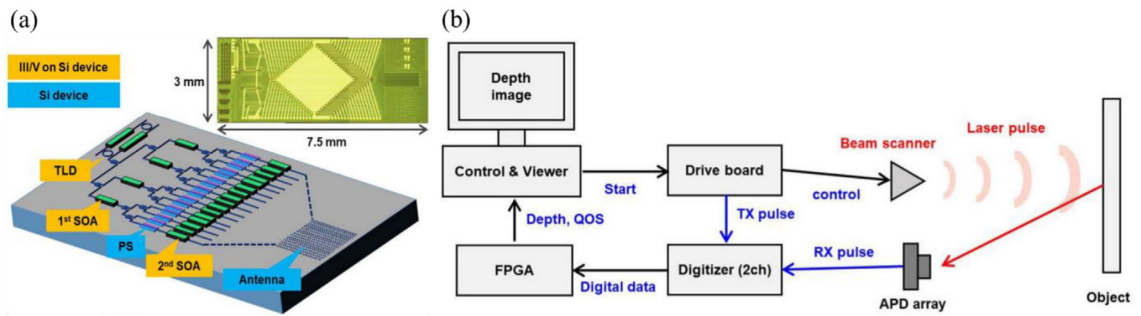


Figure 1.5: (a) Silicon integrated LiDAR chip. Contains TLD: tunable laser diode. SOA: semiconductor optical amplifier. PS: phase shifter. (b) Configuration of the TOF LiDAR. [Li+22]

1.1.3 Optical computing

When dealing with complex problems, optical computing utilizing PICs brings notable advantages. First is the capability for high-speed data processing. Photons propagate at the speed of light and can carry more information per unit of time. This allows for data processing at extremely high speeds, much faster than traditional electronic computing. Then there are the low-energy consumption characteristics. Optical computing with PICs has lower optical losses. Moreover, it can process multiple data streams in parallel using techniques like WDM, which is crucial for handling large-scale computations and big-data analytics [Tak+18]. Hybrid optoelectronic systems can be seamlessly integrated into optoelectronic systems and can make up for the lack of all-optical computing at this stage. Optoelectronic digital-analog hybrid chips can merge the precision and scalability of digital computing with the continuous signal-processing capabilities of analog systems. The integrated neurophotonic processing

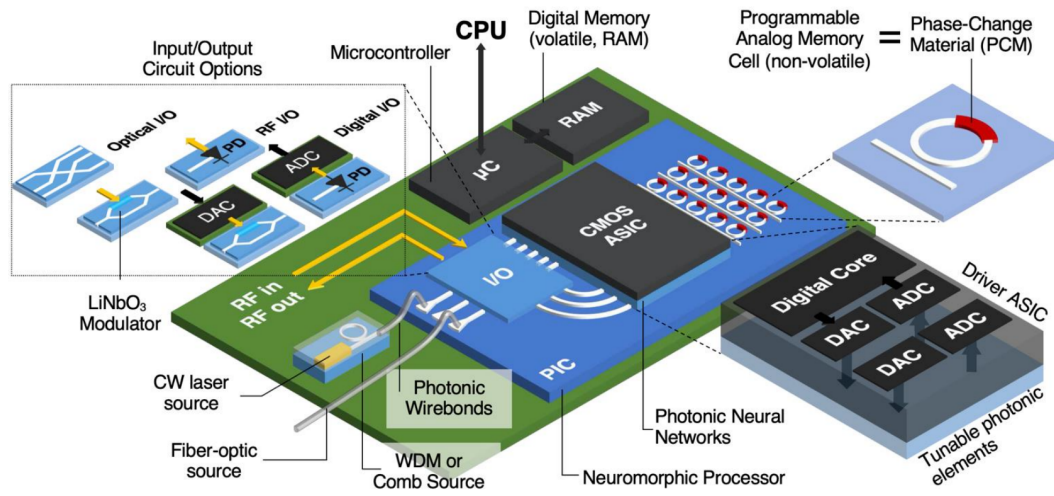


Figure 1.6: Neuromorphic photonic processor architecture. [Sha+21b]

chip illustrated in Fig. 1.6 contains both analog and digital modules. The digital part brings the convenience of being programmable and easily scalable [Sha+21b].

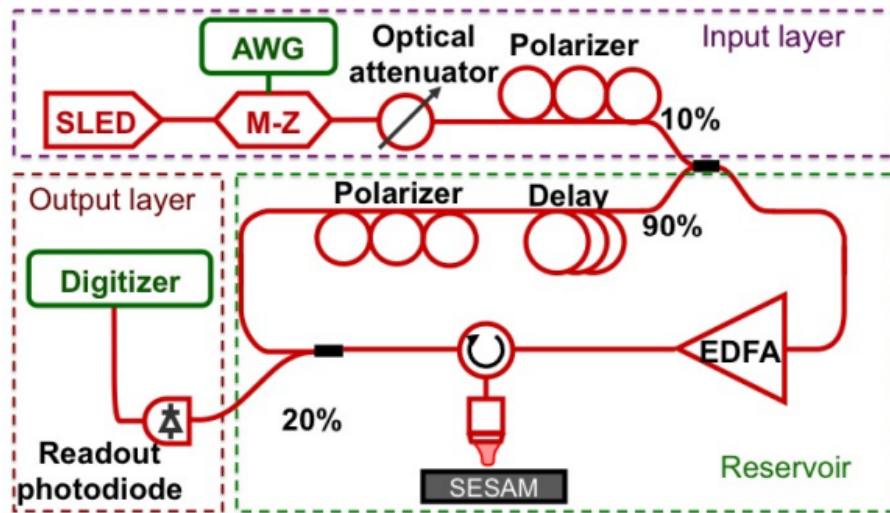


Figure 1.7: Schematic of all-optical reservoir computer. [Dej+14]

Additionally, all-analog optoelectronic computing systems excel in tasks that require the processing of continuous data streams, such as real-time signal processing, where their speeds can surpass those of traditional digital computing. Optical systems inherently offer high bandwidth and capacity, making them an ideal choice for handling

large-scale continuous data streams in applications like high-speed imaging and complex signal analysis. Techniques like optical reservoir computing can fully leverage the analog nature of signals in applications such as optical neural networks and advanced scientific simulations. Fig. 1.7 shows a setup for an optical reservoir computation where the semiconductor saturable absorber mirror (SESAM) provides a fully passive nonlinearity. photonic integration of these components will contribute to the efficiency and miniaturization of optical computers [Dej+14; VBS17].

1.1.4 Quantum photonics

Integrated optical quantum technology has enabled on-chip generation, processing, and detection of quantum states of light at scales and complexities ranging from few-component circuits occupying centimeter-sized dimensions and operating on two photons to close to thousands of components occupying millimeter-sized dimensions and integrally generating multi-photon states. Quantum light sources, nonlinear components, and quantum state detection components can be integrated into optical quantum chips for on-chip quantum key distribution (QKD), quantum computing, quantum sensing, and other applications [Cha+23; Die+16; Els+20].

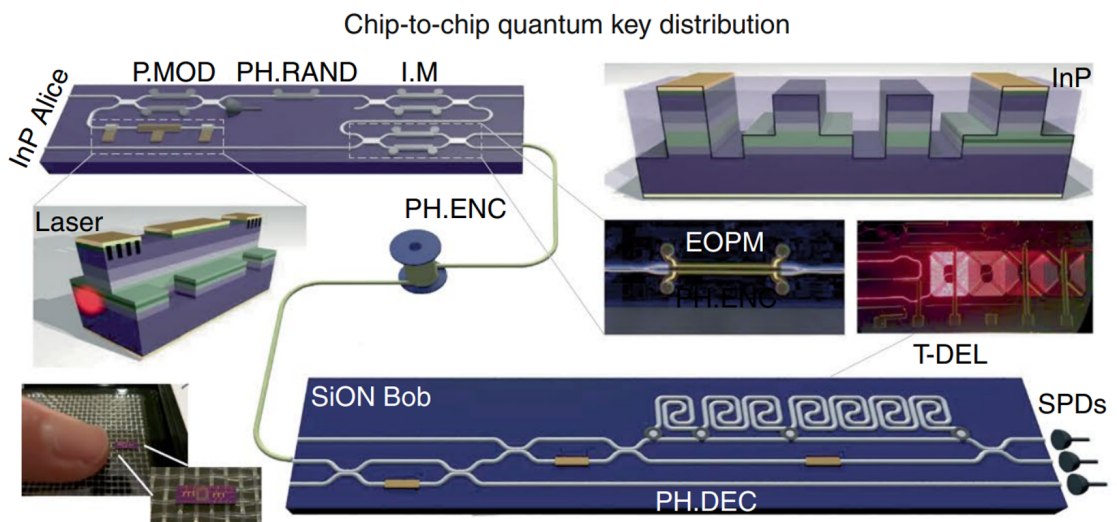


Figure 1.8: Integrated photonic devices based on InP-based and SiN-based quantum key distribution. [Sib+17]

In 2017, M. G. Thompson et al. reported a chip-based quantum state emitter based on indium phosphide (InP) and a receiver chip based on silicon nitride (SiN), achieving low-error-rate QKD operations with a GHz clock [Sib+17; Wan+20]. By integrating an InP single-mode laser to generate single-photon states and transmitting them to a separately integrated receiver for key distribution, they paved the way for the successful integration of QKD into future telecommunications networks. Alternatively, the multi-photon quantum state integrated on-chip can be used as a signal source for a continuous variable QKD chip (CV-QKD) [Pau22]. These devices, combined with integrated single-photon detectors, are instrumental in advancing the integration of QKD technology into next-generation telecom networks. Alternatively, on-chip generation of continuous or discrete variables combined with components such as homodyne detectors can enable on-chip quantum computing [Gu+09; Kok+07]. Another quantum application is in gravitational wave detection, e.g. in Laser Interferometer Gravitational-Wave Observatory (LIGO) where squeezed vacuum states have been introduced to increase the sensitivity of the detectors to detect gravitational waves [Sch+10; Zha+20]. On-chip squeezed state generators can lead to more portable gravitational wave detectors.

1.2 QD lasers for monolithic integration

To realize the needs of the above applications, it is challenging but interesting work to investigate the semiconductor light sources that can be integrated on PICs. Fig. 1.9 shows the impact of the quantization on the densities of states for bulk, quantum well (QW), quantum wire, and QD. These structures have carrier confinement in zero, one, two, and three dimensions, respectively. When the motion of the carriers in the crystal is confined to a small area (the potential well attracts both electrons and holes), the energy spectrum of the carriers is quantized [ANK19]. The three-dimensional quantum confinement effect of QD allows lasers with lower threshold current (I_{th}) and higher quantum efficiency, etc.

The 2023 Nobel Prize in chemistry recognized the discovery and synthesis of nanoscale semiconductor crystals and called QD the seed of nanoscience. In addition, the rapid development of self-assembled QD lasers using metal-organic chemical vapor deposition

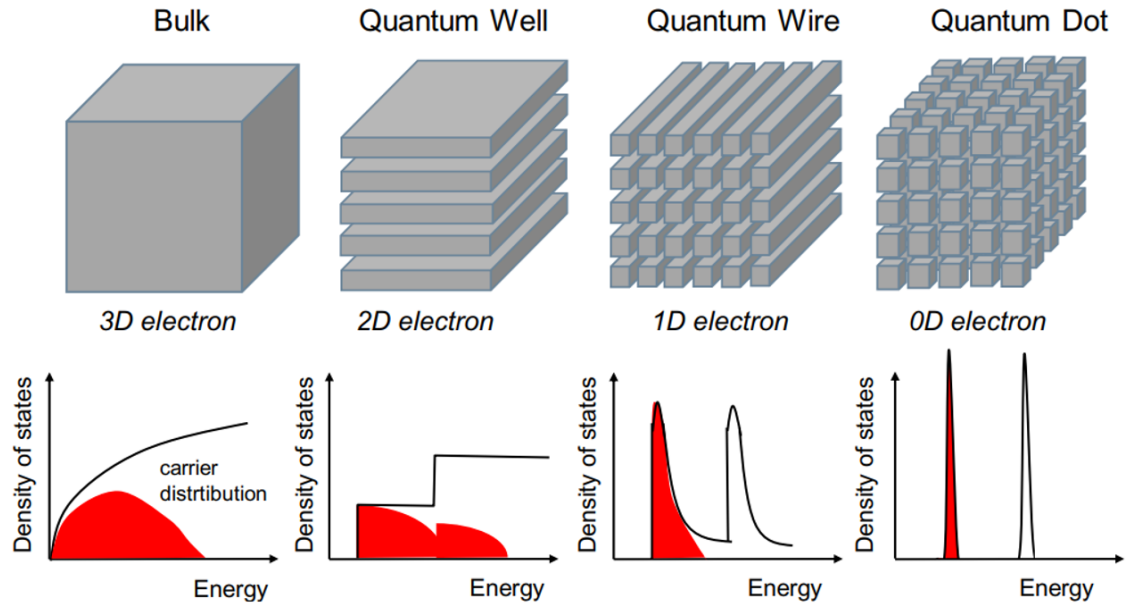


Figure 1.9: Impact of quantization on the density of states. [ANK19]

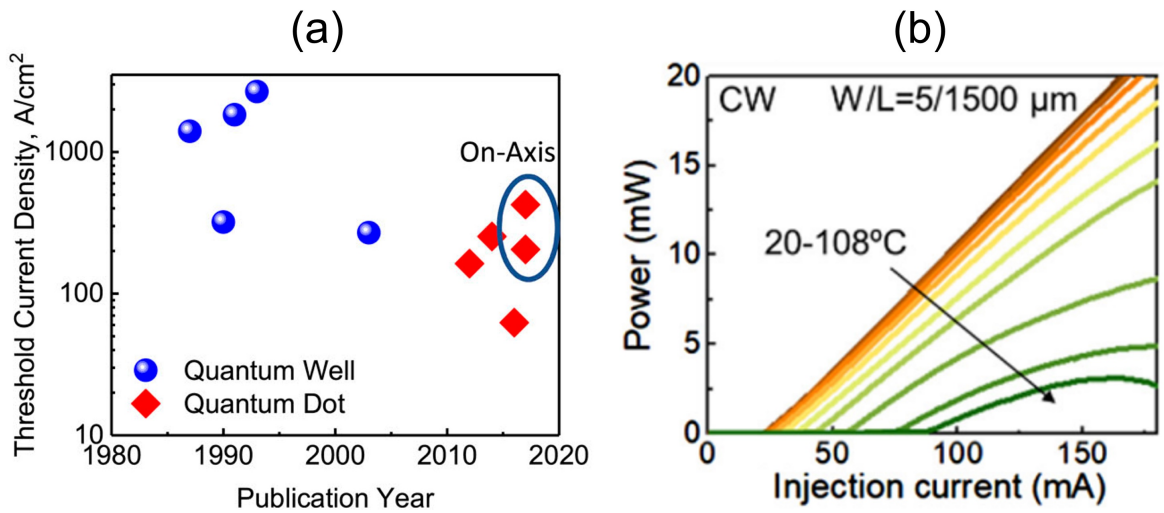


Figure 1.10: (a) Threshold current density of InAs/GaAs QD and QW lasers on silicon. [Nor+18] (b) The power-current curves at different temperatures of QD lasers. [Sha+21a]

(MOCVD), and molecular-beam epitaxy (MBE) epitaxy has been prepared by D. Bimberg's and Zh. I. Alferov's teams in 1994. The QDs are formed into three-dimensional dense nanostructures based on the Stranski-Krastanov (S-K) growth mode [BGL99; Gol+85; MS99]. In the manufacturing of PICs, a challenge that must be faced during the epitaxial growth of nanocrystals on silicon is the introduction of high-density crystal defects. These defects can limit the performance and lifespan of the devices. However, the unique electronic confinement properties of QDs reduce sensitivity to defect states like dislocation. The epitaxial growth of QD for making lasers, modulators, and photodetectors on silicon demonstrates the potential for low-cost, scalable integration. For QW lasers bonding on silicon, there is a large threshold current density. In 1999, the first QD laser with four-layer InGaAs QDs grown on silicon had a threshold current density of 3.85 kA/cm^2 at 80 K [Lin+99]. In 2018, on the CMOS-compatible on-axis (001) silicon substrate, the InAs/GaAs QD lasers can achieve threshold current densities of 200 A/cm^2 as shown in Fig. 1.10(a) [Nor+18]. For the epitaxial QD laser on-axis (001) silicon substrate, the stable output power can be maintained up to $108 \text{ }^\circ\text{C}$ as shown in Fig. 1.10(b) [Sha+21a].

1.3 Motivations

Through continuous research and optimized design of QD lasers, they not only exhibit excellent performance in terms of threshold current, power efficiency, and temperature stability but also demonstrate outstanding performance in noise suppression [AKB13; Dua+20]. In optical communication systems using advanced modulation formats such as quadrature amplitude modulation (QAM) and phase shift keying (PSK), there is a sensitivity to intensity noise, especially in high-speed, long-distance communication links. Intensity noise can directly lead to an increase in bit error rate (BER) and may reduce the overall throughput of the system [KH04]. To minimize the effect of intensity noise, laser sources with low-intensity noise are preferred in optical communication systems. Integratable silicon-based QD lasers are shown to have relative intensity noise (RIN) below -150 dB/Hz as shown in Fig. 1.11 [Lia+18].

Additionally, in a WDM system, the low and stable phase noise laser helps to

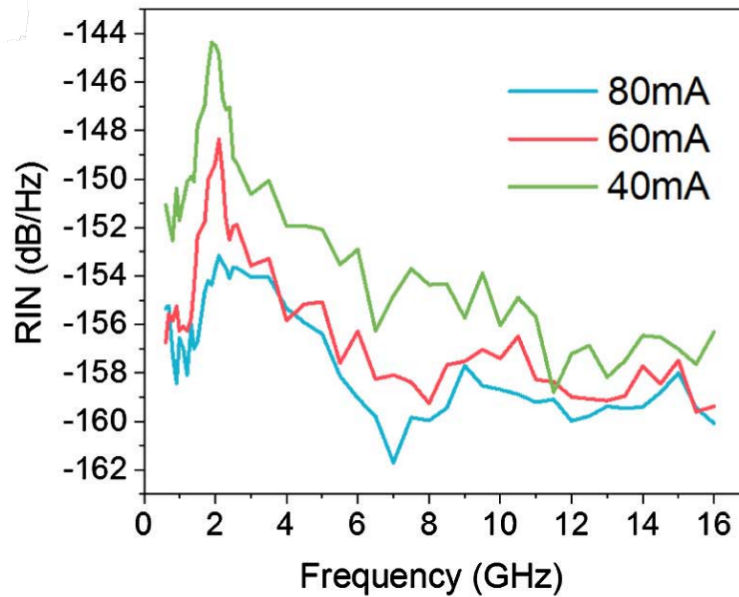


Figure 1.11: RIN spectra at bias currents of 40, 60, and 80 mA of an integrated silicon-based QD laser. [Lia+18]

improve the effectiveness of digital signal processing (DSP) algorithms in optical communication. The narrow linewidth of the laser means low phase noise, which maintains signal integrity over long distances and is critical for advanced modulation formats [Kaz86]. In optical sensing, the linewidth of the laser determines the resolution and sensitivity of the sensor [MM18]. Narrower line widths allow for more accurate measurements, which is especially important in applications such as interferometry, spectroscopy, and LiDAR systems. Also, the narrower the linewidth the longer the coherence length of the laser, favoring applications such as coherent LiDAR that require high coherence.

After designing monolithic QW lasers with structures like distributed feedback (DFB) and distributed Bragg reflector (DBR), linewidths of several hundred kHz can be achieved [Fau+12]. In recent years, monolithic QD lasers have reached linewidths with several kHz [Al+19]. Lasers integrated with micro-ring structures or self-injection configurations on silicon or SiN can achieve ultra-sharp linewidths down to the Hz level [Alk+23; Cho+22; Xia+21]. On-chip integrated narrow-linewidth light sources have provided breakthroughs for various applications. The narrow linewidth mechanism of

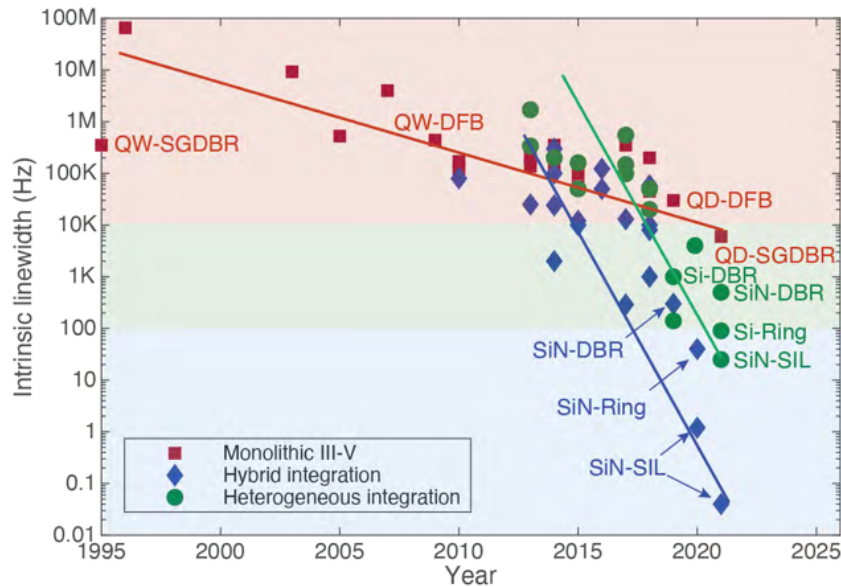


Figure 1.12: Progress in linewidth investigation of semiconductor lasers under three different integration methods. [Xia+21]

single-mode QD lasers warrants further research and discussion. Moreover, on-chip integrated QD comb lasers, especially directly modulated QD comb lasers, can raise the integration and enhance the optical transmission capacity [Kun+04]. In addition, the multi-mode signals of comb lasers can provide parallel channels for optical computing [Oka+23; Xu+20]. And QD multi-mode lasers make silicon-based integrated optical computing chips possible.

In addition to studying the inherent properties of semiconductor lasers, the dynamics of semiconductor lasers can be investigated using techniques such as optical feedback, optical injection, and optoelectronic feedback. The generated dynamics can be applied in the fields of optical communication, optical computing, optical sensing, etc [OO17]. The research on generating multiple dynamics for easily integrated QD lasers can help to expand the range of applications of PICs.

The on-chip squeezed state generation is facilitated by the easy epitaxial integration, low threshold current, and strong temperature stability of QD lasers. The PICs will also help in reducing coupling and transmission losses, ensuring the subsequent output application of the squeezed state. Utilizing QD lasers with photonic integration,

along with simple squeezed state generation methods such as low-noise pumps, optical feedback, and optical injection, will aid in the role of integrated quantum photonic chips in quantum communications and computing [Dut+15; GBY90].

1.4 Organization of this thesis

Based on the analysis of the current state of research and motivations, this dissertation is organized as follows:

Chapter 2 introduces the basic features of QD lasers. First, the electronic structures and equivalent circuits associated with QD lasers are presented. Second, the noise characteristics and linewidth enhancement factor (α_H -factor) of semiconductor lasers are introduced. Finally, α_H -factor experiments of QD multi-mode lasers and transmission experiments of silicon-based QD multi-mode lasers under optical feedback are demonstrated.

Chapter 3 presents the controlled dynamic generation characteristics of silicon-based QD lasers under optoelectronic feedback (OEF). The sensitivity of silicon-based QD lasers to OEF is higher than that of QW lasers, which has been confirmed by integral differential delay modeling and experimental time-domain signals. We believe that the various dynamic properties observed in silicon-based QD lasers with OEF loops can be effectively applied to areas such as integrated optical computing, logic, and sensing.

Chapter 4 investigates and discusses the externally injected carrier noise affecting the α_H -factor is also studied and discussed. Under quiet pumping conditions, the α_H -factor near the threshold is much smaller. Numerical modeling and experiments jointly verify this phenomenon. In addition, the simulation results show that using quiet pumping near the threshold current is beneficial to reduce the frequency noise and thus the optical linewidth. This gives us a better understanding of the noise characteristics of QD lasers. It serves as a reference for designing low-noise lasers.

Chapter 5 demonstrates the excellent squeezing performance of QD lasers under quiet pumping conditions. The squeezed states generated by QD lasers with injected carriers based on sub-Poissonian distribution show perfect optical feedback tolerance.

The noise-corrected maximum squeezing level of 5.7 dB essentially satisfies the needs of various applications. In addition, the second-order correlation function is analyzed for different feedback strengths, which perfectly match the theoretical values. This study establishes a comprehensive fundamental framework for designing compact and energy-efficient PICs integrating quantum squeezers.

Finally, Chapter 6 gives the general conclusions of this dissertation and perspectives on experimental and simulation aspects based on the current stage of research.

Bibliography

- [Alk+23] Emad Alkhazraji, Weng W Chow, Frédéric Grillot, John E Bowers, and Yating Wan. “Linewidth narrowing in self-injection-locked on-chip lasers”. In: *Light: Science & Applications* 12.1 (2023), p. 162.
- [ABC20] Nicola Andriolli, Francesca Bontempi, and Giampiero Contestabile. “InP monolithically integrated transmitters based on high speed directly modulated DFB lasers”. In: *IEEE Journal of Selected Topics in Quantum Electronics* 26.5 (2020), pp. 1–6.
- [AC17] Shamsul Arafin and Larry A Coldren. “Advanced InP photonic integrated circuits for communication and sensing”. In: *IEEE Journal of Selected Topics in Quantum Electronics* 24.1 (2017), pp. 1–12.
- [ANK19] Yasuhiko Arakawa, Takahiro Nakamura, and Jinkwan Kwoen. “Quantum dot lasers for silicon photonics”. In: *Semiconductors and Semimetals*. Vol. 101. Elsevier, 2019, pp. 91–138.
- [AKB13] Dejan Arsenijević, M Kleinert, and Dieter Bimberg. “Phase noise and jitter reduction by optical feedback on passively mode-locked quantum-dot lasers”. In: *Applied Physics Letters* 103.23 (2013).
- [BGL99] Dieter Bimberg, Marius Grundmann, and Nikolai N Ledentsov. *Quantum dot heterostructures*. John Wiley & Sons, 1999.
- [Cha+23] Jin Chang, Jun Gao, Iman Esmaeil Zadeh, Ali W Elshaari, and Val Zwiller. “Nanowire-based integrated photonics for quantum information and quantum sensing”. In: *Nanophotonics* 12.3 (2023), pp. 339–358.

-
- [CGV22] Qixiang Cheng, Madeleine Glick, and Thomas Van Vaerenbergh. “Special topic on photonics and AI in information technologies”. In: *APL Photonics* 7.8 (2022).
- [Cho+22] Weng W Chow, Yating Wan, John E Bowers, and Frédéric Grillot. “Analysis of the spontaneous emission limited linewidth of an integrated III–V/SiN laser”. In: *Laser & Photonics Reviews* 16.6 (2022), p. 2100620.
- [Dej+14] Antoine Dejonckheere, François Duport, Anteo Smerieri, Li Fang, Jean-Louis Oudar, Marc Haelterman, and Serge Massar. “All-optical reservoir computer based on saturation of absorption”. In: *Optics express* 22.9 (2014), pp. 10868–10881.
- [DMH23] Radosvet Desislavov, Fernando Martínez-Plumed, and José Hernández-Orallo. “Trends in AI inference energy consumption: Beyond the performance-vs-parameter laws of deep learning”. In: *Sustainable Computing: Informatics and Systems* 38 (2023), p. 100857.
- [Die+16] Christof P Dietrich, Andrea Fiore, Mark G Thompson, Martin Kamp, and Sven Höfling. “GaAs integrated quantum photonics: Towards compact and multi-functional quantum photonic integrated circuits”. In: *Laser & Photonics Reviews* 10.6 (2016), pp. 870–894.
- [Dua+20] Jianan Duan et al. “Effect of p-doping on the intensity noise of epitaxial quantum dot lasers on silicon”. In: *Optics Letters* 45.17 (2020), pp. 4887–4890.
- [Dut+15] Avik Dutt, Kevin Luke, Sasikanth Manipatruni, Alexander L Gaeta, Paulo Nussenzveig, and Michal Lipson. “On-chip optical squeezing”. In: *Physical Review Applied* 3.4 (2015), p. 044005.
- [Els+20] Ali W Elshaari, Wolfram Pernice, Kartik Srinivasan, Oliver Benson, and Val Zwiller. “Hybrid integrated quantum photonic circuits”. In: *Nature photonics* 14.5 (2020), pp. 285–298.
- [Fal+20] Fabio Falconi et al. “A combined radar & lidar system based on integrated photonics in silicon-on-insulator”. In: *Journal of Lightwave Technology* 39.1 (2020), pp. 17–23.

- [Fau+12] Mickaël Faugeron et al. “High-power tunable dilute mode DFB laser with low RIN and narrow linewidth”. In: *IEEE photonics technology letters* 25.1 (2012), pp. 7–10.
- [GBY90] Lars Gillner, Gunnar Björk, and Yoshihisa Yamamoto. “Quantum noise properties of an injection-locked laser oscillator with pump-noise suppression and squeezed injection”. In: *Physical Review A* 41.9 (1990), p. 5053.
- [Gol+85] L Goldstein, F Glas, JY Marzin, MN Charasse, and G Le Roux. “Growth by molecular beam epitaxy and characterization of InAs/GaAs strained-layer superlattices”. In: *Applied Physics Letters* 47.10 (1985), pp. 1099–1101.
- [Gu+09] Mile Gu, Christian Weedbrook, Nicolas C Menicucci, Timothy C Ralph, and Peter van Loock. “Quantum computing with continuous-variable clusters”. In: *Physical Review A* 79.6 (2009), p. 062318.
- [HO21] Hao Hu and Leif K Oxenløwe. “Chip-based optical frequency combs for high-capacity optical communications”. In: *Nanophotonics* 10.5 (2021), pp. 1367–1385.
- [KH04] Joseph M Kahn and Keang-Po Ho. “Spectral efficiency limits and modulation/detection techniques for DWDM systems”. In: *IEEE Journal of selected topics in quantum electronics* 10.2 (2004), pp. 259–272.
- [Kaz86] L Kazovsky. “Performance analysis and laser linewidth requirements for optical PSK heterodyne communications systems”. In: *Journal of light-wave technology* 4.4 (1986), pp. 415–425.
- [Kok+07] Pieter Kok, William J Munro, Kae Nemoto, Timothy C Ralph, Jonathan P Dowling, and Gerard J Milburn. “Linear optical quantum computing with photonic qubits”. In: *Reviews of modern physics* 79.1 (2007), p. 135.
- [Kra+19] Michael Krainak et al. “Integrated photonics for NASA applications”. In: *Components and Packaging for Laser Systems V*. Vol. 10899. SPIE. 2019, pp. 75–94.
- [Kun+04] M Kuntz et al. “Direct modulation and mode locking of 1.3 μm quantum dot lasers”. In: *New Journal of Physics* 6.1 (2004), p. 181.

- [Li+22] Nanxi Li, Chong Pei Ho, Jin Xue, Leh Woon Lim, Guanyu Chen, Yuan Hsing Fu, and Lennon Yao Ting Lee. “A progress review on solid-state LiDAR and nanophotonics-based LiDAR sensors”. In: *Laser & Photonics Reviews* 16.11 (2022), p. 2100511.
- [Lia+18] Mengya Liao et al. “Low-noise 1.3 μm InAs/GaAs quantum dot laser monolithically grown on silicon”. In: *Photonics Research* 6.11 (2018), pp. 1062–1066.
- [Lin+99] KK Linder, J Phillips, O Qasaimeh, XF Liu, S Krishna, P Bhattacharya, and JC Jiang. “Self-organized In 0.4 Ga 0.6 As quantum-dot lasers grown on Si substrates”. In: *Applied physics letters* 74.10 (1999), pp. 1355–1357.
- [MM18] Paul A Morton and Michael J Morton. “High-power, ultra-low noise hybrid lasers for microwave photonics and optical sensing”. In: *Journal of Lightwave Technology* 36.21 (2018), pp. 5048–5057.
- [MS99] Kohki Mukai and Mitsuru Sugawara. “Suppression of temperature sensitivity of interband emission energy by an InGaAs overgrowth on self-assembled InGaAs/GaAs quantum dots”. In: *Technical Digest. Summaries of papers presented at the Conference on Lasers and Electro-Optics. Post-conference Edition. CLEO’99. Conference on Lasers and Electro-Optics (IEEE Cat. No. 99CH37013)*. IEEE. 1999, p. 489.
- [Nis+18] Hidetaka Nishi et al. “Integration of eight-channel directly modulated membrane-laser array and SiN AWG multiplexer on Si”. In: *Journal of Lightwave Technology* 37.2 (2018), pp. 266–273.
- [Nor+18] J. Norman, D. Jung, Y. T. Wan, and J. E. Bowers. “Perspective: The future of quantum dot photonic integrated circuits”. In: *APL photonics* 3.3 (2018), p. 030901.
- [OO17] Junji Ohtsubo and Junji Ohtsubo. *Semiconductor lasers and theory*. Springer, 2017.
- [Oka+23] Yoshitomo Okawachi, Bok Young Kim, Michal Lipson, and Alexander L Gaeta. “Chip-scale frequency combs for data communications in computing systems”. In: *Optica* 10.8 (2023), pp. 977–995.

- [Pas+12] Vittorio MN Passaro, Corrado de Tullio, Benedetto Troia, Mario La Notte, Giovanni Giannoccaro, and Francesco De Leonardis. “Recent advances in integrated photonic sensors”. In: *Sensors* 12.11 (2012), pp. 15558–15598.
- [Pau22] Tuhin Paul. “Photonic Integration with III-V Semiconductor Technologies”. PhD thesis. Université d’Ottawa/University of Ottawa, 2022.
- [Al-+19] Mustafa Al-Qadi, Maurice O’Sullivan, Chongjin Xie, and Rongqing Hui. “Phase noise measurements and performance of lasers with non-white FM noise for use in digital coherent optical systems”. In: *Journal of Lightwave Technology* 38.6 (2019), pp. 1157–1167.
- [Sch+10] Roman Schnabel, Nergis Mavalvala, David E McClelland, and Ping K Lam. “Quantum metrology for gravitational wave astronomy”. In: *Nature communications* 1.1 (2010), p. 121.
- [Sha+21a] C. Shang et al. “High-temperature reliable quantum-dot lasers on Si with misfit and threading dislocation filters”. In: *Optica* 8.5 (2021), pp. 749–754.
- [Sha+21b] Bhavin J Shastri, Alexander N Tait, Thomas Ferreira de Lima, Wolfram HP Pernice, Harish Bhaskaran, C David Wright, and Paul R Prucnal. “Photonics for artificial intelligence and neuromorphic computing”. In: *Nature Photonics* 15.2 (2021), pp. 102–114.
- [Sib+17] Philip Sibson et al. “Chip-based quantum key distribution”. In: *Nature communications* 8.1 (2017), p. 13984.
- [Tak+18] Kosuke Takano, Chihiro Sugano, Masanobu Inubushi, Kazuyuki Yoshimura, Satoshi Sunada, Kazutaka Kanno, and Atsushi Uchida. “Compact reservoir computing with a photonic integrated circuit”. In: *Optics express* 26.22 (2018), pp. 29424–29439.
- [VBS17] Guy Van der Sande, Daniel Brunner, and Miguel C Soriano. “Advances in photonic reservoir computing”. In: *Nanophotonics* 6.3 (2017), pp. 561–576.

-
- [Wan+20] J. W. Wang, F. Sciarrino, A. Laing, and M. G. Thompson. “Integrated photonic quantum technologies”. In: *Nature Photonics* 14.5 (2020), pp. 273–284.
- [Xia+21] Chao Xiang, Steven M Bowers, Alexis Bjorlin, Robert Blum, and John E Bowers. “Perspective on the future of silicon photonics and electronics”. In: *Applied Physics Letters* 118.22 (2021).
- [Xu+20] Xingyuan Xu et al. “Photonic perceptron based on a Kerr Microcomb for high-speed, scalable, optical neural networks”. In: *Laser & Photonics Reviews* 14.10 (2020), p. 2000070.
- [Zha+20] Yuhang Zhao et al. “Frequency-dependent squeezed vacuum source for broadband quantum noise reduction in advanced gravitational-wave detectors”. In: *Physical review letters* 124.17 (2020), p. 171101.

CHAPTER 2

Fundamentals of Quantum Dot Lasers

This chapter intends to review the basic features of QD lasers. First, the electronic structure and the equivalent circuit are introduced. Secondly, the noise characteristics and linewidth enhancement factor are presented. Finally, the effect of the optical feedback tolerance of QD lasers on the direct-modulation experiments is presented.

2.1 Electronic structure

The development of laser technology is marked by a continuous drive to manipulate light and matter on ever smaller scales, leading to significant advances in performance and applications. QD lasers allow precise control of the size and shape of the quantum dots, enabling customization of their optical properties [Gar+21]. Fig. 2.1 shows a schematic diagram of the conduction band (CB) part of the electronic structure of a QD laser. It can be found that the active medium is made of a three-dimensional barrier layer or separate confinement heterostructure (SCH), a two-dimensional carrier reservoir state (RS), and spatially three-dimensionally constrained dots. A band offset ΔE_c of the corresponding band in the active medium can be observed. And the critical diameter D_{\min} of the QD laser is closely related to ΔE_c . The relationship between them satisfies the following equation [BGL99].

$$D_{\min} = \frac{\pi\hbar}{\sqrt{(2m_e^*\Delta E_c)}} \quad (2.1)$$

where the critical value of the QD size D_{\min} can be derived according to the condition of the existence of at least one electron or hole energy level or both of them. \hbar is the reduced Planck constant and m_e^* is the effective electron mass. This is also the criterion for discrete potential well determination. Based on the diameter of the self-assembled QDs, it can be assumed that the electronic structure of the QD laser is a three-dimensional potential well containing discretized energy levels.

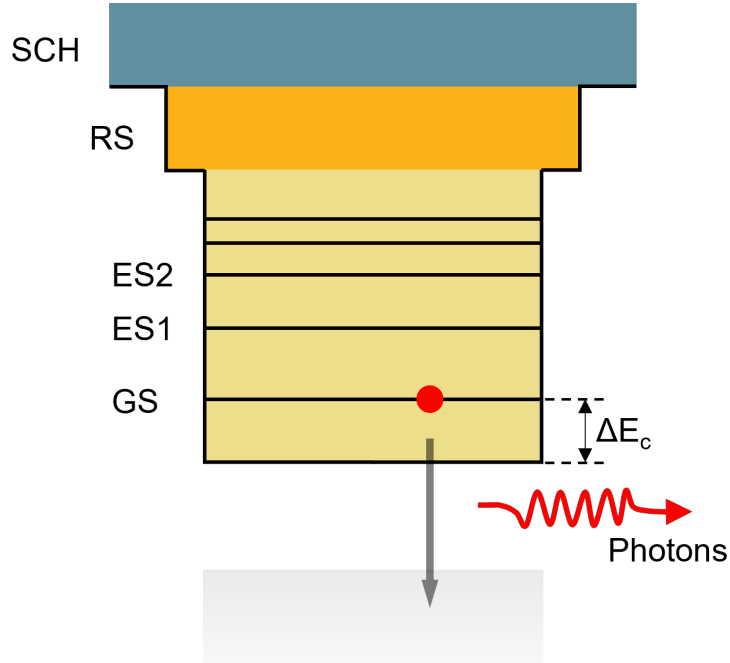


Figure 2.1: Electronic schematic of a QD (conductive band).

Quasi-continuum carrier reservoirs contain localized energy states of dots, resulting in small energy separations and therefore overlapping states at higher energies. At lower energies, the discrete states in the conductive band (CB) are separated by tens of meV. From the charge carriers generated in the SCH layer that begin to track the flow of carriers in the QD laser, the carriers then pass through the SCH layer and arrive at the RS. The thickness of the SCH determines the carrier transport time in this section, generally on the order of a few picoseconds [Ura+01; Usk+98]. The

carriers then enter the active medium where the dynamics are driven by three main processes: carrier capture, carrier relaxation, and carrier escape. The capture process is the process by which carriers are captured from the RS to the excited states (ES₁ and ES₂), and even directly from the RS to the ground state (GS). Moreover, carriers will be relaxed from the high-energy ES to the GS. In addition, few carriers will escape from GS to ES or even to RS, and the carriers in GS will undergo stimulated emission in GS due to recombination between electrons and holes. Of course, carriers can also undergo excited emission at ES, and there is a quenching mechanism for the emissions at GS and ES [FMB05].

2.2 Equivalent circuit

The semiconductor laser, as a typical optoelectronic device, has static characteristics that can be equated to a circuit consisting of a resistor, a capacitor, and an inductor [Har+82]. Resistance models the damping generated by the spontaneous and stimulated recombination. In addition, a nonradiation composite portion is also included. The inductance represents the resonance phenomenon of the laser. The capacitance contains the diffusion capacitance C_d of the active layer and the space charge capacitance C_{sc} .

In the case of a simple single-mode semiconductor laser, for example, the rate equations for the carrier (N) and photon densities (S) can be closely related to the parameters of the equivalent circuit. The single-mode semiconductor laser can be decomposed into three equivalent circuits, parasitic circuit, electrical circuit, and optical circuit, as shown in Fig. 2.2. Then based on the relationship of the current flowing through each element, the system of equations for the electrical and optical circuits can be obtained [Din+22].

$$I = C_d \frac{dV_j}{dt} + I_n + I_r + I_{st} \quad (2.2)$$

$$\Gamma_p \beta_{sp} I_r + \Gamma_p I_{st} = C_{ph} \frac{dV_{ph}}{dt} + \frac{V_{ph}}{R_{ph}} \quad (2.3)$$

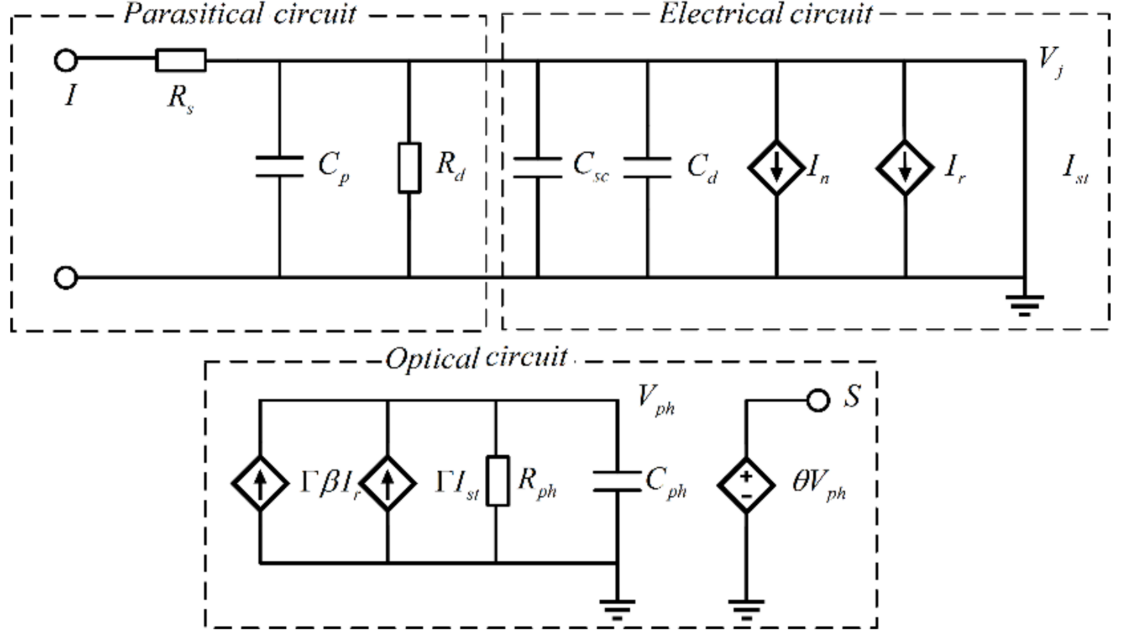


Figure 2.2: Equivalent circuit model diagram of a single mode semiconductor laser. It includes three parts: parasitic circuit, electrical circuit, and optical circuit. [Din+22]

where I is the injection current and V_j is the junction voltage. I_n , I_r , and I_{st} are the nonradiative recombination current, radiative recombination current, and stimulated emission current. Γ_p is the optical confinement factor, β_{sp} is the spontaneous emission factor. $V_{ph} = SV_a V_T$ is the optical voltage related to the photon density S , the thermal voltage V_T and the active layer volume V_a . $R_{ph} = V_T \tau_p / q$ and $C_{ph} = q / V_T$ are the equivalent resistance and capacitance of the optical circuit part, where the τ_p is photon lifetime and q is the elementary charge. The rate equations for a semiconductor laser can be obtained by bringing in the following expression.

$$C_d = \frac{qVN_e}{2V_T} \exp\left(\frac{V_j}{2V_T}\right) \quad (2.4)$$

$$I_n = qVR_n(N) \quad (2.5)$$

$$I_r = qVR_r(N) \quad (2.6)$$

$$I_{st} = qV \frac{g_0 (N - N_0)}{1 + \varepsilon S} S \quad (2.7)$$

$$N = N_e [e^{V_j/2V_T} - 1] \quad (2.8)$$

where the N_e is the equilibrium carrier density. N_0 is the transparent carrier concentration. ε is the gain compression factor, g_0 is the gain coefficient, τ_n is the carrier lifetime, $R_n(N)$ is the rate of nonradiative recombination while the $R_r(N)$ is radiative recombination rate. Thus, the rate equations of semiconductor lasers with simple energy structures are as follows.

$$\frac{dN}{dt} = \frac{I}{qV_a} - R_n(N) - R_r(N) - \frac{g_0 (N - N_0)}{1 + \varepsilon S} S \quad (2.9)$$

$$\frac{dS}{dt} = \Gamma_p \frac{g_0 (N - N_0)}{1 + \varepsilon S} S + \Gamma_p \beta_{sp} \frac{N}{\tau_n} - \frac{S}{\tau_p} \quad (2.10)$$

For QD lasers with complex carrier energy level structures as in Fig. 2.1, it is necessary to consider their RS and ES equivalent circuits. In addition, for complex carrier dynamics, the rate equations for small-signal analysis are worth investigating.

2.3 Noise characteristics

In semiconductor lasers, the lasing process is affected by quantum fluctuations, which alter the intensity and phase of the optical field. This leads to variations in both frequency and intensity, known as frequency and intensity noise [CKS12].

2.3.1 Intensity noise

Based on the rate equations in the previous section, it is clear that a static parameter such as output power, can be simulated by determining the injection current as well

as other laser parameters. The relationship between output power $P(t)$ and photon density of a semiconductor laser is as follows [Din+22].

$$P(t) = \frac{h\nu c}{2n_r L} \frac{\ln(1/(R_1 R_2)) (1 - R_1)}{(1 - \sqrt{R_1 R_2}) (1 + \sqrt{R_1/R_2})} S(t) \quad (2.11)$$

where the $h\nu$ is the photon energy corresponding to the wavelength emitted by the laser, c/n_r is the speed of light in a medium with a refractive index of n_r , L is the cavity length of the laser. R_1 and R_2 are the reflectivities of the cavity facets on two sides. For the ideal case, where there is no carrier and photon noise, the output power over time is constant (P_0), as shown in the left panel of Fig. 2.3. For real output power, spontaneous emission and carrier noise will induce intrinsic power fluctuations with a variance of $\delta P(t)^2$ as shown in the right panel of Fig. 2.3 [CCM12].

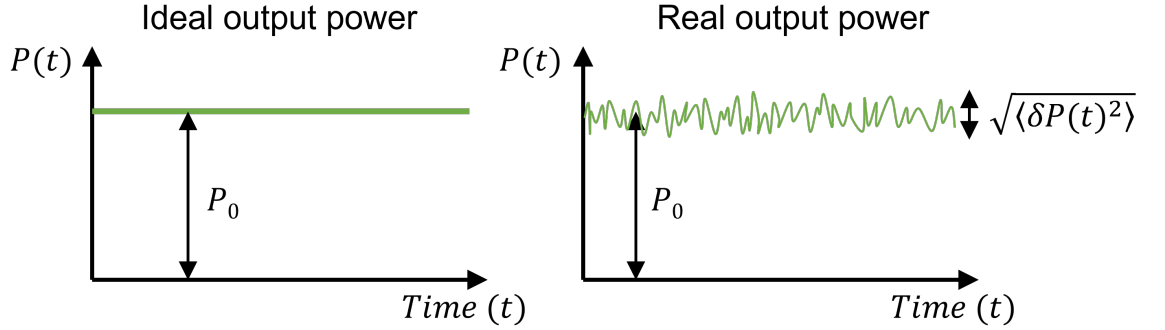


Figure 2.3: Schematic diagram of the ideal and real output power of a semiconductor laser with DC pump.

Relative Intensity Noise (RIN) quantifies the level of noise associated with intensity fluctuations of a light source. The RIN of a laser is defined as follows.

$$RIN = \frac{\langle \delta P(t)^2 \rangle}{P_0^2} \quad (2.12)$$

A louder RIN reduces the signal-to-noise ratio (SNR), which reduces the BER of an optical communication system [AY08]. Although the SNR can be remedied by increasing the pump current, it increases energy consumption. Therefore, low RIN

lasers have been the priority of research. QD lasers have proven to be a low RIN light source, with InAs/GaAs QD devices having RIN levels as low as -150 to -160 dB/Hz [Cap+07; Gri+21]. These noise studies are restricted to classical noise. In the quantum realm, it has been shown that controlling the injected carrier noise can reduce the RIN below than quantum limit [YMN86], which is part of Chapter 5 on squeezed states that needs to be emphasized.

2.3.2 Frequency noise

In the model, by standard small-signal analysis of the rate equation with Langevin noise, the phase variation $\delta\phi(\omega)$ in the frequency domain of the laser field can be obtained, ω being the angular frequency. The relation between frequency noise (FN) and the phase variance is expressed as [Dua+18b; Oht08],

$$FN(\omega) = \left| \frac{j\omega}{2\pi} \delta\phi(\omega) \right|^2 \quad (2.13)$$

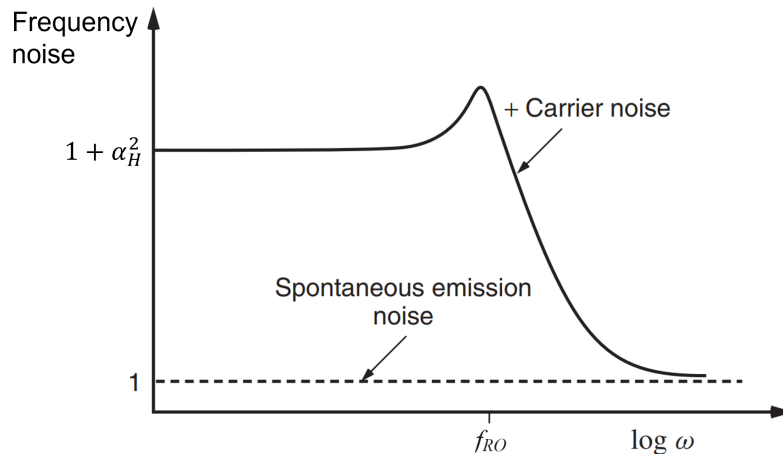


Figure 2.4: Frequency noise spectrum showing the contribution of carrier noise and spontaneous emission noise. [CCM12]

Low-frequency flicker noise, spontaneous emission noise, and noise caused by the flow and combination of carriers in each energy level collectively determine the FN

in semiconductor lasers. The remaining noise sources control the intrinsic spectral linewidth of the laser. Fig. 2.4 illustrates the different contributors to the FN and their effect on the noise curve. When the frequency is much higher than the relaxation oscillation frequency f_{RO} , the spontaneous emission noise determines the Schawlow-Townes linewidth $\Delta\nu_{ST}$. The $\Delta\nu_{ST}$ has the following relationship with the parameters of the semiconductor laser [CCM12].

$$\Delta\nu_{ST} = \frac{\Gamma_p g_{m,th} v_g^2 \alpha_m h\nu}{4\pi P_0} n_{sp} \quad (2.14)$$

where $g_{m,th}$ is the material gain at threshold. v_g is the group velocity. α_m is the mirror loss of the laser cavity. n_{sp} is the population inversion factor. However, when the frequency is much lower than the f_{RO} , the spontaneous emission and carrier fluctuations together shape the laser linewidth and broaden the ST linewidth by a factor of $(1 + \alpha_H^2)$, denoted as $\Delta\nu = \Delta\nu_{ST}(1 + \alpha_H^2)$ with α_H the linewidth enhancement factor.

2.3.3 Linewidth enhancement factor

In 1967, while investigating the noise theory of oscillators, M. Lax found that phase fluctuations made them unstable and broadened the signal line width [Lax67]. In the same year, H. Haug and H. Haken derived the oscillator equations with a fluctuation-driven term from first principles to describe the complex field amplitude of semiconductor lasers [HH67]. The noise of the linewidth and laser emission intensity above and below the threshold was calculated. At this time, the linewidth enhancement factor had not been conceptualized. In 1982, C. H. Henry introduced a model for the linewidth of single-mode semiconductor lasers and the concept of linewidth enhancement factor [Hen82]. Additionally, A. Yariv and colleagues developed a noise theory for semiconductor lasers, treating carrier density as a dynamic variable. This theory integrates the relationship between carrier density and refractive index [HVV83; Vah+83].

According to the Lamb semiclassical laser treatment [Lam64], the laser field E is related to the macroscopic polarization $P_r = \epsilon_0 \chi E$ [CKS12]. ϵ_0 is the vacuum permittivity and χ is the complex optical susceptibility ($\chi = \chi_r + i\chi_i$). E is the electric field amplitude. The material gain (G) and carrier-induced refractive index

(δn) are related to the imaginary and real parts of the susceptibility respectively, and their expressions are given below for a fixed carrier number N ,

$$G = -\frac{\omega}{c} \text{Im}\{\chi\} = -\frac{\omega}{\epsilon_0 c} \frac{\text{Im}\{P_r\}}{E} \quad (2.15)$$

$$\delta n = \frac{1}{2} \text{Re}\{\chi\} = \frac{1}{2\epsilon_0} \frac{\text{Re}\{P_r\}}{E} \quad (2.16)$$

The α_H -factor of the coupling between gain and refractive index change, i.e., amplitude and phase, is expressed as follows [OB87; Yam+93],

$$\alpha_H = \frac{\partial \chi_r / \partial N}{\partial \chi_i / \partial N} = -2 \frac{\omega}{c} \frac{d\delta n / dN}{dG / dN} = -\frac{4\pi}{\lambda} \frac{d\delta n / dN}{dG / dN} \quad (2.17)$$

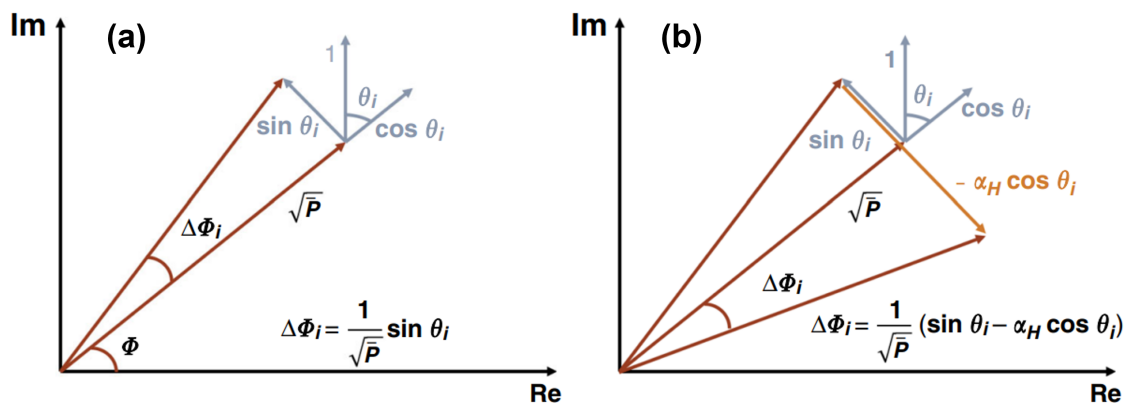


Figure 2.5: The schematic diagrams illustrate that the phase variations is affected by (a) the direct effect of spontaneous emission only and (b) the combined effect of spontaneous emission and phase-amplitude coupling. [Gri+21]

with λ the lasing wavelength, $d\delta n/dN$ the differential refractive index, dG/dN the differential gain. Fig. 2.5 illustrates how spontaneous emission and the carrier noise influence the phase fluctuations of a laser, consequently affecting FN and optical linewidth [Gri+21]. The gray arrows represent the phase fluctuations due to spontaneous emission, while the orange arrows indicate the region of phase fluctuations due to carrier noise-induced α_H -factor changes. The QD lasers have also been demonstrated to have low FN and α_H -factor [Alk+23; Wan+21a], as analyzed in Chapter 4.

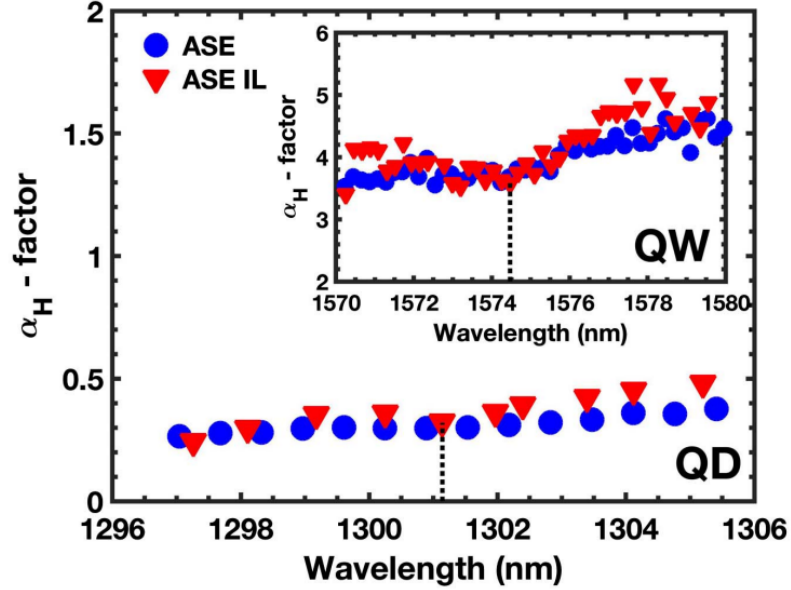


Figure 2.6: Spectral dependence of the α_H -factor measured by ASE methods for the epitaxial QD laser. The inset shows the α_H -factor values for the QW laser. [Dua+19b]

In pursuit of massive data transmission capabilities and increased integration density for silicon-based photonic integrated circuits, QD lasers present superior integration compatibility with silicon chips compared to QW lasers. The α_H -factor of QD lasers is significantly smaller than that of their QW counterparts, thanks to the more symmetric gain profile in the QD active medium. Fig. 2.6 depicts a QD laser exhibiting a wavelength-dependent alpha less than 0.5, and even as low as 0.3 around the gain peak. In contrast, the QW laser's alpha factor can be up to an order of magnitude greater than that of the QD laser [Dua+19b]. Such stark differences underscore the superior characteristics of QD lasers.

A higher α_H -factor typically increases the laser's sensitivity to optical feedback. This means that even minimal levels of optical feedback can lead to significant changes in laser output, thereby reducing the threshold for feedback-induced effects such as coherence collapse or mode hopping. Lasers with a larger α_H -factor may exhibit a broader range of dynamic behaviors under optical feedback, including periodic oscillations and chaos at lower levels of feedback. As illustrated in Fig. 2.7, the spectral and frequency variations of QD and QW lasers under optical feedback are compared.

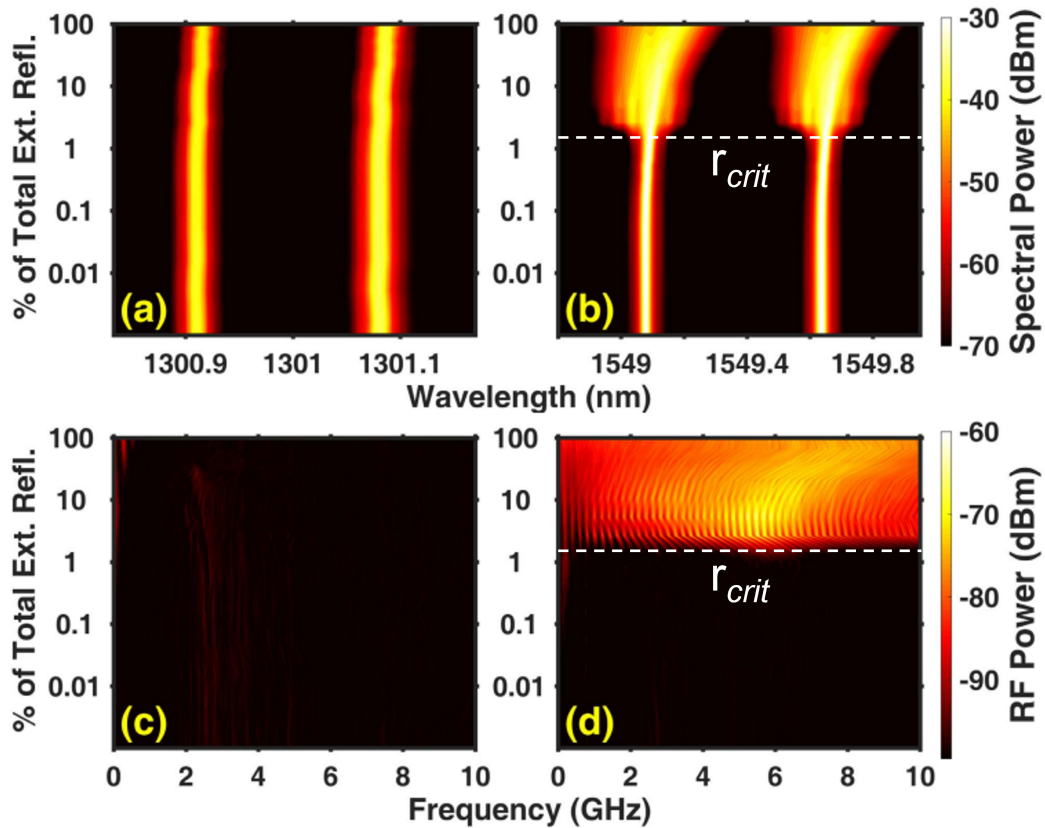


Figure 2.7: (a) Optical and (c) RF spectral mappings of the QD laser as a function of the feedback strength; (b) Optical and (d) RF spectral mappings of the QW laser as a function of the feedback strength. [Dua+19a]

The QW laser with a larger α_H -factor experiences dynamic transitions at around 3% optical feedback intensity, while the QD laser remains stable under any level of optical feedback [Dua+19a]. Therefore, the α_H -factor directly influences the occurrence of optical instabilities under optical feedback. This bifurcation point is defined as the critical feedback level (r_{crit}), which can be estimated by the following expression [CCM12; Don+19; HP90],

$$r_{crit} \propto \frac{1 + \alpha_H^2}{\alpha_H^4} \quad (2.18)$$

2.4 Spectral dependent α_H -factor for QD lasers

The α_H -factor plays a pivotal role in the coherent phenomena exhibited by semiconductor lasers. Notably, previous research has demonstrated that the dynamics of frequency combs in QD lasers are significantly influenced by FWM via the α_H -factor [Dua+22]. Additionally, this parameter has been associated with the generation of frequency-modulated combs [Don+21]. In light of these findings, acquiring accurate measurements of the α_H -factor's dispersion throughout the entire optical spectrum is essential for a more comprehensive understanding of how this parameter affects frequency comb dynamics. Preliminary investigations on the α_H -factor of quantum cascade laser (QCL) have been conducted [Opa+21]. In this section, we will demonstrate the spectral dispersion of the α_H -factor investigated in an InAs/GaAs QD multi-mode laser. For this purpose, the optical phase modulation technique was used to track the α_H -factor parameter of each longitudinal mode above the threshold. The results are also compared to a reference QW laser.

2.4.1 Introduction of α_H -factor extraction techniques

► Amplified spontaneous emission (ASE)

To more completely evaluate the influence of the α_H -factor on laser performance, it is essential to determine this parameter with high accuracy. The α_H -factor can be extracted by several methods. Some measurement techniques give access to the material α_H -factor whereas some others reflect the device α_H -factor.

Below the lasing threshold, the ASE method is commonly used to extract the spectral-dependent material α_H -factor [HC83]. It relies on measuring the net modal gain change (dG) and tracking the wavelength shift at different sub-threshold bias currents which reflects the differential refractive index (dn). The differential refractive index is determined by monitoring the shift in frequency of the longitudinal mode resonance. Concurrently, the differential gain is ascertained by quantifying the net modal gain (G_{net}) reflected as the gain ripple within the ASE spectrum. This differential gain corresponds to the variation in net modal gain, which can be extracted using the following expression [Bog+00; Dua+18a]:

$$G_{net} = \frac{1}{L} \ln \left(\frac{1}{\sqrt{R_1 R_2}} \frac{\sqrt{x} - 1}{\sqrt{x} + 1} \right) \quad (2.19)$$

where L is the cavity length, x is the peak-to-valley intensity ratio, and R_1 and R_2 are the front and rear facets, respectively. The differential refractive index within the active layer is connected to the shift in wavelength λ_m through the relation $d\lambda_m/\lambda_m = \Gamma_p dn/n$, where λ_m is the central modal wavelength and n is the refractive index. This relationship suggests that the α_H -factor can be reformulated in terms of a measurable parameter, as demonstrated by the following formula,

$$\alpha_H = - \frac{4n\pi}{\lambda_m^2} \frac{d\lambda_m/dI}{dG_{net}/dI} \quad (2.20)$$

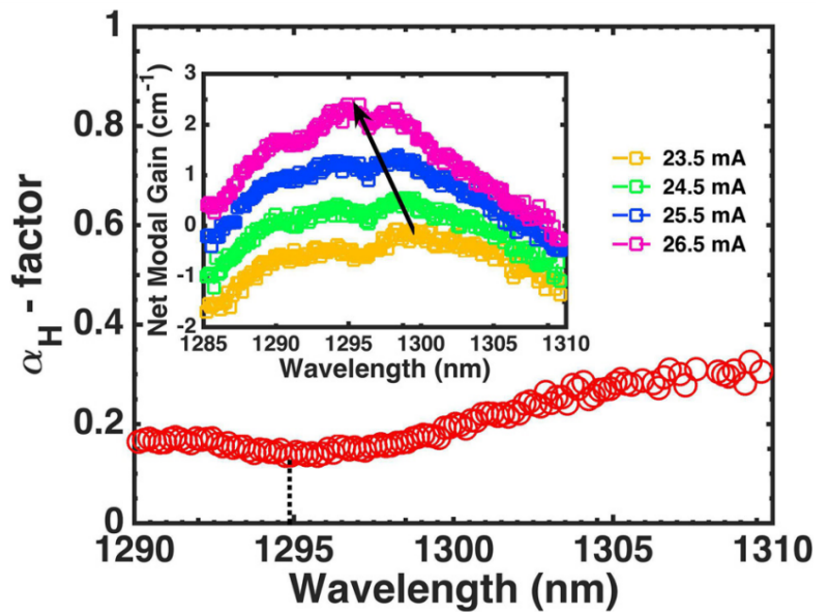


Figure 2.8: The α_H -factor as a function of wavelength for a p-doped QD laser at room temperature. The black dashed line indicates the peak FP gain (1295 nm). The inset indicates the net modal gain spectra for different sub-threshold bias current conditions. [Dua+18a]

As depicted in the inset of Fig. 2.8, the net modal gain which varies with different currents is illustrated. By correlating the data on wavelength shifts with the previously mentioned equations, the dependency of α_H -factor on the wavelength can be ascertained, a relationship that is graphically represented in Fig. 2.8. It is important to

note, however, that this approach is not applicable for extracting the α_H -factor above the threshold current and is susceptible to temperature-induced variations if thermal conditions are not properly addressed.

► Optical injection-locking

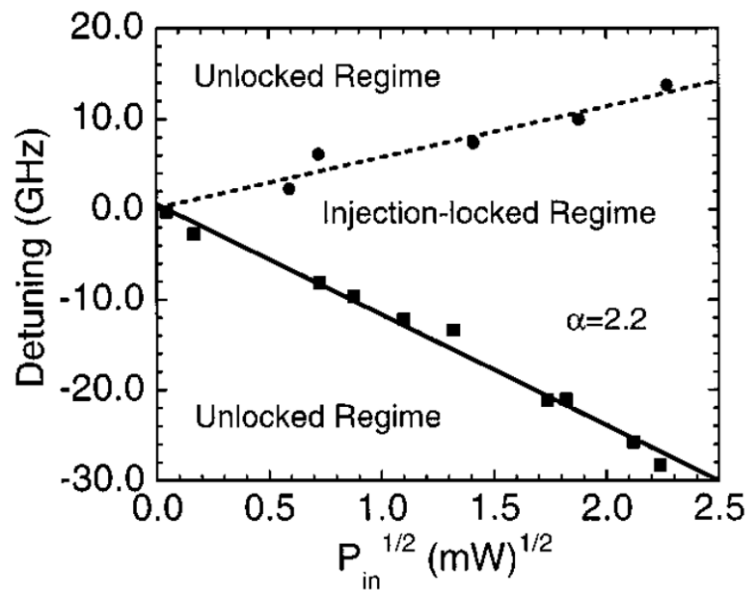


Figure 2.9: The locked and unlocked states separated by the injected boundaries are used for the α_H -factor extraction. [LJC01]

The measurement of α_H -factor above the threshold relies on other measurement methods, such as the optical injection-locking. In this technique, a single-mode master laser serves as the source for injecting light into the slave laser. The slave laser should be a multi-mode operation to be easily locked. Once the mode of the slave laser has been successfully injection-locked, it's necessary to adjust both the input power and the frequency detuning ($\Delta\omega$) of the master laser. Following these adjustments, the output power and the frequency detuning parameters of the slave laser should be documented to confirm the regimes of injection-locked and unlocked. Fig. 2.9 illustrates the locking range of the slave laser as determined by optical injection. The clear boundaries between linear injection-locked and unlocked are observable, and the

boundaries for positive and negative detuning are asymmetric due to the non-zero α_H -factor.

The overall locking range of semiconductor lasers can be characterized by an expression for the asymmetric locking bandwidth $[\Delta f_{\min} \Delta f_{\max}]$ derived from the rate equations as follows [Pet+88].

$$\Delta f_{\min} = -\frac{c}{2nL} \sqrt{\frac{S_i}{S} (1 + \alpha_H^2)} < \Delta f < \frac{c}{2nL} \sqrt{\frac{S_i}{S}} = \Delta f_{\max} \quad (2.21)$$

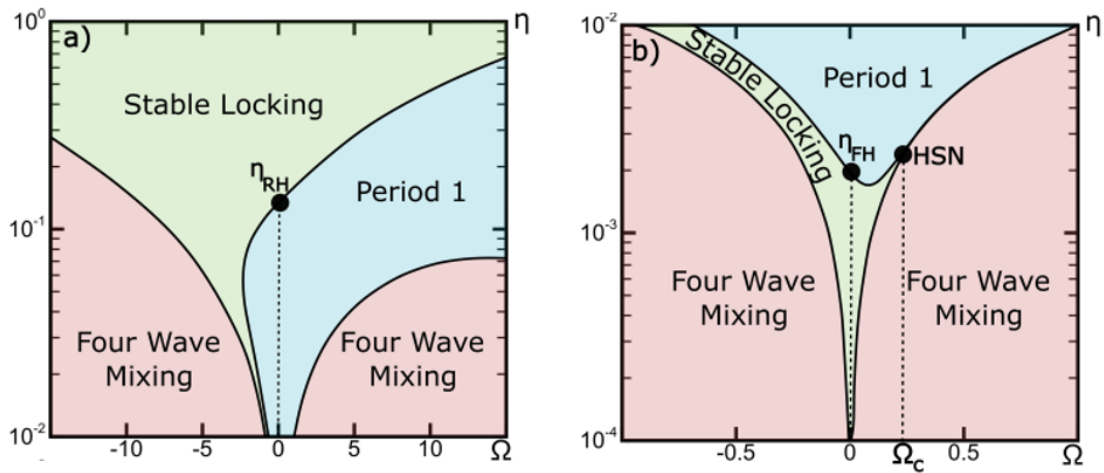


Figure 2.10: Generalized stability diagram of a semiconductor laser showing the positions of the four main operating states of the injection-locked system (a) strong injection and (b) weak injection. [HKL21]

The S_i is the injected optical power from the master laser and S is the slave laser's optical power. c is the speed of light in a vacuum. In this way, the boundary of negative detuning and the corresponding power is brought into the above equation to obtain the α_H -factor. It is worth noting that this technique is limited to multimode lasers although it can extract α_H -factor above the threshold. Moreover, it was not possible to assess the effect of the superposition of the injected light and slave laser on the α_H factor.

There is another method based on optical injection-locked to extract the α_H -factor above the threshold current which can also be used for single-mode lasers. When a laser is subjected to optical injection, can be observed by finely adjusting the detuning and

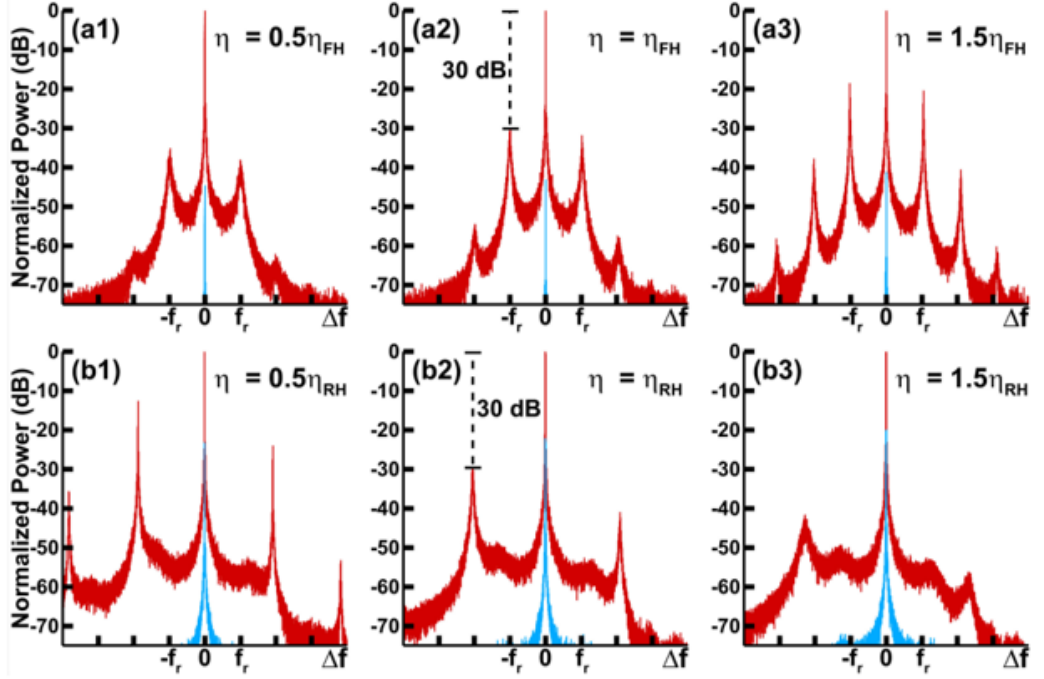


Figure 2.11: The optical spectrum of the injection-locked system at different injection levels near the Hopf bifurcation point when detuning is zero. (a) η_{FH} (b) η_{RH} . The bifurcation point is defined as the injection level when the side mode suppression ratio crosses 30 dB. [HKL21]

injection power, beyond simply describing it as locked or unlocked. Fig. 2.10 shows the regions corresponding to various states exhibited by a semiconductor laser under optical injection, such as stable locking, FWM, and periodic resonant states [HKL21].

From the ordinary differential equation (ODE) model of the optically-injected semiconductor laser, it has been shown that the α_H -factor can be directly extracted from the expression below [HKL21]:

$$\frac{\Delta f_c / f_r}{\eta_{FH} / \eta_{RH}} = \frac{1}{2\sqrt{2}} \sqrt{(1 + 1/\alpha_H^2)(\alpha_H^2 - 1)^3} \quad (2.22)$$

where f_r is the free-running relaxation frequency. Δf_c is the measured critical detuning, which is located between stable locking, period 1, and FWM, which is also called the Hopf-saddle-node (HSN) point. When applied with zero detuning, η_{FH} and η_{RH} correspond to the optical injection levels at forward and reverse Hopf bifurcation

points respectively. When performing experiments, it is necessary to know the path loss from the master laser to the slave laser to calculate an accurate ratio of η_{FH}/η_{RH} .

To obtain two Hopf points with zero-detuning, we placed a master laser at the zero-detuning position and slowly increased the injection power, and then we observed the spectral changes. Fig. 2.11 shows the spectral curves at different injection powers. The injection level at which the side mode suppression ratio (SMSR) crosses 30 dB is the bifurcation point. To obtain HSN points, it is necessary to slowly adjust the detuning in addition to determining the boundaries using the 30 dB-SMSR to see if a single boundary occurs only when the injection strength is increased. The α_H -factor of the optical injected main mode can be obtained by bringing the parameters of the three Hopf bifurcation points into Eq. 2.22. This technique can be used to extract α_H -factor above the threshold current for both single-mode or multi-mode lasers. However, the process of multi-mode extraction is cumbersome. Additionally, the effects of optical injection cannot be ignored.

► High-speed modulation

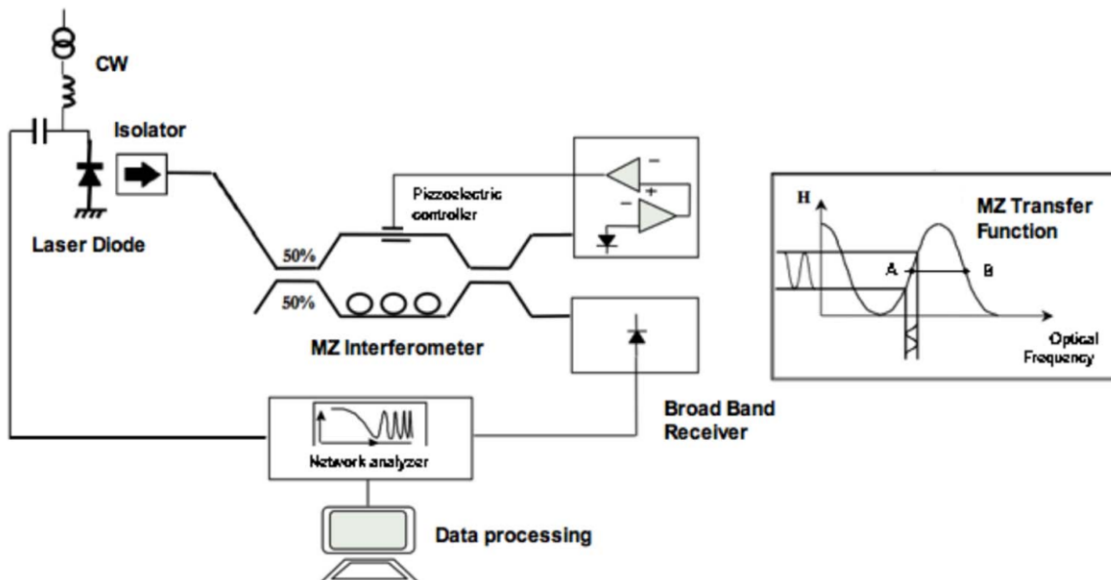


Figure 2.12: Experimental setup for determining AM, FM response, and the α_H -factor. The insert illustrates the transfer function of the interferometer. [PG11]

Using a tunable Mach–Zehnder (MZ) interferometer as an optical discriminator, the α_H -factor above the threshold current of laser diodes can be extracted, as shown in Fig. 2.12 for the experimental setup. It relies on high-frequency laser current modulation to produce amplitude modulation (AM) and frequency modulation (FM). The α_H -factor can be calculated from the ratio of FM to AM as follows.

$$\frac{FM}{AM} \rightarrow 2\frac{\beta}{m} = \alpha_H \sqrt{1 + \left(\frac{f_c}{f_m}\right)^2} \quad (2.23)$$

where the β is the modulation rate in frequency and m in power, f_c is the corner frequency and f_m the modulation frequency. The α_H -factor can be derived directly from the ratio of FM to AM only if the modulation frequency is much higher than the corner frequency of the laser. [PG11; SBK86]. This method has the advantage of providing amplitude and phase information over a wide frequency range, allowing for a more detailed understanding of linear chirp characteristics compared to other traditional methods [PG11]. This method allows us to obtain the α_H -factor for the actual operation of the lasers.

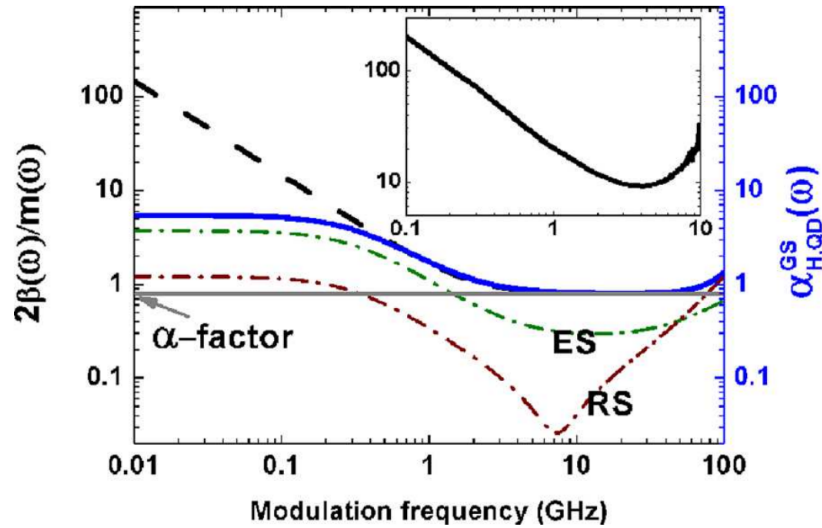


Figure 2.13: Modulation frequency dependence of the FM/AM ratio (dashes) and the α_H -factor (thick solid line). The horizontal line indicates the lowest level for the regular α_H -factor of the laser. The inset shows the experimental curve of the FM-AM ratio of a QD laser. [Wan+14]

Additionally, C. Wang et al. proposed a semi-analytical model for studying phase-amplitude coupling in QD semiconductor lasers. This model takes into account the influence of carrier populations in the excited states and the two-dimensional carrier reservoir on the refractive index changes. The α_H -factor was calculated based on simulations using the FM/AM technique. From the linearized rate equation, the ratio of FM-AM exponent is obtained as [Wan+14],

$$2\frac{\beta}{m} = 2\frac{\delta\omega_{LS}/\omega}{\delta S_{GS}/S_{GS}} \quad (2.24)$$

where ω is the modulation angular frequency. $\delta\omega_{LS}$ satisfies this relationship $\delta\omega_{LS} = j\omega\delta\phi$, which is related to phase variations. S_{GS} represents the number of photons in the rate equations and is considered to be the cause of amplitude variations. Fig. 2.13 displays the results of the α_H -factor's variation with modulation frequency based on simulations and experiments using the FM/AM technique.

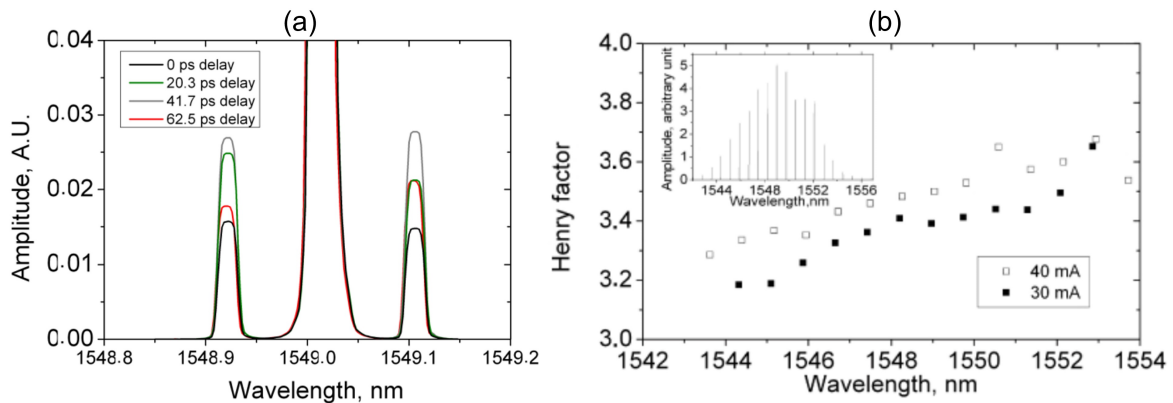


Figure 2.14: (a) The normalized spectra, i.e., a longitudinal mode and modulation sidebands, were obtained under four different optical delay conditions. (b) The α_H -factor for the longitudinal mode of the FP QW laser. The inset shows the emission spectrum. [Pro+11]

Alternatively, the α_H -factor can be extracted using optical phase modulation (OPM). it is a simplified FM/AM method to extract the α_H -factor of a multi-mode laser simultaneously without the need for an optical filter. J. G. Provost et al. obtained the spectrum of Fig. 2.14(a) by directly modulating the FP laser and adjusting the quadrature delay corresponding to the modulation frequency. The α_H -factor was then calculated using the intensity of the side modes. The expression is as follows,

$$\alpha_H = \frac{\text{Im}(\sqrt{Q_{-1}Q_{+1}})}{\text{Re}(\sqrt{Q_{-1}Q_{+1}})} \quad (2.25)$$

with,

$$Q_{-1} = (I_{-1}^1 - I_{-1}^3) + j(I_{-1}^0 - I_{-1}^2) \quad (2.26)$$

$$Q_{+1} = (-I_{+1}^1 + I_{+1}^3) + j(I_{+1}^0 - I_{+1}^2) \quad (2.27)$$

where $I_{\pm 1}^n$ means the side-modes intensity when the optical delay is $n/(4f_m)$ ($n = 0, 1, 2, 3$). The calculated alpha for all longitudinal modes is shown in Fig. 2.14(b).

In addition, there is a pulse measurement method based on the modulation setup as shown in Fig. 2.15(a) for α_H -factor extraction [SR23]. By recording the modulated spectra, the phase ϕ and relative intensity $I(t)$ changes can be calculated and then fitted to obtain α_H -factor. Fig. 2.15(b) shows the experimental data and fitted curves of phase with $\log(I(t))$. The fitted equation for the α_H -factor is as follows,

$$\frac{d\phi}{dI} = \frac{\alpha_H}{2I} \implies \phi(t) = \phi_0 + \frac{\alpha_H}{2} \ln\left(\frac{I(t)}{I_0}\right) \quad (2.28)$$

where ϕ_0 is the first phase curve and I_0 is the first intensity curve taken as references.

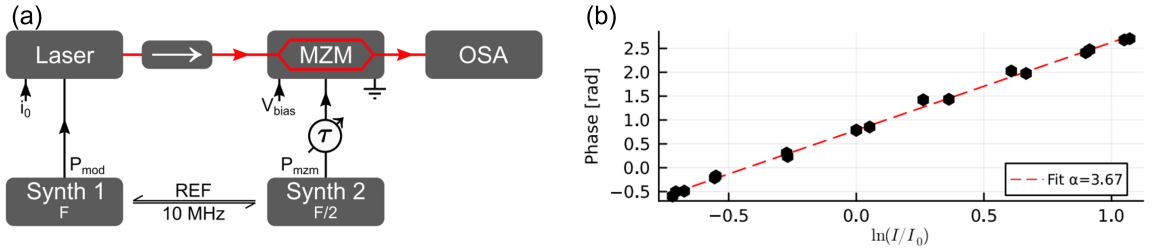


Figure 2.15: (a) Experimental setup. (b) The phase plotted as a function of $\log(I(t))$ [SR23]

2.4.2 Static characteristics

In this experiment, we have investigated an InAs/GaAs QD FP laser (from the QD Laser, Inc., Japan) whose active region consists of eight layers of InAs QDs, which are directly grown on a GaAs substrate using a solid-source molecular beam epitaxy system

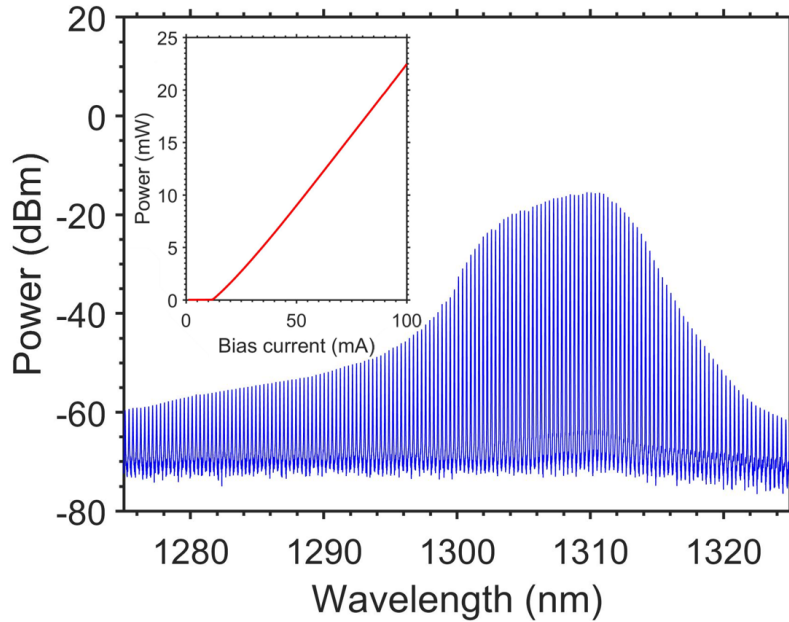


Figure 2.16: Optical spectrum measured at twice threshold current, and the insert shows power-current characteristics.

[Nis+17]. There is a 37.5 nm-thick GaAs barrier between each QD layer. The QDs are densely packed at a rate of $5.9 \times 10^{10} \text{ cm}^{-2}$, ensuring a high optical gain. The laser's physical structure measures $750 \mu\text{m}$ in length and features a ridge waveguide that is $2 \mu\text{m}$ wide. The front and rear reflection facets are asymmetrically coated to reflect 30% and 90% of light, respectively. The device primarily exhibits ground state emission at a wavelength of 1310 nm, with the multi-mode lasing spectrum at a drive current of 25 mA showcased in Fig. 2.16. It is important to note that within the studied pump current range, the excited state transitions remain undetected. The inset of the figure presents the light-current characteristics, indicating a threshold current (I_{th}) of 12.5 mA. Throughout the experimental procedures, the QD laser is maintained at a steady temperature of 20 °C.

2.4.3 Experimental setup

Fig. 2.17 presents the experimental setup used for performing the extraction of the α_H -factor with the OPM. Details regarding the ASE method have already been described

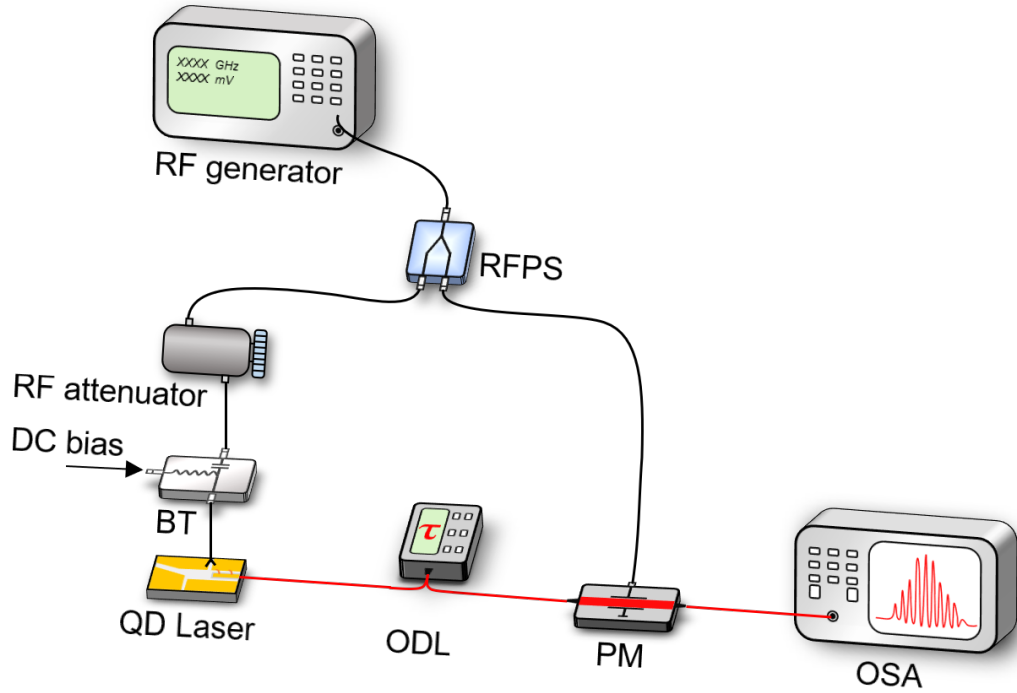


Figure 2.17: Schematic of the experimental setup of the OPM technique. PM: Phase Modulator; ODL: Optical Delay Line; OSA: Optical Spectrum Analyzer; BT: Bias Tee; RFPS: RF Power Splitter (RFPS). The black line is the circuit, the red line is the light path.

before. To start, the tunable RF signal (with modulation frequency f_m) is divided into two channels by an RF Power Splitter (RFPS) and used to simultaneously modulate the QD laser and phase modulator (PM). The sinusoidal wave signal applied to the QD laser is controlled by the RF variable attenuator to keep it within the small signal modulation. In addition, the bias tee (BT) allows the QD laser to be pumped by direct current. The laser beam is coupled with an antireflection (AR) coated lens-end fiber and then passes through an optical delay line (ODL) before entering the PM to control the delay between the optical and electrical signal at the input of the PM. Finally, the modulated signal is sent to an optical spectrum analyzer (OSA). In this method, four optical spectra corresponding to different delays ($n/(4f_m)$, with n an integer) are used to properly extract the α_H -factor.

2.4.4 Results for optical phase modulation

Fig. 2.18(a) illustrates the modulated spectrum at a modulation frequency of $f_m = 13$ GHz with zero delay. The modulation impacts the entire spectrum, resulting in side-modes emerging at each comb line. To delve deeper into the effect of delay on the modulation spectrum. Fig. 2.18(b) presents an enlarged view of a single longitudinal mode and its associated modulation sidebands for four distinct optical delays (presented in a normalized optical spectrum format). Variations in delay lead to changes in the sideband intensities, which can be quantified using an OSA. Here, since the relationship between the corner frequency and the modulation frequency is unknown, the modulation frequency-dependent α_m -factor can be determined as follows [Pro+11],

$$\alpha_m = \frac{Im(\sqrt{Q_{-1}Q_{+1}})}{Re(\sqrt{Q_{-1}Q_{+1}})} \quad (2.29)$$

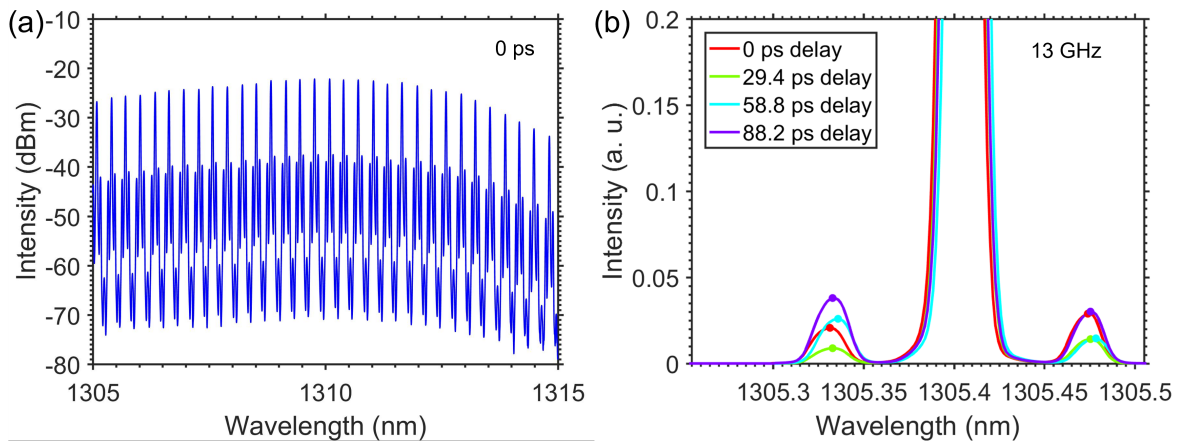


Figure 2.18: (a) Modulated optical spectrum at zero delays with $f_m = 13$ GHz, and (b) Close-up on one longitudinal mode and the modulation sidebands obtained for four different optical delays.

Finally, it is known that the modulation α_m -factor is related to the corner frequency f_c and the modulation frequency f_m . [PG11]

$$\alpha_m = \alpha_H \sqrt{1 + \left(\frac{f_c}{f_m}\right)^2} \quad (2.30)$$

where the f_c is defined as $f_c = (v_g P / 2\pi) \times (\delta g / \delta P)$, with v_g the group velocity, P the output power, and $\delta g / \delta P$ a nonzero parameter due to the nonlinear gain associated to coulomb scattering and carrier heating. According to the above Equation, when $f_m \gg f_c$, the α_H -factor can be accurately extracted.

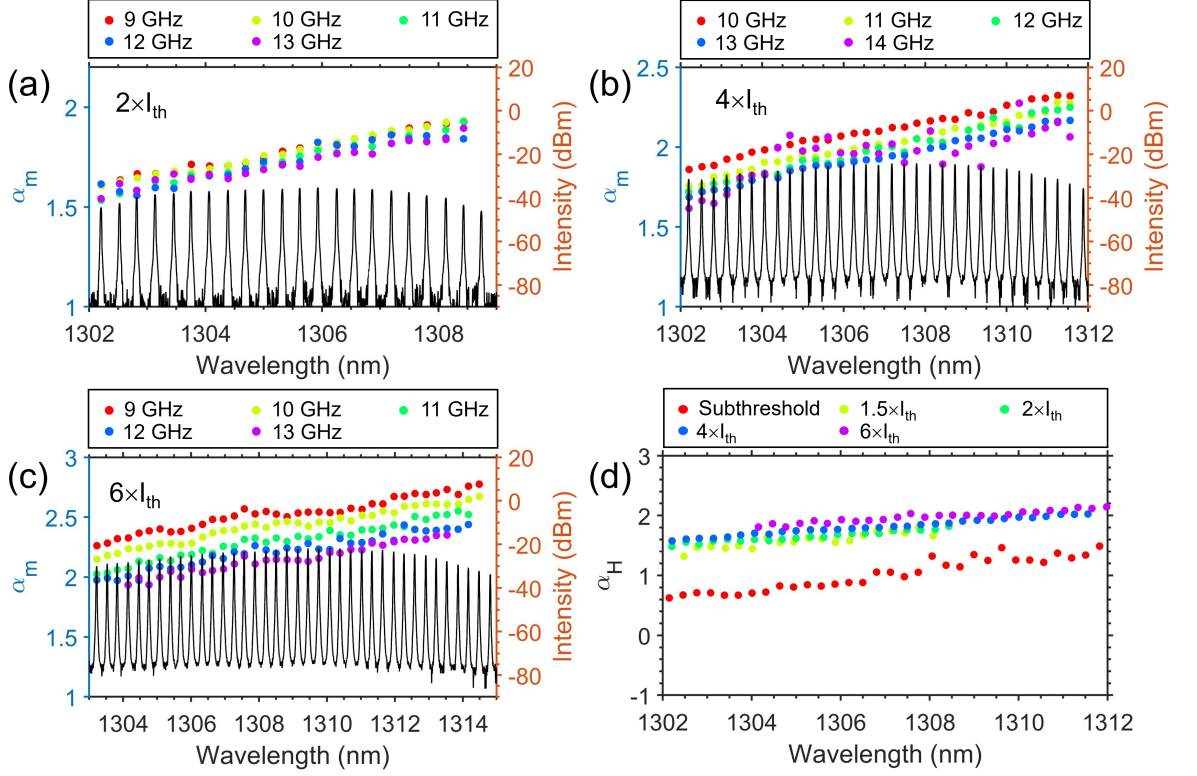


Figure 2.19: (a) The α_m -factor measured for each comb line for different modulation frequencies and at $\times 2$ threshold current, (b) $\times 4$ threshold current, and (c) $\times 6$ threshold current, (d) the α_H -factor for different pump currents extracted from the optical phase modulation and ASE methods.

Fig. 2.19(a), (b), and (c) display the optical spectra and the retrieved α_m for 18 comb lines under different modulation frequencies at $\times 2$, $\times 4$, and $\times 6$ threshold current. The extracted α_m shows a linear upward trend as the lasing wavelength increases over a large bandwidth range. On one hand, the α_m increases with the pump current which has already been reported elsewhere [Don+21]. On the other hand, under the same pump current, the α_m decreases with the modulation frequency increasing from 9 GHz to 13 GHz. It is worth stressing that the influence of modulation frequency is amplified

at high bias conditions where f_c is increased. In addition, it has been shown that the longitudinal modes located far away from the optical gain peak are less efficiently modulated by the sidebands, which results in inaccuracy in extracting the α_H -factor. To overcome this issue, a flat-top behavior is required for the optical spectra. Owing to the broad 10 dB bandwidth emitted from the device studied, we can retrieve the α_H -factors over 20 modes in this study. In this context, the OPM method is beneficial for extending its functionality to characterize frequency comb sources that have flat-top spectra.

Then, fixing the pump current and taking the α_m values at the gain peak for different modulation frequencies, Eq. 2.30 is used for curve-fitting the corner frequency and subsequently to extract the exact α_H . Given that the accuracy to extract the α_H -factor approaches its maximum when $f_c \ll f_m$, one takes $f_m = 13$ GHz at which $\alpha_m \simeq \alpha_H$. Therefore, when the QD laser is running at twice the threshold current, the α_H -factor at the gain peak is about 1.6 whereas at four times and six times the threshold current it is about 1.8 and 2.0, respectively as shown in Fig. 2.19(d). We also plot the sub-threshold α_H -factor measured with the ASE method (red). The α_H -factor below the threshold is significantly smaller than the α_H -factor above the threshold, which is attributed to the carrier changes caused by the population inversion [MHU06].

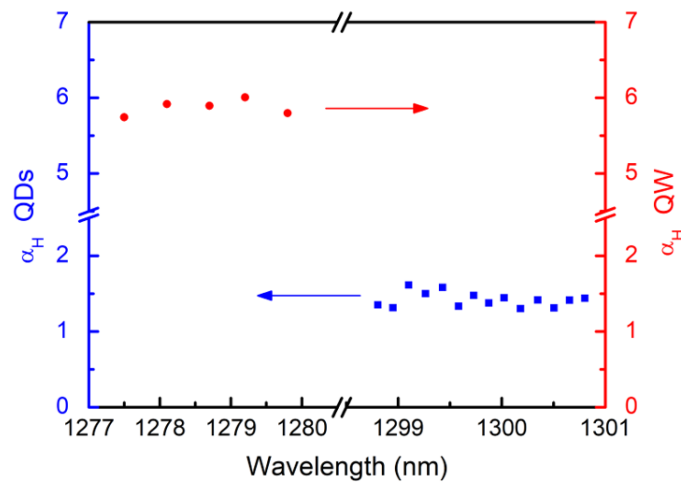


Figure 2.20: Spectral dependent α_H factor of QW (red) and QD (blue) lasers measured at twice the threshold.

Previous comparisons between the α_H -factors of QD and QW lasers were limited to sub-threshold levels as shown in Fig. 2.6. However, when lasers operate above the threshold current, the relationship between their characteristics at that moment and the α_H -factor requires further investigation. Therefore, it is necessary to utilize optical phase modulation methods to extract and compare the α_H -factors of a QD laser and a QW laser operating above their threshold currents. Fig. 2.20 shows the α_H -factors of the QD FP and QW FP lasers at twice the threshold current extracted by the optical phase modulation method, with the QD laser still exhibiting much lower α_H -factors. The significance of low α_H -factor silicon-based QD lasers will be demonstrated in the following transmission experiments.

2.5 Directly modulated QD laser with high optical feedback resistance

When faced with the necessity of silicon-based integrated chips with high information capacity. Back reflection at the chip level would pose a significant challenge, as it would lead to severe instabilities in the laser source [Gri+20]. Given that developing an on-chip optical isolator that has low loss and sufficient isolation remains a challenge, it is important to develop feedback-insensitive sources [Mat+18]. The QD lasers are highly resistant to optical reflection by virtue of their small α_H -factor [Dua+19a]. To develop a more compact optical transceiver by taking advantage of the QD laser, a further investigation of the reflection sensitivity under direct modulation is necessary. Indeed, although directly modulated lasers are more energy efficient and have higher linearity in short-range microwave photonic links, the addition of a single-tone modulation can make them more sensitive to external feedback [Uch12]. In this section, research on the feedback sensitivity of direct modulated epitaxial QD lasers on silicon will be shown.

2.5.1 Experimental setup

The epitaxial QD laser was grown on a GaP/Si template. The active region contains five periods of QD layers, each separated by a 37.5 nm GaAs spacer that includes 10

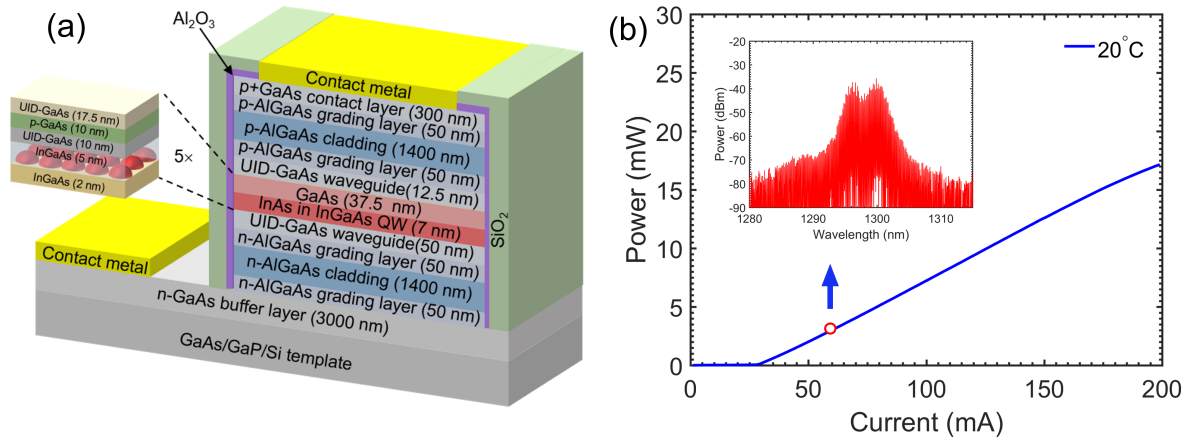


Figure 2.21: (a) Schematic of epitaxial QD laser device structure. (b) Power-current characteristics at 20 °C. The inset is the spectrum of the QD laser at 60 mA.

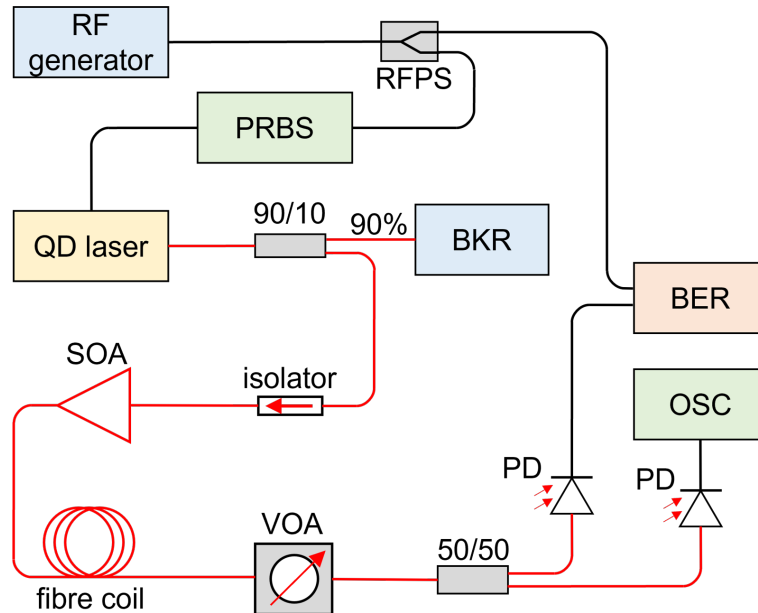


Figure 2.22: Schematic of the experimental setup. The black lines show the electrical circuit and the red lines show the light path.

nm of p-type material and the density of QDs is about $5.9 \times 10^{10} \text{ cm}^{-2}$. The FP cavity of the laser is 1.35 mm long, with $4 \mu\text{m}$ wide ridge deeply etched (through the active region), and two top contacts for electrical injection. The cavity facets are symmetric with a power reflectivity of approximately 32%. The epitaxial structure of this QD laser is shown in Fig. 2.21(a). Fig. 2.21(b) shows the light current characteristics at 20°C where the threshold current (I_{th}) is 30 mA. The inset displays the optical spectrum measured at 60 mA ($2 \times I_{th}$) that corresponds to the operation condition. The QD lasers on Si are known for their near-zero α_H -factor. For the device studied, the α_H -factor is below unity in the operating condition [Hua+20]. A straightforward consequence of the low α_H -factor is a better immunity against optical feedback, thanks to a weaker interaction between the intra-cavity and reflected light fields [Gri+20].

2.5.2 Transmission results

The research on direct modulation of silicon-based epitaxial quantum dot lasers will greatly increase the integration density of optical transmission chips. In addition, considering that on-chip optical feedback increases the BER, etc., the study of epitaxial QD lasers that are insensitive to optical feedback and can be directly modulated at high speeds will save the space of optical isolators and further improve the integration to meet the goal of high-speed and high-capacity optical transmission. To investigate the modulation properties of the QD laser with or without optical feedback, the experimental setup is shown in Fig. 2.22. The QD laser is directly modulated by the digital generator with a pseudo-random binary sequence (PRBS) and a bit sequence length of $2^7 - 1$ and the applied modulation format is on-off keying (OOK). The QD laser was not optimized for high-speed modulation without specific RF packaging, so we did not use a longer sequence length. At the same time, the clock signal is fed into the error detector as a reference signal. Afterwards, the emission from the QD laser is coupled into an anti-reflection (AR) coated lens-end fiber and it is divided into two paths, the feedback path and the output path. On the feedback path, 90% coupled power is sent to the back-reflector (BKR) that consists of a mirror and a variable optical attenuator (VOA). The latter is used to change the feedback strength, which is defined as the ratio of returned power to the free-space output power. In this configuration, the achievable

feedback strength ranges from -61 dB to -9 dB. The other 10% of the coupled power is isolated and then amplified by a semiconductor optical amplifier (SOA). The signal is transmitted over a 2 km single-mode fiber coil. At the end, a variable optical attenuator (VOA) is used to tune the received power of the error detector to analyze the BER performance. A high-speed oscilloscope (OSC) is used to capture the eye diagram. The PD converts the optical signal into an electrical signal before entering the BER tester or OSC.

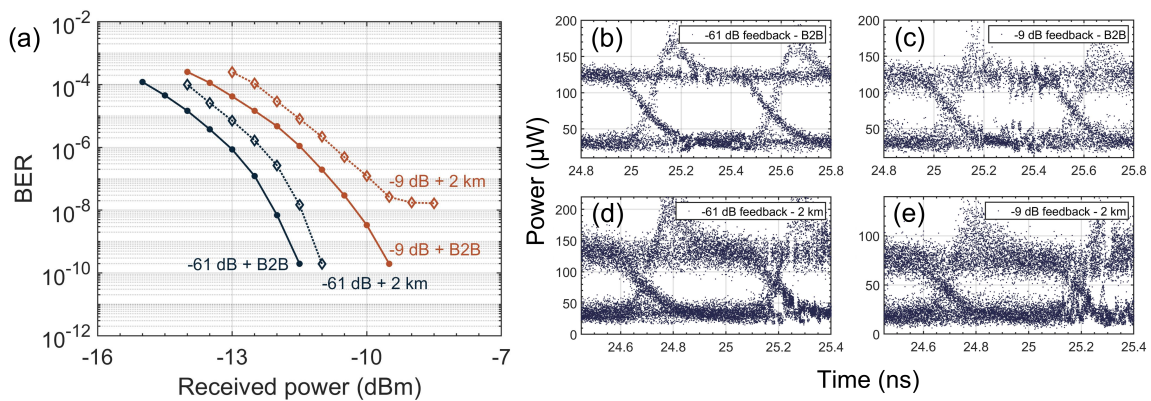


Figure 2.23: (a) BER plots at 2 Gbps for back-to-back (B2B) and after transmission (2 km) with and without feedback for the QD laser at 20 °C. The pump current is $2 \times I_{th}$. The eye diagrams (b) without feedback and (c) with feedback when back-to-back. The eye diagrams (d) without feedback and (e) with feedback after 2 km transmission.

The high-speed response of the QD laser is carried out at twice the threshold current and room temperature. The BERs of the QD laser at 2 Gbps with and without feedback after back-to-back (B2B) and 2 km fiber transmission are plotted in Fig. 2.23(a). For the calculation of the feedback strength, we use the feedback strength of BKR (the maximum feedback strength of BKR is -2.2 dB) and include the setup loss (2.7 dB) and the coupling loss (4.1 dB) then get the feedback strength (the maximum feedback strength is -9 dB) [Che+21; Wan+21b]. When the feedback strength is -61 dB, which is effectively similar to the free-running operation, the minimum BER of the device studied approaches 10^{-10} in the B2B operation and after 2 km transmission. However, a 0.7 dB power penalty is observed after 2 km transmission at the BER level of 10^{-9} , which is attributed to the chromatic dispersion in the fiber. The eye diagrams are

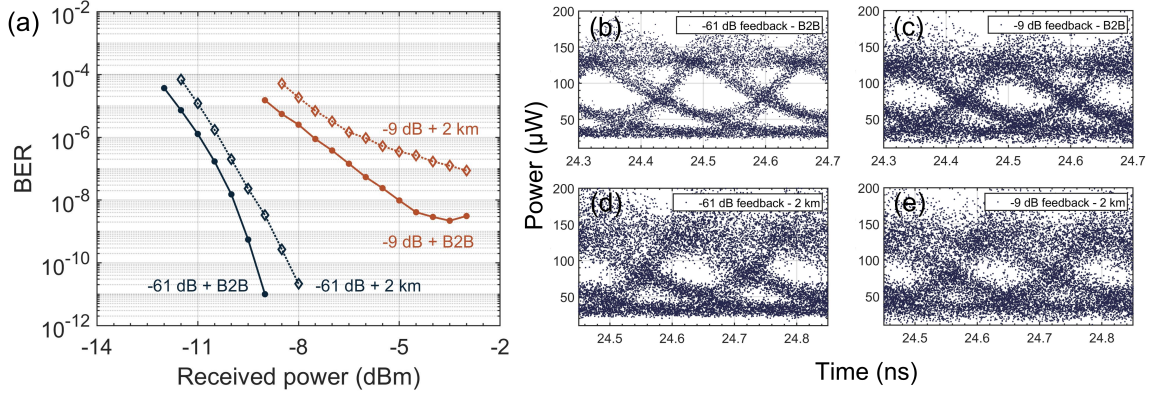


Figure 2.24: (a) BER plots at 6 Gbps for back-to-back (B2B) and after transmission (2 km) with and without feedback for the QD laser at 20 °C. The pump current is $2 \times I_{th}$. The eye diagrams (b) without feedback and (c) with feedback when back-to-back. The eye diagrams (d) without feedback and (e) with feedback after 2 km transmission.

thus measured in the condition of high received power. In both B2B and transmission operations, the eye diagram is wide and clear contours as shown in Fig. 2.23(b) and (d). By increasing the feedback strength to -9 dB, a minimum BER approaching 10^{-10} is still ensured in the B2B operation. Despite the 2 dB power penalty that is induced by the optical feedback at the BER level of 10^{-8} , the eye diagram remains open as shown in Fig. 2.23(c). Nevertheless, the BER performance is degraded after 2 km transmission leading to a penalty floor with -9 dB optical feedback. We define the minimum measured BER level as residual BER (RBER). In the transmission operation, the RBER level is 10^{-8} . As shown in Fig. 2.23(e), the eye diagram is still open, but the contours are a little blurred. To investigate how the BER QD laser behaves under the same optical feedback conditions but operates at a higher modulation rate, Fig. 2.24(a) depicts the BER plot with a modulation rate of 6 Gbps. Under a weak feedback strength at -61 dB, the increase of modulation rate from 2 to 6 Gbps keeps an error-free operation in both B2B and transmission configurations, and a BER level below 10^{-10} is always obtained. However, a 2 dB power penalty at the BER level of 10^{-8} results from the increase in modulation rate. It is worth stressing that the degradation due to optical feedback is amplified when the modulation rate is higher. By increasing the feedback strength to -9 dB, the RBER level in the B2B operation is above 10^{-9} ,

where the received power is -3 dBm. After 2 km transmission, the BER level is further increased to 10^{-7} . Despite the degradation of BER performance, the QD laser still exhibits a reasonable transmission under optical feedback. With a 6 Gbps modulation rate applied, the eye diagrams are open but narrowed and the contours remain clear with or without feedback in B2B operation. It can be noticed that when BER is less than 10^{-8} , there are open and clear eyes. With -9 dB feedback, the BER increases and is greater than 10^{-8} after 2 km transmission, so the eye becomes blurred. There is a weak overshoot above each eye which may be caused by the high modulation voltage (2 V) used in the study [TTL21]. The IEEE 802.3ah standard indicates that the reflection tolerance of optical interconnects should be higher than -26 dB [Com+07]. Hence, there will not be such large feedback (-9 dB) in short-distance data transmission, so the actual BER will perform better at 6 Gbps modulation rate and will be less than 10^{-8} . Furthermore, the silicon-based QD laser still meets the KP4 forward error correction (KP4-FEC) certified BER of 2×10^{-4} at 6 Gbps rates and strong feedback [Ozo+19].

It was found that increasing the received power does not reduce the BER when strong feedback is present. In the future, we may have to continue to optimize laser performance by utilizing on-chip integrated light sources with customized design and packaging. In the latter, the speed of the data transfer can be further improved by considering an improved drive signal transmission.

2.6 Summary

In summary, this chapter presents the electronic structure of QD lasers, the equivalent circuit of semiconductor lasers and their corresponding rate equations, noise characteristics (including relative intensity noise, frequency noise, and α_H -factor), experiments on the α_H -factor of QD multi-mode lasers, and transmission characterization of optical feedback-insensitive QD lasers.

- I extracted the α_H -factor below and above the threshold whereby the spectral dependence of this parameter was performed for each longitudinal mode. The much lower α_H -factor of QD lasers compared to QW contributes to the development of optical isolator-free PICs.

- I have performed direct modulation experiments using silicon-based epitaxial QD lasers with low α_H -factor under different optical feedback conditions. At room temperature, we can implement modulation rates of 6 Gbps for QD lasers and withstand strong feedback. The optical feedback insensitivity property is beneficial for optical communication silicon photonic chips. The experimental results provide an encouraging argument for the high-density integration of silicon-based epitaxial QD lasers for silicon photonics applications.

Bibliography

- [AY08] Moustafa Ahmed and Minoru Yamada. “Effect of intensity noise of semiconductor lasers on the digital modulation characteristics and the bit error rate of optical communication systems”. In: *Journal of Applied Physics* 104.1 (2008).
- [Alk+23] Emad Alkhazraji, Weng W Chow, Frédéric Grillot, John E Bowers, and Yating Wan. “Linewidth narrowing in self-injection-locked on-chip lasers”. In: *Light: Science & Applications* 12.1 (2023), p. 162.
- [BGL99] Dieter Bimberg, Marius Grundmann, and Nikolai N Ledentsov. *Quantum dot heterostructures*. John Wiley & Sons, 1999.
- [Bog+00] A. Bogatov, A. Boltaseva, A. E. Drakin, M. A. Belkin, and V. P. Konyayev. “Anomalous dispersion, differential gain, and dispersion of the α -factor in InGaAs/AlGaAs/GaAs strained quantum-well semiconductor lasers”. In: *Semiconductors* 34.10 (2000), pp. 1207–1213.
- [Cap+07] A Capua, L Rozenfeld, V Mikhelashvili, G Eisenstein, M Kuntz, M Laemmlin, and D Bimberg. “Direct correlation between a highly damped modulation response and ultra low relative intensity noise in an InAs/GaAs quantum dot laser”. In: *Optics express* 15.9 (2007), pp. 5388–5393.
- [Che+21] Jia-Jian Chen, Zi-Hao Wang, Wen-Qi Wei, Ting Wang, and Jian-Jun Zhang. “Sole Excited-State InAs Quantum Dot Laser on Silicon with Strong Feedback Resistance”. In: *Asia Communications and Photonics Conference*. Optical Society of America. 2021, T4A–171.

- [CKS12] Weng W Chow, Stephan W Koch, and Murray III Sargent. Semiconductor-laser physics. Springer Science & Business Media, 2012.
- [CCM12] Larry A Coldren, Scott W Corzine, and Milan L Mashanovitch. Diode lasers and photonic integrated circuits. John Wiley & Sons, 2012.
- [Com+07] IEEE Computer Society LAN/MAN Standards Committee et al. “IEEE Standard for Information technology-Telecommunications and information exchange between systems-Local and metropolitan area networks-Specific requirements Part 11: Wireless LAN Medium Access Control (MAC) and Physical Layer (PHY) Specifications”. In: IEEE Std 802.11[^] (2007).
- [Din+22] Qingan Ding et al. “Continuous current-injected waveforms shaping for suppressing relaxation oscillations of direct modulation based on equivalent circuit model”. In: Optics Express 30.11 (2022), pp. 19273–19287.
- [Don+21] B. Z. Dong et al. “Dynamic performance and reflection sensitivity of quantum dot distributed feedback lasers with large optical mismatch”. In: Photonics Research 9.8 (2021), pp. 1550–1558.
- [Don+19] Bozhang Dong et al. “Influence of the polarization anisotropy on the linewidth enhancement factor and reflection sensitivity of 1.55- μm InP-based InAs quantum dash lasers”. In: Applied Physics Letters 115.9 (2019).
- [Dua+18a] J Duan, H Huang, D Jung, Z Zhang, J Norman, JE Bowers, and F Grillot. “Semiconductor quantum dot lasers epitaxially grown on silicon with low linewidth enhancement factor”. In: Applied Physics Letters 112.25 (2018), p. 251111.
- [Dua+19a] Jianan Duan, Heming Huang, Bozhang Dong, Daehwan Jung, Justin C Norman, John E Bowers, and Frederic Grillot. “1.3- μm Reflection Insensitive InAs/GaAs Quantum Dot Lasers Directly Grown on Silicon”. In: IEEE Photonics Technology Letters 31.5 (2019), pp. 345–348.

- [Dua+19b] Jianan Duan, Heming Huang, Bozhang Dong, Justin C Norman, Zeyu Zhang, John E Bowers, and Frédéric Grillot. “Dynamic and nonlinear properties of epitaxial quantum dot lasers on silicon for isolator-free integration”. In: *Photonics Research* 7.11 (2019), pp. 1222–1228.
- [Dua+18b] Jianan Duan, Xing-Guang Wang, Yue-Guang Zhou, Cheng Wang, and Frederic Grillot. “Carrier-noise-enhanced relative intensity noise of quantum dot lasers”. In: *IEEE Journal of Quantum Electronics* 54.6 (2018), pp. 1–7.
- [Dua+22] Jianan Duan et al. “Four-wave mixing in 1.3 μm epitaxial quantum dot lasers directly grown on silicon”. In: *Photonics Research* 10.5 (2022), pp. 1264–1270.
- [FMB05] S Fathpour, Zetian Mi, and P Bhattacharya. “High-speed quantum dot lasers”. In: *Journal of Physics D: Applied Physics* 38.13 (2005), p. 2103.
- [Gar+21] F Pelayo García de Arquer, Dmitri V Talapin, Victor I Klimov, Yasuhiko Arakawa, Manfred Bayer, and Edward H Sargent. “Semiconductor quantum dots: Technological progress and future challenges”. In: *Science* 373.6555 (2021), eaaz8541.
- [Gri+21] Frédéric Grillot, Jianan Duan, Bozhang Dong, and Heming Huang. “Uncovering recent progress in nanostructured light-emitters for information and communication technologies”. In: *Light: Science & Applications* 10.1 (2021), p. 156.
- [Gri+20] Frédéric Grillot et al. “Physics and applications of quantum dot lasers for silicon photonics”. In: *Nanophotonics* 9.6 (2020), pp. 1271–1286.
- [Har+82] Christoph Harder, Joseph Katz, S Margalit, J Shacham, and Amnon Yariv. “Noise equivalent circuit of a semiconductor laser diode”. In: *IEEE Journal of Quantum Electronics* 18.3 (1982), pp. 333–337.
- [HVV83] Christoph Harder, Kerry Vahala, and Amnon Yariv. “Measurement of the linewidth enhancement factor α of semiconductor lasers”. In: *Applied Physics Letters* 42.4 (1983), pp. 328–330.

- [HH67] H Haug and H Haken. “Theory of noise in semiconductor laser emission”. In: *Zeitschrift für Physik A Hadrons and nuclei* 204.3 (1967), pp. 262–275.
- [HP90] Jochen Helms and Klaus Petermann. “A simple analytic expression for the stable operation range of laser diodes with optical feedback”. In: *IEEE Journal of Quantum Electronics* 26.5 (1990), pp. 833–836.
- [HC83] ID Henning and JV Collins. “Measurements of the semiconductor laser linewidth broadening factor”. In: *Electronics Letters* 22.19 (1983), pp. 927–929.
- [Hen82] C. Henry. “Theory of the linewidth of semiconductor lasers”. In: *IEEE Journal of Quantum Electronics* 18.2 (1982), pp. 259–264.
- [HKL21] Daniel J Herrera, Vassilios Kovanis, and Luke F Lester. “Using transitional points in the optical injection locking behavior of a semiconductor laser to extract its dimensionless operating parameters”. In: *IEEE Journal of Selected Topics in Quantum Electronics* 28.1 (2021), pp. 1–9.
- [Hua+20] H Huang, J Duan, B Dong, J Norman, D Jung, JE Bowers, and F Grillo. “Epitaxial quantum dot lasers on silicon with high thermal stability and strong resistance to optical feedback”. In: *APL Photonics* 5.1 (2020), p. 016103.
- [Lam64] Willis E Lamb Jr. “Theory of an optical maser”. In: *Physical Review* 134.6A (1964), A1429.
- [Lax67] Melvin Lax. “Classical noise. V. Noise in self-sustained oscillators”. In: *Physical Review* 160.2 (1967), p. 290.
- [LJC01] G. Liu, X. M. Jin, and S. L. Chuang. “Measurement of linewidth enhancement factor of semiconductor lasers using an injection-locking technique”. In: *IEEE photonics Technology letters* 13.5 (2001), pp. 430–432.
- [Mat+18] M Matsuda, N Yasuoka, K Nishi, K Takemasa, T Yamamoto, M Sugawara, and Y Arakawa. “Low-noise characteristics on 1.3- μm -wavelength quantum-dot DFB lasers under external optical feedback”. In: *2018 IEEE International Semiconductor Laser Conference (ISLC)*. IEEE. 2018, pp. 1–2.

- [MHU06] S. Melnik, G. Huyet, and A. V Uskov. “The linewidth enhancement factor α of quantum dot semiconductor lasers”. In: *Optics Express* 14.7 (2006), pp. 2950–2955.
- [Nis+17] K. Nishi, K. Takemasa, M. Sugawara, and Y. Arakawa. “Development of quantum dot lasers for data-com and silicon photonics applications”. In: *IEEE Journal of Selected Topics in Quantum Electronics* 23.6 (2017), pp. 1–7.
- [Oht08] J Ohtsubo. “Semiconductor Lasers Stability, Instability and Chaos Second, Enlarged Edition”. In: *SPRINGER SERIES IN OPTICAL SCIENCES* 111 (2008).
- [Opa+21] Nikola Opačak et al. “Spectrally resolved linewidth enhancement factor of a semiconductor frequency comb”. In: *Optica* 8.9 (2021), pp. 1227–1230.
- [OB87] M. Osinski and J. Buus. “Linewidth broadening factor in semiconductor lasers—An overview”. In: *IEEE Journal of Quantum Electronics* 23.1 (1987), pp. 9–29.
- [Ozo+19] Oskars Ozolins et al. “100 Gbaud PAM4 link without EDFA and post-equalization for optical interconnects”. In: *45th European Conference on Optical Communication (ECOC 2019)*. IET. 2019, pp. 1–4.
- [Pet+88] Isabelle Petitbon, Philippe Gallion, Guy Debarge, and Claude Chabran. “Locking bandwidth and relaxation oscillations of an injection-locked semiconductor laser”. In: *IEEE Journal of Quantum Electronics* 24.2 (1988), pp. 148–154.
- [PG11] J. G. Provost and F. Grillot. “Measuring the chirp and the linewidth enhancement factor of optoelectronic devices with a Mach–Zehnder interferometer”. In: *IEEE Photonics Journal* 3.3 (2011), pp. 476–488.
- [Pro+11] J. G. Provost, A. Martinez, A. Shen, and A. Ramdane. “Single step measurement of optical transmitters Henry factor using sinusoidal optical phase modulations”. In: *Optics express* 19.22 (2011), pp. 21396–21403.

- [SBK86] R Schimpe, JE Bowers, and TL Koch. “Characterisation of frequency response of 1.5 μm InGaAsP DFB laser diode and InGaAs PIN photodiode by heterodyne measurement technique”. In: *Electronics letters* 22.9 (1986), pp. 453–454.
- [SR23] Brian Siquin and Marco Romanelli. “Determination of the linewidth enhancement factor of semiconductor lasers by complete optical field reconstruction”. In: *Optics Letters* 48.4 (2023), pp. 863–866.
- [TTL21] A Tussupov, AT Tokhmetov, and NI Listopad. “Semiconductor Optical Amplifiers For Reach Extension of WDM/TDM Gigabit Passive Optical Network”. In: *2021 IEEE International Conference on Smart Information Systems and Technologies (SIST)*. IEEE. 2021, pp. 1–6.
- [Uch12] Atsushi Uchida. *Optical communication with chaotic lasers: applications of nonlinear dynamics and synchronization*. John Wiley & Sons, 2012.
- [Ura+01] Junji Urayama, Theodore B Norris, Jasprit Singh, and Pallab Bhattacharya. “Observation of phonon bottleneck in quantum dot electronic relaxation”. In: *Physical review letters* 86.21 (2001), p. 4930.
- [Usk+98] AV Uskov, J McInerney, F Adler, H Schweizer, and MH Pilkuhn. “Auger carrier capture kinetics in self-assembled quantum dot structures”. In: *Applied physics letters* 72.1 (1998), pp. 58–60.
- [Vah+83] K Vahala, LC Chiu, S Margalit, and A Yariv. “On the linewidth enhancement factor α in semiconductor injection lasers”. In: *Applied Physics Letters* 42.8 (1983), pp. 631–633.
- [Wan+21a] Yating Wan et al. “High Speed Evanescent Quantum-Dot Lasers on Si”. In: *Laser & Photonics Reviews* 15.8 (2021), p. 2100057.
- [Wan+14] Cheng Wang, M Osiński, J Even, and F Grillot. “Phase-amplitude coupling characteristics in directly modulated quantum dot lasers”. In: *Applied Physics Letters* 105.22 (2014).

-
- [Wan+21b] Zi-Hao Wang, Wen-Qi Wei, Qi Feng, Ting Wang, and Jian-Jun Zhang. “InAs/GaAs quantum dot single-section mode-locked lasers on Si (001) with optical self-injection feedback”. In: *Optics Express* 29.2 (2021), pp. 674–683.
- [YMN86] Y Yamamoto, S Machida, and O Nilsson. “Amplitude squeezing in a pump-noise-suppressed laser oscillator”. In: *Physical Review A* 34.5 (1986), p. 4025.
- [Yam+93] Takayuki Yamanaka, Yuzo Yoshikuni, Kiyoyuki Yokoyama, Wayne Lui, and Shunji Seki. “Theoretical study on enhanced differential gain and extremely reduced linewidth enhancement factor in quantum-well lasers”. In: *IEEE journal of quantum electronics* 29.6 (1993), pp. 1609–1616.

CHAPTER 3

Optoelectronic Feedback with Quantum Dot Lasers

3.1 Introduction

In contrast to ideal linear devices that provide a direct proportional relationship between input and output, semiconductor lasers exhibit excellent nonlinear dynamics [GKE97; Sim+95]. These nonlinear dynamics are primarily due to the interaction between the light field and the carrier density within the gain medium. This carrier-photon interaction is inherently nonlinear. It can also be derived from the differential equations for the photons and carriers of the semiconductor lasers [OO17]. There is a need to obtain the nonlinear dynamics of lasers to develop various applications where having $\alpha_H > 0$. Emerging applications using silicon photonic devices are rapidly heating up, such as microwave generation [JL09], optical chaos cryptography [Gas+04], optical sensing [Wan+17], and optical computing [Mou+23]. All these applications are related to the nonlinear dynamic properties of semiconductor lasers. However, the smaller α_H -factor of QD lasers does not favor their ability to generate nonlinear dynamics under optical feedback. In this chapter, the dynamics generation of QD lasers is the focus of the demonstration.

3.1.1 External control methods

Then several methods that can generate nonlinear dynamics will be analyzed to obtain the corresponding application possibilities.

► Optical injection

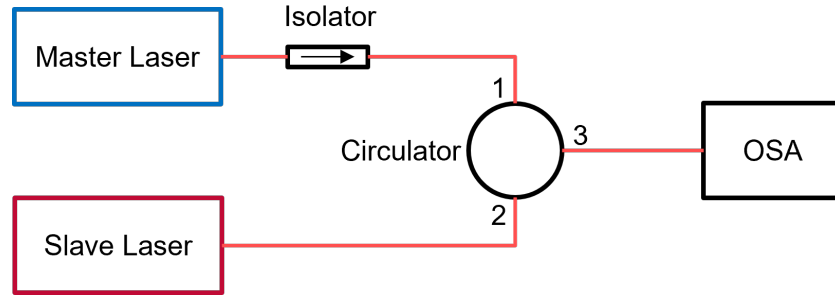


Figure 3.1: Schematic diagram of optical injection setup.

Fig. 3.1 illustrates the schematic diagram of the experimental setup for optical injection. As mentioned in Chapter 3, the dynamics boundary or Hopf points of the laser after optical injection are utilized to extract the α_H -factor. Numerous researches have shown that rich dynamics can be generated in QD lasers by optical injection [Gou+07; Ott14]. K. Lüdge's research indicates that under optical injection conditions, the dynamic characteristics of QD lasers are also affected by the Coulomb scattering process, and can be optimized through bandgap structure engineering [Pau+12]. They conducted a numerical analysis of the nonlinear dynamics as a function of the computed scattering lifetimes. The optical injection term was considered in the differential equations for photons (n_{ph}) and phase (Φ), and K is the injection strength with the expression $K = \sqrt{\frac{T_{inj}n_{inj}}{n_{ph}^0}}$ where T_{inj} is the transmission coefficient and $T_{inj}n_{inj}$ is the injected photon density in the active region. In the rate equations, the transport processes of electron occupation probabilities (ρ_e) and hole occupation probabilities (ρ_h) were also taken into account as expressed below,

$$\dot{n}_{\text{ph}} = n_{\text{ph}} \left[2\bar{W}Z_a^{\text{QD}} (\rho_e + \rho_h - 1) - 2\kappa \right] + \frac{\beta_{\text{sp}}}{A} 2Z_a^{\text{QD}} R_{\text{sp}} (\rho_e, \rho_h) + \frac{2K}{\tau_{\text{in}}} \sqrt{n_{\text{ph}} n_{\text{ph}}^0} \cos(\Phi - 2\pi\Delta v_{\text{inj}} t) \quad (3.1)$$

$$\dot{\Phi} = \frac{\alpha_H}{2} \left[2\bar{W}Z_a^{\text{QD}} (\rho_e + \rho_h - 1) - 2\kappa \right] + \frac{K}{\tau_{\text{in}}} \sqrt{\frac{n_{\text{ph}}^0}{n_{\text{ph}}}} \sin(\Phi - 2\pi\Delta v_{\text{inj}} t) \quad (3.2)$$

where the W is the Einstein coefficient for spontaneous emission. Z_a^{QD} is the number of QD inside the active region. 2κ is the optical intensity loss. β_{sp} is the spontaneous emission factor. A is the in-plane area of QW on either side of QD. $R_{\text{sp}}(\rho_e, \rho_h)$ denotes the spontaneous emission of one QD. τ_{in} is the photon round trip time in the cavity. n_{ph}^0 is the steady-state photon density without injection. v_{inj} is the input detuning.

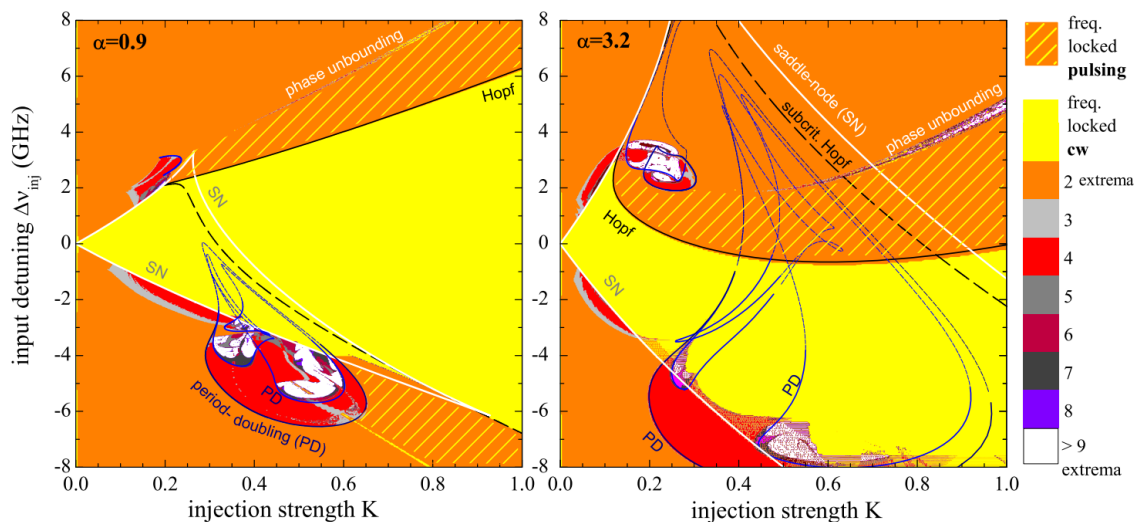


Figure 3.2: Two-parameter bifurcation diagrams showcasing (a) α_H -factor = 0.9 and (b) α_H -factor = 3.2 are presented. The diagram is color-coded to denote the count of extremal values, that is, the total number of maxima and minima in the photon density. [Pau+12]

Based on the aforementioned rate equations, varying the detuning and injection strength yields dynamic bifurcation diagrams. Fig.3.2(a) and (b) present two bifurcation diagrams under different α_H -factor, 0.9 and 3.2. Areas in light yellow represent average frequency locking characterized by a constant photon density, indicative of

continuous-wave lasing. The cross-hatched area in shades of yellow and orange illustrates oscillatory photon density behavior (featuring one minimum and one maximum) while maintaining a locked average frequency. The solid lines in blue, black, and white signify the boundaries of Period-Doubling, Hopf, and Saddle-Node (SN) bifurcations, respectively. Therefore, if one desires to obtain a broad window of dynamic characteristics under optical injection conditions, a laser with a larger α_H -factor will be beneficial. Moreover, different dynamics can be precisely controlled through the injection strength and detuning.

► External optical feedback

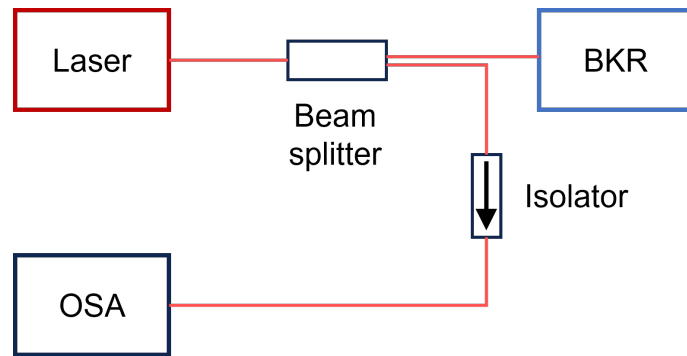


Figure 3.3: Schematic diagram of external optical feedback setup. BKR: back reflector.

Generating nonlinear dynamics using external optical feedback is more suitable for on-chip integration than optical injection because the tunable wavelength master laser is not required. The simplified schematic diagram of external optical feedback is shown in Fig. 3.3. A model was used to perform a targeted investigation of the QD laser dynamics under optical feedback. The delay terms for the number of photons and phase are considered to represent the feedback changes in photon and phase, defining the delay as τ [Glo+12]. For the simulation, $\tau = 16$ was set equivalent to an external cavity feedback distance of 2.4 cm. As shown in Fig. 3.4, the solution results at $\alpha_H = 0.9$ appear less rich compared to those at $\alpha_H = 3$. At higher α_H -factor, there is a transition from stable to unstable periodic processes, and each process is characterized by bifurcations and chaotic states. This also corroborates the conclusions drawn in Chapter 3 regarding the influence of the α_H -factor on optical feedback.

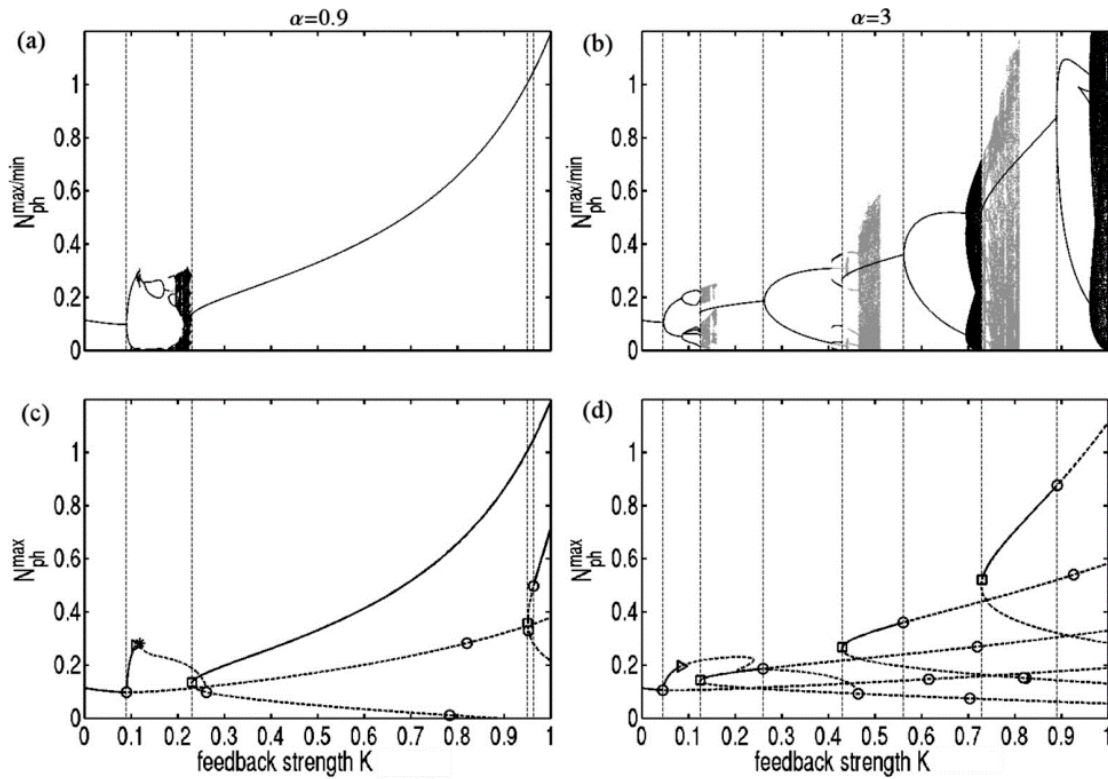


Figure 3.4: Single-parameter bifurcation diagram of the photon number N_{ph} concerning the feedback strength, obtained from direct numerical integration [(a), (b)] and path continuation using delay differential equations [(c), (d)]. The upper figures show the maximum and minimum photon densities $N_{\text{ph}}^{\text{min/max}}$, while the lower figures display only the maximum values $N_{\text{ph}}^{\text{max}}$. The α_{H} -factor is set to 0.9 for the left column and 3 for the right column. [Glo+12]

B. Dong et al. experimentally investigated the dynamics of a QD laser grown on silicon under delayed optical feedback strengths and identified a range of dynamic states of periodic oscillations [Don+21]. Fig.3.5 displays the dynamic changes of the QD laser at different cavity lengths. Under a long-cavity (> 10 cm) feedback, the device maintained a chaos-free state even when the feedback strength was around 70%. When the external cavity length was reduced to the short-cavity scale (< 10 cm) typical in photonic integrated circuits, the occurrence of periodic oscillations happened only at extremely high levels of feedback strength, much higher than what is common within photonic integrated chips. Thus, QD lasers on silicon with a smaller α_{H} -factor have a very strong tolerance to optical feedback leading to full immunity.

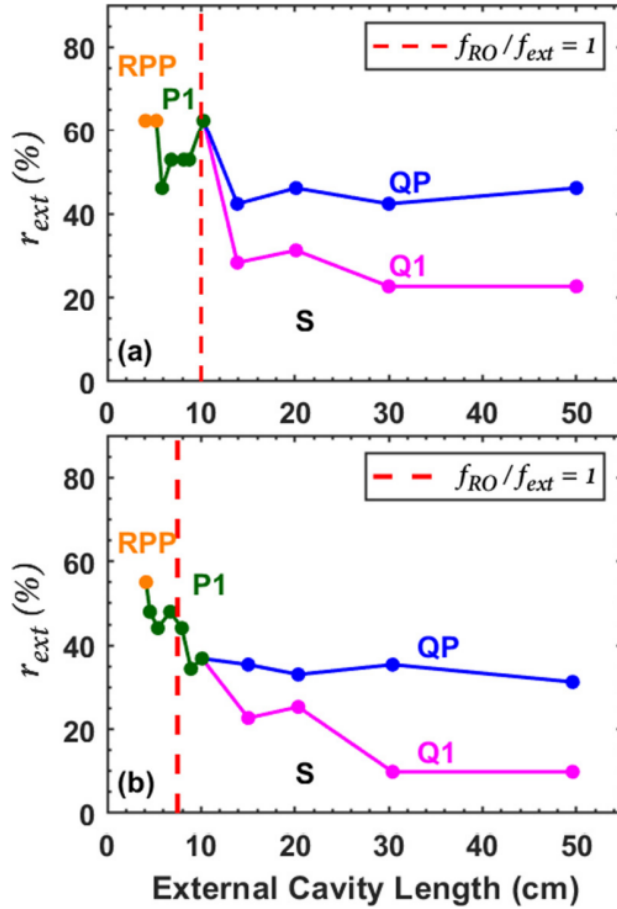


Figure 3.5: Mapping of the dynamic states of the QD laser under different feedback strengths and external cavity lengths at drive currents of (a) 125 mA and (b) 160 mA. [Don+21]

► Injection current modulation

Additionally, there is potential for dynamics generation in semiconductor lasers through direct current modulation as shown in the schematic of the setup in Fig. 3.6. M. Yamada et al. have investigated the mode dynamics associated with sinusoidal modulation of single-mode QW laser [AY12]. The dynamics were studied over a wide range of modulation frequencies and depths based on a semiconductor laser rate equation model. The results, as shown in Fig. 3.7, indicate that depending on the modulation conditions, there are six distinct waveforms of the modulation signal; three have continuous periodic waveforms with multi-mode oscillations (CPSRO: continuous periodic

signal with relaxation oscillations; CPS: continuous periodic signal; CPPD: continuous periodic signal with period doubling), while the others are characterized by periodic pulsed waveforms with single mode oscillations (PPRO: periodic pulse with relaxation oscillations; PP: periodic pulse; PPPD: periodic pulse with period doubling).

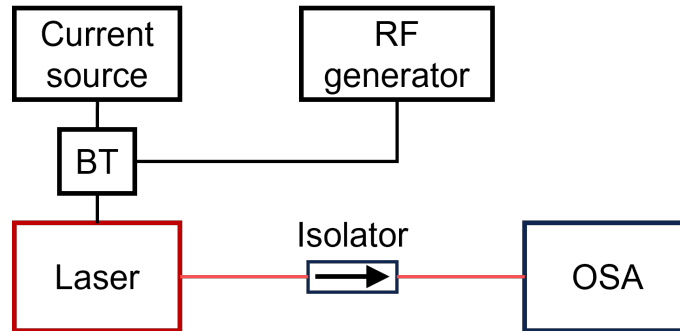


Figure 3.6: Schematic diagram of injection current modulation. BT: bias tee.

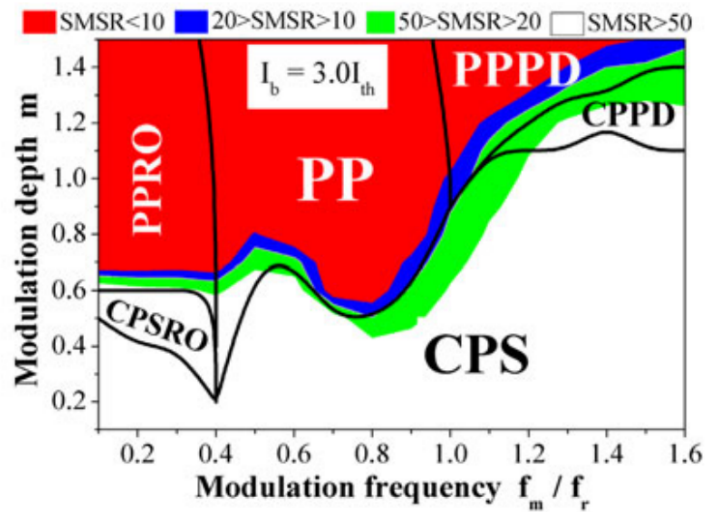


Figure 3.7: The graph of modulation index versus modulation frequency for the types of modulated laser signals. [AY12]

► Optoelectronic feedback

Optoelectronic feedback (OEF) is an appealing method to activate nonlinear behaviors in laser diodes, as an OEF loop can be considered a closed-loop oscillator and

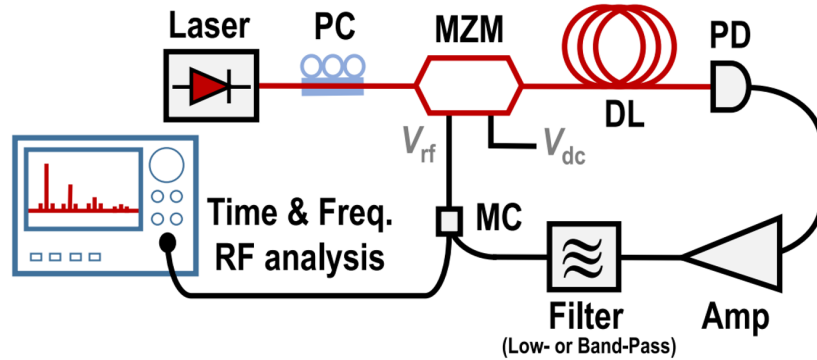


Figure 3.8: Experimental setup for Ikeda-like OEF with modulator. [Che+19]

is known for exhibiting diverse interesting dynamics. In a structure of Ikeda-like OEF, the loop is usually expressed by decomposing into four elements containing the linear gain, the nonlinear function, the band-pass filter, and the loop delay. The nonlinear function is the key to introducing nonlinear characteristics. The nonlinear component like the Mach-Zehnder modulator (MZM) can be introduced to enrich the system nonlinearity and obtain different dynamics, as shown in Fig. 3.8. Although these additional elements enhance the dynamical diversity, they also complicate the fabrication process which is somewhat unwanted for silicon-based integration.

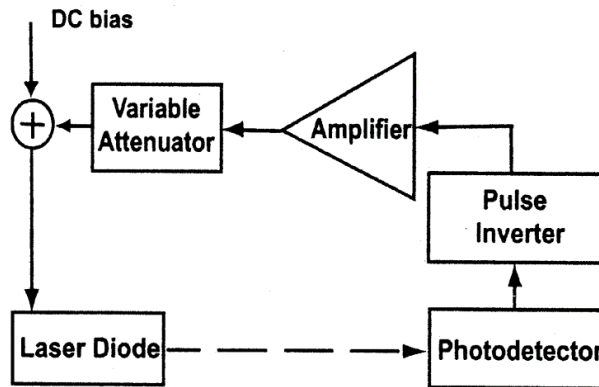


Figure 3.9: Schematic diagram of the experimental setup for delayed optoelectronic feedback semiconductor laser system. [LL03]

On the other hand, it has been attempted to utilize the nonlinear processes of optoelectronic conversion devices as the nonlinear function for OEF. Some studies

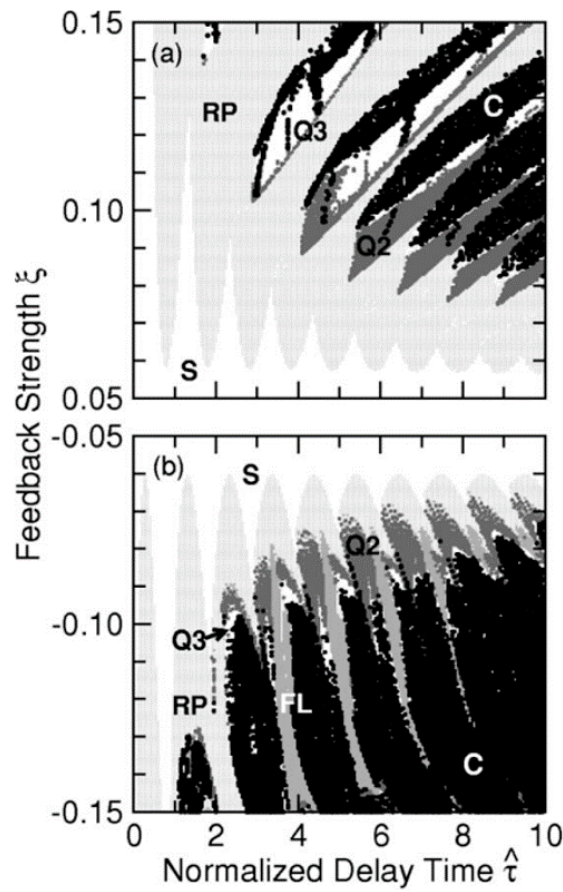


Figure 3.10: (a) Mapping of dynamic states for the positive OEF and (b) negative OEF. S: Stable state. RP: Regular pulsing. Q2: Bi-frequency quasiperiodic pulsing. Q3: Tri-frequency quasiperiodic pulsing. FL: Frequency-locked pulsing. C: Chaotic pulsing. [LL03]

focused on semiconductor lasers that directly AC-coupled in OEF loops, where the laser was connected to the bias tee (BT) allowing the pump current to enter from the DC-arm and the feedback signal from the AC-arm [Isl+21; LL03]. F. Lin et al. carried out both numerical and experimental research on the nonlinear dynamics of semiconductor lasers with delayed negative optoelectronic feedback [LL03]. They employed a model based on rate equations to compare the dynamic mapping and bifurcation diagrams of systems with delayed negative OEF against those with delayed positive OEF, where the OEF term was integrated into the carrier differential equation. As demonstrated in Fig. 3.10, both systems adhered to a quasiperiodic route to chaos, exhibiting regular

pulsing, quasiperiodic pulsing, and chaotic pulsing states.

M. Islam et al. reported the generation of optical square waves in semiconductor lasers under negative OEF [Isl+21]. The optoelectronic oscillator is based on the nonlinear effects present in a feedback loop that includes a QW laser diode and a photo-diode, with the loop driven into saturation by an amplifier. The repetition rate of the SW is a multiple of the reciprocal of the loop delay, and the duty cycle can be modified by adjusting the injection current. To validate these outcomes, they added a set of equations with band-pass filters to the rate equations. The model produced results consistent with experimental observations and demonstrated the generation of optical square waves. Considering the increased computational load due to multiple electronic components in the loop and the potential for unclear square waveforms, the model requires further optimization.

3.1.2 Applications

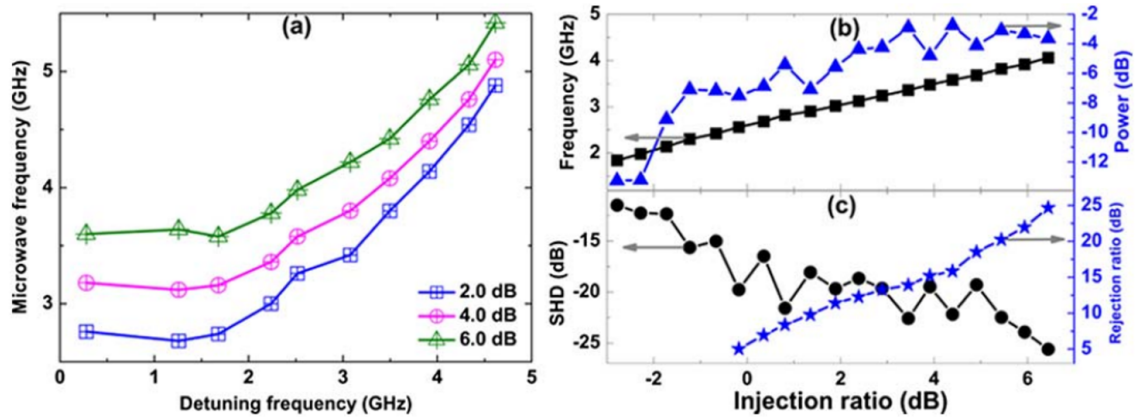


Figure 3.11: (a) Variation of the frequency of local minimum period 1 with detuning frequency for different optical injection strengths. (b) Variation of microwave frequency and power with optical injection strength. (c) Trend of the second harmonic distortion (SHD) and sideband rejection ratio with detuning frequency. [Wan+16]

► Microwave generation

Microwave generation using semiconductor lasers is one of the most straightforward applications of nonlinear dynamics. By inducing optical injection [JL09; Wan+16], ex-

ternal optical feedback [LHD14], injected current modulation [VL82], or other interaction of laser modes, semiconductor lasers can generate microwave and millimeter-wave frequencies. This capability has vital applications in telecommunications where the demand for high bandwidth and the proliferation of wireless services necessitate stable and tunable microwave sources. The generation of these signals via laser diodes can often be more precise and less noisy compared to traditional electronic oscillators. As shown in Fig. 3.11, the QD laser under optical injection produces a period-one oscillation of the microwave frequency and that can be continuously controlled by adjusting the frequency detuning.

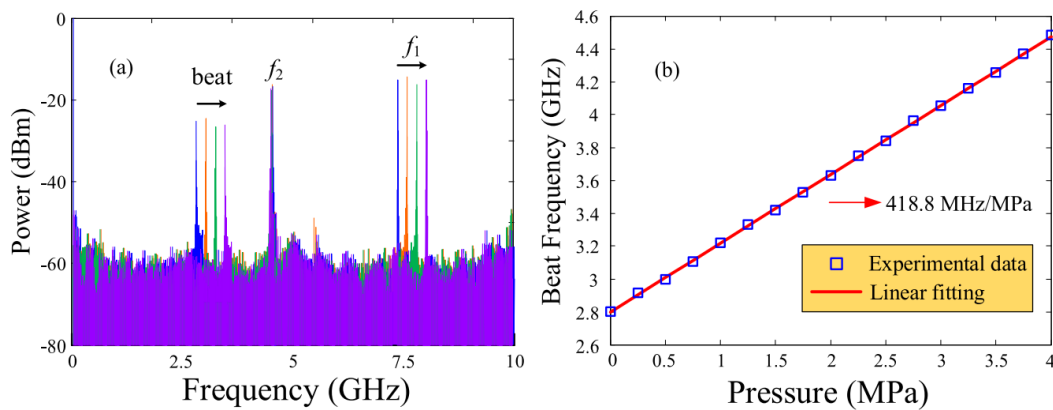


Figure 3.12: (a) Superimposed electrical spectra of microwave signals generated at different pressures. (b) Measured beat frequency as a function of applied pressure. [Wan+17]

► Optical sensing

Optical sensing is another important application area that benefits from the extreme sensitivity of semiconductor lasers to external conditions. Utilizing the nonlinear dynamic properties of these lasers, the sensors can detect small changes in environmental parameters, such as pressure [Wan+17]. The fiber Bragg grating was inserted into the OEF loop pressure was applied, and the frequency generated by the loop shifted in response to the pressure. This sensitive phase shift results in highly accurate pressure detection as shown in Fig. 3.12. The resulting precision optical sensors can be used in areas such as environmental monitoring and industrial process control.

with mid-infrared light was realized for the first time.

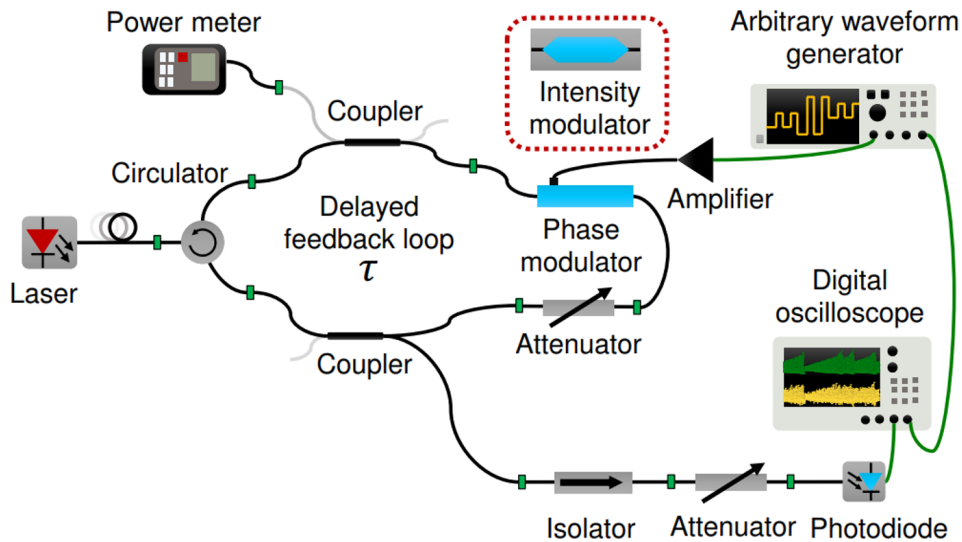


Figure 3.14: Experimental setup of reservoir computing using a semiconductor laser with feedback modulation function. [KHU22]

► Optical computing

Optical computing is probably the most innovative application of nonlinear dynamics of semiconductor lasers [McM23]. Representative of Optical computing is reservoir computing which utilizes the high-dimensional dynamics of nonlinear systems for information processing. Once in these states, semiconductor lasers provide a rich store of dynamics that can be used for parallel computation, useful in tasks such as pattern recognition and signal processing. The utilization of optical injection, optical feedback, and optoelectronic feedback to generate various nonlinear dynamics can all be applied to reservoir computing [VBS17]. Fig. 3.14 illustrates an experimental setup for reservoir computing based on an optical feedback-modulated external cavity semiconductor laser [KHU22]. In this scheme, the input signal was injected into the feedback loop of the semiconductor laser by intensity or phase modulation of the optical feedback signal. The reservoir was then used to perform a chaotic time series prediction task and to compare the performance of the intensity and phase modulation schemes. The

results show that a high-dimensional mapping from the input signal to the response laser output trajectory can be achieved using phase modulation of the feedback signal.

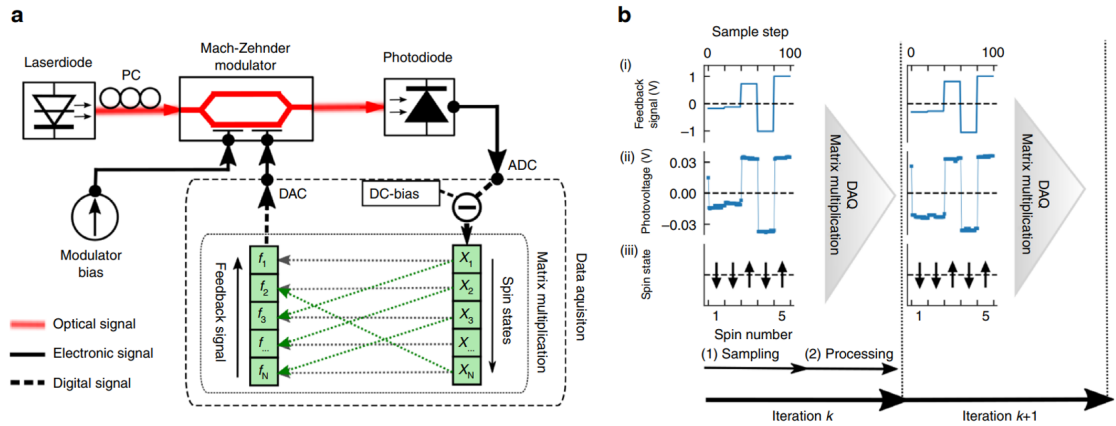


Figure 3.15: (a) Experimental schematic of the coherent Ising machine based on OEF. (b) Working principle. (1) In the sampling stage, (i) feedback signal generation, (ii) spin amplitude measurement, (iii) spin states sign determination. (2) In the processing stage, digital processing and matrix multiplication of spins. [BVV19]

Ising machines that simulate the behavior of magnetic spins use networks of coupled semiconductor lasers to solve complex optimization problems. These systems can find the lowest energy configuration of the spin network and thus efficiently find solutions to traditional computer computationally intensive problems. [Bab+19; TY14]. At this stage, this Ising machine utilizing an optoelectronic feedback loop also needs to utilize the involvement of a modulator. F. Böhm, et al. proposed and tested the concept of a programmable coherent Ising machine based on optoelectronic oscillators with self-feedback [BVV19]. The artificial spins are generated in dynamical bifurcations induced by the feedback and are encoded in the intensities of coherent states. This eliminates the need for nonlinear optical processes or large external cavities, offering significant advantages in terms of stability and cost. If the nonlinearity of the semiconductor laser is utilized for direct OEF [Che+20], the coherent Ising machine can be further simplified, facilitating the development of silicon-based integrated Ising machines.

3.2 Optoelectronic feedback with epitaxial QD lasers

In Chapter 2, I demonstrated the strong optical feedback tolerance of the QD laser. Therefore, if there is a need to manufacture a silicon-integrated dynamic generator, alternative approaches should be explored. The method involving optical injection requires the integration of a tunable-wavelength single-mode laser, which adds complexity to the device fabrication process, and the introduction of intense injected light can also result in irreversible damage. Hence, both optical injection and optical feedback with QD lasers are not effective means for silicon-integrated dynamics generators. In this section, the nonlinear dynamics of epitaxial QD lasers on silicon in an optoelectronic feedback loop were investigated through experimental and numerical approaches. I will show that OEF is a powerful technique for generating various nonlinear dynamics.

3.2.1 OEF experimental configuration

A silicon-based QD Fabry-Perot (FP) laser was used for the optical source in the OEF loop. The epitaxial structure of the laser is consistent with the directly modulated laser in the previous section. The InAs/GaAs FP laser is 1.35 mm long and has a 3.5 μm wide ridge waveguide. The cavity facets have power reflectivity of 60% and 99% on the front and rear facets, respectively. Fig. 3.16 displays the tabletop experiment used for studying OEF in the silicon-based QD laser. The feedback loop contains an optical isolator to eliminate back-reflections into the QD laser. While it may not be strictly necessary, its presence guarantees that the dynamics I present in this study strictly arise from optoelectronic feedback rather than optical feedback. The QD laser's output light traverses a loop containing both optical (semiconductor optical amplifier (SOA)) and electrical components (photodetector (PD), amplifier, radio-frequency (RF) attenuator, RF splitter, and BT). The SOA was used so that the QD laser meets the conditions for strong OEF at the low pump while being compatible with silicon-based integration. The electrical amplifier allows the investigation of strong OEF conditions, while the RF attenuator prevents circuit overloading. All the gains and losses in the OEF loop make up the total feedback strength. The pump current is set at twice the threshold for all tests, channeled to the laser via the BT's DC arm, with

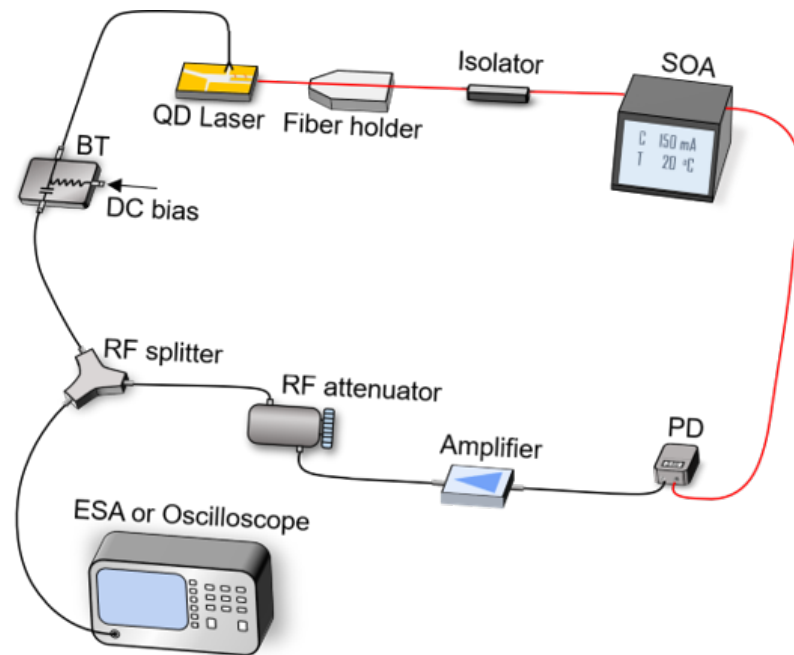


Figure 3.16: The tabletop experiment was used for studying optoelectronic feedback in the silicon-based QD laser (the solid red lines represent the optical path and the solid black lines represent the electrical path).

feedback conveyed through its AC arm. The post-attenuator, pre-BT electrical signal is monitored using an oscilloscope. Given that the low-noise amplifier inverts the nature within the PD when coupled with the electrical loop amplifier, a net negative feedback signal is produced. With an anode-grounded laser architecture, the overall feedback sign is positive due to the negative nature of both the injection-terminal voltage and the feedback signal. Feedback strength is gauged by the OEF loop's electrical amplifier gain, with a total delay of 250 ns corresponding to a frequency of about 4 MHz.

The optical output power-current-voltage (PIV) characteristics are shown in Fig. 3.17(a) for temperatures of 20 °C and 30 °C, respectively. The threshold current is found to increase from 12 mA to 20 mA with temperature. Fig. 3.17(b) shows the variation of the voltage across the laser electrodes with increasing OEF strength at different temperatures and twice the threshold current. Since the maximum gain of the electrical amplifier is 30 dB, it was attenuated with a maximum 10 dB attenuator on top of that, so the labeled feedback strength was in the range of 20 to 30 dB. This

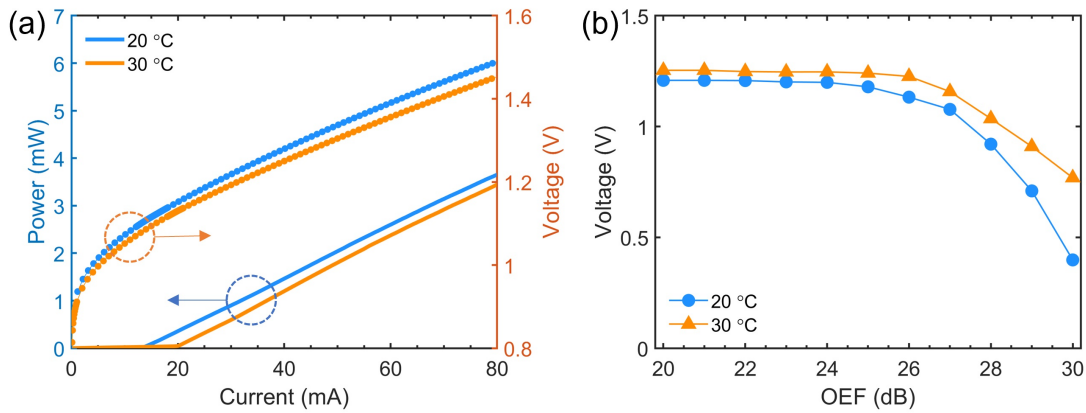


Figure 3.17: (a) Optical power-voltage with bias current. (b) The measured voltage applied on the QD laser concerning the OEF strength.

measurement demonstrates the existence of a critical point beyond which the voltage drops down rapidly. At 20 °C, this drop-off point appears at a feedback strength of 24 dB, while at 30 °C, it appears at 26 dB. Furthermore, the voltage drop rate is faster at lower temperatures. This effect might be due to the stronger electrical feedback negative signal brought by the high laser's output power at lower temperatures. This drop-off point may be associated with the dynamics transition point of the QD laser.

3.2.2 Enhanced nonlinear dynamic under OEF

Fig. 3.18(a) and (b) show the electrical spectra of the QD laser under OEF at 20 °C and 30 °C, respectively. At 20 °C, the QD laser begins to show a high-intensity signal at a frequency of 0.5 GHz as the OEF strength increases from 21 dB to 23 dB. When the feedback strength continues to increase, the low-frequency noise below 100 MHz gradually intensifies, as shown in Figures 2a and 2c. Typically, the carriers in semiconductor lasers operating at higher temperatures are subject to thermal effects that alter the carrier transport processes as well as the gain of the laser, which can lead to more complex dynamic changes [Pat+99]. As shown in Fig. 3.18(b) and (d), the initial oscillation at 0.5 GHz at 20 °C gets much more prominent and even expands on a larger frequency range when the temperature is raised to 30 °C. At the same time, the QD laser exhibits a chaotic-like spectrum state with a wide bandwidth of about 5 GHz.

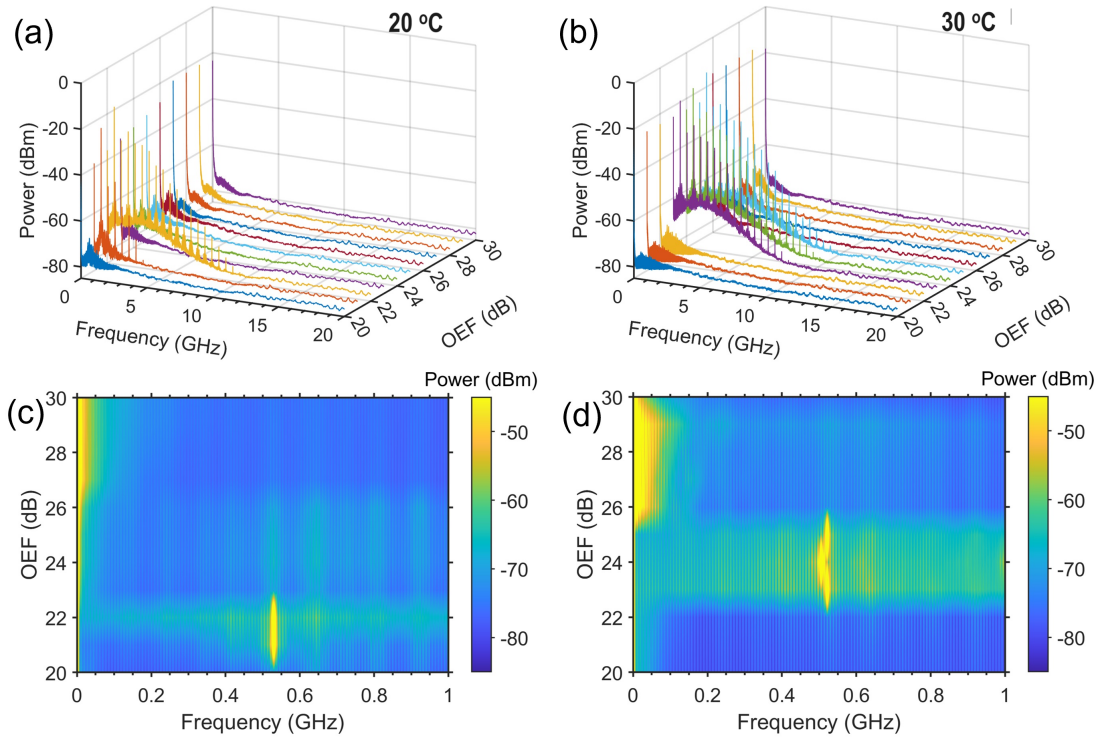


Figure 3.18: Temperature impact on the dynamics of the QD laser with OEF. Electrical spectra were measured under different OEF strengths at (a) 20 °C and (b) 30 °C respectively. (c) and (d) are the corresponding mappings of the electrical spectra in the 1 GHz range at 20 °C and 30 °C respectively.

The low-frequency noise gets stronger at higher feedback strength. Contrasting with conventional optical feedback systems, where QD lasers typically exhibit insensitivity, this study reveals a distinct characteristic: In contrast to external optical feedback, QD lasers can manifest a wealth of nonlinear dynamics under OEF. Subsequently, I undertake a comprehensive time-domain analysis, by systematically varying feedback strengths and operating temperatures to delve deeper into this intriguing behavior.

Fig. 3.19(a1)-(a5) depict the time-domain signals of the QD laser for different OEF strengths at 20 °C. As the feedback strength increases, the QD laser displays different waveforms ranging from (a1) sine wave, (a2) quasi-square wave, (a3) square wave, to (a4) a mixed state with fast and slow oscillations, where the fast period is shown in (a5). Both the sine wave and the quasi-square wave exhibit a 2 ns period

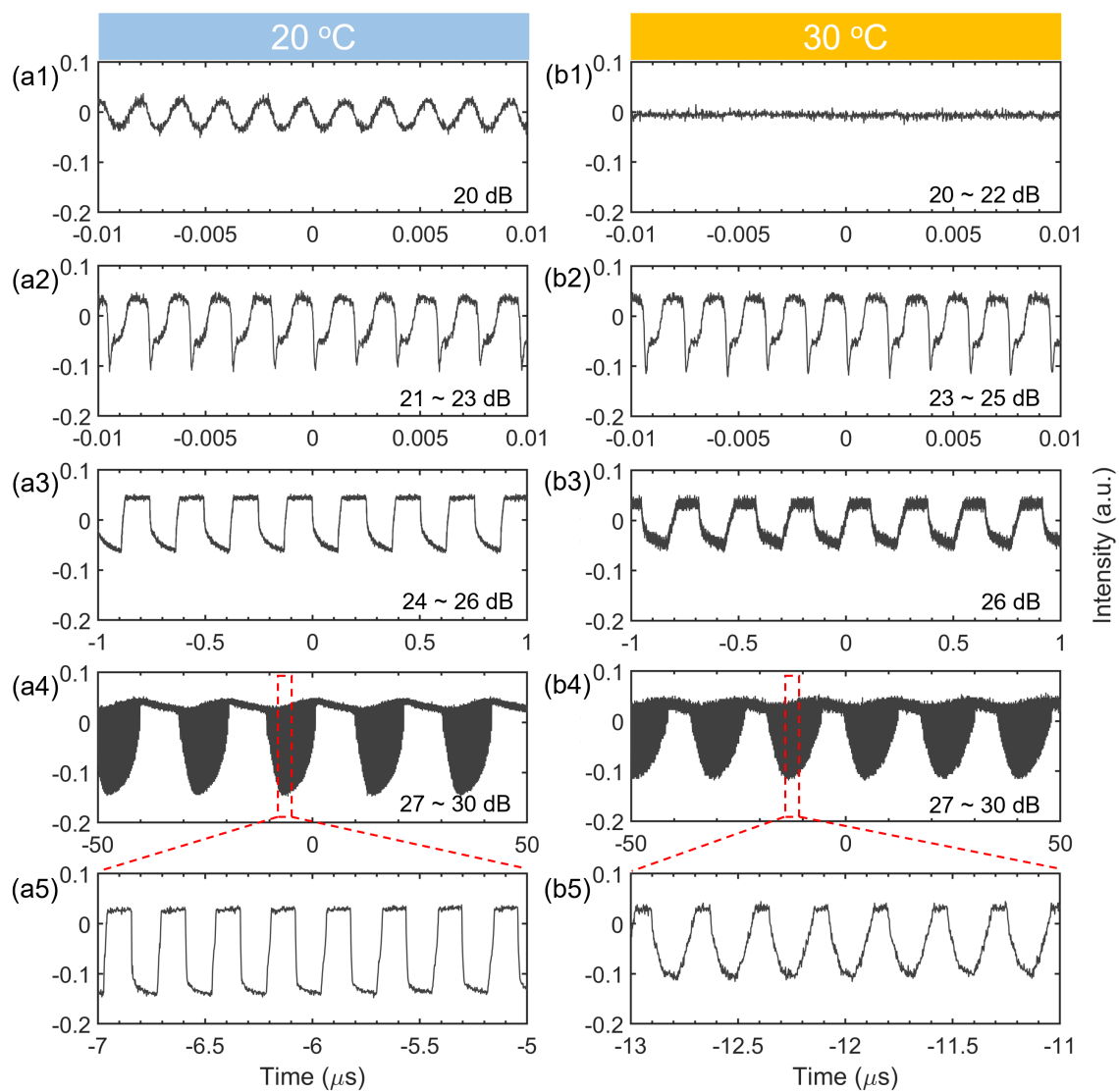


Figure 3.19: Nonlinear dynamics of the epitaxial QD laser with OEF. Experimental time dependent output of the QD laser at (a1)-(a4) 20 °C and (b1)-(b4) 30 °C with different OEF strengths. (a5) and (b5) are partial zoom-in views.

which comes from a high cut-off frequency. Due to the low amplitude of the sine wave, only a weak contribution of the 0.5 GHz peak contribution can be seen in the electrical spectrum, while the quasi-square wave corresponds to stronger frequency peaks and a chaotic-like uplift. The chaotic-like signal at this point may come from the inconsistent falling edge of the square wave-like. The period of the square wave is 250 ns, which perfectly corresponds to the OEF loop time. As for the mixed state, it is found that the slow period of 20 μ s corresponds to the wave packet occurrence whereas the fast one of 250 ns is linked to the square wave dynamics within the wave packet. As the temperature rises, a greater number of carriers are thermally excited to higher energy states, leading to the possibility of additional alterations in the laser dynamics. Therefore, by increasing the temperature to 30 °C, I found that the sine wave does not appear at lower feedback strengths, but remains steady instead while the appearance of the quasi-square wave occurs much later. Under this temperature, the mixed regime with fast and slow oscillations also appears after the square wave. These regimes displayed in Fig. 3.19(b1)-(b5) are due to the increase of thermal effects which slow down the involvement of carriers in the electrical non-linear changes.

The QD laser under study outputs a pronounced sensitivity to OEF characterized by intense and sustained dynamic features. As previously mentioned, this rich behavior is fundamentally different from the typical observations encountered with conventional optical feedback where full insensitivity has been reported [Dua+19]. To ensure a comprehensive analysis, I further investigate the key distinctions by comparing our findings with those obtained from a 1310 nm QW FP laser. By employing an identical setup at a temperature of 30 °C, I captured the time series displayed in Fig. 3.20(a). It can be found that the reference QW laser does not exhibit a square wave nor a mixed state with fast and slow oscillations observed even at the highest feedback strength of 30 dB. By varying the OEF strength, different regimes are observed from steady-state to sine wave down to quasi-triangular wave. To verify whether the reference QW laser could produce more dynamics under high feedback strengths, an additional electronic amplifier (RF Bay, LNA-1800, 1 kHz-1.8 GHz, 30 dB gain) was included in the loop. Due to limitations in the availability of electronic attenuators with a broader range, our adjustment options were restricted to a 10 dB attenuation following a 60 dB-RF signal enhancement achieved through the use of two electrical amplifiers, as depicted in Fig.

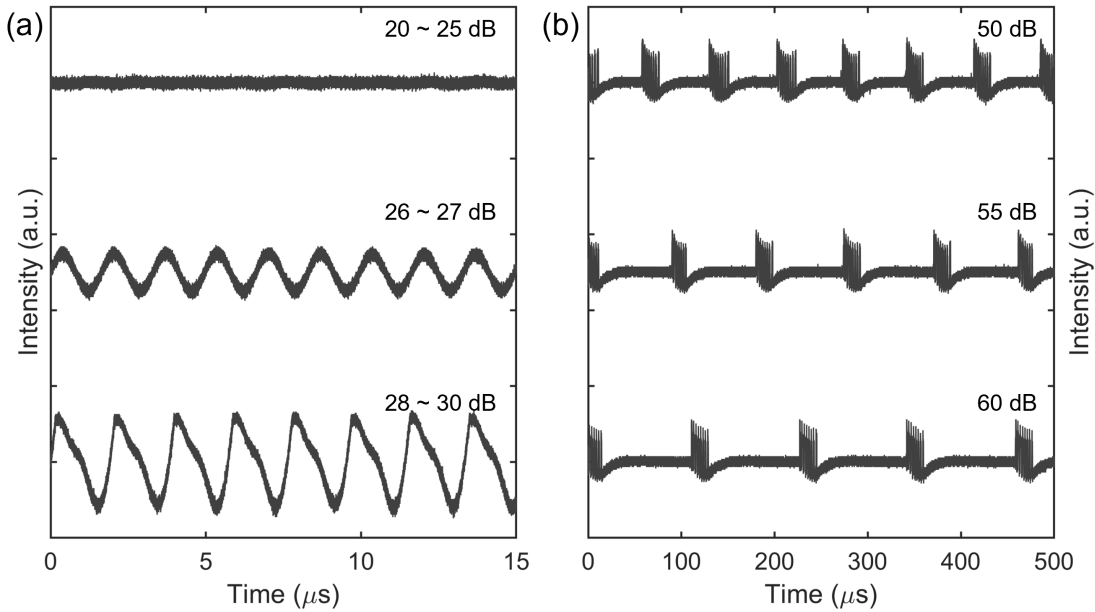


Figure 3.20: Nonlinear dynamics of the reference QW laser with OEF. (a) Experimental time series of QW laser with the same OEF setup as QD laser at different feedback strengths. (b) Time series of the QW laser after the inclusion of another electrical amplifier with feedback strengths.

3.20(b). The QW laser exhibits a mixed waveform of fast and slow oscillations under high feedback strengths. As the feedback strength increases, the slow period gradually changes. The fast period, however, remains a square wave with a constant period. This is consistent with the state of the QD laser under high feedback strength with one electronic amplifier. As compared to the QD laser, the QW laser demonstrates extreme OEF insensitivity while it is more sensitive to conventional optical feedback than the QD laser. A comparison of the dynamic generation of the QD laser with that of the QW laser under OEF is shown in Table 3.1.

Dynamics	sine wave	quasi-square wave	square wave	mixed states
QD	✓	✓	✓	✓
QW	✓	✗	✗	✓

Table 3.1: Comparison about the dynamics generation between QD and QW lasers

3.2.3 Theoretical analysis and modeling

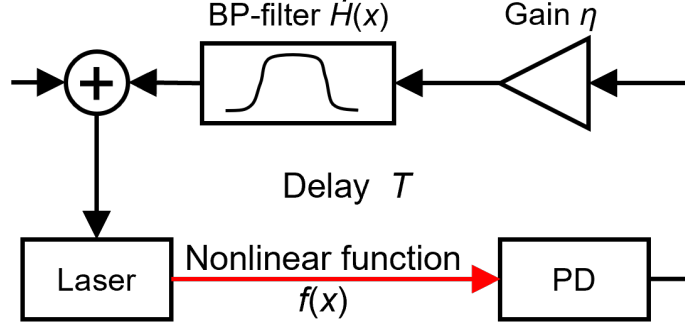


Figure 3.21: A block diagram depicting the time-domain representation of the Ikeda-like OEF loop. The variable $x(t)$ undergoes counterclockwise circulation and interacts with the four key components within the loop.

Based on the theory of Ikeda-like ring-cavity and band-pass filter systems, the OEF loop can be modeled with four elements namely by considering a band-pass filter since all electrical components have bandwidth and can be regarded as a band-pass filter, the gain of the loop and its corresponding delay, and the nonlinear transfer function as illustrated in Fig. 3.21 [Ike79; Mbé+15]. Exploiting the significant spectral separation between the low cutoff frequency, $f_L = 50$ kHz, and the high cutoff frequency, $f_H = 0.5$ GHz, we can model this band-pass filter as a cascade of two first-order linear filters, comprising a high-pass and a low-pass filter. In addition, the loop delay time $T = 250$ ns determines the period of the time domain signal. The input voltage $V_{in}(t)$ and output voltage $V_{out}(t)$ of a cascaded band-pass filter are linked by the equation:

$$\hat{H}(V_{out}(t)) \equiv \left[1 + \frac{f_L}{f_H}\right] V_{out}(t) + \frac{1}{2\pi f_H} \frac{dV_{out}(t)}{dt} + 2\pi f_L \int_{t_0}^t V_{out}(s) ds = V_{in}(t) \quad (3.3)$$

The optical power P at the output of the optical fiber undergoes conversion into an electrical signal through the PD, which follows a time-delayed relationship expressed as $S \times P(t - T)$. Here, S represents the power-dependent responsivity of the PD, and

T signifies the time delay resulting from fiber propagation. Importantly, the output voltage of the PD corresponds to the voltage $V_{\text{in}}(t)$ applied to the input of the band-pass filter. Furthermore, the relationship between $V_{\text{RF}}(t)$ and the output voltage can be described as $V_{\text{RF}}(t) = \eta V_{\text{out}}(t)$, where η serves as a conversion factor encompassing all linear gains and losses (both electrical and optical) within the feedback loop. Consequently, it can be demonstrated that the radio-frequency voltage $V_{\text{RF}}(t)$ adheres to the following equation:

$$\begin{aligned} \left[1 + \frac{f_L}{f_H}\right] V_{\text{RF}}(t) + \frac{1}{2\pi f_H} \frac{dV_{\text{RF}}(t)}{dt} + 2\pi f_L \int_{t_0}^t V_{\text{RF}}(s) ds \\ = \eta f_{\text{NL}} [V_{\text{RF}}(t - T)] \end{aligned} \quad (3.4)$$

The nonlinearity transfer function of the feedback loop denoted as $f_{\text{NL}} [V_{\text{RF}}(t - T)] = S \times P(t - T)$, which is directly dependent on the RF voltage. By taking into account $f_L \ll f_H$, we can reformulate this transfer function in a dimensionless form as follows:

$$x(t) + \tau \frac{dx(t)}{dt} + \frac{1}{\theta} \int_{t_0}^t x(s) ds = \eta f_{\text{NL}} [x(t - T)] \quad (3.5)$$

In this context, I define the system variable as $x(t) = V_{\text{RF}}(t)/V_{\text{REF}}$, where $V_{\text{REF}} = 1$ V serves as a convenient reference voltage, ensuring that $|x(t)| = |V_{\text{RF}}|$. The dimensionless feedback loop linear gain η . Moreover, I introduce several time parameters: $\tau = 1/2\pi f_H$, and $\theta = 1/2\pi f_L$, which correspond to the high-pass and low-pass cut-off frequencies, respectively.

In OEF architectures, signal conversion often uses a sinusoidal transfer function in a phase or intensity modulator. Alternatively, the seeding laser itself can serve as an electrical-to-optical converter [Che+20]. Building on this, we propose a modeling approach leveraging the "elbow" nonlinearity in the power-intensity transfer function of lasers. This nonlinearity results from laser threshold, carrier leakage, and gain compression, creating piecewise characteristics. The PD can also exhibit nonlinearity due to saturation. The overall transfer function encompasses a cascade of nonlinearities from both the laser and PD. To determine the nonlinearity transfer function of QD lasers and QW lasers individually, I conduct experiments using a setup comprising different laser diodes and the same PD in the open-loop configuration. In

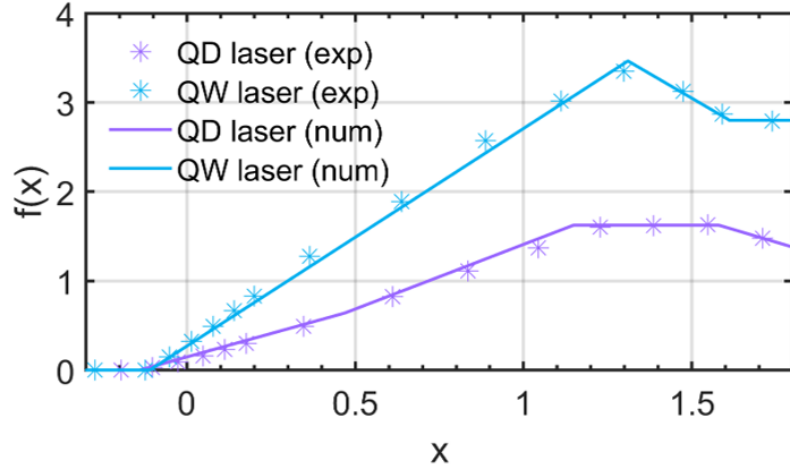


Figure 3.22: The experimental and numerical nonlinearity transfer functions of QD (purple) and QW (blue) lasers, respectively.

this setup, an input voltage V is applied to the laser diode, gradually increased, and both this voltage and the corresponding output voltage V_{PD} at the PD are recorded. These recorded data points are then utilized to generate the plotted points shown in Fig. 3.22. The PD remains in the linear region until the lasers reach the saturation region (the response curve of the PD can be found on the official website: <https://www.discoverysemi.com/ProductPages/DSC710720.php>). Therefore, the response curve of the PD in the nonlinearity transfer function can be taken as a linear line. The characteristic inflection points of the nonlinearity transfer function are mainly determined by the difference in the power-voltage curves of the lasers. Subsequently, I interpolate these points using piecewise transfer functions for the QD laser (f_{QD}) and for the QW laser (f_{QW}) which read as follows:

$$f_{QD}(x) = \begin{cases} 0, & x \leq -0.14 \\ 1.05x + 0.15, & -0.14 < x \leq 0.47 \\ 1.45x - 0.04, & 0.47 < x \leq 1.15 \\ 1.62, & 1.15 < x \leq 1.58 \\ -1.12x + 3.39, & x > 1.58 \end{cases} \quad (3.6)$$

$$f_{QW}(x) = \begin{cases} 0, & x \leq -0.11 \\ 2.44x + 0.27, & -0.11 < x \leq 1.31 \\ -2.2x + 6.35, & 1.31 < x \leq 1.61 \\ 2.80, & x > 1.61 \end{cases} \quad (3.7)$$

The coefficients of the piecewise transfer functions are calculated through linear interpolation based on the available experimental data points. The obtained results demonstrate a remarkable level of agreement between the experimental observations and the numerical modeling. The specific segmentation points used in the interpolation process are determined by considering key factors such as the laser threshold, saturation transitions, and saturation drop point. Furthermore, it is important to reiterate that the variable x should not be confused with the input voltage (V) applied to the laser diode as recorded in previous measurements. Rather, x refers to the radio-frequency voltage V_{RF} , which is derived from the difference between the input voltage and the polarization voltage (V_{bias}) of the laser when operating at twice the threshold current during OEF operation. In the case of the QD laser, the value of V_{bias} is 1.30 V, while for the QW laser, it is 1.19 V. Moreover, the function $f(x)$ corresponds to the detection voltage (V_{PD}) of the PD. Once all the simulation parameters are obtained, equation (3) can be reformulated as an iDDE [Che+19; Che+20] such as:

$$\dot{y} = x \quad (3.8)$$

$$\tau \dot{x} = -x - \frac{1}{\theta} y + \eta f_{NL}[x_T] \quad (3.9)$$

where $y = \int_{t_0}^t x(s) ds$, $x_T \equiv x(t - T)$. $f_{NL}[x_T]$ is represented in detail by Equ. 3.6 and 3.7.

I conduct an investigation and comparison of the dynamic behavior of QD and QW lasers by varying the linear gain (η), which serves also as the feedback strength, in the feedback loop. The bifurcation diagrams of the QD and QW lasers, obtained by manipulating the feedback strength, are shown in Fig. 3.23(a) and (b), respectively. The bifurcation diagram of the QD laser reveals three distinct operational regimes: steady

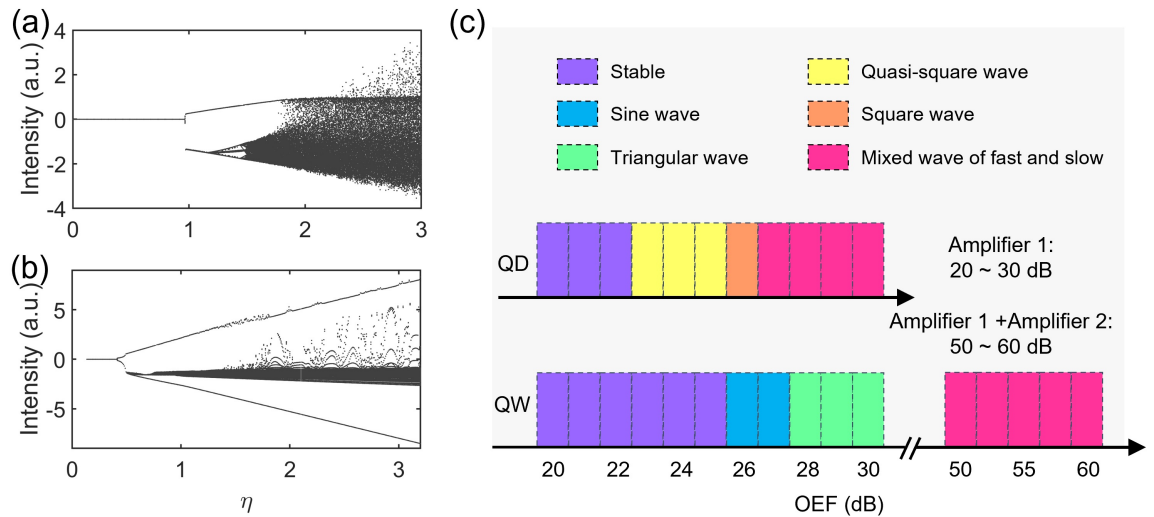


Figure 3.23: Simulated bifurcation diagrams of (a) QD and (b) QW lasers. (c) Experimental dynamical regions were observed in QD and QW lasers, respectively.

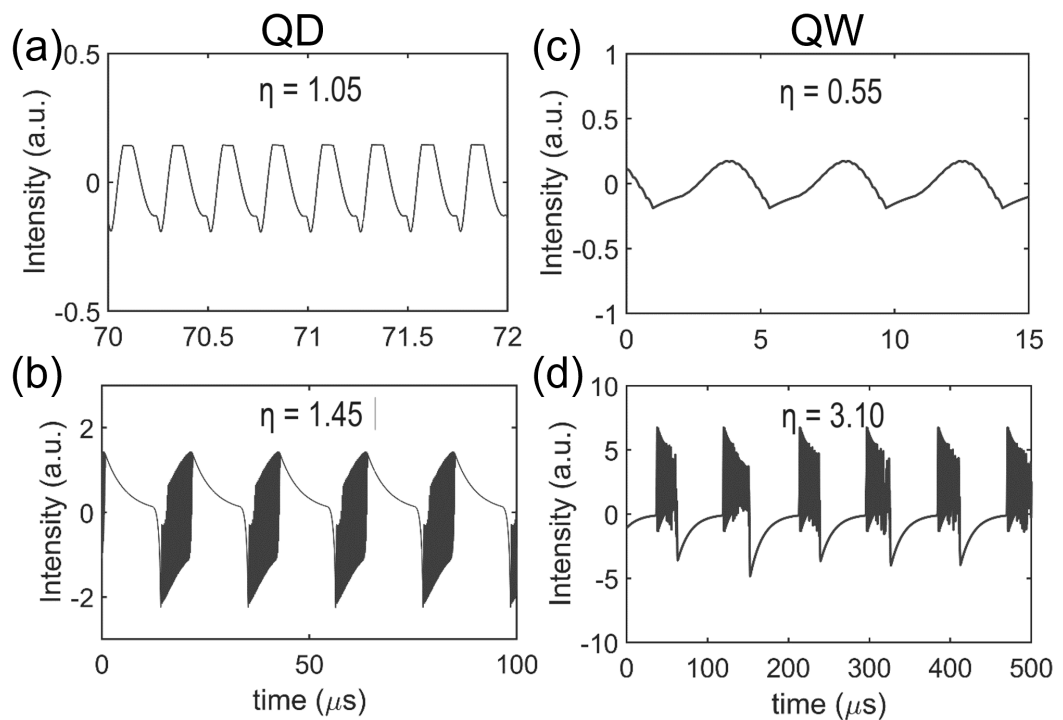


Figure 3.24: Simulated time series of the (a)-(b) QD and (c)-(d) QW laser.

state, single-period region, and multi-period region. Interestingly, the QD laser exhibits a lower feedback strength requirement to enter the multi-period region, characterized by a mixed waveform of fast and slow oscillations, as observed in the experimental results. The simulated time series corresponding to the red arrows in Fig. 3.24(a) and (b) depict the square wave and mixed waveform of fast and slow oscillations of the QD laser. It is worth noting that the periods and waveforms of these simulated time series align closely with the experimental curves displayed in Fig. 3.19. While the QW laser is kept in a sinusoidal state at low feedback strength as shown in Fig. 3.24(c). Very strong feedback ($\eta = 3.1$) is required to achieve fast and slow oscillations, as shown in Fig. 3.24(d), which perfectly matches the experimental data at high feedback strength in Fig. 3.20. Fig. 3.23(c) illustrates the experimentally obtained dynamic intervals for the QD and QW lasers at a temperature of 30°C. In particular, the QD laser demonstrates a wide range of dynamics with a single electrical amplifier. On the contrary, the QW laser exhibits stable performance and necessitates higher feedback strength to induce dynamic behavior, corroborating the trends observed in the simulated bifurcation diagram. Additionally, for QD lasers, a fast sine wave and quasi-sine wave emerge within a narrow window between the steady state and the square wave. This observation is primarily evident in experiments conducted at elevated temperatures, possibly attributed to the power decrease at higher temperatures and the resulting reduction in feedback strength variation, which facilitates the adjustment of the feedback strength to this particular point.

Our results effectively showcase the relationship between the nonlinear transfer function contributed by semiconductor lasers and time delay in the OEF loop, leading to intricate dynamical patterns. The power-current-voltage features of lasers critically influence the OEF loop's nonlinear dynamics. Past research indicates that basic transfer functions yield quasi-sinusoidal time traces [CWC16], while more complex functions like Van der Pol's can cause chaos [Che+17]. Similarly, QW lasers produce specific oscillations at high feedback strengths [Che+20]. Other OEF loops with different lasers show limited dynamics [Isl+21]. It should be noted that the QD laser used above without a direct-modulation design produces high frequency oscillations at 0.5 GHz. A direct-modulation design of the QD laser would allow for higher period oscillations. In addition, the present OEF loop has a long delay and can only obtain a square wave with

a period of 250 ns. Future on-chip designs can significantly reduce the delay time and obtain a square wave signal with a higher frequency as a clock signal. Furthermore, QD lasers have a complex PIV characteristic with multiple segments and are more prone to saturation than QW lasers. As QD lasers have a much higher gain compression factor coefficient ($\sim 10^{-16} \text{ cm}^3$), about ten times that of QW lasers ($\sim 10^{-17} \text{ cm}^3$) [Bim+97]. This increased compression is linked to the slower carrier relaxation rate in QDs because of their unique zero-dimensional structure with the wetting layer energy states [LS09; NGJ04]. This structure limits carrier accommodation and the saturation photon number in the cavity. The QD lasers' energy level structure results in more complex power-current curves [Hua+18; RLL14]. If there is a ground state quenching in the QD laser, it leads to a PIV curve with kinks and saturation zones. Future OEF experiments might use QD lasers with this emission, adding to the complexity of the nonlinearity transfer function.

3.3 Summary

In this chapter, I explored the nonlinear dynamics of QD lasers operating under external controls namely with OEF. I discovered peculiar properties that are summarized below:

- To permit QD lasers to generate multiple dynamics as well, the response of a silicon-based QD laser under OEF was explored both experimentally and numerically for the first time. Increasing OEF strength prompts the QD laser to traverse various dynamical regimes, including steady states, square waves, and mixed waveforms of fast and slow oscillations. A broadened square wave regime emerges as the temperature drops, beneficial for optical clock applications.
- Unlike conventional optical feedback, I discovered that the epitaxial QD lasers display a much higher sensitivity to OEF than QW lasers, which is fully confirmed via an integral-differential delay model and experimental time domain signals. I believe that the various dynamical properties observed in the silicon-based QD laser with an OEF loop can be applied to areas such as integrated optical computing, logic, and sensing.

Bibliography

- [AY12] Moustafa Ahmed and M Yamada. “Mode oscillation and harmonic distortions associated with sinusoidal modulation of semiconductor lasers”. In: *The European Physical Journal D* 66 (2012), pp. 1–9.
- [Bab+19] Masoud Babaeian et al. “A single shot coherent Ising machine based on a network of injection-locked multicore fiber lasers”. In: *Nature communications* 10.1 (2019), p. 3516.
- [Bim+97] D Bimberg, N Kirstaedter, NN Ledentsov, Zh I Alferov, PS Kop’Ev, and VM Ustinov. “InGaAs-GaAs quantum-dot lasers”. In: *IEEE Journal of selected topics in quantum electronics* 3.2 (1997), pp. 196–205.
- [BVV19] Fabian Böhm, Guy Verschaffelt, and Guy Van der Sande. “A poor man’s coherent Ising machine based on opto-electronic feedback systems for solving optimization problems”. In: *Nature communications* 10.1 (2019), p. 3538.
- [Che+19] Yanne K Chembo, Daniel Brunner, Maxime Jacquot, and Laurent Larger. “Optoelectronic oscillators with time-delayed feedback”. In: *Reviews of Modern Physics* 91.3 (2019), p. 035006.
- [Che+20] Géraud R Goune Chengui, Kengne Jacques, Paul Woafu, and Yanne K Chembo. “Nonlinear dynamics in an optoelectronic feedback delay oscillator with piecewise linear transfer functions from the laser diode and photodiode”. In: *Physical Review E* 102.4 (2020), p. 042217.

- [Che+17] Géraud R Goune Chengui, Jimmi H Talla Mbé, Alain Francis Talla, Paul Wofo, and Yanne K Chembo. “Dynamics of optoelectronic oscillators with electronic and laser nonlinearities”. In: *IEEE Journal of Quantum Electronics* 54.1 (2017), pp. 1–7.
- [CWC16] Géraud Russel Goune Chengui, Paul Wofo, and Yanne K Chembo. “The simplest laser-based optoelectronic oscillator: An experimental and theoretical study”. In: *Journal of Lightwave Technology* 34.3 (2016), pp. 873–878.
- [Don+21] B. Z. Dong et al. “Dynamic performance and reflection sensitivity of quantum dot distributed feedback lasers with large optical mismatch”. In: *Photonics Research* 9.8 (2021), pp. 1550–1558.
- [Dua+19] Jianan Duan, Heming Huang, Bozhang Dong, Daehwan Jung, Justin C Norman, John E Bowers, and Frederic Grillot. “1.3- μm Reflection Insensitive InAs/GaAs Quantum Dot Lasers Directly Grown on Silicon”. In: *IEEE Photonics Technology Letters* 31.5 (2019), pp. 345–348.
- [Gas+04] Nicolas Gastaud, Stéphane Poinsot, Laurent Larger, JM Merolla, M Hanna, Jean-Pierre Goedgebuer, and François Malassenet. “Electro-optical chaos for multi-10 Gbit/s optical transmissions”. In: *Electronics letters* 40.14 (2004), p. 1.
- [GKE97] A Gavrielides, Vassilios Kovanis, and Thomas Erneux. “Analytical stability boundaries for a semiconductor laser subject to optical injection”. In: *Optics Communications* 136.3-4 (1997), pp. 253–256.
- [Glo+12] Björn Globisch, Christian Otto, Eckehard Schöll, and Kathy Lüdge. “Influence of carrier lifetimes on the dynamical behavior of quantum-dot lasers subject to optical feedback”. In: *Physical Review E* 86.4 (2012), p. 046201.
- [Gou+07] David Goulding et al. “Excitability in a quantum dot semiconductor laser with optical injection”. In: *Physical review letters* 98.15 (2007), p. 153903.

- [Hua+18] Heming Huang et al. “Analysis of the optical feedback dynamics in InAs/GaAs quantum dot lasers directly grown on silicon”. In: *Journal of the Optical Society of America B* 35.11 (2018), pp. 2780–2787. URL: <https://opg.optica.org/josab/abstract.cfm?uri=josab-35-11-2780>.
- [Ike79] Kensuke Ikeda. “Multiple-valued stationary state and its instability of the transmitted light by a ring cavity system”. In: *Optics communications* 30.2 (1979), pp. 257–261.
- [Isl+21] Md Shariful Islam, AV Kovalev, EA Viktorov, DS Citrin, and A Locquet. “Optical square-wave generation in a semiconductor laser with optoelectronic feedback”. In: *Optics Letters* 46.24 (2021), pp. 6031–6034.
- [JL09] Yu-Shan Juan and Fan-Yi Lin. “Microwave-frequency-comb generation utilizing a semiconductor laser subject to optical pulse injection from an optoelectronic feedback laser”. In: *Optics letters* 34.11 (2009), pp. 1636–1638.
- [KHU22] Kazutaka Kanno, Afeeqah Amalina Haya, and Atsushi Uchida. “Reservoir computing based on an external-cavity semiconductor laser with optical feedback modulation”. In: *Optics Express* 30.19 (2022), pp. 34218–34238.
- [LL03] Fan-Yi Lin and Jia-Ming Liu. “Nonlinear dynamics of a semiconductor laser with delayed negative optoelectronic feedback”. In: *IEEE journal of quantum electronics* 39.4 (2003), pp. 562–568.
- [LHD14] Kai-Hung Lo, Sheng-Kwang Hwang, and Silvano Donati. “Optical feedback stabilization of photonic microwave generation using period-one nonlinear dynamics of semiconductor lasers”. In: *Optics Express* 22.15 (2014), pp. 18648–18661.
- [LS09] Kathy Ludge and Eckehard Scholl. “Quantum-dot lasers—desynchronized nonlinear dynamics of electrons and holes”. In: *IEEE Journal of Quantum Electronics* 45.11 (2009), pp. 1396–1403.

- [Mbé+15] Jimmi H Talla Mbé, Alain F Talla, Geraud R Goune Chengui, Aurélien Coillet, Laurent Larger, Paul Woafu, and Yanne K Chembo. “Mixed-mode oscillations in slow-fast delayed optoelectronic systems”. In: *Physical review E* 91.1 (2015), p. 012902.
- [McM23] Peter L McMahon. “The physics of optical computing”. In: *Nature Reviews Physics* 5.12 (2023), pp. 717–734.
- [Mou+23] George Mourgias-Alexandris et al. “Analog Iterative Machine (AIM): using light to solve quadratic optimization problems with mixed variables”. In: *arXiv preprint arXiv:2304.12594* (2023).
- [NGJ04] Torben Roland Nielsen, Paul Gartner, and Frank Jahnke. “Many-body theory of carrier capture and relaxation in semiconductor quantum-dot lasers”. In: *Physical Review B* 69.23 (2004), p. 235314.
- [OO17] Junji Ohtsubo and Junji Ohtsubo. *Semiconductor lasers and theory*. Springer, 2017.
- [Ott14] Christian Otto. *Dynamics of Quantum Dot Lasers: Effects of Optical Feedback and External Optical Injection*. Springer Science & Business Media, 2014.
- [Pat+99] A Patane, A Polimeni, M Henini, L Eaves, PC Main, and G Hill. “Thermal effects in quantum dot lasers”. In: *Journal of applied physics* 85.1 (1999), pp. 625–627.
- [Pau+12] Johannes Pausch, Christian Otto, Egle Tylaite, Niels Majer, Eckehard Schöll, and Kathy Lüdge. “Optically injected quantum dot lasers: impact of nonlinear carrier lifetimes on frequency-locking dynamics”. In: *New Journal of Physics* 14.5 (2012), p. 053018.
- [RLL14] Andre Roehm, Benjamin Lingnau, and Kathy Luedge. “Understanding ground-state quenching in quantum-dot lasers”. In: *IEEE Journal of Quantum Electronics* 51.1 (2014), pp. 1–11.
- [Sim+95] TB Simpson, Jia-Ming Liu, Athanasios Gavrielides, Vassilios Kovanis, and PM Alsing. “Period-doubling cascades and chaos in a semiconductor laser with optical injection”. In: *Physical review A* 51.5 (1995), p. 4181.

-
- [Spi+21] Olivier Spitz et al. “Private communication with quantum cascade laser photonic chaos”. In: *Nature communications* 12.1 (2021), p. 3327.
- [TY14] Kenta Takata and Yoshihisa Yamamoto. “Data search by a coherent Ising machine based on an injection-locked laser network with gradual pumping or coupling”. In: *Physical Review A* 89.3 (2014), p. 032319.
- [VBS17] Guy Van der Sande, Daniel Brunner, and Miguel C Soriano. “Advances in photonic reservoir computing”. In: *Nanophotonics* 6.3 (2017), pp. 561–576.
- [VL82] J Van der Ziel and R Logan. “Generation of short optical pulses in semiconductor lasers by combined dc and microwave current injection”. In: *IEEE Journal of Quantum Electronics* 18.9 (1982), pp. 1340–1350.
- [Wan+16] Cheng Wang, Ravi Raghunathan, Kevin Schires, Sze-Chun Chan, Luke F Lester, and Frédéric Grillot. “Optically injected InAs/GaAs quantum dot laser for tunable photonic microwave generation”. In: *Optics letters* 41.6 (2016), pp. 1153–1156.
- [Wan+17] Yiping Wang, Ming Wang, Wei Xia, Xiaoqi Ni, and Dajian Wu. “Optical fiber Bragg grating pressure sensor based on dual-frequency optoelectronic oscillator”. In: *IEEE Photonics Technology Letters* 29.21 (2017), pp. 1864–1867.

CHAPTER 4

Effects of Injected Carrier Noise on Quantum Dot Lasers

The amplitude-phase coupling of the α_H -factor has been described in Chapter 2. This phase-amplitude coupling induces variations in optical linewidth, multi-mode state, and nonlinear dynamics of the laser [CCM12; Don+19; Hen82]. In this chapter, I am focusing on the fact that the α_H -factor of a QD laser is affected by externally injected carriers and affects the frequency noise, linewidth, etc. of the QD laser. Research in this Chapter will assist in the generation of squeezed states in Chapter 5.

4.1 What affects the linewidth enhancement factor?

The α_H -factor as an amplitude and phase-dependent parameter is worthwhile to characterize and analyze the noise properties of lasers. Then, the effects of both material intrinsic parameters and external controllable parameters on α_H -factor need to be considered.

4.1.1 Active medium

Studies have shown that the α_H -factor in InAs/GaAs QD lasers is much lower than that in QW lasers in Chapter 2. This reduction is attributed to the discrete energy levels in QD gain materials and the decreased carrier interactions, which diminish the

carrier-induced changes in the refractive index. These discrete energy levels are the critical reason for the lower α_H -factor in InAs/GaAs QD lasers [Dua+18a]. According to the definition of α_H -factor, it can be seen that the ratio of differential gain and differential refractive index determines the magnitude of α_H -factor. The material gain G and changes in refractive index n as a function of carrier density N in QW (top) and QD (bottom) lasers are contrasted in Fig. 4.1. For the QW medium, the refractive index's zero-crossing point strays from the peak of the gain curve at both low and high carrier densities, leading to a nonzero α_H -factor. Conversely, in a QD medium with symmetrical gain profiles, the refractive index's differential shift at the laser's photon energy is precisely zero for all carrier density levels. Consequently, an ideal QD laser that exhibits symmetric gain characteristics would have an α_H -factor of zero which is also proofed in the simulation [Zha+19].

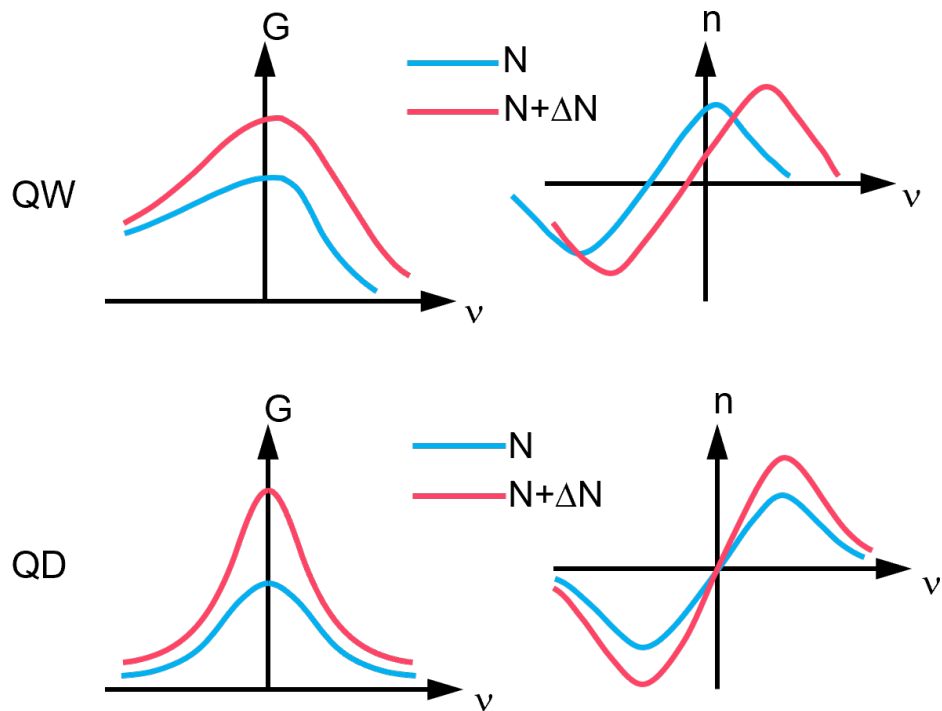


Figure 4.1: Schematic of the variation of gain G and refractive index n with carrier density N for QD and QW lasers.

4.1.2 Pump ratio

Typically, the α_H -factor increases with the pump current of a laser. This is because the carrier density within the active region of a semiconductor laser significantly influences the α_H -factor [MHU06]. Due to the Kramers-Kronig relations, which link the real and imaginary parts of the refractive index, the refractive index in the active region is a function of the carrier density [OB87]. As the carrier density increases, it leads to changes in the refractive index, thereby causing variations in the α_H -factor. In QD lasers, the laser wavelength can be switched from GS to ES as the pump current increases, which means that carriers accumulate in ES when the carriers in GS are filled. The filling of ES inevitably increases the α_H -factor of GS. Considering the gain changes in GS and ES, the output power (P)-dependent α_H -factor of QD can be written as [Gri+08; Jin+23],

$$\alpha_H(P) = \alpha_g (1 + \varepsilon_P P) + \frac{\alpha_e}{1 - \frac{g_{th}}{g_{max} - g_{th}} \varepsilon_P P} \quad (4.1)$$

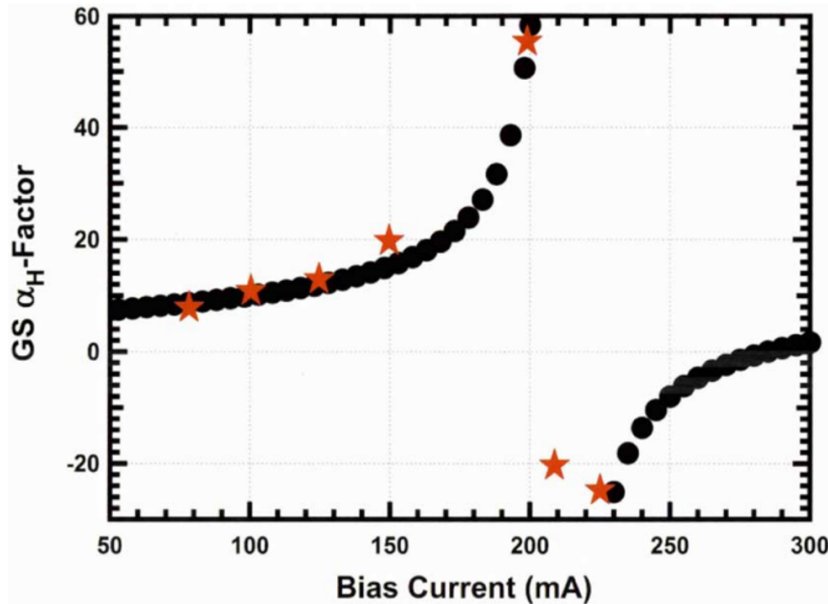


Figure 4.2: Calculated GS α_H -factor with the bias current (black dots). Red stars are experimental data. [Gri+08]

where α_g denotes the change in GS index due to the GS gain variation, and α_e denotes the change in ES index due to the ES gain variation. g_{max} , g_{th} , and ϵ_P is the maximum gain, the gain at the threshold, and the gain compression coefficient related to the output power, respectively. Fig. 4.2 illustrates the measured alpha of the GS and the result fitted with the Eq. 4.1. For QW lasers with homogeneous broadened gain medium, it is only required the first term in Eq. 4.1 as its α_H -factor above the threshold current, and the linewidth enhancement factor at the threshold current (α_0) replaces α_g .

4.1.3 Carrier fluctuations

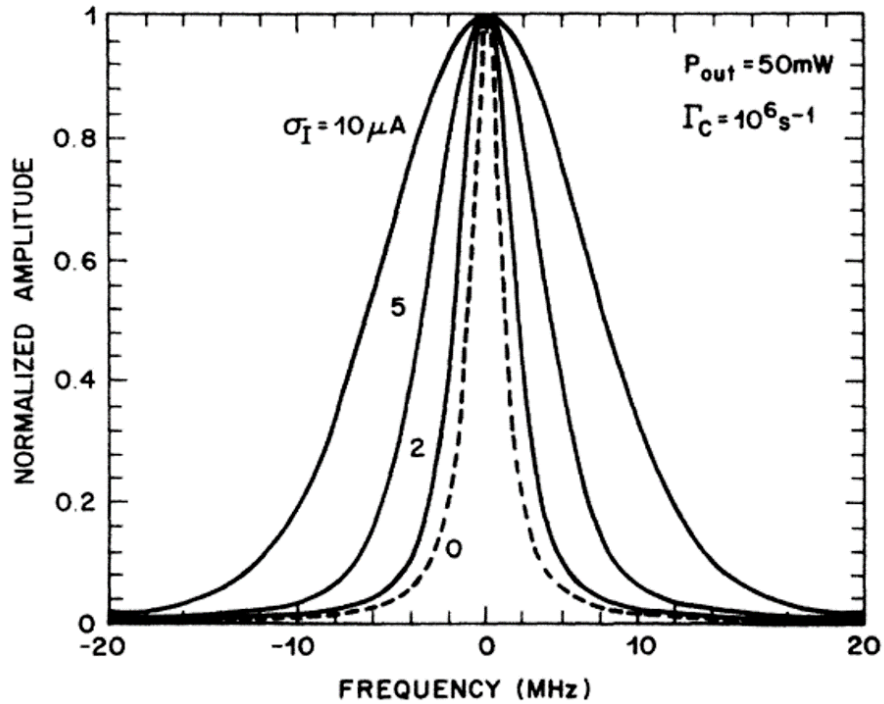


Figure 4.3: Linewidth with an increase in the current noise σ_I at 50 mW output power. [AR88]

Semiconductor lasers serve as crucial components in electro-optical conversion, where the characteristics of injected carriers directly influence the transport of these carriers within energy levels, their recombination processes, and the light emission

properties. G. P. Agrawal et al. have conducted research into how fluctuations in these injected carriers can affect the spectral linewidth of semiconductor lasers [AR88]. In the theoretical model, it was hypothesized that the time scale of the external carrier fluctuations exceeds the inherent time scale of relaxation oscillations. Consequently, the model employs a non-Markovian random force within the rate equations that govern carrier dynamics to account for these fluctuations. Additionally, it was revealed that the effect of current fluctuations on the spectral linewidth of semiconductor lasers does not depend on the output power. Then, α_H -factor, which is closely related to linewidth, may be affected by external carrier fluctuations. As shown in Fig. 4.3, increasing carrier fluctuations at the same power directly broadens the optical linewidth. In the absence of carrier fluctuations ($\sigma_I = 0$), it exhibits a Lorentzian line shape.

4.2 Carrier noise of electrical pump

Typically, a low noise current source (i.e. a quiet pump) is required to reduce the impact of external electrical noise when investigating the noise properties of a semiconductor laser [Bar+10; Liu+19; Mal+21]. Therefore, if one can transfer a constant carrier sequence into a quiet photon stream, then one would obtain sub-shot noise light. When the semiconductor laser is pumped by a normal pump, the electrons are bunched, whereas the electrons are anti-bunched under a quiet pump for which the electrons stream does not show fluctuations in spacing, superior to the shot noise [YMR92]. This latter property directly transforms the photon distribution with sub-Poissonian statistics hence leading to the generation of non-classical states of light such as squeezed fields [MY187; ML18; MY20]. As a semiconductor laser is a combination of a resistor-capacitor and an inductor [KSY12], it is important to better understand how the effects of the external carrier noise impact the electro-optical properties. Let us stress that prior works have deeply investigated the noise features from the laser junction but not that from other circuit components like that from the current source [VG97]. These external noise sources greatly affect the behavior of injected carriers, which thus influences the laser-stimulated emission process.

In this section, the effect of external noise is investigated both numerically and

experimentally using a QD DFB laser. That will exclude multi-mode interactions and use exactly the rate equation for a single mode. The effects of carrier noise on the α_H -factor is usually analyzed by adding carrier, photon, and phase Langevin noise into a semi-classical model based on rate equations [Dua+18b]. However, the carrier noise originating from the external current source is rarely considered in the literature [Arn95; Arn97], and even less for QD semiconductor lasers. Thereby, we implement the noise source and quiet current source conditions directly into our rate equation model. The α_H -factor is subsequently extracted from the frequency noise calculated through the diffusion coefficients. In addition to that, in our experiments, the effects of carrier transport are taken into account by considering two different current sources with distinct resistances. Previous studies indicated that semiconductor lasers exhibit different noise characteristics in such different bias conditions [MYI87; MY88], which can greatly affect the physical properties of the QD laser such as the α_H -factor.

4.2.1 Definition of quiet pump

Fig. 6.2 shows two current pumps for the QD laser: (a) normal pump and (b) quiet pump. The effect of the pump on the laser is described with an equivalent circuit, where R_d is the junction differential resistance of the laser, L is the parasitic inductance, and C is the parasitic capacitance. The differential resistance emulates the damping resulting from the spontaneous and stimulated recombination terms in the rate equation. The inductance represents the resonance wavelength of the laser. The capacitance contains the active layer diffusion capacitance and space charge capacitance of the laser [TP83a; TP83b]. The normal pump can be achieved practically when the laser junction differential resistance $R_d = (dI/dV)^{-1}$ is much larger than the internal resistance R_s of the pump whereas the quiet pump is obtained in the opposite limit. It should be emphasized that the current noise in semiconductor lasers is a combination of thermal diffusion noise and generation-recombination noise about the minority carrier. [YMN86; YH92]. These noise events arise sequentially and cause the departure of the minority carrier density from the equilibrium. Then, the external circuit would restore the steady-state distribution of minority carriers and regulate their injection into the active region via the relaxation process. For instance, when

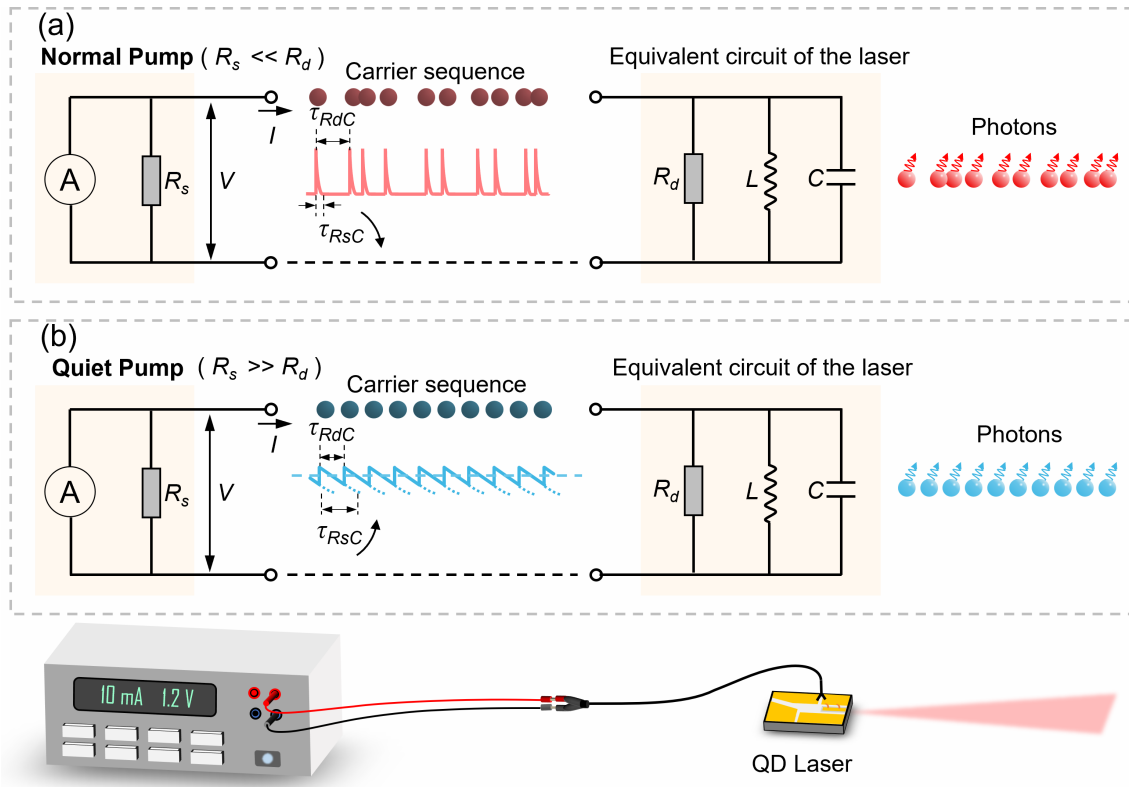


Figure 4.4: Schematic diagram of the theoretical model illustrating the relationship between injected carriers and photons in a semiconductor laser driven by (a) a normal pump and (b) a quiet pump.

one has the normal pump with an infinitesimal source resistance R_s , this relaxation process would be completed with a negligible delay time $\tau_{R_s C} = R_s C$. As a result, the laser does not memorize the previous event and thus each event occurs independently from the statistical point of view, which is exactly the physical origin for the full-shot noise or photon Poissonian distribution as shown in Fig. 6.2(a). On the contrary, if one has a quiet pump with a considerable source resistance R_s , the modulation of minority carriers cannot be instantaneously eliminated by the external circuit because of a large time delay $\tau_{R_s C}$. Therefore, the junction voltage is allowed to fluctuate by the thermal diffusive transit and generation-recombination events as shown in Fig. 6.2(b). In this context, if the recombination events exceed the average value, the junction voltage decreases due to the excess thermal diffusive transit. However, since this

junction-voltage decrease is not recovered in time, the thermal diffusive transit rate temporarily decreases hence resulting in fewer recombination events. This sequence works as a self-feedback stabilization mechanism for regulating the pumping process, which potentially has a significant impact on the α_H -factor and the noise spectrum. The two pumps were experimentally measured to exhibit different noise characteristics as shown in Fig. 6.3.

4.2.2 Carrier noise measurement

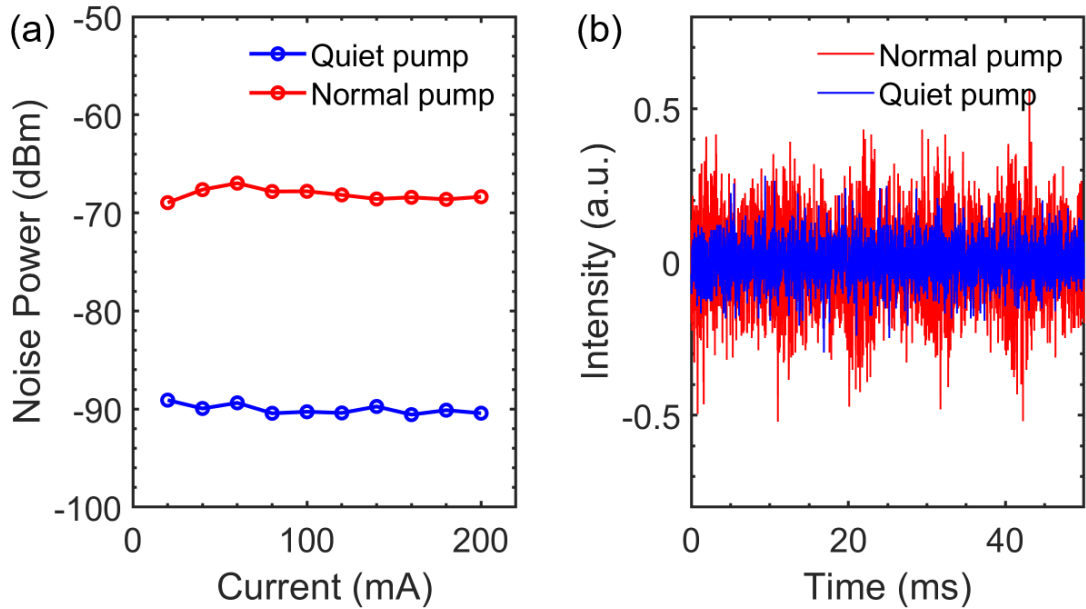


Figure 4.5: (a) The noise power and (b) the noise fluctuation of normal and quiet pumps.

To compare the current noise of different pumps, I drove the pump's drive current through a 10Ω resistor. The current noise was measured by coupling the voltage fluctuation on the resistor through a 10 nF capacitor to a low-noise amplifier with an input impedance of 50Ω . We chose this resistor and capacitor to closely match the laser resistor's value, aiming to capture the noise fluctuation of the current source near the laser load. The amplified signal was then analyzed using an electrical spectrum analyzer and an oscilloscope. We compared the noise characteristics of the normal and quiet pumps. The noise points in Fig. 6.3(a) are extracted from the noise at 50 MHz

of the electrical spectrum. The noise is stable at different currents of both pumps. So we measured the noise fluctuation at 100 mA. Both the electrical spectrum and the time-domain fluctuations demonstrate the reliability of our comparative experiments.

4.3 Numerical simulation and experimental analysis

4.3.1 Semi-classical rate equations

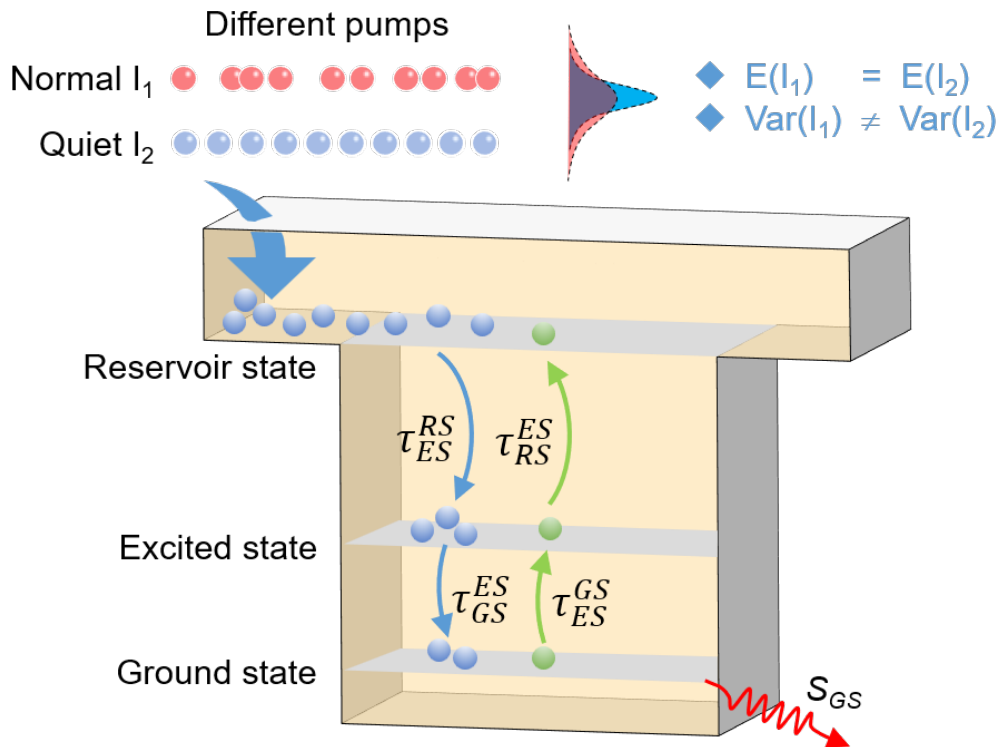


Figure 4.6: Schematic representation of the electronic structure and carrier dynamics in a QD for normal pumping conditions and quiet pumping conditions. The two current sources are distinguished by the fact that the currents are expected to be equal and the quiet pump has a small current variance.

A quiet pump with a sub-Poissonian carrier distribution and a normal pump with a Gaussian carrier distribution can be well described by using a stochastic model [MY20;

ZG22b]. However, in this kind of representation, the inclusion of the phase term influencing the α_H -factor is rather complicated. Instead, the frequency noise and the α_H -factor of a QD laser can be better modeled with a rate equation approach [Wan+14; Zho+20]. Here, we incorporate into these rate equations the various noise contributions by taking into account the different current sources. As shown in Fig. 6.4, the QD carrier dynamics are described by considering a three-energy level system. The model assumes a single-mode emission which is exactly the configuration achieved with the QD DFB laser under study. Besides, it holds under the assumption that the active region consists of only one QD ensemble, where the nanostructures are interconnected by a two-dimensional reservoir state (RS)[Wan+16]. The QD contains two bound states: a two-fold degenerate ground state (GS) and a four-fold degenerate excited state (ES). QDs are implicitly assumed to be always neutral, electrons and holes are treated as electron-hole pairs, which means that the system is only composed of excitonic energy states. Carriers are supposed to be injected directly from the contacts into the RS levels. When different pumps set the same current, it can be assumed that the current expected value is the same, but the variance is different. The different variances represent different noise levels. The coupled rate equations on carrier, phase, and photon dynamics read as follows:

$$\frac{dN_{RS}}{dt} = \frac{\eta I}{q} + \frac{N_{ES}}{\tau_{RS}^{ES}} - \frac{N_{RS}}{\tau_{ES}^{RS}}(1 - \rho_{ES}) - \frac{N_{RS}}{\tau_{RS}^{spon}} + F_{RS} \quad (4.2)$$

$$\frac{dN_{ES}}{dt} = \left(\frac{N_{RS}}{\tau_{ES}^{RS}} + \frac{N_{GS}}{\tau_{ES}^{GS}}\right)(1 - \rho_{ES}) - \frac{N_{ES}}{\tau_{GS}^{ES}}(1 - \rho_{GS}) - \frac{N_{ES}}{\tau_{RS}^{ES}} - \frac{N_{ES}}{\tau_{ES}^{spon}} + F_{ES} \quad (4.3)$$

$$\frac{dN_{GS}}{dt} = \frac{N_{ES}}{\tau_{GS}^{ES}}(1 - \rho_{GS}) - \frac{N_{GS}}{\tau_{ES}^{GS}}(1 - \rho_{ES}) - \Gamma_p \nu_g g_{GS} S_{GS} - \frac{N_{GS}}{\tau_{GS}^{spon}} + F_{GS} \quad (4.4)$$

$$\frac{dS_{GS}}{dt} = \left(\Gamma_p \nu_g g_{GS} - \frac{1}{\tau_p}\right) S_{GS} - \beta_{SP} \frac{N_{GS}}{\tau_{GS}^{spon}} + F_S \quad (4.5)$$

$$\frac{d\phi}{dt} = \Delta\omega_N^{GS} + \Delta\omega_N^{ES} + \Delta\omega_N^{RS} + F_\phi \quad (4.6)$$

where the carrier numbers in the GS, ES, and RS energy levels are denoted by N_{RS} , N_{ES} , and N_{GS} respectively while S_{GS} is the photon number in the GS and ϕ accounts for

the phase of the electrical field. The carrier dynamics are shortly described as follows. First, carriers are captured from the RS to the ES with a capture time τ_{ES}^{RS} then they relax from the ES down to the GS level with a relaxation time τ_{GS}^{ES} . Carriers can also be thermally re-emitted from the ES to the RS with an escape time τ_{RS}^{ES} . Similar dynamic behavior is followed for the carrier population on the GS level concerning the ES. In addition, carriers can also recombine spontaneously with spontaneous emission times τ_{RS}^{spon} , τ_{ES}^{spon} , and τ_{GS}^{spon} at RS, ES, and GS levels, respectively. As shown in Eq. 6.2, the pumping term $\eta I/q$ incorporates the injection efficiency η and q the elementary charge. Lastly, it should be pointed out that ρ_{ES} , ρ_{GS} correspond to the carrier occupation probabilities into the ES and GS while β_{sp} is the fraction of the spontaneous emission coupled in the lasing mode, Γ_p is the optical confinement factor, v_g is the group velocity and $\Delta\omega_N^{RS,ES,GS}$ accounts for the frequency shift of the carrier-induced laser field relative to the frequency. $F_{RS,ES,GS,S,\phi}$ are the Langevin noise terms. The parameters of the three-energy level rate equation model are shown in Table 6.1. The GS transition energy (0.95 eV) corresponds to the wavelength of the QD laser used in the experiment. Other parameters are referred to in the literature on 1310 nm wavelength QD DFB lasers [FM07; Kir+96].

The characteristics of the QD laser are investigated by small signal analysis. By using the Langevin approach, we investigate the characteristics of the frequency noise, where the different carrier noises imposed by different current sources will be reflected. We introduce $F_{RS}(t)$, $F_{ES}(t)$, $F_{GS}(t)$, $F_S(t)$, and $F_\phi(t)$ as Langevin noise terms into the carrier, photon, and phase rate equations. Moreover, the correlation strength of noise sources is $\langle F_i(t) F_j(t') \rangle = 2D_{i-j}\delta(t-t')$, where indexes i, j refer to N_{RS} , N_{ES} , N_{GS} , S , and Φ where D_{i-j} is the diffusion coefficient between two noise sources that are delta correlated. Fig. 6.5 briefly explains the reservoir model to characterize the laser noise performance. Here, the correlation strengths of the various Langevin noise sources can be determined by observing the rates of inflow and outflow into and out of the different reservoirs. Current-related noise enters the system through D_{R-R} , hence the inclusion of the current term in D_{R-R} [CCM12]. Pumped carriers are injected into the laser structure ($\eta I/q$). We considered carrier noise fluctuations on sub-nanosecond time scales since carrier noise remains distinguishable at frequencies higher than GHz. At this point the carrier noise time scale coincides with carrier lifetimes (ns) and photon

Symbol	Physical description	Value
E_{RS}	RS transition energy	1.15 eV
E_{ES}	ES transition energy	1.01 eV
E_{GS}	GS transition energy	0.95 eV
τ_{ES}^{RS}	RS to ES capture time	1.3 ps
τ_{GS}^{ES}	ES to GS relaxation time	1.2 ps
τ_{ES}^{GS}	GS to ES escape time	0.12 ns
τ_{RS}^{ES}	ES to RS escape time	5.35 ns
τ_{RS}^{spon}	RS spontaneous emission time	0.5 ns
τ_{ES}^{spon}	ES spontaneous emission time	0.5 ns
τ_{GS}^{spon}	GS spontaneous emission time	1.2 ns
τ_p	Photon lifetime	8.1 ps
β_{sp}	Spontaneous emission factor	1×10^{-4}
a_{RS}	RS Differential gain	$2.5 \times 10^{-15} \text{ cm}^2$
a_{ES}	ES Differential gain	$1.0 \times 10^{-14} \text{ cm}^2$
a_{GS}	GS Differential gain	$5.0 \times 10^{-15} \text{ cm}^2$
ζ	Gain compression factor	$2.0 \times 10^{-16} \text{ cm}^3$
Γ_p	Optical confinement factor	0.06
α_{GS}	GS contribution to α_H -factor	1.50
N_B	Total dot number	4.3×10^6
V_B	Active region volume	$3.75 \times 10^{-11} \text{ cm}^3$
V_{RS}	RS region volume	$3.0 \times 10^{-12} \text{ cm}^3$

Table 4.1: Material and optical parameters of InAs/GaAs QD laser [FM07; Kir+96]

lifetimes (ps) of almost one order of magnitude, so the diffusion coefficient between the two noise sources is delta-correlated [AR88]. Then, some carriers participate in the spontaneous emission, and others go to the ES energy level and participate in the subsequent dynamical processes. After the process of spontaneous and stimulated emission of ES, some of the carriers reach the GS energy level. Finally, let us stress that the QD laser under study only emits on the GS transition therefore the stimulated emission in ES is not considered.

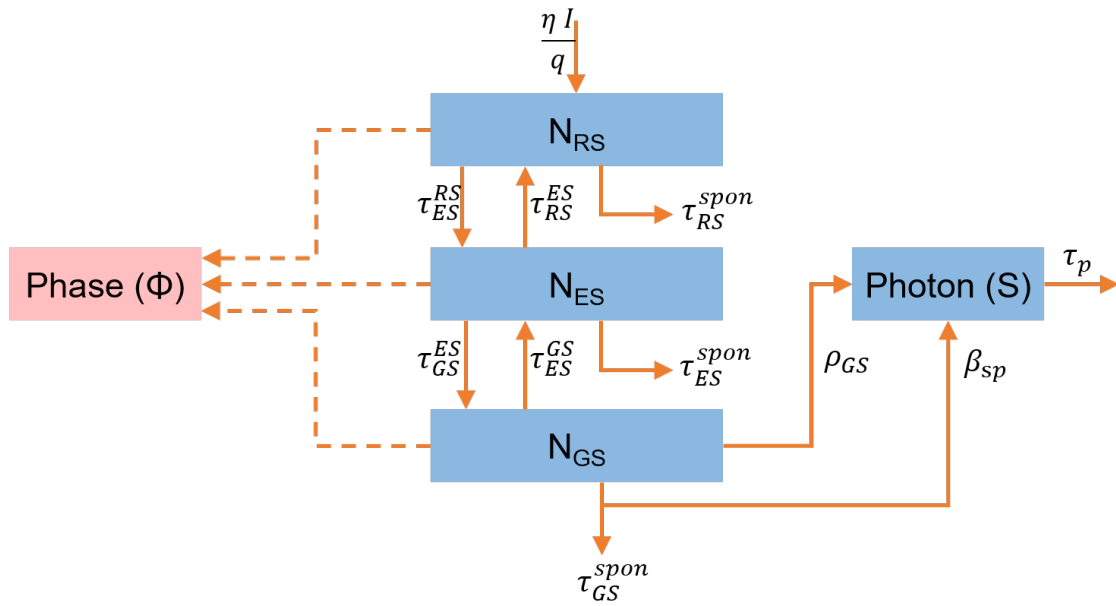


Figure 4.7: Reservoir model used in the rate equation analysis of the QD laser. Each solid line arrow in the flow chart represents the number of particles flowing per unit of time. The dashed lines represent the relationship to the phase.

After the analysis of the particle flows into/out of the different reservoirs using the method described in [CCM12; ZG22a], the diffusion coefficients can be derived as follows. This would be the critical aspect of distinguishing the different carrier noises from different sources.

$$D_{R-R} = \frac{\eta I}{q} + \frac{N_{ES}}{\tau_{RS}^{ES}} + \frac{N_{RS}}{\tau_{ES}^{RS}}(1 - \rho_{ES}) + \frac{N_{RS}}{\tau_{RS}^{spon}} \quad (4.7)$$

$$D_{E-E} = \left(\frac{N_{RS}}{\tau_{ES}^{RS}} + \frac{N_{GS}}{\tau_{ES}^{GS}} \right) (1 - \rho_{ES}) + \frac{N_{ES}}{\tau_{GS}^{ES}} (1 - \rho_{GS}) + \frac{N_{ES}}{\tau_{RS}^{ES}} + \frac{N_{ES}}{\tau_{ES}^{spon}} \quad (4.8)$$

$$D_{G-G} = \frac{N_{ES}}{\tau_{GS}^{ES}} (1 - \rho_{GS}) + \frac{N_{GS}}{\tau_{ES}^{GS}} (1 - \rho_{ES}) + \Gamma_p \nu_g g_{GS} S_{GS} + \frac{N_{GS}}{\tau_{GS}^{spon}} \quad (4.9)$$

$$D_{S-S} = \left(\Gamma_p \nu_g g_{GS} - \frac{1}{\tau_p} \right) S_{GS} + \beta_{SP} \frac{N_{GS}}{\tau_{GS}^{spon}} \quad (4.10)$$

$$D_{\phi-\phi} = \Delta\omega_N^{GS} + \Delta\omega_N^{ES} + \Delta\omega_N^{RS} \quad (4.11)$$

$$D_{R-E} = - \left[\frac{N_{RS}}{\tau_{ES}^{RS}} (1 - \rho_{ES}) + \frac{N_{ES}}{\tau_{RS}^{ES}} \right] \quad (4.12)$$

$$D_{E-G} = - \left[\frac{N_{GS}}{\tau_{ES}^{GS}} (1 - \rho_{ES}) + \frac{N_{ES}}{\tau_{GS}^{ES}} (1 - \rho_{GS}) \right] \quad (4.13)$$

$$D_{G-S} = - \left[\beta_{SP} \frac{N_{GS}}{\tau_{GS}^{spon}} + \Gamma_p \nu_g g_{GS} S_{GS} \right] \quad (4.14)$$

$$D_{R-G} = D_{R-S} = D_{R-\phi} = D_{E-S} = D_{E-\phi} = D_{G-\phi} = D_{S-\phi} = 0 \quad (4.15)$$

Following Cramer's rule [McC66] and the above diffusion coefficients, the frequency noise (FN) of the QD laser can be derived as follows.

$$FN(\omega) = \langle |\delta\omega_S(\omega)|^2 \rangle = \left\langle \left| j\omega \frac{\Delta\phi}{\Delta} \right|^2 \right\rangle \quad (4.16)$$

where $\omega = 2\pi f$, and f is the measured optical frequency. Δ is the determinant obtained from the system.

$$\Delta = \det \begin{bmatrix} \gamma_{11} + j\omega & -\gamma_{12} & 0 & 0 & 0 \\ -\gamma_{21} & \gamma_{22} + j\omega & -\gamma_{23} & 0 & 0 \\ 0 & -\gamma_{32} & \gamma_{33} + j\omega & -\gamma_{34} & 0 \\ 0 & 0 & -\gamma_{43} & \gamma_{44} + j\omega & -\gamma_{45} \\ 0 & 0 & -\gamma_{53} & -\gamma_{54} & \gamma_{55} + j\omega \end{bmatrix} \quad (4.17)$$

$$\Delta_\phi = \det \begin{bmatrix} \gamma_{11} + j\omega & -\gamma_{12} & 0 & 0 & F_{RS} \\ -\gamma_{21} & \gamma_{22} + j\omega & -\gamma_{23} & 0 & F_{ES} \\ 0 & -\gamma_{32} & \gamma_{33} + j\omega & -\gamma_{34} & F_{GS} \\ 0 & 0 & -\gamma_{43} & \gamma_{44} + j\omega & F_S \\ 0 & 0 & -\gamma_{53} & -\gamma_{54} & F_\phi \end{bmatrix} \quad (4.18)$$

The γ_{mn} (m and n = 1,2,3,4,5) are the results of linearizing the rate equations by small-signal analysis [Dua+18b]. The above determinant operates as follows,

$$\Delta_\phi = |D_R M_{R-\phi} - D_E M_{E-\phi} + D_G M_{G-\phi} - D_S M_{S-\phi} + D_\phi M_{\phi-\phi}| \quad (4.19)$$

The determinants of the matrices contained are as follows. \mathbf{M}_{i-j} are the algebraic cofactors of Δ_ϕ .

$$M_{R-\phi} = \begin{vmatrix} -\gamma_{21} & \gamma_{22} + j\omega & -\gamma_{23} & 0 \\ 0 & -\gamma_{32} & \gamma_{33} + j\omega & -\gamma_{34} \\ 0 & 0 & -\gamma_{43} & \gamma_{44} + j\omega \\ 0 & 0 & -\gamma_{53} & -\gamma_{54} \end{vmatrix} \quad (4.20)$$

$$M_{E-\phi} = \begin{vmatrix} \gamma_{11} + j\omega & -\gamma_{12} & 0 & 0 \\ 0 & -\gamma_{32} & \gamma_{33} + j\omega & -\gamma_{34} \\ 0 & 0 & -\gamma_{43} & \gamma_{44} + j\omega \\ 0 & 0 & -\gamma_{53} & -\gamma_{54} \end{vmatrix} \quad (4.21)$$

$$M_{G-\phi} = \begin{vmatrix} \gamma_{11} + j\omega & -\gamma_{12} & 0 & 0 \\ -\gamma_{21} & \gamma_{22} + j\omega & -\gamma_{23} & 0 \\ 0 & 0 & -\gamma_{43} & \gamma_{44} + j\omega \\ 0 & 0 & -\gamma_{53} & -\gamma_{54} \end{vmatrix} \quad (4.22)$$

$$M_{S-\phi} = \begin{vmatrix} \gamma_{11} + j\omega & -\gamma_{12} & 0 & 0 \\ -\gamma_{21} & \gamma_{22} + j\omega & -\gamma_{23} & 0 \\ 0 & -\gamma_{32} & \gamma_{33} + j\omega & -\gamma_{34} \\ 0 & 0 & -\gamma_{53} & -\gamma_{54} \end{vmatrix} \quad (4.23)$$

$$M_{\phi-\phi} = \begin{vmatrix} \gamma_{11} + j\omega & -\gamma_{12} & 0 & 0 \\ -\gamma_{21} & \gamma_{22} + j\omega & -\gamma_{23} & 0 \\ 0 & -\gamma_{32} & \gamma_{33} + j\omega & -\gamma_{34} \\ 0 & 0 & -\gamma_{43} & \gamma_{44} + j\omega \end{vmatrix} \quad (4.24)$$

The detailed expression for FN can be obtained by substituting \mathbf{M}_{i-j} into the expressions for Δ_ϕ and $FN(\omega)$ as follows.

$$\begin{aligned} FN(\omega) &= \left\langle \frac{\omega^2}{|\Delta|^2} |D_R M_{R-\phi} - D_E M_{E-\phi} + D_G M_{G-\phi} - D_S M_{S-\phi} + D_\phi M_{\phi-\phi}|^2 \right\rangle \\ &= \frac{\omega^2}{|\Delta|^2} \left\{ \langle D_R D_R^* \rangle M_{R-\phi} M_{R-\phi}^* - \langle D_R D_E^* \rangle M_{R-\phi} M_{E-\phi}^* + \langle D_R D_G^* \rangle M_{R-\phi} M_{G-\phi}^* \right. \\ &\quad - \langle D_R D_S^* \rangle M_{R-\phi} M_{S-\phi}^* + \langle D_R D_\phi^* \rangle M_{R-\phi} M_{\phi-\phi}^* + \langle D_E D_E^* \rangle M_{E-\phi} M_{E-\phi}^* \\ &\quad - \langle D_E D_R^* \rangle M_{E-\phi} M_{R-\phi}^* - \langle D_E D_G^* \rangle M_{E-\phi} M_{G-\phi}^* + \langle D_E D_S^* \rangle M_{E-\phi} M_{S-\phi}^* \\ &\quad - \langle D_E D_\phi^* \rangle M_{E-\phi} M_{\phi-\phi}^* + \langle D_G D_G^* \rangle M_{G-\phi} M_{G-\phi}^* + \langle D_G D_R^* \rangle M_{G-\phi} M_{R-\phi}^* \\ &\quad - \langle D_G D_E^* \rangle M_{G-\phi} M_{E-\phi}^* - \langle D_G D_S^* \rangle M_{G-\phi} M_{S-\phi}^* + \langle D_G D_\phi^* \rangle M_{G-\phi} M_{\phi-\phi}^* \\ &\quad + \langle D_S D_S^* \rangle M_{S-\phi} M_{S-\phi}^* - \langle D_S D_R^* \rangle M_{S-\phi} M_{R-\phi}^* + \langle D_S D_E^* \rangle M_{S-\phi} M_{E-\phi}^* \\ &\quad - \langle D_S D_G^* \rangle M_{S-\phi} M_{G-\phi}^* - \langle D_S D_\phi^* \rangle M_{S-\phi} M_{\phi-\phi}^* + \langle D_\phi D_\phi^* \rangle M_{\phi-\phi} M_{\phi-\phi}^* \\ &\quad - \langle D_\phi D_R^* \rangle M_{\phi-\phi} M_{R-\phi}^* - \langle D_\phi D_E^* \rangle M_{\phi-\phi} M_{E-\phi}^* + \langle D_\phi D_G^* \rangle M_{\phi-\phi} M_{G-\phi}^* \\ &\quad \left. - \langle D_\phi D_S^* \rangle M_{\phi-\phi} M_{S-\phi}^* \right\} \quad (4.25) \end{aligned}$$

Since some correlation strengths are zero, the $FN(\omega)$ can be simplified as,

$$\begin{aligned}
FN(\omega) &= \left\langle \frac{\omega^2}{|\Delta|^2} |D_R M_{R-\phi} - D_E M_{E-\phi} + D_G M_{G-\phi} - D_S M_{S-\phi} + D_\phi M_{\phi-\phi}|^2 \right\rangle \\
&= \frac{\omega^2}{|\Delta|^2} \left\{ \langle |D_{R-R}|^2 \rangle |M_{R-\phi}|^2 + \langle |D_{E-E}|^2 \rangle |M_{E-\phi}|^2 + \langle |D_{G-G}|^2 \rangle |M_{G-\phi}|^2 \right. \\
&\quad + \langle |D_{S-S}|^2 \rangle |M_{S-\phi}|^2 + \langle |D_{\phi-\phi}|^2 \rangle |M_{\phi-\phi}|^2 - 2 \langle D_{R-E} D_{R-E}^* \rangle \text{Re} \left(M_{R-\phi} M_{R-\phi}^* \right) \\
&\quad \left. - 2 \langle D_{E-G} D_{E-G}^* \rangle \text{Re} \left(M_{E-\phi} M_{G-\phi}^* \right) - 2 \langle D_{G-S} D_{G-S}^* \rangle \text{Re} \left(M_{G-\phi} M_{S-\phi}^* \right) \right\} \quad (4.26)
\end{aligned}$$

4.3.2 Comparison of numerical and experimental results

The diffusion coefficient D_{R-R} serves as our key parameter for correlating frequency noise and current source noise. When using a normal pump to drive the laser, we consider that the current noise term $\eta I/q$ affects the QD laser through the reservoir state into the active medium. When the quiet pump is considered, we can remove the $\eta I/q$ from the D_{R-R} and thus assume that the current is noise-free for the QD laser. According to the above theory, the FN curves are obtained under different current sources as shown in Fig. 6.6(a-d). As the current increases, the frequency noise issued from the two current sources gradually approaches the low-frequency plateau. The FN value at low frequency corresponds to the optical linewidth ($\Delta\nu_{OL}$) of the QD laser, while that at the high-frequency plateau gives the Schawlow-Townes linewidth ($\Delta\nu_{ST}$). It can be seen that the FN's response at high frequency does not depend on the current sources. In other words, whatever normal pump or quiet pump, it does not affect the spontaneous emission noise dominated by the characteristics of the gain medium. The peak between the two plateaus arising above the threshold current corresponds to the relaxation oscillation frequency (f_{RO}) of the QD laser. To this end, when the frequency is lower than f_{RO} , the FN is determined not only by the spontaneous emission but also by the carrier fluctuations, and the optical linewidth can be expressed as $\Delta\nu_{OL} = \Delta\nu_{ST}(1+\alpha_H^2)$. Therefore, as the optical linewidth is driven by different carrier noises, the linewidth enhancement factor is influenced. In addition, maps displayed in Fig. 6.6(e) and 6.6(f) show that when the laser operates with a quiet pump, the laser shows a broader range of low FN. The inflection point at the resonance frequency near 1.8 times threshold is attributed to the spontaneous emission factor ($\beta_{sp} = 1 \times 10^{-4}$). Due

to the limited spontaneous emission efficiency, the laser output power has a nonlinear relationship with the above-threshold current. Overall, these simulations unlock how the carrier noise originating from the current source impacts the FN of the QD laser in particular near the threshold transition.

In the following, the α_H -factor was extracted from the FN simulations and compared to the experiments for different current source conditions. To do so, the α_H -factor was extracted around and above the threshold current using an optical phase modulation method described in Chapter 2. The modulation of the QD DFB laser at high frequency (13 ~ 18 GHz) leads to distinct side modes in the optical spectrum and the side modes at different optical delays are used to retrieve the α_H -factor. The experiment is performed at room temperature (20 °C). Such an approach allows us to retrieve the pump current dependence of the α_H -factor with and without quiet conditions. Experimental results are depicted in Fig. 6.7(a) and compared with simulations (solid lines). Near the threshold current, it is shown that the α_H -factor becomes much smaller under quiet pumping conditions. For instance at threshold, with a normal pump, the α_H -factor is about 1.7 while it is reduced to 0.5 with quiet pumping. The louder the carrier noise, the easier it is to be captured by defect states and to affect the efficiency of the stimulated emission. Indeed, the optical phase modulation requires sufficient power from the laser which is hardly the case when operating near the threshold. Despite that, we demonstrate that the measured α_H -factors are qualitatively in good agreement with those from the simulations. Interestingly, previous work also showed a rise of the α_H -factor extracted in a QD laser from ASE and normal pump across the threshold, but the exact reasons for this phenomenon remain unclear [Dua+18a]. Whereas, with the quiet carriers driving, the α_H -factor of the QD laser near threshold current only appears as a step due to population inversion, which was also simulated in the reference [MHU06]. The α_H -factor doesn't drop to zero at the sub-threshold but approximates a minute value of approximately 0.02. Even when the effect of external carrier noise was eliminated in quiet pumping simulations, the impacts of spontaneous emission and other intrinsic noises on the sub-threshold α_H -factor remain, leading to a diminished α_H -factor value that is not entirely zero. Furthermore, both our experimental and simulation results show that no more differences are observed as the current increases. The α_H -factor becomes independent of the carrier noise.

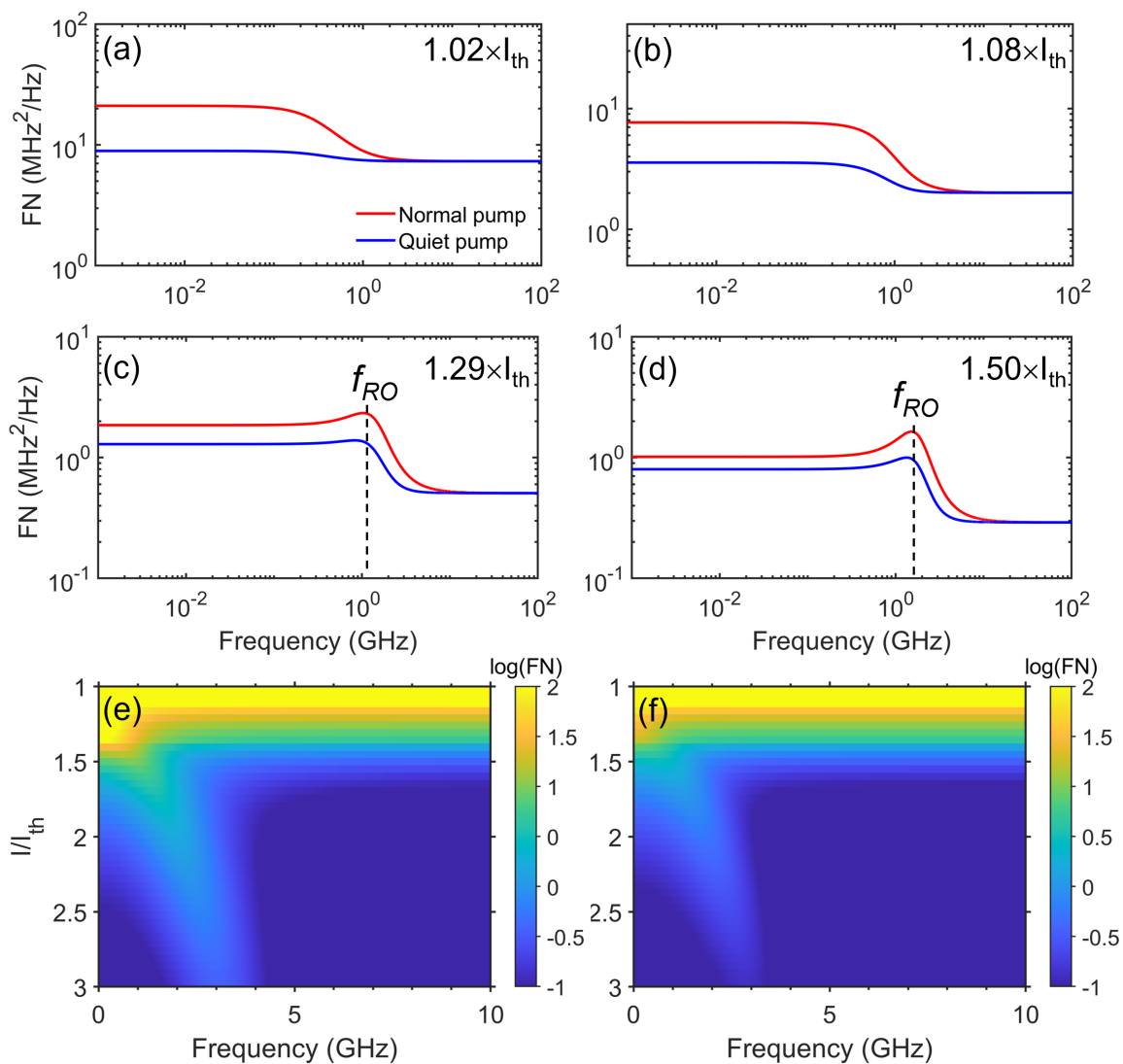


Figure 4.8: Simulated frequency noise spectra of the QD laser with normal pump (red line) and quiet pump (blue line) at different bias currents (a-d). The FN mapping is mapped as a function of normalized bias pump and frequency under (e) normal pump and (f) quiet pump.

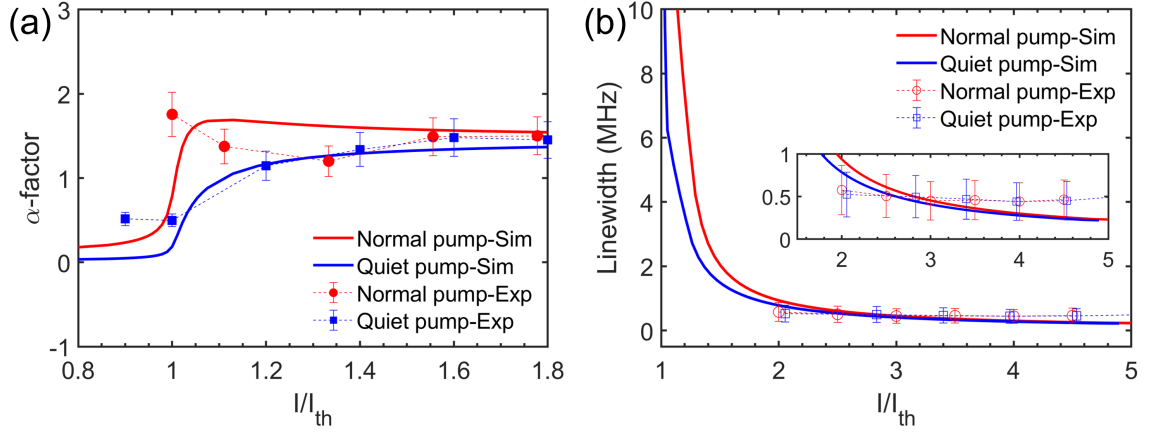


Figure 4.9: Experimental (dotted line) and simulated (solid line) (a) α_H -factor and (b) optical linewidth with bias current under different pumps.

As the optical linewidth is linked to the α_H -factor, the measurement of the QD DFB laser's linewidth is also performed with a delayed self-heterodyne interferometer at 20 °C. Results are shown by the dots in Fig. 6.7(b) for both normal and quiet pump conditions. To extract the linewidths, a Voigt fitting profile is used. Due to technical limitations on the coupled output power, the optical linewidths could only be extracted above twice the threshold current. As expected, we found that the linewidth evolves with the injection current with a sharp decrease above the threshold from several MHz down to a stable value of approximately 500 kHz which is typical for a QD laser [SL05]. At high pump current, there is no significant difference in the optical linewidth when driven by different current sources, which is also consistent with the simulation results. However, when the laser is driven slightly above the threshold, simulations reveal that the use of a normal pump only contributes to increasing the linewidth. For instance, at 1.5 times the threshold current, the optical linewidth is 1.8 MHz with the quiet pump is against 3.2 MHz for the normal pumping conditions. The α_H -factor obtained under different noise conditions of the pump directly determines the tendency of the linewidth. The linewidth will be expanded in a squared α_H -factor manner. The overlap of α_H -factor at high currents also makes the linewidth independent of different noise conditions pump. Therefore, the impacts of external carrier noise on frequency noise dramatically extend to both the α_H -factor and the optical linewidth.

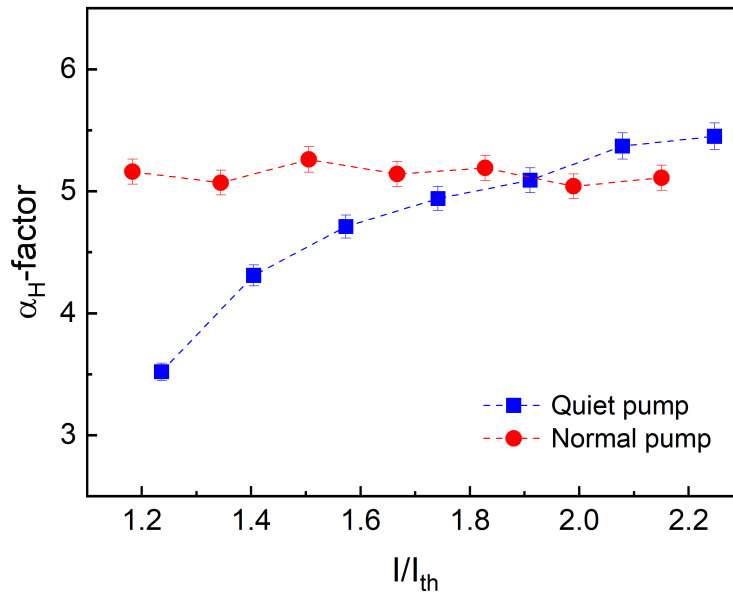


Figure 4.10: The experimental α_H -factor of QW laser with normal and quiet pumps.

As a comparison, we also use different pumps to drive a reference QW DFB laser and apply the optical injection-locked method for α_H -factor extraction [Din+23]. The QW laser also exhibits a gap near the threshold. The gap gradually disappears as the current increases as shown in Fig. 6.8. This also demonstrates the universality of the effect of external carrier noise on lasers, independent of the measurement method and active layer material.

4.4 Summary

In this chapter, the effect of external carrier fluctuations on the frequency noise and α_H -factor of QD lasers is comprehensively investigated.

- First, the reasons causing different external carrier noises were theoretically analyzed. The noise spectra of different current sources were measured to visualize the differences in external carrier fluctuations.
- The effect of external carrier fluctuations on the α_H -factor of a QD DFB laser was investigated. With the quiet pump, the α_H -factor is found to be much smaller

around the threshold as compared to normal pump conditions. Numerical models and experiments together verify this interesting phenomenon. On top of that, simulations also highlight that the use of the quiet pump near the threshold current is beneficial for reducing the frequency noise and subsequently the optical linewidth, but has less impact at high currents. It must be emphasized that the α_H -factor of the QW laser under different pumps also demonstrates similar behavior to those of the QD laser. Overall, I believe that these results are essential for the development of ultra-low noise oscillators that can produce light below or close to the level of shot noise.

Bibliography

- [AR88] Govind P Agrawal and R Roy. “Effect of injection-current fluctuations on the spectral linewidth of semiconductor lasers”. In: *Physical Review A* 37.7 (1988), p. 2495.
- [Arn95] J. Arnaud. “Classical theory of laser noise”. In: *Optical and Quantum Electronics* 27.2 (1995), pp. 63–89.
- [Arn97] J. Arnaud. “Detuned inhomogeneously broadened laser linewidth”. In: *Quantum and Semiclassical Optics: Journal of the European Optical Society Part B* 9.4 (1997), p. 507.
- [Bar+10] S Bartalini et al. “Observing the intrinsic linewidth of a quantum-cascade laser: beyond the Schawlow-Townes limit”. In: *Physical review letters* 104.8 (2010), p. 083904.
- [CCM12] Larry A Coldren, Scott W Corzine, and Milan L Mashanovitch. *Diode lasers and photonic integrated circuits*. John Wiley & Sons, 2012.
- [Din+23] Shihao Ding, Nate Doggett, DJ Herrera, Heming Huang, Vassilios Kovanis, LF Lester, and Frédéric Grillot. “Full parameter extraction of a temperature-insensitive quantum well DFB laser using an optical injection technique”. In: *Physics and Simulation of Optoelectronic Devices XXXI*. Vol. 12415. SPIE. 2023, pp. 76–81.
- [Don+19] Bozhang Dong et al. “Influence of the polarization anisotropy on the linewidth enhancement factor and reflection sensitivity of 1.55- μm InP-based InAs quantum dash lasers”. In: *Applied Physics Letters* 115.9 (2019).

- [Dua+18a] J Duan, H Huang, D Jung, Z Zhang, J Norman, JE Bowers, and F Grillot. “Semiconductor quantum dot lasers epitaxially grown on silicon with low linewidth enhancement factor”. In: *Applied Physics Letters* 112.25 (2018), p. 251111.
- [Dua+18b] Jianan Duan, Xing-Guang Wang, Yue-Guang Zhou, Cheng Wang, and Frederic Grillot. “Carrier-noise-enhanced relative intensity noise of quantum dot lasers”. In: *IEEE Journal of Quantum Electronics* 54.6 (2018), pp. 1–7.
- [FM07] Andrea Fiore and Alexander Markus. “Differential gain and gain compression in quantum-dot lasers”. In: *IEEE Journal of Quantum Electronics* 43.4 (2007), pp. 287–294.
- [Gri+08] Frédéric Grillot, Béatrice Dagens, Jean-Guy Provost, Hui Su, and Luke F Lester. “Gain Compression and Above-Threshold Linewidth Enhancement Factor in 1.3- μm InAs-GaAs Quantum-Dot Lasers”. In: *IEEE Journal of Quantum Electronics* 44.10 (2008), pp. 946–951.
- [Hen82] C. Henry. “Theory of the linewidth of semiconductor lasers”. In: *IEEE Journal of Quantum Electronics* 18.2 (1982), pp. 259–264.
- [Jin+23] Zhiyong Jin et al. “Reflection sensitivity of dual-state quantum dot lasers”. In: *Photonics Research* 11.10 (2023), pp. 1713–1722.
- [KSY12] Jungsang Kim, Seema Somani, and Yoshihisa Yamamoto. *Nonclassical light from semiconductor lasers and LEDs*. Vol. 5. Springer Science & Business Media, 2012.
- [Kir+96] N Kirstaedter et al. “Gain and differential gain of single layer InAs/GaAs quantum dot injection lasers”. In: *Applied physics letters* 69.9 (1996), pp. 1226–1228.
- [Liu+19] Songtao Liu et al. “High-channel-count 20 GHz passively mode-locked quantum dot laser directly grown on Si with 4.1 Tbit/s transmission capacity”. In: *Optica* 6.2 (2019), pp. 128–134.

- [MYI87] S Machida, Y Yamamoto, and Y Itaya. “Observation of amplitude squeezing in a constant-current-driven semiconductor laser”. In: *Physical review letters* 58.10 (1987), p. 1000.
- [MY88] Susumu Machida and Yoshihisa Yamamoto. “Ultrabroadband amplitude squeezing in a semiconductor laser”. In: *Physical review letters* 60.9 (1988), p. 792.
- [Mal+21] A Malik, C Xiang, L Chang, W Jin, J Guo, M Tran, and J Bowers. “Low noise, tunable silicon photonic lasers”. In: *Applied Physics Reviews* 8.3 (2021), p. 031306.
- [McC66] DE McCumber. “Intensity fluctuations in the output of cw laser oscillators. I”. In: *Physical Review* 141.1 (1966), p. 306.
- [MHU06] S. Melnik, G. Huyet, and A. V Uskov. “The linewidth enhancement factor α of quantum dot semiconductor lasers”. In: *Optics Express* 14.7 (2006), pp. 2950–2955.
- [ML18] J Mork and GL Lippi. “Rate equation description of quantum noise in nanolasers with few emitters”. In: *Applied Physics Letters* 112.14 (2018), p. 141103.
- [MY20] Jesper Mork and Kresten Yvind. “Squeezing of intensity noise in nanolasers and nanoLEDs with extreme dielectric confinement”. In: *Optica* 7.11 (2020), pp. 1641–1644.
- [OB87] M. Osinski and J. Buus. “Linewidth broadening factor in semiconductor lasers—An overview”. In: *IEEE Journal of Quantum Electronics* 23.1 (1987), pp. 9–29.
- [SL05] Hui Su and Luke F Lester. “Dynamic properties of quantum dot distributed feedback lasers: high speed, linewidth and chirp”. In: *Journal of Physics D: Applied Physics* 38.13 (2005), p. 2112.
- [TP83a] R Tucker and David J Pope. “Microwave circuit models of semiconductor injection lasers”. In: *IEEE Transactions on Microwave Theory and Techniques* 31.3 (1983), pp. 289–294.

- [TP83b] R Tucker and Di Pope. “Circuit modeling of the effect of diffusion on damping in a narrow-stripe semiconductor laser”. In: *IEEE Journal of Quantum Electronics* 19.7 (1983), pp. 1179–1183.
- [VG97] J-L Vey and Philippe Gallion. “Semiclassical model of semiconductor laser noise and amplitude noise squeezing. I. Description and application to Fabry-Perot laser”. In: *IEEE journal of quantum electronics* 33.11 (1997), pp. 2097–2104.
- [Wan+14] Cheng Wang, Benjamin Lingnau, Kathy Lüdge, Jacky Even, and Frédéric Grillot. “Enhanced dynamic performance of quantum dot semiconductor lasers operating on the excited state”. In: *IEEE Journal of quantum electronics* 50.9 (2014), pp. 1–9.
- [Wan+16] Cheng Wang, Jun-Ping Zhuang, Frédéric Grillot, and Sze-Chun Chan. “Contribution of off-resonant states to the phase noise of quantum dot lasers”. In: *Optics express* 24.26 (2016), pp. 29872–29881.
- [YMN86] Y Yamamoto, S Machida, and O Nilsson. “Amplitude squeezing in a pump-noise-suppressed laser oscillator”. In: *Physical Review A* 34.5 (1986), p. 4025.
- [YH92] Yoshihisa Yamamoto and Hermann A Haus. “Effect of electrical partition noise on squeezing in semiconductor lasers”. In: *Physical Review A* 45.9 (1992), p. 6596.
- [YMR92] Yoshihisa Yamamoto, Susumu Machida, and Wayne H Richardson. “Photon number squeezed states in semiconductor lasers”. In: *Science* 255.5049 (1992), pp. 1219–1224.
- [Zha+19] Zeyu Zhang, Daehwan Jung, Justin C Norman, Weng W Chow, and John E Bowers. “Linewidth enhancement factor in InAs/GaAs quantum dot lasers and its implication in isolator-free and narrow linewidth applications”. In: *IEEE Journal of Selected Topics in Quantum Electronics* 25.6 (2019), pp. 1–9.

-
- [ZG22a] Shiyuan Zhao and Frédéric Grillot. “Modeling of Amplitude Squeezing in a Pump-Noise-Suppressed Interband Cascade Laser”. In: *IEEE Photonics Journal* 14.3 (2022), pp. 1–8.
- [ZG22b] Shiyuan Zhao and Frédéric Grillot. “Stochastic Model of Sub-Poissonian Quantum Light in an Interband Cascade Laser”. In: *Physical Review Applied* 18.6 (2022), p. 064027.
- [Zho+20] Yueguang Zhou, Jianan Duan, Frédéric Grillot, and Cheng Wang. “Optical noise of dual-state lasing quantum dot lasers”. In: *IEEE Journal of Quantum Electronics* 56.6 (2020), pp. 1–7.

CHAPTER 5

Amplitude Squeezed States of Quantum Dot Lasers

In the swiftly advancing domain of optical science and technology, there is a growing focus on the creation and use of ultra-low-noise light sources. These sources play pivotal roles in both classical optical areas as well as in newer quantum optical fields such as quantum communication, quantum computing, and quantum sensing [Kok+07; Pir+18; Sca+09]. It has been shown that shot noise caused by background light is a limiting factor in optical transmission systems. The shot noise leads to a power loss of several dB and increases the transmission BER [Wan+11]. Remarkably, the squeezed state, a quantum light source light below shot noise, can offer great potential for quantum applications that break through classical optical limitations. Firstly, this chapter will show the fundamental concepts of squeezed states, how they are generated, etc. Then it will present the results of generating the amplitude squeezed state by using a QD laser. I further experimentally present the optical feedback insensitive amplitude squeezed state properties of the QD laser. The above findings contribute to the development of silicon-based integrated quantum chips.

5.1 Introduction

The squeezed states of light have found wide applications in quantum information processing and quantum metrology [Car+21; Gat+19; Sch+10]. The idea of squeezed states follows from the Heisenberg uncertainty principle. The expression for the elec-

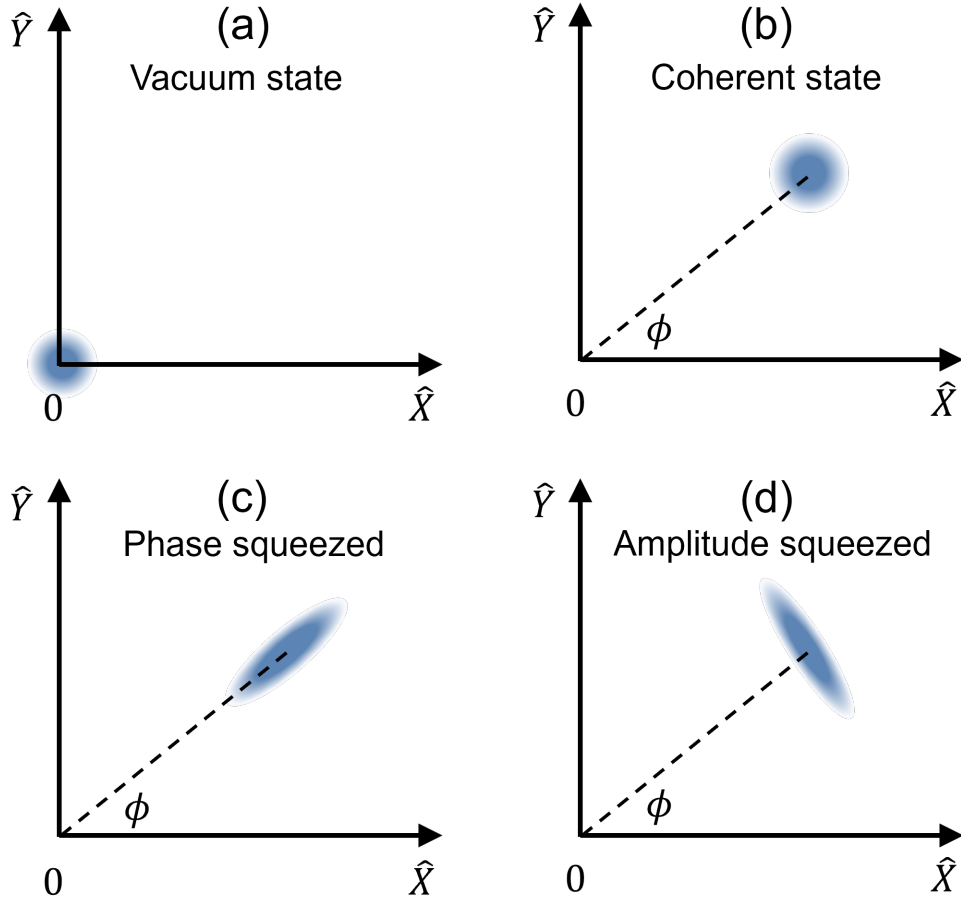


Figure 5.1: Different states represented in the phasor diagram: (a) vacuum state, (b) coherent state, (c) phase squeezed state, (d) amplitude squeezed state.

tric field operator at all phase angles ϕ is $E(\phi) = \hat{X} \cos \phi + \hat{Y} \sin \phi$, where $\hat{X} = (\hat{a} + \hat{a}^\dagger)/\sqrt{2}$ and $\hat{Y} = (\hat{a} - \hat{a}^\dagger)/\sqrt{2}i$ are stated to be the quadrature operators. \hat{a} and \hat{a}^\dagger are the annihilation and creation operators, respectively [BR19; HG88; Hil87]. Whereas the squeezed states need to be introduced incrementally from the vacuum state which is the quantum state with the lowest possible energy. In quantum field theory, even the vacuum state exhibits fluctuations due to Heisenberg's uncertainty principle as shown in Fig. 5.1(a). In vacuum or near-vacuum conditions, where the number of photons is very low, the fluctuations in the number of photons become more prominent, which is essentially shot noise level (SNL) also known as standard quantum limit (SQL). At this point, the fluctuations of the different quadrature components are equal in phase space,

$\langle(\Delta\hat{X})^2\rangle = \langle(\Delta\hat{Y})^2\rangle$. The coherent state can be obtained by applying the displacement operator ($\bar{\alpha}$) to the vacuum state, and the fluctuations of its different orthogonal components are the same in phase space as shown in Fig. 5.1(b). Fig. 5.1(c) shows the phase squeezed state. The amplitude squeezed state is demonstrated by Fig. 5.1(d) [BR19; Xu+19]. Amplitude squeezed states are usually more favorable for applications such as quantum precision measurements and quantum information transmission because low amplitude noise leads to improved measurement accuracy and transmission efficiency. The amplitude squeezed state is also known as the photon number squeezed state, which is defined as having a photon number noise $\langle\Delta\hat{n}^2\rangle$ below the SNL and the relationship between the photon number and the phase noise is $\langle\Delta\hat{n}^2\rangle\langle\Delta\hat{\phi}^2\rangle = 1/4$. If the fluctuations of any of the quadrature components reduce to less than SNL, then it is called a quadrature squeezed state.

5.1.1 Balanced homodyne detection

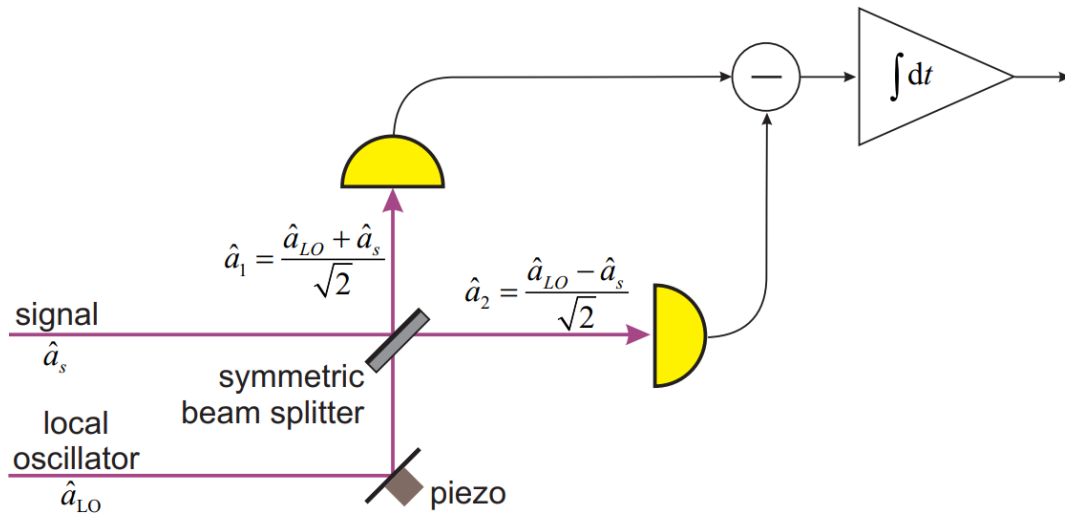


Figure 5.2: Schematic diagram of the balanced homodyne detection [Lvo15]

Balanced homodyne detection is particularly important for measuring and analyzing the squeezed states and the most common way to detect the squeezed states [BC91; Hei+22]. Fig. 5.2 shows the use of a piezo to precisely control the phase difference

between the signal and the local oscillator (LO). The output of the beam splitter is directed to two photodetectors and the difference between their outputs is measured. This balancing behavior effectively eliminates common noises and isolates the subtle quantum properties of the squeezed state, which is crucial for accurately measuring the characteristics of squeezed states with noise levels below the SQL. Certainly, this setup also permits observation of the SQL to help calibrating the strength of the squeezed states.

5.1.2 Quantization of the squeezed states

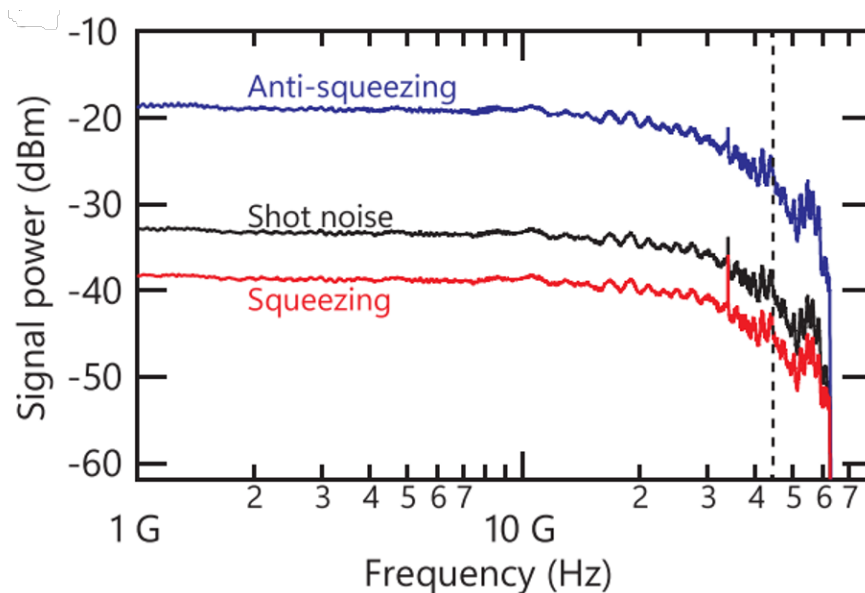


Figure 5.3: Anti-squeezing, shot noise, and squeezing curves in the frequency domain. [Ino+23]

Based on the balanced homodyne detection technique, it is possible to utilize different approaches to characterize quantum light, in particular squeezed states. For amplitude squeezed states, squeezing typically manifests only within a certain frequency range. Analysis of the intensity noise spectrum helps in understanding the squeezing bandwidth and the squeezing level [YH86; YMR92]. During the experiment, an electrical spectrum analyzer is used to record the signal after differential amplification within a selected frequency range, and the phase of the LO is adjusted to find the point where

the squeezed state is strongest. As shown in Fig. 5.3, the anti-squeezing and squeezing curves are obtained at different phases and compared with the shot noise of coherent light, allowing for the observation of the squeezed level and bandwidth of the squeezed states [Ino+23].

For the coherent state, the photon statistic is Poissonian distributed in agreement with the shot noise. For the amplitude squeezed state, the photon number noise decreases, and its photon number distribution exhibits a sub-Poissonian distribution narrower than the Poissonian distribution. The phenomenon was observed in resonance fluorescence in [SM83]. These three photon distributions (anti-squeezing, SNL, squeezing) are shown in Fig. 5.4. In the experiment, the differentially amplified photoelectric statistics signals are recorded by a real-time oscilloscope which satisfies the bandwidth requirement. To clarify, the experimentally obtained photoelectron distribution histograms of coherent states need to satisfy the theoretical Poissonian distribution calculated as $P(n) = e^{-\langle n \rangle} \langle n \rangle^n / n!$, where $\langle n \rangle$ is the average number of primary photoelectrons, given by $I_p T / q$. I_p is the photocurrent, T is the measurement time interval.

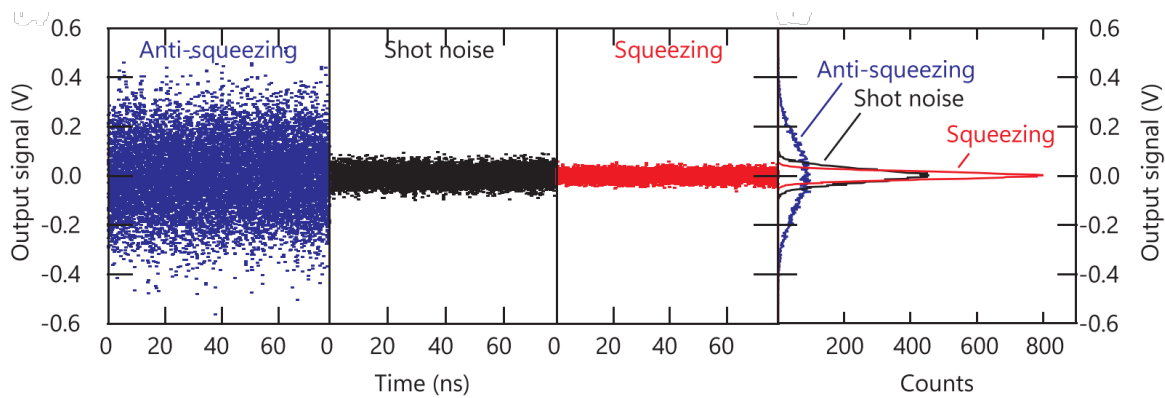


Figure 5.4: Anti-squeezing, shot noise, and squeezing time traces and their corresponding photon statistics. [Ino+23]

Additionally, the Wigner function, as a fundamental tool in quantum optics and quantum mechanics, provide a quasi-probability distribution in phase space for various quantum states [Aga87; Yos+13]. It is particularly useful for visualizing and analyzing the states of quantum systems, especially for the visualization of squeezed states. Numerous measurements of the observed value of the electric field can yield the proba-

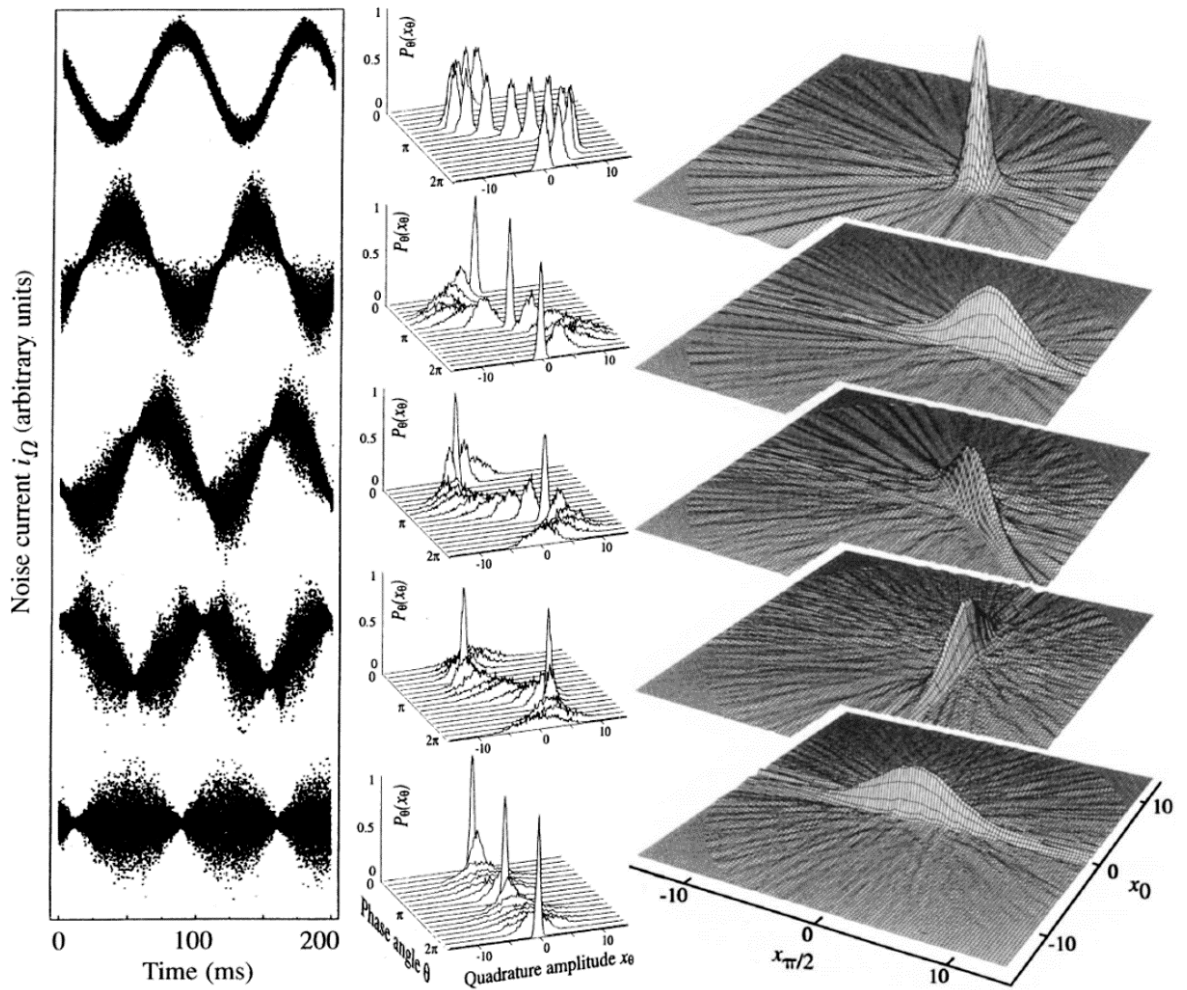


Figure 5.5: Noisy traces (left), quadrature distribution (center), and reconstructed Wigner function for the generated different quantum states (right). [BSM97]

bility distribution $P_\theta(x_\theta)$ for its characteristic value x_θ , where $\theta \in [0, \pi]$ is the relative phase between the signal to be measured and the LO. The set of distributions $P_\theta(x_\theta)$ could then be measured to reconstruct the quantum states, which takes advantage of the fact that the distribution $P_\theta(x_\theta)$ is the margin Poissonian of the Wigner function $W(x, y)$ in rotating coordinates as shown in the following expression [BSM97; Leo97].

$$P_\theta(x_\theta) = \int_{-\infty}^{\infty} W(x_\theta \cos \theta - y_\theta \sin \theta, x_\theta \sin \theta + y_\theta \cos \theta) dy_\theta \quad (5.1)$$

There $y_\theta = -x \sin \theta + y \cos \theta$. $W(x, y)$ can then be obtained by back-projecting from the set P_θ via the inverse Radon transform [KAJ04].

Fig. 5.5 illustrates the Wigner functions for different quantum states, from top to bottom, the coherent state, the phase squeezed state, the phase-specific squeezed state, the amplitude squeezed state, and the squeezed vacuum state. Therefore, the probability density distribution wave packets at different phases can well demonstrate the variation of the shape of the squeezed state with phase [BSM97].

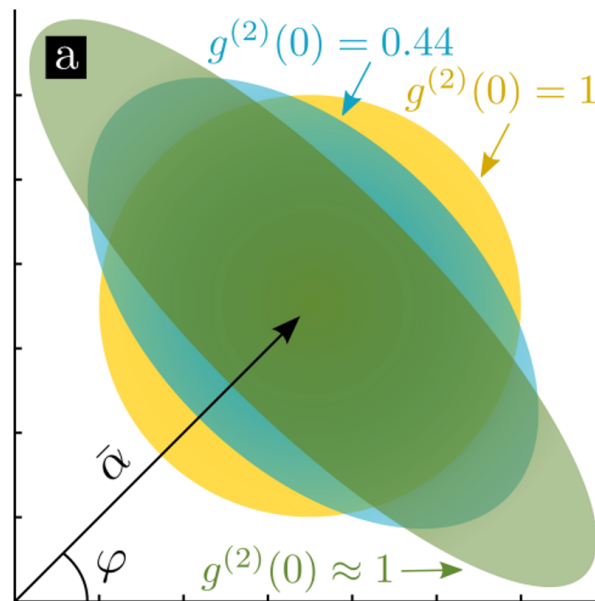


Figure 5.6: Second-order correlation functions for ideal amplitude squeezed states with different squeezing parameters. [LDC14]

Another measure of fluctuations in light field intensity is the second-order correlation function $g^{(2)}(\tau)$ which can be extracted by Hanbury Brown and Twiss (HBT) experiment [Ale16; KDK89; LDC14; McK+03]. The τ represents the delay of the two arms in the HBT setup. The zero-delayed second-order correlation function $g^{(2)}(0)$ can exhibit the behavior between photons in the light beam, bunching, or antibunching. The amplitude squeezed state of the emitted photon antibunching beam suppresses the probability of detecting two photons simultaneously in the HBT setup. Optimized amplitude squeezing produces the $g^{(2)}(0)$ value, i.e., $g^{(2)}(0) < 1$ for single-mode amplitude squeezed state as shown in Fig. 5.6 [LDC14]. The $g^{(2)}(0)$ does not vary linearly with the squeezing level and will be infinitely close to 1 at stronger squeezing.

5.1.3 Applications of amplitude squeezing

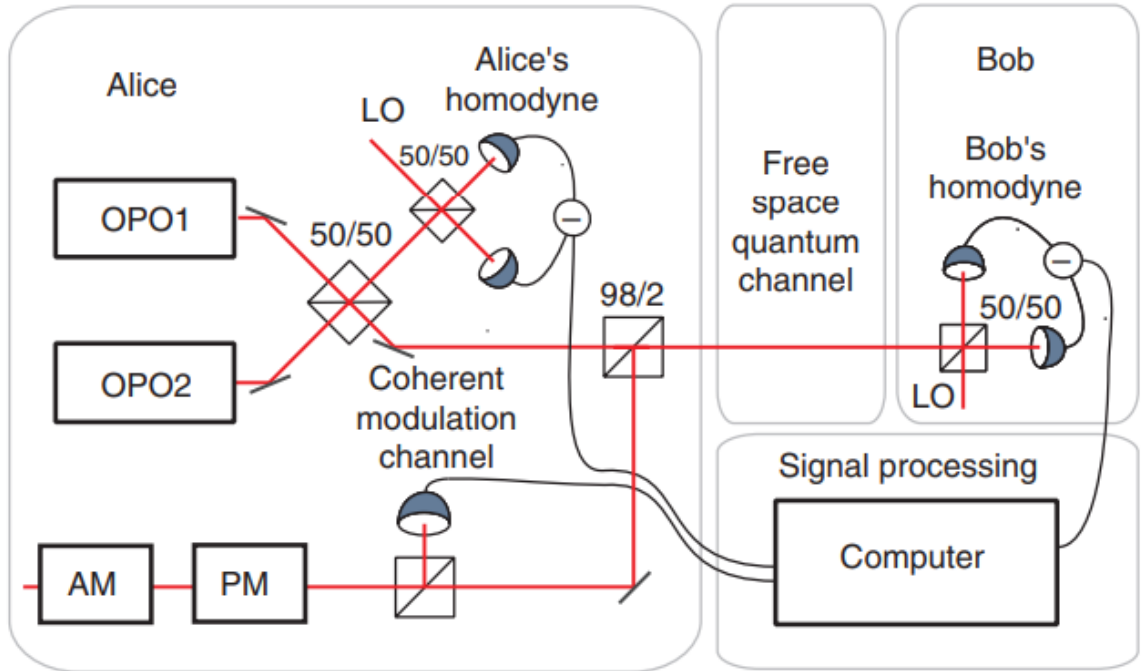


Figure 5.7: The CV-QKD experimental set-up. The two OPOs each produce a squeezed state. The squeezed states interfere with the BS to form a two-mode squeezed state. The amplitude or phase quadrature of one mode is measured by Alice's homodyne detector. The other mode is carefully phase-locked to a coherently modulated auxiliary mode. [Mad+12]

The diverse applications of the squeezed state are the driving force of our research in this field. In the domain of quantum information science, amplitude squeezed states are essential for quantum communication. They are a key component in executing the CV-QKD protocol. This protocol employs quantum mechanical principles to guarantee secure communication channels. For instance, L. Madsen et al. proposed and experimentally validated a CV-QKD protocol. The quantum key distribution protocol they developed can tolerate more noise than the ideal continuous variable coherent state protocol's set benchmark [Mad+12]. The experimental setup is illustrated in Fig. 5.7.

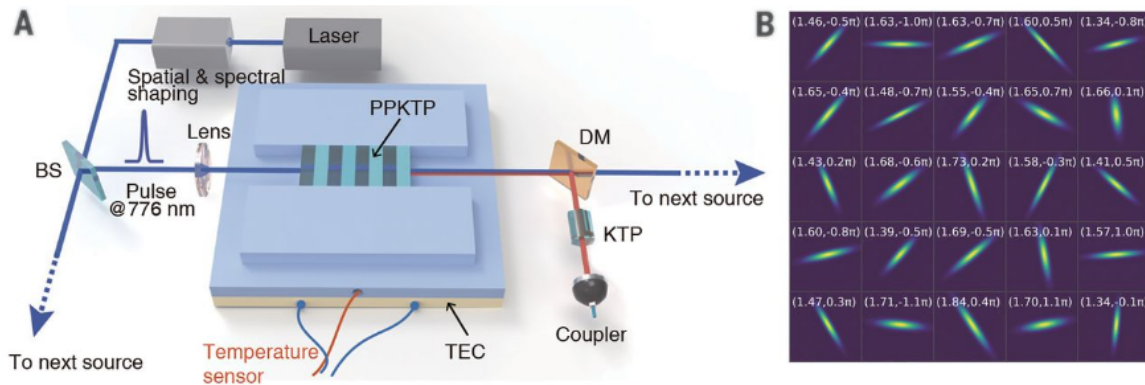


Figure 5.8: Quantum light sources for Gaussian boson sampling. (a) Schematic diagram of the experimental setup for generating two-mode squeezed states. (b) The Wigner function of 25 squeezed states. [Zho+20]

In addition, there is a fervent interest in researching quantum computers to improve the efficiency of specific algorithms. Recently, J. Pan et al. discussed the photonic quantum computer 'Jiuzhang' with enormous arithmetic power, which generates up to 76 output photon clicks. The sampling rate exceeds current state-of-the-art analog strategies and supercomputers by a factor of approximately 10^{14} [Zho+20]. Whereas in this photonic quantum computer, the two-mode squeezed states were used as quantum light sources, as shown in Fig. 5.8.

Meanwhile, in the field of quantum sensing, amplitude-squeezed states are used to fabricate sensors with unprecedented precision. The application of polarized squeezed light to the spin-noise spectroscopy of atomic clusters has been investigated as shown in Fig. 5.9 [Luc+16]. And it was found that squeezing improves the statistical sensitivity,

which reflects the quantum advantage.

In addition, gravitational wave detection requires ultra-high precision detection techniques. The amplitude squeezed states allow for the detection of incredibly faint signals from cosmic events, such as the collision of black holes or neutron stars. This enhanced sensitivity is crucial for advancing our understanding of the universe and testing the predictions of general relativity. The gravitational wave interferometer shown in Fig. 5.10 is capable of very high sensitivity by combining a Michelson interferometer with a squeezed state source [McC+21].

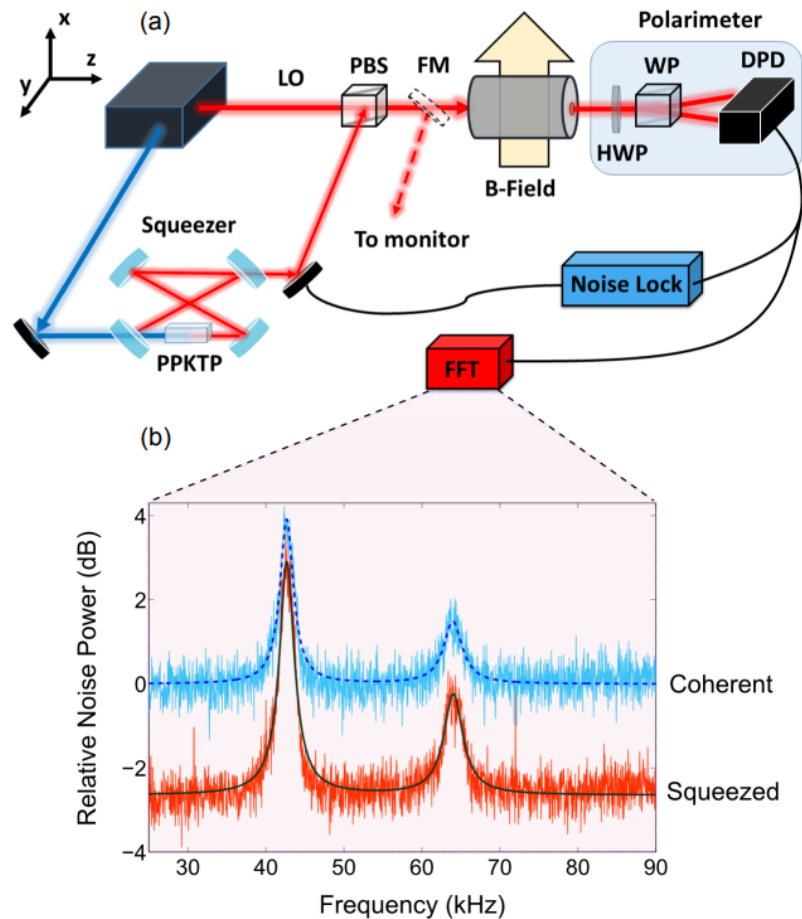


Figure 5.9: Squeezed light in spin noise spectroscopy (a) experimental setup and (b) corresponding noise spectra. [Luc+16]

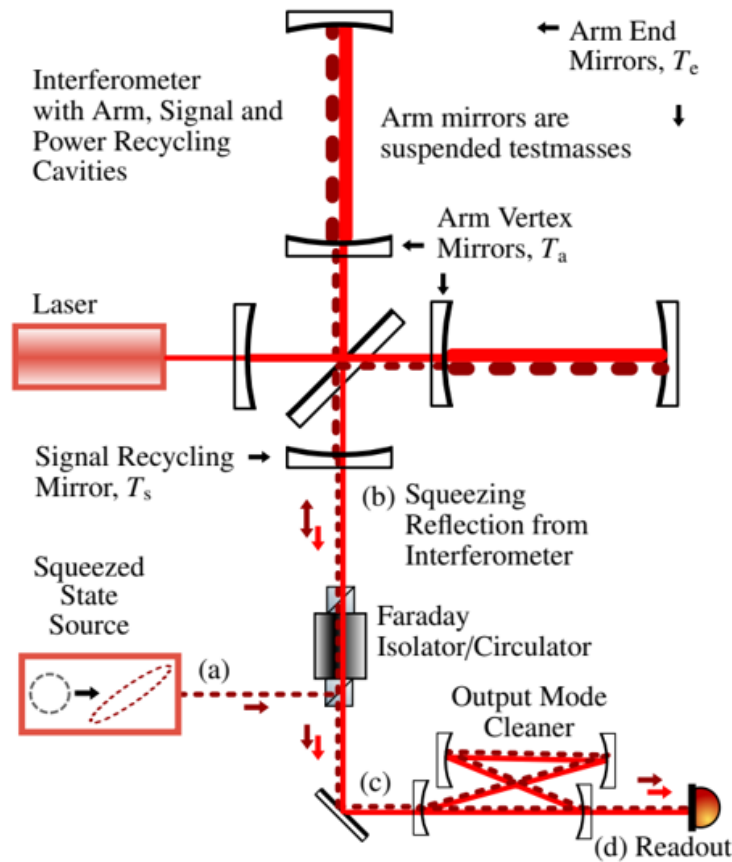


Figure 5.10: The diagram of the interferometer layout shows the propagation of the source laser (red solid line) and the squeezed light (burgundy dashed line). [McC+21]

5.1.4 Techniques for amplitude squeezed state generation

To obtain squeezed states, sophisticated experiments mostly using $\chi^{(2)}$ or $\chi^{(3)}$ optical nonlinearities [Fox+95; Jah+23] have been proposed. There are various platforms wherein these nonlinearities can be evoked. On one hand, there's the use of nonlinear crystals which have historically been the workhorse for generating squeezed states [Jun+22; Tas+21]. Fig. 5.11 demonstrates the utilization of a nonlinear periodically poled potassium titanyl phosphate (PPKTP) type I crystal as the optical parametric oscillator (OPO), resulting in an amplitude squeezed state [Jun+22]. The nonlinear crystals, while well-established, might lack the desired miniaturization for some applications.

With the advent of integrated photonics, on-chip nonlinearities that utilize structures such as micro rings to generate phenomena such as the Kerr effect have begun to receive attention. [Gui+23; McK+22; Yan+21; Zha+20]. The signal of four-wave mixing from micro ring could bring a wide comb squeezed states as shown in Fig. 5.12. In these cases, a squeezed light source with an over 10 dB-high squeezed level (SL) can be obtained. However, the complexity and high cost of the process remain a bottleneck for integrated applications.

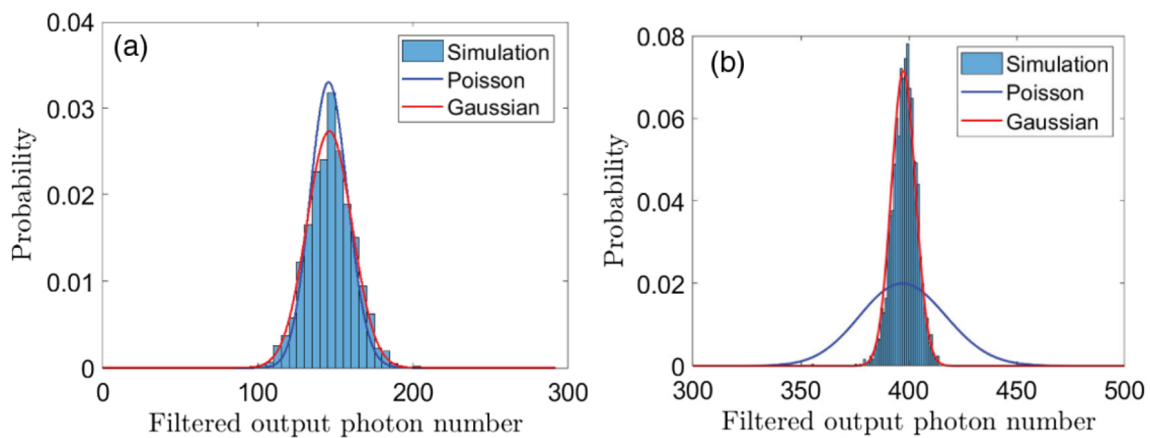


Figure 5.13: Photon distributions of nano light emitter diode under (a) normal pump (b) quiet pump. [MY20]

Another essential method for producing squeezed states involves using external sub-Poissonian distributed carriers from a quiet pump. The noise properties of the pump can significantly influence the SL. At the early stage, Y. Yamamoto et al. have demonstrated that using a quiet pump to drive QW lasers can produce single-mode amplitude squeezed states and a substantial amount of theoretical research has been conducted on this [MYI87; YMN86; YMR92]. Some investigations have shown that the injection of sub-Poissonian distributed carriers can be transformed into sub-Poissonian photon emission, thus achieving squeezed states as shown in Fig. 5.13. Taking advantage of the optoelectric conversion process that is related to the laser structure and the quantum confinement effect of the active region, several investigations have shown that the injection of sub-Poissonian distributed carriers can be transformed into sub-Poissonian photon emission, thus achieving amplitude squeezed states of light [Den+21; MY20;

RM91].

Y. Yamamoto et al. also demonstrated theoretically and experimentally that optical injection-locked techniques can improve the amplitude squeezing intensity of quiet pump-based semiconductor lasers [Ino+93]. Additionally, the weak dispersive optical feedback based on a quiet pump can further enhance the SL [JCG99; Kit+94; YMR92]. This is because the changes in amplitude and phase interactions introduced by the optical feedback process alter the emission characteristics of the laser [KYS95; Pet95]. In this backdrop, the QD laser emerges as a competent candidate as an on-chip squeezed state generator thanks to their superior characteristics like high quantum efficiency, easy integration, and reflection insensitivity [Gri+21; Lia+21].

5.2 Amplitude squeezed states experiments

The results in Chapter 3 prove that quiet pumps can improve noise characteristics, which was demonstrated both experimentally and theoretically [Din+23]. Here, it will be shown how to use a quiet pump to drive a QD laser to generate the amplitude squeezed states. Based on the microscopic theory of junction current noise in the active layer of a semiconductor laser, it is known that the pump fluctuations of a semiconductor laser are thermal noise that could be lower than the SNL. That is exactly the reason why electrically pumped semiconductor lasers have the potential for amplitude squeezing [YMN86].

5.2.1 Experimental setup

A diagram of the experimental setup is illustrated in Fig. 5.14. A 1.31 μm single-mode QD DFB laser was utilized, which features a highly reflective (HR) coating (95%) on the rear facet and an anti-reflection (AR) coating (3%) on the front facet. To maintain a stable temperature of 20 $^{\circ}\text{C}$, I used a thermoelectric temperature controller (ILX Lightwave LDT-5748). The QD laser's threshold current was measured to be 9 mA. The stable single-longitudinal-mode operation was realized over a wide pump current range. I employed a self-homodyne detection for the squeezing measurement. Compared to balanced homodyne detection, the LO input is missing because the photon

number squeezed states we studied have amplitude noise below SNL over a large phase range. The QD DFB laser was coupled into the fiber with 30% coupling efficiency and precisely driven by a quiet pump (ILX Lightwave LDX-3620). A 30 dB optical isolator was imperative because even a minimal amount of back-reflected light leads to excessive intensity noise. After the isolator, the laser output was then coalesced at a tunable BS, ensuring optimal optical balance, and were incident upon a balanced photodetector (BPD, Discovery Semiconductors DSC-R405ER) with 30 dB common-mode rejection ratio (CMRR). The differential photocurrent fluctuations were amplified using a custom-built low-noise electronic amplifier and subsequently analyzed via an ESA (Rohde & Schwarz, 43 GHz) to extract the radio frequency noise spectrum. This balanced detection methodology markedly mitigates intensity noise, offering a significant improvement over single photodiode detection systems.

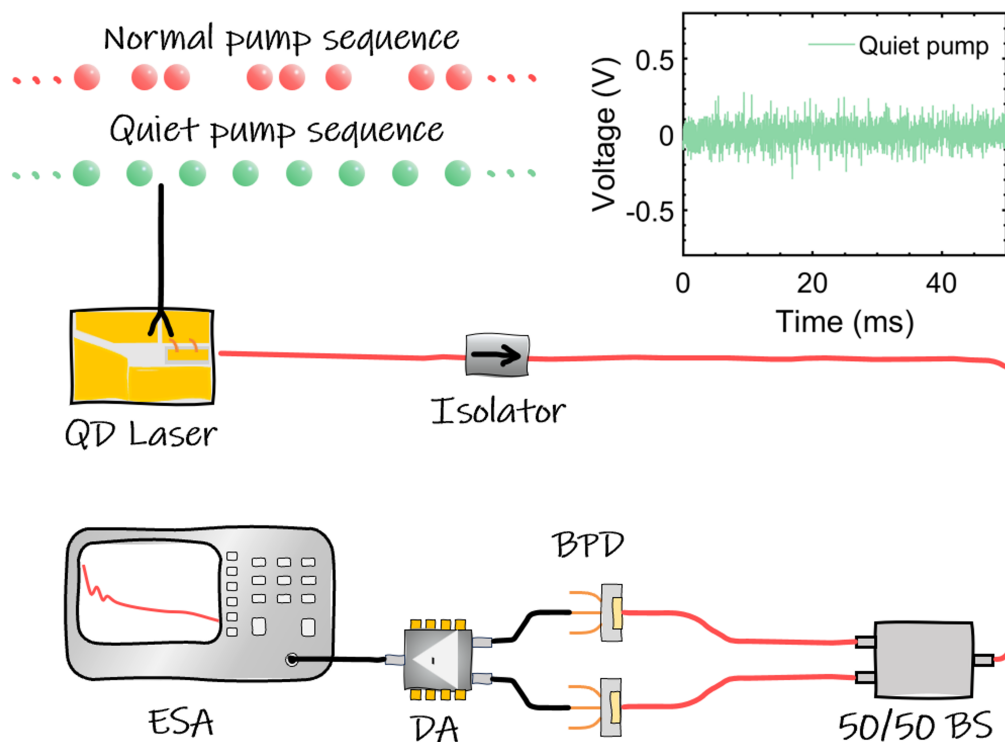


Figure 5.14: Experimental setup for amplitude squeezed state generation with quiet pump. The inset shows the time series fluctuations of the quiet pump and the voltage is the signal read from oscilloscope.

5.2.2 Squeezing characteristics

First of all, it is crucial to accurately calibrate the SNL or SQL. For this purpose, we use a normal pump (Keithley 2401, current source mode) to drive the QD DFB laser. If the RF signal of SNL remains constant, the SNL can be determined accordingly. When performing amplitude squeezed state measurements, the QD DFB laser is driven by a quiet pump. The latter is set to operate at 40 mA ($4.4 \times I_{th}$) at 20 °C in order to check the squeezing properties could be used for future room-temperature and high bias current conditions. The resolution bandwidth (RBW) of the spectrum analyzer was set to 200 kHz and the video bandwidth (VBW) was set to 500 Hz when the RF noise spectrum was recorded. All traces were corrected for thermal background noise subtraction.

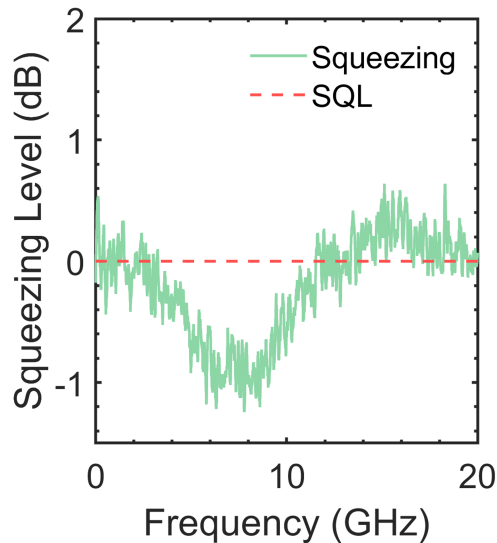


Figure 5.15: The measured RF noise power spectral density at 40 mA.

Fig. 5.15 presents the measured RF noise spectra of the QD laser, offering a comparative analysis between amplitude squeezing (illustrated by the green curve) and the calibrated SQL, represented by the red dashed curve. In the frequency range of 3 GHz to 12 GHz, the RF noise power spectra demonstrate a notable reduction beneath the SQL, with the maximum noise reduction reaching 0.9 dB at 8 GHz. Consequently, our focus shifts to photon statistics to further substantiate the amplitude squeezing

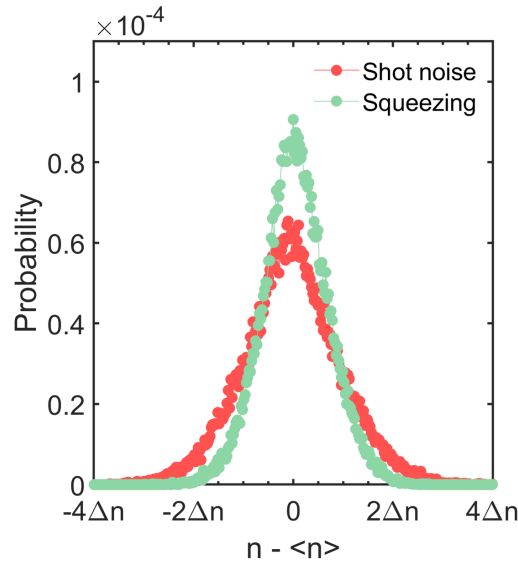


Figure 5.16: Histogram calculated from the raw data acquired by the oscilloscope.

phenomenon.

Fig. 5.16 provides the measured photon statistics, elucidating the differences in photon number distributions ascertained from experimental data (captured by the oscilloscope with 20 GHz bandwidth). Each time trace is averaged over 5 frames and the sampling rate is 20 Gbps. In these analyses, the histograms representing SQL consistently align with a Poissonian distribution. Notably, under conditions of reduced pump noise, the observed distribution narrows, manifesting sub-Poissonian traits. In the figure, the horizontal coordinate is the difference between the photon number n and the mean photon number $\langle n \rangle$ and is scaled by the variance n of the photon number Δn .

5.3 Reflection-insensitive amplitude squeezed states of QD laser

For the future development of integrated optical quantum chips, the study of reflection-insensitive amplitude squeezing generators based on QD lasers can help to improve the integration density. Here, I verified the stability of the quantum noise of the QD

laser by applying optical feedback. In addition, by investigating the zero-delay second-order correlation function, I proved the robust feedback insensitivity of the amplitude squeezed states of the QD laser.

5.3.1 Experimental setup

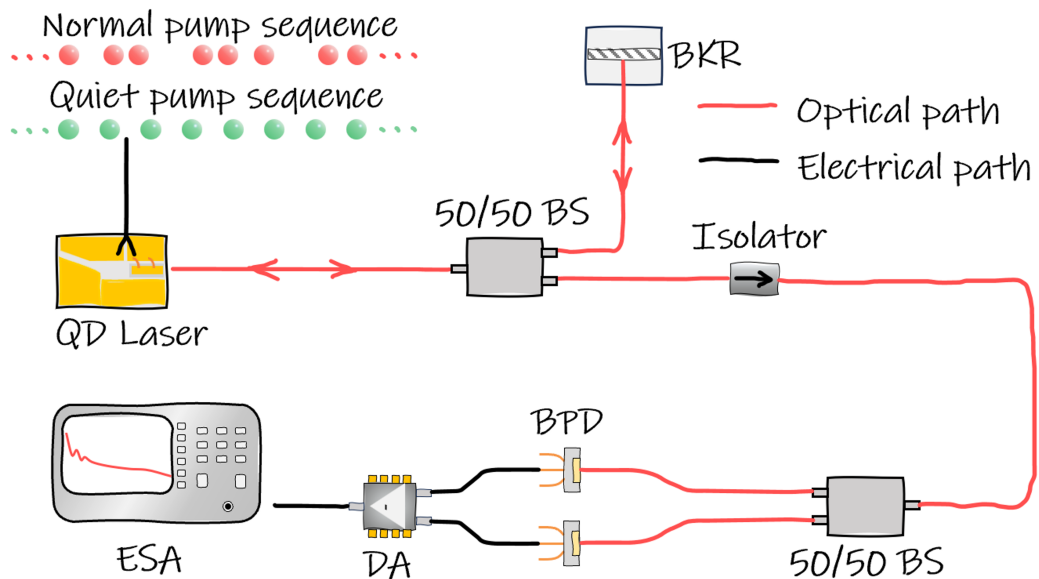


Figure 5.17: Experimental setup for amplitude squeezed state generation employing optical feedback. DA: differential amplifier.

Fig. 5.17 displays the tabletop experiment used for extracting the squeezing characteristics in the presence of external optical feedback. It involves a quiet pump for amplitude squeezed state generation and the balanced homodyne detection part. First, it is critical to calibrate the SNL accurately, as previously described. The 50/50 beam-splitter (BS) and back reflector (BKR) in front of the optical isolator are removed when the SNL calibration is performed. When performing amplitude squeezed state measurements, the QD DFB laser was driven by a quiet pump 40 mA ($4.4 \times I_{th}$). The laser beam was then split into two paths by a 50/50 BS. The first path led to the BKR which consists of a mirror and a variable attenuator (from -2.3 dB to -55 dB). The total feedback strength is defined as the attenuation of the BKR combined with the coupling loss of the laser and the loss of the feedback optical path. The second path

was assigned the task of detecting the squeezed signal, which was measured in the same way as in the previous section.

5.3.2 Comparison between QD and QW lasers

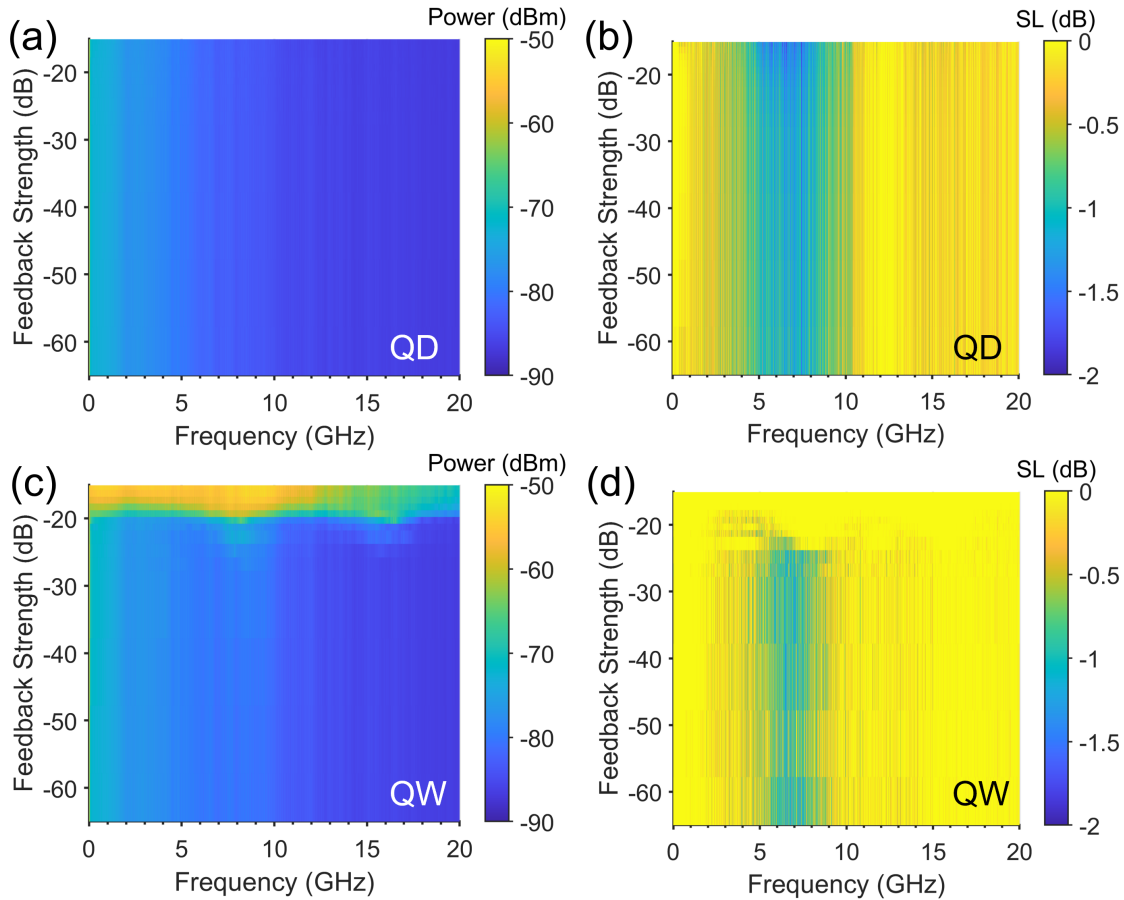


Figure 5.18: Measured classical noise at different feedback strengths for (a) QD laser and (c) QW laser. Squeezing level at different feedback strengths for (b) QD laser and (d) QW laser.

A QW DFB laser with a threshold current of 8.5 mA and a lasing wavelength of $1.31 \mu\text{m}$ close to that of the QD DFB laser is used for reference experiments. Before investigating the quantum noise, I first analyze the response of the classical noise to external optical feedback for both the QD and QW DFB lasers as shown in Fig. 5.18(a) and (c). For the QW laser, there is a critical feedback level of -21 dB above which instabilities such as periodic oscillations and chaotic states appear. In contrast,

the QD laser remains stable regardless of the range of feedback strengths. To further investigate the superiority of QD lasers in terms of quantum noise, I also compare the amplitude squeezing performance of the QW laser with that of the QD laser regarding the noise level and squeezing bandwidth. As shown in Fig. 5.18(b) and (d), negative values indicate the occurrence of squeezing regimes whereas positive ones signify anti-squeezing operation. These diagrams demonstrated that the QD DFB laser displays a broadband squeezing and high SL characteristics which is even slightly intensified as the feedback strength increases. On the other hand, the QW laser also exhibits a squeezing behavior but with a smaller SL along with a narrower bandwidth of 6 GHz which is almost twice narrower than the 13 GHz achieved with the QD laser because QD lasers generally feature lower values of the depletion layer capacitance and lower photon lifetime. This can be explained by the squeezing bandwidth expression given by Y. Yamamoto et al [IY93]. Also, it has to be noted that due to the occurrence of the critical feedback level, the QW laser does not display a squeezing regime above -21 dB. In other words, the large feedback sensitivity of the QW material contributes to fundamentally limiting the squeezing performance through a sharp suppression of the squeezing regime. These maps confirm the high potential of the QD gain chip as a feedback-insensitive source both in the context of classical and quantum noise.

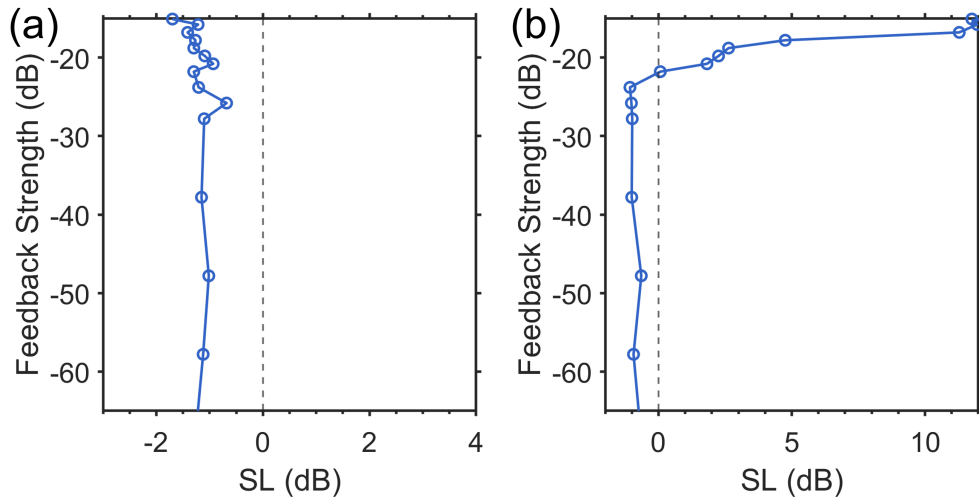


Figure 5.19: The squeezing level of (a) QD laser and (b) QW laser under different optical feedback strengths at room temperature.

The SL in Fig. 5.19 results from the difference between the actual noise spectrum and SQL spectrum. Negative values indicate the squeezed states. The QD laser's squeezing behavior under optical feedback is shown in Fig. 5.19(a). As optical feedback strength increases, the SL steadily rises from 0.9 dB without feedback to 1.7 dB at the strongest feedback level of -18.8 dB. However, the QW laser's SL increases from 0.8 dB to 1.0 dB with optical feedback below -24 dB. With a further increase of the optical feedback strength, the squeezing is lost (SL > 0), which is caused by the phase-amplitude fluctuation enhanced by the optical feedback. This echoes prior research indicating enhanced squeezing performance with weak optical feedback [Kit+94]. QD lasers not only have great potential as classical light sources but can be also as stable integrated quantum light sources with enhanced squeezing performance.

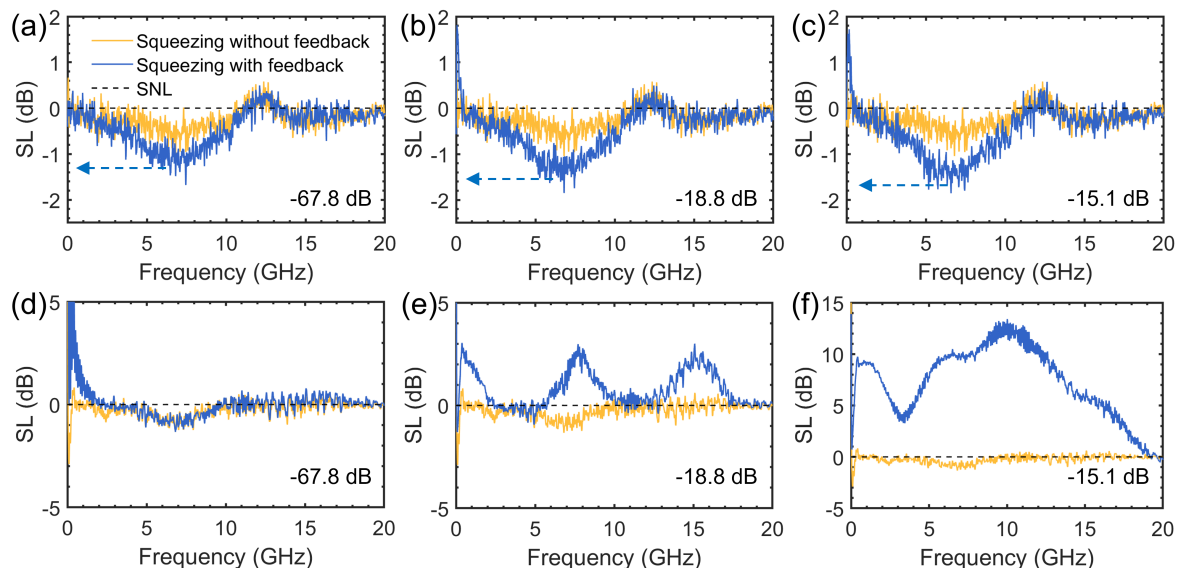


Figure 5.20: Squeezing level spectrum for (a)-(c) QD laser and (d)-(f) QW laser without or with optical feedback under -67.8 dB, -18.8 dB, and -15.1 dB respectively.

Additionally, the comparison of the SL spectra of both QD and QW lasers before and after optical feedback allows us to further understand the detailed process of noise evolution. Fig. 5.20(a)-(c) display the SL spectra of the QD laser without optical feedback and with feedback strengths of -67.8 dB, -18.8 dB, and -15.1 dB, respectively. Fig. 5.20(d)-(f) present the results for the QW laser under the same conditions. For the QD laser, as the optical feedback strength increases, the SL gradually increases

with a maximum value of 1.9 dB at 6 GHz. On the contrary, the QW laser maintains a squeezed state operation whereas beyond -21 dB optical feedback strength, the squeezed state vanishes, and the noise spectrum exhibits a periodic oscillation which further develops into a chaotic state at higher feedback intensities. In the latter case, it is interesting to stress that the noise like is found 10 dB higher than the SQL.

5.3.3 Non-ideal homodyne detection correction

When considering the loss of the BS and the vacuum contributions in the setup, the quantum efficiency (η_q) usually needs to be close to 0.9 to guarantee the effectiveness of the squeezed states. To express the propagation loss and the effect of vacuum fluctuations on the single-mode amplitude squeezed state, the following equation is considered [Lvo15].

$$\langle \Delta X_{out}^2 \rangle = \eta_q \langle \Delta X_{sig}^2 \rangle + (1 - \eta_q) \langle \Delta X_{vac}^2 \rangle \quad (5.2)$$

where $\langle \Delta X_{out}^2 \rangle$ is the variance of the measured squeezed state signal, $\langle \Delta X_{sig}^2 \rangle$ is the variance of the initially generated squeezed state signal, and $\langle \Delta X_{vac}^2 \rangle$ is the variance of the vacuum signal from unused BS arm. η_q contains electrical noise (η_{elec}) and the efficiency of the photodetector (η_{PD}), the quality of the interference between the beams in front of the photodetectors (η_{mod}). Finally, the η_{elec} is related to the shot-noise clearance (SNC) of the homodyne detector defined such as $\eta_{elec} = 1 - 1/SNC$. In the experiment, the homodyne detector has a SNC of 20 dB and a linearity value of 0.01. The expression giving the efficiency of the photodetector is $\eta_{PD} = S_{PD} \times (\hbar\omega/e)$ where $S_{PD} = 0.95$ A/W corresponds to the typical photosensitivity of the InGaAs photodetector while \hbar is the reduced Planck constant, ω the laser angular frequency, and e the elementary charge of the electron. Considering the self-homodyne detection, the interference between LO and signal is quite high, and η_{mod} can be taken as 0.94 [GG01]. Based on the product of the three efficiencies, the η_q is of 0.86 and the weights of the squeezed state and vacuum fluctuations can be obtained as $\sqrt{\eta_q} = 0.927$ and $\sqrt{1 - \eta_q} = 0.374$, respectively. The weight of the squeezing signal is higher compared to the vacuum fluctuations and therefore the SL results are reliable [Kou21; Leo97;

Lvo15].

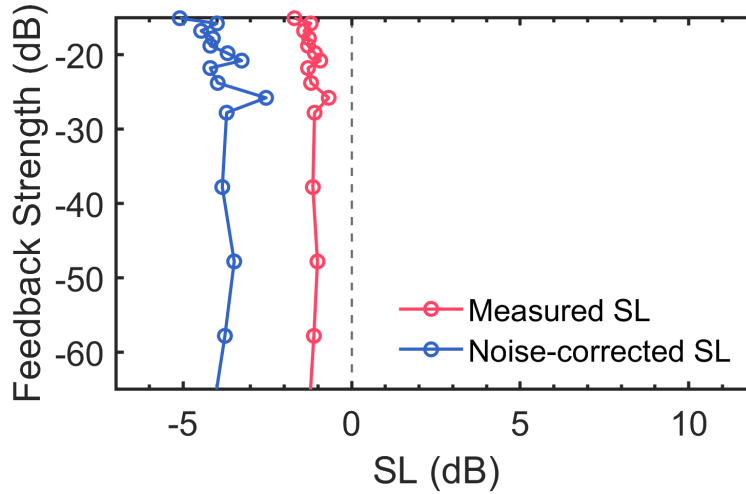


Figure 5.21: The noise-corrected SL of QD laser under different optical feedback strengths.

In addition, to identify the limits of our QD squeezer, the various contributions of the loss originating from all the different optical components are also considered. Given the total quantum efficiency (including the coupling efficiency of 0.4 and optical efficiency of 0.6) and taking the $\langle \Delta X_{vac}^2 \rangle$ as 1/2, the noise-corrected SL (SL_{corr}) can be obtained by transforming the experimentally obtained SL to a linear value by substituting $\langle \Delta X_{out}^2 \rangle$ in the Eq. (1) [Lvo15]. After noise correction, the actual squeezing level of the QD laser can be obtained as shown in Fig. 5.21. In this case, the squeezing level is as high as 5.1 dB of the strongest optical feedback. It is foreseeable that future QD laser silicon-based integrated squeezed-state sources could reduce the impact of transmission noise and be more favorable to on-chip application needs.

5.4 Analysis of second-order correlation function

To further validate the quantum characteristics of the aforementioned squeezed states, the second-order correlation function $g^{(2)}(\tau)$ serves as a convincing metric to evaluate whether a light exhibits anti-bunching, bunching, or coherent. If the second-order correlation function at zero delay $g^{(2)}(0)$ is less than 1, it can be confirmed as a single-mode amplitude squeezed light source [Gro+07].

5.4.1 Relationship between the squeezed characteristics and the second-order correlation function

The second-order correlation function can be expressed as follows [LDC14; OCP18],

$$g^{(2)}(\tau) = \frac{\langle \hat{a}^\dagger(0)\hat{a}^\dagger(\tau)\hat{a}(\tau)\hat{a}(0) \rangle}{\langle \hat{a}^\dagger(0)\hat{a}(0) \rangle \langle \hat{a}^\dagger(\tau)\hat{a}(\tau) \rangle} \quad (5.3)$$

where \hat{a} and \hat{a}^\dagger is the field creation and annihilation operators. When considering the zero-delay condition, the equation above can be simplified as,

$$g^{(2)}(0) = \frac{\langle \hat{a}^\dagger \hat{a}^\dagger \hat{a} \hat{a} \rangle}{\langle \hat{a}^\dagger \hat{a} \rangle^2} = \frac{\langle (\hat{a}^\dagger \hat{a})^2 \rangle - \langle \hat{a}^\dagger \hat{a} \rangle^2}{\langle \hat{a}^\dagger \hat{a} \rangle^2} \quad (5.4)$$

After substitution by covariance matrix operations and operator expressions, the $g^{(2)}(0)$ expression for single-mode light is expressed as follows [Ale16; OCP18],

$$\begin{aligned} g^{(2)}(0) &= 2 + \{ (1 + 2\bar{n}_{th}) \sinh(2r) \\ &\quad \times [(1 + 2\bar{n}_{th}) \sinh(2r) + 4\bar{\alpha}^2 \cos \psi] - 4\bar{\alpha}^4 \} \\ &\quad \times [(1 + 2\bar{n}_{th}) \cosh(2r) + 2\bar{\alpha}^2 - 1]^{-2} \end{aligned} \quad (5.5)$$

Where $\bar{\alpha}$ is the displacement amplitude. \bar{n}_{th} is the mean photon of the thermal state. r is a squeezed parameter. Given that, $\psi = 2\phi$ with ϕ the phase in the phasor diagram, ψ can be set to π , which is the value for the amplitude squeezed state. It's important to highlight that every parameter mentioned above can be transformed into the experimental data corresponding to the squeezed state. The subsequent equation illustrates the relationship between the displacement amplitude, the squeezing parameter, and the mean photon in the thermal state [LDC14].

$$\bar{\alpha}[r, \bar{n}_{th}] = \sqrt{\frac{(2\bar{n}_{th} + 1)(e^r \bar{n}_{th} + \sinh(r)) \sinh(2r)}{e^{-3r}(e^{2r} - (2\bar{n}_{th} + 1))}} \quad (5.6)$$

The mean photon of the thermal state is a parameter intrinsically related to both the temperature and the energy of photons at a particular wavelength. Furthermore,

the squeezing parameter is correlated with the squeezing level. The comprehensive expressions detailing these relationships are presented in the following manner.

$$\bar{n}_{\text{th}} = [e^{(\frac{h\nu}{k_b T})} - 1]^{-1} \quad (5.7)$$

$$SL = -10\log_{10}(e^{-2r}) \quad (5.8)$$

As the lasing wavelength is $1.31 \mu\text{m}$, and the operating temperature is $20 \text{ }^\circ\text{C}$, \bar{n}_{th} can be calculated to be approximately 0.04. Through the noise spectrum, it is known that without external optical feedback, the maximum squeezing level of the QD laser is about 0.9 dB. The measured $g^{(2)}(0)$ corresponds to the SL at all frequencies, so we cannot just use the maximum SL for the squeezing parameter operation. Here, I use 0.45 dB to represent the average SL at all frequencies. Hence, the fitted $g^{(2)}(0)$ of QD and QW laser under optical feedback strengths can be obtained, as shown in Fig. 5.22.

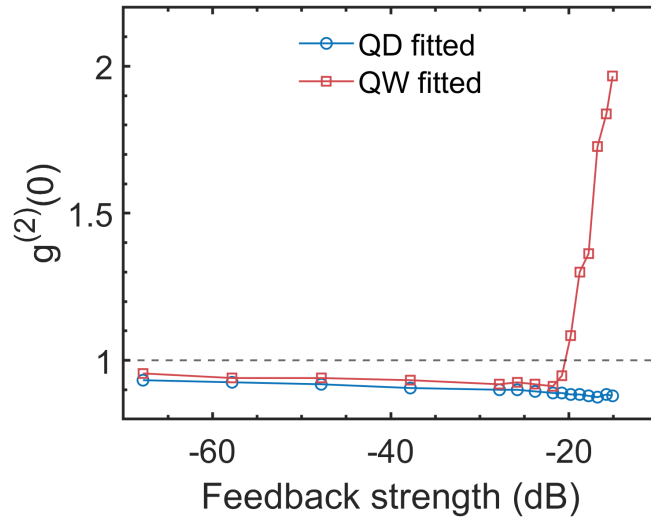


Figure 5.22: The fitted $g^{(2)}(0)$ of QD and QW laser under different optical feedback strengths.

It can be observed that, under the conditions of the quiet pump, the $g^{(2)}(0)$ of the QD laser fitted from the squeezed state gradually decreases with the feedback strength, namely dropping from 0.98 to around 0.96. On the other hand, the $g^{(2)}(0)$ derived from

the QW laser is consistent with the SL. When the feedback strength is less than -24 dB, the $g^{(2)}(0)$ slightly declines, reaching a minimum of approximately 0.97. When the feedback strength exceeds the critical feedback level of -21 dB, it rapidly increases above 1 and approaches 2, hence indicating that the QW laser operates within a chaotic state at high feedback strength. The $g^{(2)}(0)$ is entirely consistent with the parameters of the laser's squeezed state, which validates the accuracy of the squeezing characteristic measurement.

5.4.2 Experimental results

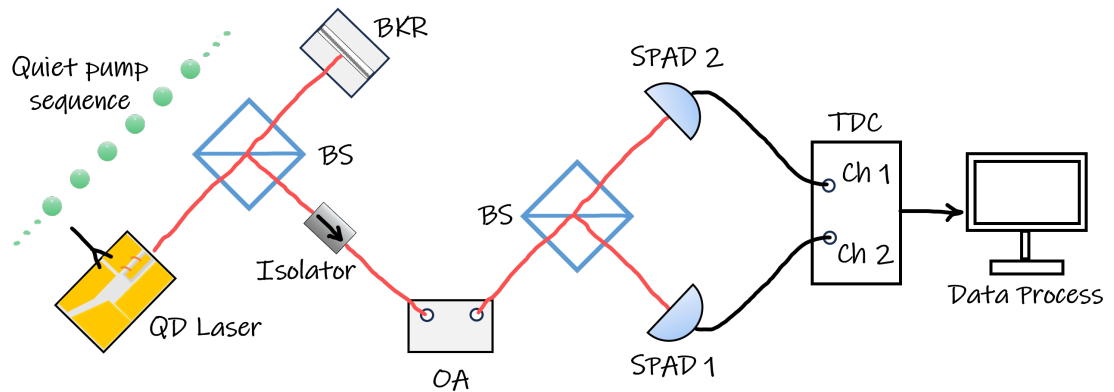


Figure 5.23: Experimental setup for amplitude squeezed state generation employing optical feedback.

To bolster the reliability of the previously mentioned theoretical parameters, I assembled a $g^{(2)}(0)$ testing platform. Fig. 5.23 illustrates the Hanbury Brown and Twiss (HBT) setup, devised for measuring $g^{(2)}(0)$. In this arrangement, both QD (Quantum Dot) and QW (Quantum Well) lasers were individually driven by a subdued pump. After this, the laser light traverses through two optical attenuators, which offer a peak attenuation of up to 110 dB. This precautionary measure is instituted to guarantee that the optical power impinging upon the single-photon detectors is maintained within a secure range. Proceeding further, an impeccably 50/50 optical beamsplitter is employed to bifurcate the laser light equitably into twin paths, ensuring a balanced dual-arm configuration between the two single-photon avalanche detectors (SPADs, sourced

from ID Quantique, model ID200). The ensuing photocurrent signals, generated by the detectors, are subsequently directed into a time-to-digital converter (TDC, sourced from ID Quantique, model ID800) to ascertain the coherence interlinking the signals. Throughout the measurement process, the coincidence time interval δ is determinedly set at 50 ns, while the total testing duration T spans 2 seconds. During this period, the count rates R_1 and R_2 for the two channels are meticulously logged. Additionally, the coincidence events R_{12} interceding between the two channels are also assiduously compiled. By leveraging this dataset, the normalized $g^{(2)}(0)$ can be calculated employing the subsequent equation [McK+03; Zhu+12].

$$g^{(2)}(0) = \frac{R_{12}}{\delta TR_1 R_2} \quad (5.9)$$

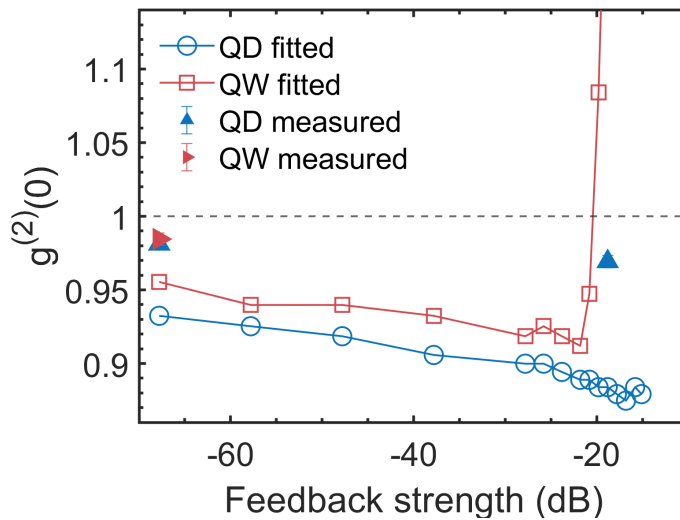


Figure 5.24: The comparison of fitted and experimental $g^{(2)}(0)$.

The $g^{(2)}(0)$ values for the QD laser under weak feedback strength (-67.8 dB) and at a high feedback intensity (-18.8 dB) are 0.9835 ± 0.0029 and 0.9692 ± 0.0043 , respectively. The $g^{(2)}(0)$ trends for the QW laser are also consistent with the fitted ones. 0.9852 ± 0.0032 at weak feedback strength (-67.8 dB) and 1.7213 ± 0.0037 at high feedback strength (-18.8 dB), where the squeezed state disappears. The error is determined from multiple counts. The increased anti-bunching characteristics of photons from the

QD laser demonstrate that the amplitude squeezing performance is preserved and enhanced under optical feedback. The measured results of $g^{(2)}(0)$ perfectly demonstrate the tendency of the squeezing state of QD and QW lasers analyzed by the electric spectrum to vary with the optical feedback. Noteworthy is that the feedback light could affect the quantum noise of the laser due to the amplitude-phase coupling and spontaneous emission contribution reduction [KYS95; Pet95]. With a smaller linewidth enhancement factor, the QD laser is more likely to exhibit lower relative intensity noise and a stronger suppression of amplitude squeezed state noise under optical feedback. Additionally, I believe that the reduction in the photon lifetime due to the increased photon density in the cavity, gain saturation, and the reduced depletion layer capacitance will further increase the squeezing bandwidth [IY93; KYS95].

5.5 Summary

In this Chapter, I have demonstrated that QD lasers showcase superior squeezing performance under quiet pumping and that their quantum noise possesses notable tolerance to optical feedback, particularly when compared to QW lasers. Additionally, examining the second-order correlation function substantiates the reliability of the aforementioned concepts. This research establishes a comprehensive foundational framework for devising future compact, energy-efficient photonic integrated circuits in quantum applications.

- In the second section, the quantum dot lasers are shown to be capable of achieving broadband amplitude squeezed states at room temperature in the frequency range from 3 GHz to 12 GHz, and have a squeezing intensity of 0.9 dB without noise correction.
- In the third section, the squeezed states generated by QD lasers based on injected carriers with sub-Poissonian distribution show perfect optical feedback tolerance. Moreover, it has a SL of up to 5.1 dB after noise correction, which meets the needs of various applications.
- Then, the ultra-optical feedback insensitivity of the squeezed state of the QD laser was verified by analyzing and measuring the second-order correlation function of

the squeezed states. Reconstruction of squeezed states using Wigner functions will be the focus of my attention in the future.

Bibliography

- [Aga87] GS Agarwal. “Wigner-function description of quantum noise in interferometers”. In: *Journal of Modern Optics* 34.6-7 (1987), pp. 909–921.
- [Ale16] Moorad Alexanian. “Temporal second-order coherence function for displaced-squeezed thermal states”. In: *Journal of Modern Optics* 63.10 (2016), pp. 961–967.
- [BR19] Hans-A Bachor and Timothy C Ralph. *A guide to experiments in quantum optics*. John Wiley & Sons, 2019.
- [BC91] Samuel L Braunstein and David D Crouch. “Fundamental limits to observations of squeezing via balanced homodyne detection”. In: *Physical Review A* 43.1 (1991), p. 330.
- [BSM97] Gerd Breitenbach, S Schiller, and J Mlynek. “Measurement of the quantum states of squeezed light”. In: *Nature* 387.6632 (1997), pp. 471–475.
- [Car+21] Fernando R Cardoso, Daniel Z Rossatto, Gabriel PLM Fernandes, Gerard Higgins, and Celso J Villas-Boas. “Superposition of two-mode squeezed states for quantum information processing and quantum sensing”. In: *Physical Review A* 103.6 (2021), p. 062405.
- [Den+21] Hui Deng, Gian Luca Lippi, Jesper Mørk, Jan Wiersig, and Stephan Reitzenstein. “Physics and Applications of High- β Micro-and Nanolasers”. In: *Advanced Optical Materials* 9.19 (2021), p. 2100415.

- [Din+23] Shihao Ding, Shiyuan Zhao, Heming Huang, and Frédéric Grillot. “Impact of external carrier noise on the linewidth enhancement factor of a quantum dot distributed feedback laser”. In: *Optics Express* 31.21 (2023), pp. 35343–35353.
- [Fox+95] AM Fox, JJ Baumberg, M Dabbicco, B Huttner, and JF Ryan. “Squeezed light generation in semiconductors”. In: *Physical Review Letters* 74.10 (1995), p. 1728.
- [Gat+19] Dario Gatto, Paolo Facchi, Frank A Narducci, and Vincenzo Tamma. “Distributed quantum metrology with a single squeezed-vacuum source”. In: *Physical Review Research* 1.3 (2019), p. 032024.
- [Gri+21] Frédéric Grillot, Jianan Duan, Bozhang Dong, and Heming Huang. “Uncovering recent progress in nanostructured light-emitters for information and communication technologies”. In: *Light: Science & Applications* 10.1 (2021), p. 156.
- [Gro+07] Nicolai B Grosse, Thomas Symul, Magdalena Stobińska, Timothy C Ralph, and Ping Koy Lam. “Measuring photon antibunching from continuous variable sideband squeezing”. In: *Physical Review Letters* 98.15 (2007), p. 153603.
- [GG01] Frédéric Grosshans and Philippe Grangier. “Effective quantum efficiency in the pulsed homodyne detection of a n-photon state”. In: *The European Physical Journal D-Atomic, Molecular, Optical and Plasma Physics* 14 (2001), pp. 119–125.
- [Gui+23] Melissa A Guidry, Daniil M Lukin, Ki Youl Yang, and Jelena Vučković. “Multimode squeezing in soliton crystal microcombs”. In: *Optica* 10.6 (2023), pp. 694–701.
- [Hei+22] Joscha Heinze, Karsten Danzmann, Benno Willke, and Henning Vahlbruch. “10 dB quantum-enhanced michelson interferometer with balanced homodyne detection”. In: *Physical Review Letters* 129.3 (2022), p. 031101.
- [HG88] Richard W Henry and Sharon C Glotzer. “A squeezed-state primer”. In: *American Journal of Physics* 56.4 (1988), pp. 318–328.

- [Hil87] Mark Hillery. “Amplitude-squared squeezing of the electromagnetic field”. In: *Physical Review A* 36.8 (1987), p. 3796.
- [IY93] A Imamog and Y Yamamoto. “Noise suppression in semiconductor p-i-n junctions: Transition from macroscopic squeezing to mesoscopic Coulomb blockade of electron emission processes”. In: *Physical Review Letters* 70.21 (1993), p. 3327.
- [Ino+23] Asuka Inoue et al. “Toward a multi-core ultra-fast optical quantum processor: 43-GHz bandwidth real-time amplitude measurement of 5-dB squeezed light using modularized optical parametric amplifier with 5G technology”. In: *Applied Physics Letters* 122.10 (2023).
- [Ino+93] S Inoue, S Machida, Y Yamamoto, and H Ohzu. “Squeezing in an injection-locked semiconductor laser”. In: *Physical Review A* 48.3 (1993), p. 2230.
- [Jah+23] Mandana Jahanbozorgi, Zijiao Yang, Shuman Sun, Haoran Chen, Ruxuan Liu, Beichen Wang, and Xu Yi. “Generation of squeezed quantum microcombs with silicon nitride integrated photonic circuits”. In: *Optica* 10.8 (2023), pp. 1100–1101.
- [JCG99] F Jeremie, C Chabran, and Philippe Gallion. “Generation of amplitude-squeezed light from 1550 nm distributed feedback semiconductor laser under wavelength selective optical feedback conditions”. In: *Applied Physics Letters* 75.23 (1999), pp. 3614–3616.
- [Jun+22] Jonas Junker, Dennis Wilken, Nived Johny, Daniel Steinmeyer, and Michèle Heurs. “Frequency-dependent squeezing from a detuned squeezer”. In: *Physical Review Letters* 129.3 (2022), p. 033602.
- [KDK89] MS Kim, FAM De Oliveira, and PL Knight. “Properties of squeezed number states and squeezed thermal states”. In: *Physical Review A* 40.5 (1989), p. 2494.
- [KAJ04] T Kiss, P Adam, and J Janszky. “Gauss filtered back projection for the reconstruction of the Wigner function”. In: *Acta Physica Hungarica Series B, Quantum Electronics* 20 (2004), pp. 47–50.

- [Kit+94] J Kitching, R Boyd, A Yariv, and Y Shevy. “Amplitude noise reduction in semiconductor lasers with weak, dispersive optical feedback”. In: *Optics Letters* 19.17 (1994), pp. 1331–1333.
- [KYS95] J Kitching, A Yariv, and Y Shevy. “Room temperature generation of amplitude squeezed light from a semiconductor laser with weak optical feedback”. In: *Physical Review Letters* 74.17 (1995), p. 3372.
- [Kok+07] Pieter Kok, William J Munro, Kae Nemoto, Timothy C Ralph, Jonathan P Dowling, and Gerard J Milburn. “Linear optical quantum computing with photonic qubits”. In: *Reviews of modern physics* 79.1 (2007), p. 135.
- [Kou21] Tiphaine Kouadou. “Single-pass generation and detection of ultrafast multimode squeezed light”. PhD thesis. Sorbonne université, 2021.
- [LDC14] Marc-Antoine Lemonde, Nicolas Didier, and Aashish A Clerk. “Anti-bunching and unconventional photon blockade with Gaussian squeezed states”. In: *Physical Review A* 90.6 (2014), p. 063824.
- [Leo97] Ulf Leonhardt. *Measuring the quantum state of light*. Vol. 22. Cambridge university press, 1997.
- [Lia+21] Di Liang, Sudharsanan Srinivasan, Antoine Descos, Chong Zhang, Geza Kurczveil, Zhihong Huang, and Raymond Beausoleil. “High-performance quantum-dot distributed feedback laser on silicon for high-speed modulations”. In: *Optica* 8.5 (2021), pp. 591–593.
- [Luc+16] Vito Giovanni Lucivero, Ricardo Jiménez-Martínez, Jia Kong, and Morgan W Mitchell. “Squeezed-light spin noise spectroscopy”. In: *Physical Review A* 93.5 (2016), p. 053802.
- [Lvo15] Alexander I Lvovsky. “Squeezed light”. In: *Photonics: Scientific Foundations, Technology and Applications* 1 (2015), pp. 121–163.
- [MYI87] S Machida, Y Yamamoto, and Y Itaya. “Observation of amplitude squeezing in a constant-current-driven semiconductor laser”. In: *Physical review letters* 58.10 (1987), p. 1000.

- [Mad+12] Lars S Madsen, Vladyslav C Usenko, Mikael Lassen, Radim Filip, and Ulrik L Andersen. “Continuous variable quantum key distribution with modulated entangled states”. In: *Nature communications* 3.1 (2012), p. 1083.
- [McC+21] L McCuller et al. “LIGO’s quantum response to squeezed states”. In: *Physical Review D* 104.6 (2021), p. 062006.
- [McK+03] Jason McKeever, Andreea Boca, A David Boozer, Joseph R Buck, and H Jeff Kimble. “Experimental realization of a one-atom laser in the regime of strong coupling”. In: *Nature* 425.6955 (2003), pp. 268–271.
- [McK+22] Timothy P McKenna et al. “Ultra-low-power second-order nonlinear optics on a chip”. In: *Nature Communications* 13.1 (2022), p. 4532.
- [MY20] Jesper Mork and Kresten Yvind. “Squeezing of intensity noise in nanolasers and nanoLEDs with extreme dielectric confinement”. In: *Optica* 7.11 (2020), pp. 1641–1644.
- [OCP18] Stefano Olivares, Simone Cialdi, and Matteo GA Paris. “Homodyning the $g(2)(0)$ of Gaussian states”. In: *Optics Communications* 426 (2018), pp. 547–552.
- [Pet95] Klaus Petermann. “External optical feedback phenomena in semiconductor lasers”. In: *IEEE Journal of Selected Topics in Quantum Electronics* 1.2 (1995), pp. 480–489.
- [Pir+18] Stefano Pirandola, B Roy Bardhan, Tobias Gehring, Christian Weedbrook, and Seth Lloyd. “Advances in photonic quantum sensing”. In: *Nature Photonics* 12.12 (2018), pp. 724–733.
- [RMY91] WH Richardson, S Machida, and Y Yamamoto. “Squeezed photon-number noise and sub-Poissonian electrical partition noise in a semiconductor laser”. In: *Physical review letters* 66.22 (1991), p. 2867.
- [Sca+09] Valerio Scarani, Helle Bechmann-Pasquinucci, Nicolas J Cerf, Miloslav Dušek, Norbert Lütkenhaus, and Momtchil Peev. “The security of practical quantum key distribution”. In: *Reviews of modern physics* 81.3 (2009), p. 1301.

- [Sch+10] Roman Schnabel, Nergis Mavalvala, David E McClelland, and Ping K Lam. “Quantum metrology for gravitational wave astronomy”. In: *Nature communications* 1.1 (2010), p. 121.
- [SM83] R Short and L Mandel. “Observation of sub-Poissonian photon statistics”. In: *Physical review letters* 51.5 (1983), p. 384.
- [Tas+21] Joel F Tasker et al. “Silicon photonics interfaced with integrated electronics for 9 GHz measurement of squeezed light”. In: *Nature Photonics* 15.1 (2021), pp. 11–15.
- [Wan+11] Ke Wang, Ampalavanapillai Nirmalathas, Christina Lim, and Efstratios Skafidas. “Impact of background light induced shot noise in high-speed full-duplex indoor optical wireless communication systems”. In: *Optics express* 19.22 (2011), pp. 21321–21332.
- [Xu+19] Chuan Xu et al. “Sensing and tracking enhanced by quantum squeezing”. In: *Photonics Research* 7.6 (2019), A14–A26.
- [YH86] Y Yamamoto and HA Haus. “Preparation, measurement and information capacity of optical quantum states”. In: *Reviews of Modern Physics* 58.4 (1986), p. 1001.
- [YMN86] Y Yamamoto, S Machida, and O Nilsson. “Amplitude squeezing in a pump-noise-suppressed laser oscillator”. In: *Physical Review A* 34.5 (1986), p. 4025.
- [YMR92] Yoshihisa Yamamoto, Susumu Machida, and Wayne H Richardson. “Photon number squeezed states in semiconductor lasers”. In: *Science* 255.5049 (1992), pp. 1219–1224.
- [Yan+21] Zijiao Yang, Mandana Jahanbozorgi, Dongin Jeong, Shuman Sun, Olivier Pfister, Hansuek Lee, and Xu Yi. “A squeezed quantum microcomb on a chip”. In: *Nature Communications* 12.1 (2021), p. 4781.
- [Yos+13] Jun-ichi Yoshikawa, Kenzo Makino, Shintaro Kurata, Peter van Loock, and Akira Furusawa. “Creation, storage, and on-demand release of optical quantum states with a negative Wigner function”. In: *Physical Review X* 3.4 (2013), p. 041028.

-
- [Zha+20] Yun Zhao, Yoshitomo Okawachi, Jae K Jang, Xingchen Ji, Michal Lipson, and Alexander L Gaeta. “Near-degenerate quadrature-squeezed vacuum generation on a silicon-nitride chip”. In: *Physical Review Letters* 124.19 (2020), p. 193601.
- [Zho+20] Han-Sen Zhong et al. “Quantum computational advantage using photons”. In: *Science* 370.6523 (2020), pp. 1460–1463.
- [Zhu+12] Jun Zhu, Xiaoxiang Chen, Peng Huang, and Guihua Zeng. “Thermal-light-based ranging using second-order coherence”. In: *Applied optics* 51.20 (2012), pp. 4885–4890.

CHAPTER 6

Conclusions and Perspectives

In this thesis, both the classical and quantum properties of QD lasers have been analyzed and investigated.

Firstly, the α_H -factor below and above the threshold current in a multi-mode QD laser has been effectively extracted and analyzed. The commonly used ASE method facilitates the convenient extraction of the α_H -factor below the threshold current. The laser operates practically at a high pump current, and the precise extraction of the α_H -factor above the threshold current contributes to the analysis of parameters such as the linewidth that are related to the α_H -factor. Here, the method of optical phase modulation was employed to extract the α_H -factor above the threshold current for multi-mode operation, demonstrating its dependence on the spectrum and current. Additionally, compared to QW, QD lasers exhibited a lower α_H -factor, aiding in the development of PICs without optical isolators. Additionally, we conducted direct modulation experiments on silicon-based epitaxial QD lasers under various optical feedback conditions. The QD laser achieved a modulation rate of 6 Gbps, and due to its lower α_H -factor, it could withstand strong feedback. The experimental results provide evidence for the high-density integration of silicon-based epitaxial QD lasers in silicon photonics applications.

Secondly, it is because the QD laser possesses a lower α_H -factor that QD lasers under optical feedback cannot generate more nonlinear dynamics. Here, the optoelectronic feedback technique was used for the dynamics generation of silicon-based QD

lasers and the dynamical processes were explored by both experimental and numerical computational methods. The optoelectronic feedback system in which the QD laser is involved exhibited a variety of dynamical states, including steady-state, square-wave, and mixed fast and slow oscillatory waveforms. Interestingly, the sensitivity of QD lasers to OEF is much higher than that of QW lasers and is confirmed by the integral differential delay model and experimental time-domain signals. We believe that this technique can be applied to areas such as integrated optical computing, logic, and sensing.

Furthermore, a comprehensive study of the external carrier noise on the α_H -factor of QD DFB lasers has been conducted through both experimental and simulation approaches. Under quiet pumping conditions, the α_H -factor is significantly smaller than that under normal pump driving, and there is excellent agreement between the semi-classical numerical model and experimental results. Simulation results indicate that using a quiet pump near the threshold current is advantageous for reducing frequency noise, thereby decreasing optical linewidth, but has a minor impact at high currents. Interestingly, the α_H -factor of QW lasers exhibits behavior similar to that of QD lasers. This work, as an early-stage investigation in Chapter 5, demonstrates the noise-suppressing effect of a quiet pump on QD laser's noise.

Finally, based on the noise suppression properties of QD lasers by quiet pump, the QD DFB laser was found to be capable of generating amplitude squeezed states under a quiet pump. Moreover, their quantum noise is remarkably tolerant to optical feedback, especially when compared to QW lasers. In addition, at a high feedback strength of -18.8 dB, the corrected squeezing intensity of the QD laser is as high as 5.0 dB. Furthermore, the study of the $g^{(2)}(0)$ confirms the reliability of the above concepts. The $g^{(2)}(0)$ of the single-mode squeezed state, exhibited the property of being less than 1, and the $g^{(2)}(0)$ of the QD laser decreased gradually with the increase of the feedback strength. In contrast, the $g^{(2)}(0)$ of QW lasers becomes greater than 1 above a feedback strength of -21 dB, indicating that the squeezed state is destroyed. This study establishes a fundamental framework for designing compact and energy-efficient optical quantum integrated circuits.

In the future, the following theoretical and experimental work can be envisioned:

- In the realm of optical computing, the work presented in Chapter 3 paves the way for future reservoir computing experiments utilizing OEF. The incorporation of OEF is poised to significantly enhance the memory and processing capabilities of reservoirs. This is achieved by introducing dynamic, time-delayed feedback into the system, making it exceptionally adept at tasks like pattern recognition and time series prediction. The intricate and rich dynamics afforded by OEF hold the promise of developing more efficient and robust reservoir computing systems. Furthermore, there is potential for pioneering experiments and models of OEF-based coherent Ising machines, aimed at tackling combinatorial optimization problems. The majority of existing literature incorporates MZM in OEF to derive nonlinear transfer equations for coherent Ising machines [BVV19; Mwa+23]. Building upon the insights, there is an opportunity to streamline this approach. The idea is to directly employ the nonlinear transfer equation of the QD laser, serving the same purpose but with a simplified setup architecture. This approach could not only enhance the efficiency of coherent Ising machines but also facilitate their on-chip integration. Such advancements have the potential to revolutionize the way complex computational problems are addressed in critical fields like cryptography, logistics, and machine learning.
- I intend to use the Wigner function to reconstruct and analyze a single-mode squeezed state. The Wigner function provides a complete quantum mechanical description of the squeezed state and visualization of the statistical distribution as shown in Fig.6.1 [Smi+93]. The Wigner function of a squeezed state shows how the uncertainty of a variable is reduced, which manifests itself as an ellipse that is narrower in one dimension than the other. On this ground, it becomes of great interest to study how optical feedback affects the elliptic Wigner function.
- I plan to investigate integrated squeezed state generators based on QD lasers. The unique properties of the QD lasers discussed in this thesis, such as low threshold current, optical feedback insensitivity, etc. make them ideal candidates for such integrated quantum photonic devices. Efficient intensity squeezed states can be generated using the QD laser and simple pump carrier noise modulation. The design and fabrication of on-chip compact and efficient nonclassical opti-

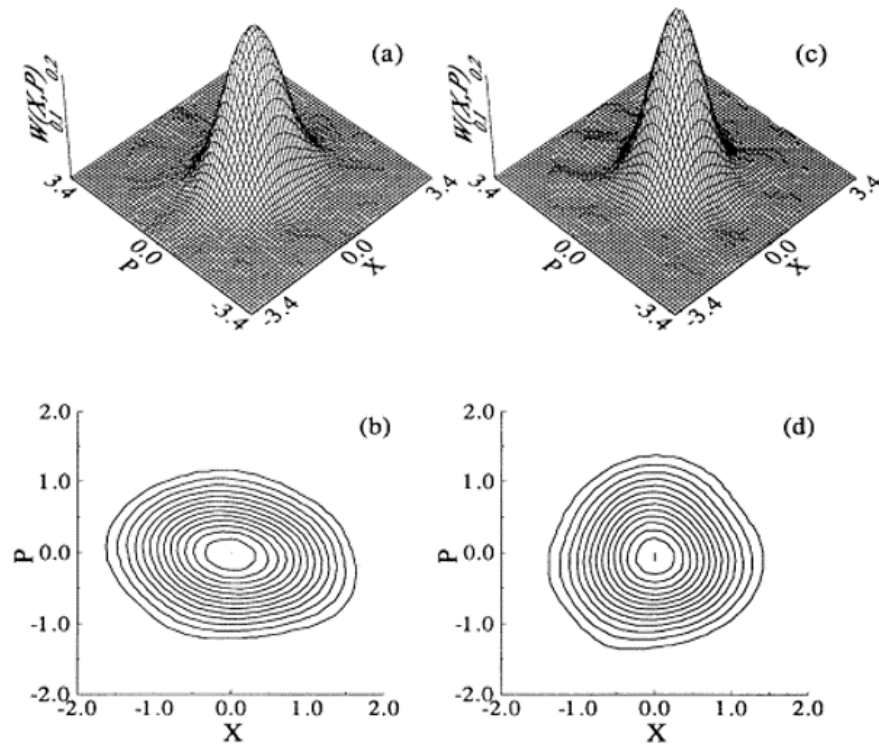


Figure 6.1: The Wigner function for (a), (b) the squeezed state and (c),(d) the vacuum state. [Smi+93]

cal generators based on QD lasers and quiet pumps can greatly reduce the loss and predictably increase the squeezing intensity. This is crucial for quantum computing, secure quantum communication, and quantum sensing.

- Mid-infrared wavelengths are typically subject to less atmospheric absorption, enhancing the reliability of long-distance free-space transmissions. Quantum cascade laser (QCL) and interband cascade laser (ICL) are well known for their ability to operate in the mid-infrared wavelengths, which is critical for overcoming environmental challenges in communications [Did+22; Did+23]. Then, if a QCL or ICL is used as an amplitude squeezed state generator, a free-space continuous-variable quantum key distribution system can be realized. Generating amplitude squeezed states under a quiet pump using QCL or ICL is part of my future work.

Bibliography

- [BVV19] Fabian Böhm, Guy Verschaffelt, and Guy Van der Sande. “A poor man’s coherent Ising machine based on opto-electronic feedback systems for solving optimization problems”. In: *Nature communications* 10.1 (2019), p. 3538.
- [Did+22] Pierre Didier et al. “High-capacity free-space optical link in the midinfrared thermal atmospheric windows using unipolar quantum devices”. In: *Advanced Photonics* 4.5 (2022), pp. 056004–056004.
- [Did+23] Pierre Didier et al. “Interband cascade technology for energy-efficient mid-infrared free-space communication”. In: *Photonics Research* 11.4 (2023), pp. 582–590.
- [Mwa+23] Nickson Mwamsojo, Frederic Lehmann, Kamel Merghem, Badr-Eddine Benkelfat, and Yann Frignac. “Optoelectronic coherent Ising machine for combinatorial optimization problems”. In: *Optics Letters* 48.8 (2023), pp. 2150–2153.
- [Smi+93] DT Smithey, M Beck, Michael G Raymer, and A Faridani. “Measurement of the Wigner distribution and the density matrix of a light mode using optical homodyne tomography: Application to squeezed states and the vacuum”. In: *Physical Review Letters* 70.9 (1993), p. 1244.

Appendix A: Publications

Journal papers

1. S. Ding, S. Zhao, H. Huang, and F. Grillot (2023). Impact of external carrier noise on the linewidth enhancement factor of a quantum dot distributed feedback laser. *Optics Express*, 31(21), 35343-35353.
2. S. Ding, B. Dong, H. Huang, J. Bowers, and F. Grillot (2022). Reflection sensitivity of InAs/GaAs epitaxial quantum dot lasers under direct modulation. *Electronics Letters*, 58(9), 363-365.
3. S. Ding, B. Dong, H. Huang, J. Bowers, and F. Grillot (2022). Spectral dispersion of the linewidth enhancement factor and four wave mixing conversion efficiency of an InAs/GaAs multimode quantum dot laser. *Applied Physics Letters*, 120(8).
4. S. Ding, S. Zhao, J. Norman, B. Dong, H. Huang, J. Bowers, and F. Grillot (2023). Unveiling the dynamical diversity of quantum dot lasers subject to optoelectronic feedback. arXiv preprint arXiv:2309.14056.
5. S. Ding, S. Zhao, H. Huang, and F. Grillot (2024). Reflection insensitive amplitude squeezed states generator based on quantum dot laser technology. (Under Review)
6. Z. Jin, H. Huang, Y. Zhou, S. Zhao, S. Ding, C. Wang, Y. Yong, X. Xu, F. Grillot, and J. Duan (2023). Reflection sensitivity of dual-state quantum dot lasers. *Photonics Research*, 11(10): 1713-1722.
7. J. Duan, B. Dong, W. Chow, H. Huang, S. Ding, S. Liu, and F. Grillot (2022). Four-wave mixing in 1.3 μm epitaxial quantum dot lasers directly grown on silicon. *Photonics Research*, 10(5), 1264-1270
8. F. Grillot, W. Chow, B. Dong, S. Ding, H. Huang, and J. Bowers (2022). Multi-mode physics in the mode locking of semiconductor quantum dot lasers. *Applied*

Sciences, 12(7), 3504.

Conference papers

1. S. Ding, S. Zhao, and F. Grillot (2023). "Multi-dynamics in silicon-based quantum dot laser through optoelectronic feedback technique" LaserPhysics (Oral Presentation), Virtual Event.
2. S. Ding, N. Doggett, D. J. Herrera, H. Huang, V. Kovanis, L. F. Lester, and F. Grillot (2023). "Full parameter extraction of a temperature-insensitive quantum well DFB laser using an optical injection technique" Physics and Simulation of Optoelectronic Devices XXXI of SPIE Photonics West (Oral Presentation), San Francisco, USA.
3. S. Ding, N. Doggett, D. J. Herrera, H. Huang, V. Kovanis, L. F. Lester, and F. Grillot (2022). "Investigation of temperature-insensitive quantum well DFB lasers using optical injection locking technique" European Semiconductor Laser Workshop (Oral Presentation), Neuchâtel, Switzerland.
4. S. Ding, B. Dong, W. Chow, J. Bowers, and F. Grillot (2022). "Enhanced four-wave mixing dynamics in epitaxial quantum dot laser on silicon" Advanced Photonics Congress, OPTICA (Oral Presentation), Maastricht, Netherlands.
5. S. Ding, B. Dong, H. Huang, J. Bowers, and F. Grillot (2022). "High reflection tolerance of silicon-based epitaxial quantum dot lasers by direct modulation" Semiconductor and Integrated OptoElectronics (Oral Presentation), Cardiff, UK.
6. S. Ding, B. Dong, and F. Grillot (2022). "Temperature and feedback insensitive 1.3- μm InAs/GaAs quantum dot lasers subject to pulse amplitude modulation" Nano, méso, micro: sciences et innovations pour la radio et la photonique, URSI-France (Oral Presentation), Palaiseau, France.
7. S. Ding, B. Dong, H. Huang, J. Bowers, and F. Grillot (2021). "The above-threshold linewidth enhancement factor of silicon-based quantum dot lasers"

- IEEE 17th International Conference on Group IV Photonics (Oral Presentation), Virtual Event.
8. S. Ding, B. Dong, H. Huang, J. Bowers, and F. Grillot (2021). "Linewidth enhancement factor measurement by using phase modulation method for epitaxial quantum dot laser on silicon" Semiconductor and Integrated OptoElectronics (Oral Presentation), Virtual Event.
 9. D. Cui, S. Ding, F. Grillot, H. Huang, and A. Bousseskou (2023). "Static and nonlinear properties of a hybrid plasmonic distributed feedback laser" International Symposium on Physics and Applications of Laser Dynamics, Metz, France.
 10. S. Zhao, S. Ding, H. Huang, I. Zaquine, N. Belabas, and F. Grillot, (2023). "Generation of non-classical light using semiconductor quantum dot lasers" IEEE Photonics Society Summer Topicals Meeting Series, Sicily, Italy.
 11. D. Cui, J. Chen, H. Huang, S. Ding, D. Costantini, R. Colombelli, A. Bousseskou, and F. Grillot, (2022). "Intensity noise and nonlinear properties of a hybrid plasmonic distributed feedback laser" IEEE Photonics Conference, Vancouver, Canada.
 12. F. Grillot, G. Callado, S. Ding, T. Verolet, J. Decobert, C. Jany, K. Hassan, S. Malhouitre, D. Make, A. Coquiard, S. Combri , A. Shen, and A. Rossi (2022). "80 GHz compact photonic microwave generation from a solitary distributed feedback laser on silicon" 28th International Semiconductor Laser Conference, Matsue, Japan.
 13. D. Cui, J. Chen, H. Huang, S. Ding, D. Costantini, R. Colombelli, A. Bousseskou, and F. Grillot (2022). "80 GHz compact photonic microwave generation from a solitary distributed feedback laser on silicon" 28th International Semiconductor Laser Conference, Matsue, Japan.

Appendix B: Résumé de thèse en français

Cette section démontre que le facteur d'amplification de largeur de raie des lasers à points quantiques est influencé par le transport externe des porteurs provenant de différentes sources de courant externes. Un modèle combinant l'équation de taux et le bruit de porteurs semi-classique est utilisé pour étudier les différents mécanismes conduisant au phénomène susmentionné dans le contexte d'un laser à rétroaction distribuée à points quantiques. Parallèlement, le facteur d'amplification de largeur de raie extrait de la méthode de modulation de phase optique montre des différences marquées lorsque le laser à points quantiques est alimenté par des pompes de différents niveaux de bruit. De plus, l'influence du bruit de porteurs externe sur le bruit de fréquence à proximité du courant de seuil du laser affecte directement l'ampleur du facteur d'amplification de la largeur de raie. Les simulations examinent également comment le transport externe des porteurs impacte le bruit de fréquence et la largeur de raie spectrale du laser à points quantiques. Dans l'ensemble, nous pensons que ces résultats revêtent une importance primordiale pour le développement d'oscillateurs ultra-basse bruit intégrés sur puce produisant de la lumière au niveau du bruit de photon ou en dessous.

• Introduction

Au cours de la dernière décennie, le trafic Internet mondial a connu une croissance exponentielle avec la multiplication des utilisateurs finaux. Les centres de données hyperscale sont largement déployés en tant que piliers de l'infrastructure de télécommunications, soutenant à la fois les usages individuels et commerciaux, d'où l'importance des émetteurs-récepteurs optiques dans la chaîne de communication. À ce stade, le bruit de phase est crucial pour le débit à haut débit. La source lumineuse la plus couramment utilisée dans les émetteurs-récepteurs optiques est le laser à puits quantique (QW), et ces dispositifs ne sont pas réputés pour être des oscillateurs à faible bruit de phase, présentant souvent une largeur de ligne optique typique de l'ordre de quelques MHz, ce qui ne peut pas être directement exploité pour l'application des systèmes de multiplexage en longueur d'onde dense (DWDM). D'autre part, une largeur de

ligne optique intrinsèque inférieure à 100 kHz a été largement rapportée dans les diodes laser fabriquées avec un matériau actif de points quantiques (QD). En effet, grâce à leur confinement tridimensionnel des porteurs et à la distribution discrète de la densité des états, les lasers à points quantiques présentent des largeurs de ligne optique d'environ un ordre de grandeur inférieur à celles de leurs homologues à puits quantique, ce qui est souhaitable pour des applications nécessitant des formats de modulation avancés, ainsi que pour le développement de nouveaux émetteurs-récepteurs basés sur la technologie à sous-porteuses, par exemple. De plus, les lasers à points quantiques sont compatibles à la fois avec l'intégration hybride et épitaxiale sur silicium et présentent une faible densité de courant de seuil, une grande stabilité thermique et une excellente tolérance au rétroéclairage optique, ce qui en fait des candidats idéaux pour les sources lumineuses sur puce et les liaisons optiques à courte portée. Ces dernières années, les lasers à points quantiques ont été à plusieurs reprises rapportés comme étant des sources lumineuses compétentes pour les circuits intégrés photoniques (CIP) basés sur le silicium, conçus non seulement pour les émetteurs-récepteurs optiques, mais aussi pour d'autres applications avancées où le faible bruit de la source laser est impératif, comme dans les gyroscopes à échelle de puce et la cryptographie quantique, pour n'en citer que quelques-unes. Dans le domaine des télécommunications, alors que le trafic de données continue d'augmenter, il est nécessaire de faire évoluer la capacité de transmission, et donc l'utilisation d'oscillateurs locaux à faible coût de quelques kHz et sous-kHz est nécessaire pour exploiter le débit de données accessible de 800 GBaud. Pour un gyroscope intégré, afin de réaliser des dispositifs de mesure rotationnelle les plus précis possible, la source lumineuse doit avoir un faible bruit pour améliorer la précision de mesure dans différentes situations. De plus, les lasers à points quantiques ont le potentiel de réaliser une distribution quantique de clés (QKD) sur puce. Enfin, en exploitant les propriétés non linéaires des lasers à points quantiques, l'amplitude des quadratures des lasers à points quantiques peut également être réduite en dessous de la limite quantique standard (SQL) pour obtenir un écrasement du bruit d'amplitude. Sur ces fronts, il est nécessaire de supprimer davantage le niveau de bruit dans les lasers à points quantiques pour fournir des options sur puce simples et peu coûteuses.

Dans ce contexte, le facteur α_H est le paramètre clé à considérer, car il quantifie le couplage de fluctuation d'amplitude-phase des lasers à semiconducteurs sous injections

de courant, et est connu comme un aspect prépondérant non seulement des effets d'amplification de la largeur de ligne mais aussi de nombreux autres aspects du laser tels que le bruit, la modulation et les propriétés de dynamique non linéaire. Dans le cadre du développement d'oscillateurs à ligne étroite ultra, il est pertinent d'étudier comment le facteur α_H et par conséquent le bruit de fréquence sont affectés par les conditions de pompage, notamment par le transport des porteurs à travers la jonction. Le facteur α_H est conventionnellement exprimé par le rapport entre les variations de l'indice de réfraction et du gain optique par rapport à la densité de porteurs, ce qui constitue une base fondamentale pour les performances en matière de bruit. Il a été démontré que le facteur α_H peut être largement réduit en utilisant des matériaux actifs de points quantiques grâce à la quantification d'énergie et au confinement de la fonction d'onde dans le potentiel hétérostructure dans les trois dimensions spatiales. L'utilisation de nanostructures de dimension zéro comme milieux actifs a prouvé leurs capacités à atteindre des oscillateurs à faible intensité et à faible bruit de phase. Étant donné cela, il est important de mieux comprendre le rôle du bruit de porteurs généré à partir de la source de courant pour fournir un moyen supplémentaire de minimiser davantage le facteur α_H . Typiquement, une source de courant à faible bruit (c'est-à-dire une pompe silencieuse) est généralement requise pour réduire l'impact du bruit électrique externe lors de l'étude des propriétés de bruit d'un laser à semiconducteurs.

- Théorie et modèle numérique

La Fig. 6.2 montre deux pompes de courant pour le laser à points quantiques : (a) pompe normale et (b) pompe silencieuse. L'effet de la pompe sur le laser est décrit avec un circuit équivalent, où R_d est la résistance différentielle de la jonction du laser, L est l'inductance parasite, et C est la capacité parasite. La résistance différentielle émule l'amortissement résultant des termes de recombinaison spontanée et stimulée dans l'équation de taux. L'inductance représente la longueur d'onde de résonance du laser. La capacité contient la capacité de diffusion de la couche active et la capacité de charge d'espace du laser. La pompe normale peut être réalisée pratiquement lorsque la résistance différentielle de la jonction du laser $R_d = (dI/dV)^{-1}$ est beaucoup plus grande que la résistance interne R_s de la pompe, tandis que la pompe silencieuse est

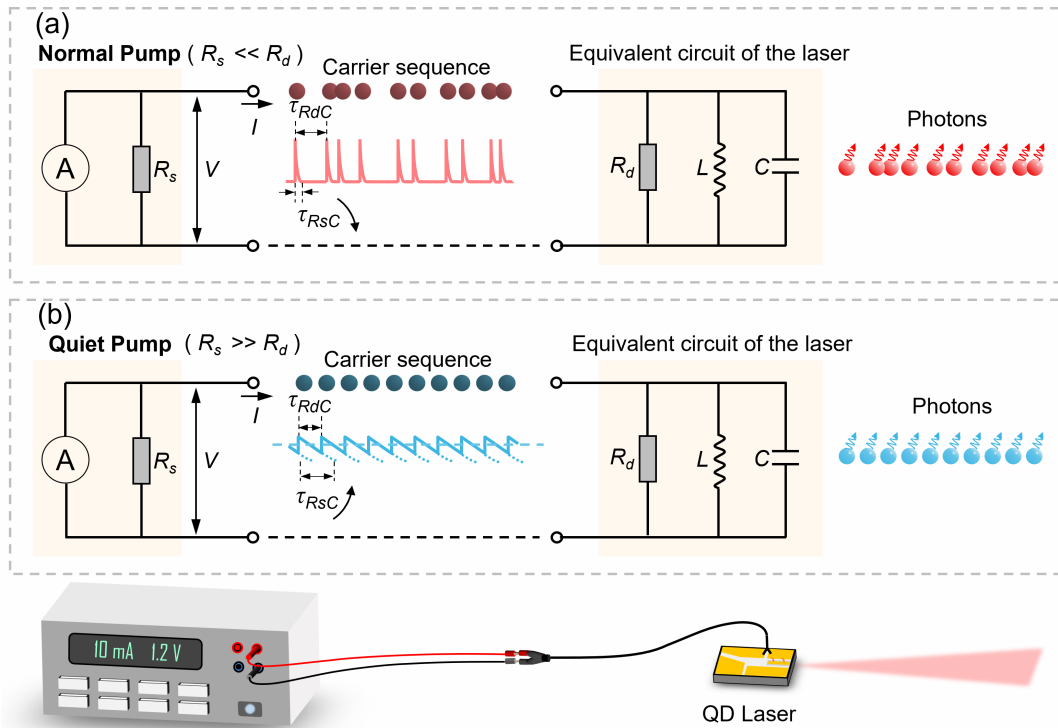


Figure 6.2: Diagramme schématique du modèle théorique illustrant la relation entre les porteurs injectés et les photons dans un laser à semiconducteurs alimenté par (a) une pompe normale et (b) une pompe silencieuse.

obtenue dans la limite opposée. Il convient de souligner que le bruit de courant dans les lasers à semiconducteurs est une combinaison de bruit de diffusion thermique et de bruit de génération-recombinaison concernant les porteurs minoritaires. Ces événements de bruit surviennent séquentiellement et provoquent le départ de la densité de porteurs minoritaires de l'équilibre. Ensuite, le circuit externe restaurerait la distribution stationnaire des porteurs minoritaires et régulerait leur injection dans la région active via le processus de relaxation. Par exemple, lorsque l'on a la pompe normale avec une résistance de source infinitésimale R_s , ce processus de relaxation serait complété avec un temps de retard négligeable $\tau_{R_s C} = R_s C$. Par conséquent, le laser ne mémorise pas l'événement précédent et donc chaque événement se produit indépendamment du point de vue statistique, ce qui est exactement l'origine physique de la distribution de bruit complet ou de photons de Poisson comme le montre la Fig. 6.2(a). Au contraire,

si l'on a une pompe silencieuse avec une résistance de source considérable R_s , la modulation des porteurs minoritaires ne peut pas être éliminée instantanément par le circuit externe en raison d'un grand délai $\tau_{R_s C}$. Par conséquent, la tension de jonction est autorisée à fluctuer par le transit diffusif thermique et les événements de génération-recombinaison comme le montre la Fig. 6.2(b). Dans ce contexte, si les événements de recombinaison dépassent la valeur moyenne, la tension de jonction diminue en raison du transit diffusif thermique excessif. Cependant, comme cette diminution de la tension de jonction n'est pas récupérée à temps, le taux de transit diffusif thermique diminue temporairement, ce qui se traduit par moins d'événements de recombinaison. Cette séquence fonctionne comme un mécanisme d'auto-rétroaction de stabilisation pour réguler le processus de pompage, ce qui peut potentiellement avoir un impact significatif sur le facteur α_H et le spectre de bruit. Les deux pompes ont été mesurées expérimentalement pour présenter des caractéristiques de bruit différentes comme le montre la Fig. 6.3.

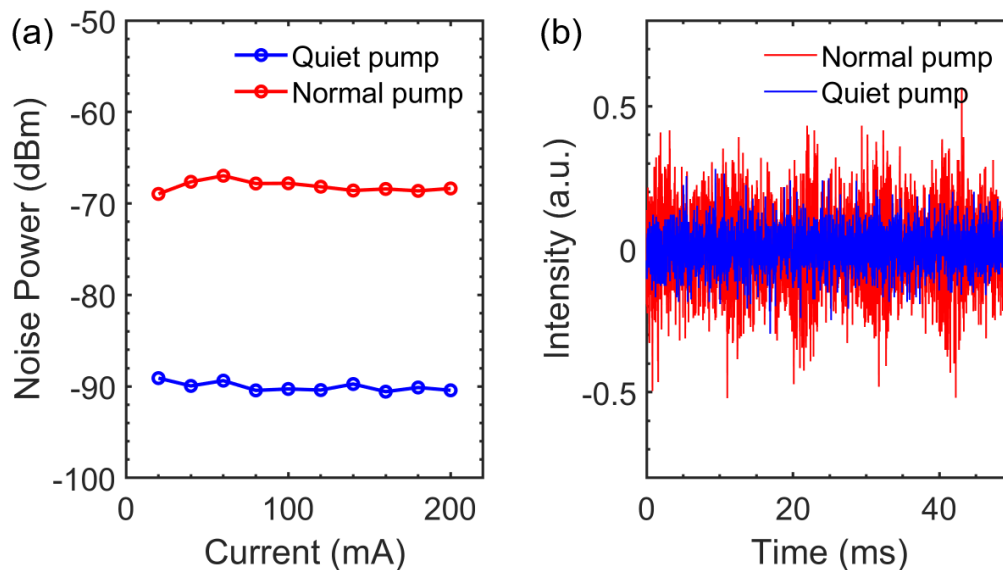


Figure 6.3: (a) La puissance de bruit et (b) la fluctuation de bruit des pompes normales et silencieuses.

Pour comparer le bruit de courant des différentes pompes, j'ai fait passer le courant d'entraînement de la pompe à travers une résistance de 10Ω . Le bruit de courant a été

mesuré en couplant la fluctuation de tension sur la résistance à travers un condensateur de 10 nF à un amplificateur à faible bruit avec une impédance d'entrée de 50 Ω . Nous avons choisi cette résistance et ce condensateur pour correspondre étroitement à la valeur de la résistance du laser, dans le but de capturer la fluctuation de bruit de la source de courant près de la charge du laser. Le signal amplifié a ensuite été analysé à l'aide d'un analyseur de spectre électrique et d'un oscilloscope. Nous avons comparé les caractéristiques de bruit des pompes normales et silencieuses. Les points de bruit dans la Fig. 6.3(a) sont extraits du bruit à 50 MHz du spectre électrique. Le bruit est stable à différents courants des deux pompes. Nous avons donc mesuré la fluctuation de bruit à 100 mA. Le spectre électrique et les fluctuations dans le domaine temporel démontrent tous deux la fiabilité de nos expériences comparatives.

- Simulation numérique et analyse expérimentale

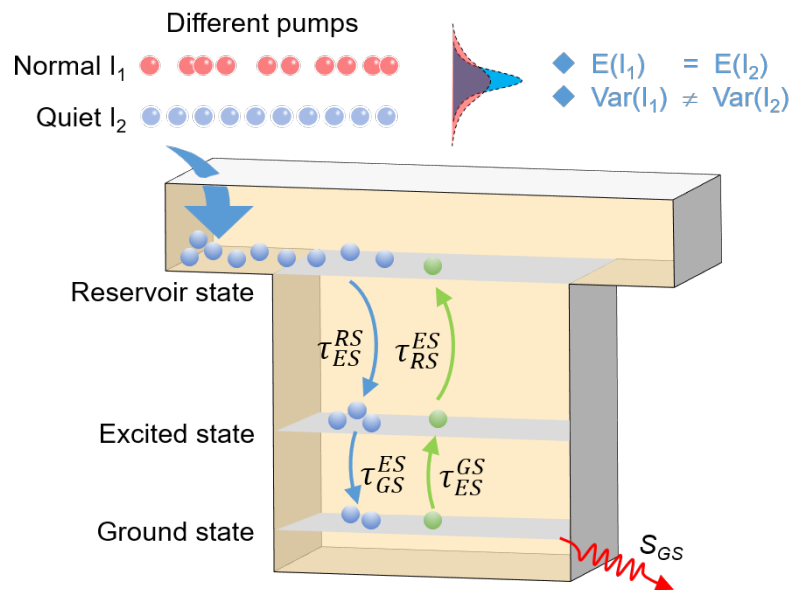


Figure 6.4: Représentation schématique de la structure électronique et de la dynamique des porteurs dans un QD pour des conditions de pompage normales et des conditions de pompage silencieuses. Les deux sources de courant sont distinguées par le fait que les courants sont censés être égaux et que la pompe silencieuse a une petite variance de courant.

Une pompe silencieuse avec une distribution de porteurs sub-poissonnienne et une pompe normale avec une distribution de porteurs gaussienne peuvent être bien décrites en utilisant un modèle stochastique. Cependant, dans ce type de représentation, l'inclusion du terme de phase influençant le facteur α_H est plutôt compliquée. Au lieu de cela, le bruit de fréquence et le facteur α_H d'un laser à points quantiques peuvent être mieux modélisés avec une approche d'équation de taux. Ici, nous incorporons dans ces équations de taux les différentes contributions au bruit en tenant compte des différentes sources de courant. Comme le montre la Fig. 6.4, la dynamique des porteurs de QD est décrite en considérant un système à trois niveaux d'énergie. Le modèle suppose une émission monomode qui correspond exactement à la configuration réalisée avec le laser à DFB QD étudié. De plus, il est supposé que la région active ne contient qu'un seul ensemble de QD, où les nanostructures sont interconnectées par un état de réservoir bidimensionnel (RS). Le QD contient deux états liés : un état fondamental dégénéré deux fois (GS) et un état excité dégénéré quatre fois (ES). Les QD sont implicitement supposés être toujours neutres, les électrons et les trous sont traités comme des paires électron-trou, ce qui signifie que le système est uniquement composé d'états d'énergie excitonique. Les porteurs sont supposés être injectés directement des contacts dans les niveaux RS. Lorsque différentes pompes définissent le même courant, on peut supposer que la valeur attendue du courant est la même, mais la variance est différente. Les différentes variances représentent différents niveaux de bruit. Les équations de taux couplées sur la dynamique des porteurs, de la phase et des photons se lisent comme suit:

$$\frac{dN_{RS}}{dt} = \frac{\eta I}{q} + \frac{N_{ES}}{\tau_{RS}^{ES}} - \frac{N_{RS}}{\tau_{ES}^{RS}}(1 - \rho_{ES}) - \frac{N_{RS}}{\tau_{RS}^{spon}} + F_{RS} \quad (6.1)$$

$$\frac{dN_{ES}}{dt} = \left(\frac{N_{RS}}{\tau_{ES}^{RS}} + \frac{N_{GS}}{\tau_{ES}^{GS}}\right)(1 - \rho_{ES}) - \frac{N_{ES}}{\tau_{GS}^{ES}}(1 - \rho_{GS}) - \frac{N_{ES}}{\tau_{RS}^{ES}} - \frac{N_{ES}}{\tau_{ES}^{spon}} + F_{ES} \quad (6.2)$$

$$\frac{dN_{GS}}{dt} = \frac{N_{ES}}{\tau_{GS}^{ES}}(1 - \rho_{GS}) - \frac{N_{GS}}{\tau_{ES}^{GS}}(1 - \rho_{ES}) - \Gamma_p \nu_g g_{GS} S_{GS} - \frac{N_{GS}}{\tau_{GS}^{spon}} + F_{GS} \quad (6.3)$$

$$\frac{dS_{GS}}{dt} = \left(\Gamma_p \nu_g g_{GS} - \frac{1}{\tau_p}\right) S_{GS} - \beta_{SP} \frac{N_{GS}}{\tau_{GS}^{spon}} + F_S \quad (6.4)$$

$$\frac{d\phi}{dt} = \Delta\omega_N^{GS} + \Delta\omega_N^{ES} + \Delta\omega_N^{RS} + F_\phi \quad (6.5)$$

où les nombres de porteurs dans les niveaux d'énergie GS, ES et RS sont désignés respectivement par N_{RS} , N_{ES} et N_{GS} tandis que S_{GS} est le nombre de photons dans le niveau GS et ϕ représente la phase du champ électrique. La dynamique des porteurs est brièvement décrite comme suit. Tout d'abord, les porteurs sont capturés du RS vers l'ES avec un temps de capture τ_{ES}^{RS} puis ils se relaxent de l'ES vers le niveau GS avec un temps de relaxation τ_{GS}^{ES} . Les porteurs peuvent également être réémis thermiquement de l'ES vers le RS avec un temps d'échappement τ_{RS}^{ES} . Un comportement dynamique similaire est suivi pour la population de porteurs au niveau GS concernant l'ES. De plus, les porteurs peuvent également se recombiner spontanément avec des temps d'émission spontanée τ_{RS}^{spon} , τ_{ES}^{spon} et τ_{GS}^{spon} aux niveaux RS, ES et GS, respectivement. Comme indiqué dans l'équation 6.2, le terme de pompage $\eta I/q$ intègre l'efficacité d'injection η et q la charge élémentaire. Enfin, il convient de souligner que ρ_{ES} , ρ_{GS} correspondent aux probabilités d'occupation des porteurs dans les niveaux ES et GS tandis que β_{sp} est la fraction de l'émission spontanée couplée dans le mode de laser, Γ_p est le facteur de confinement optique, ν_g est la vitesse de groupe et $\Delta\omega_N^{RS,ES,GS}$ représente le décalage de fréquence du champ laser induit par les porteurs par rapport à la fréquence. $F_{RS,ES,GS,S,\phi}$ sont les termes de bruit de Langevin. Les paramètres du modèle d'équation de taux à trois niveaux d'énergie sont présentés dans le Tableau 6.1. L'énergie de transition GS (0,95 eV) correspond à la longueur d'onde du laser à QD utilisée dans l'expérience. Les autres paramètres sont référencés dans la littérature sur

les lasers DFB à QD de longueur d'onde 1310 nm.

Les caractéristiques du laser à points quantiques sont étudiées par analyse du petit signal. En utilisant l'approche de Langevin, nous étudions les caractéristiques du bruit de fréquence, où les différents bruits de porteurs imposés par différentes sources de courant seront reflétés. Nous introduisons $F_{RS}(t)$, $F_{ES}(t)$, $F_{GS}(t)$, $F_S(t)$ et $F_\phi(t)$ comme termes de bruit de Langevin dans les équations de taux de porteurs, de photons et de phase. De plus, la force de corrélation des sources de bruit est $\langle F_i(t) F_j(t) \rangle = 2D_{i-j}\delta(t - t')$, où les indices i, j se réfèrent à N_{RS} , N_{ES} , N_{GS} , S et Φ où D_{i-j} est le coefficient de diffusion entre deux sources de bruit qui sont delta corrélées. La Fig. 6.5 explique brièvement le modèle de réservoir pour caractériser les performances de bruit du laser. Ici, les forces de corrélation des différentes sources de bruit de Langevin peuvent être déterminées en observant les taux d'entrée et de sortie dans les différents réservoirs. Le bruit lié au courant entre dans le système par D_{R-R} , d'où l'inclusion du terme de courant dans D_{R-R} . Les porteurs pompés sont injectés dans la structure laser ($\eta I/q$). Nous avons considéré les fluctuations de bruit de porteurs sur des échelles de temps sub-nanosecondes car le bruit de porteurs reste discernable à des fréquences supérieures au GHz. À ce stade, l'échelle de temps du bruit de porteurs coïncide avec les durées de vie des porteurs (ns) et les durées de vie des photons (ps) d'à peu près un ordre de grandeur, de sorte que le coefficient de diffusion entre les deux sources de bruit est corrélé par delta. Ensuite, certains porteurs participent à l'émission spontanée, et d'autres vont au niveau d'énergie ES et participent aux processus dynamiques ultérieurs. Après le processus d'émission spontanée et stimulée de ES, certains des porteurs atteignent le niveau d'énergie GS. Enfin, soulignons que le laser à QD étudié n'émet que sur la transition GS, donc l'émission stimulée dans ES n'est pas considérée.

Après l'analyse des flux de particules entrant/sortant des différents réservoirs selon la méthode décrite dans, les coefficients de diffusion peuvent être dérivés comme suit. Il s'agit là de l'aspect critique permettant de distinguer les différents bruits de porteurs issus de différentes sources.

Symbol	Physical description	Value
E_{RS}	RS transition energy	1.15 eV
E_{ES}	ES transition energy	1.01 eV
E_{GS}	GS transition energy	0.95 eV
τ_{ES}^{RS}	RS to ES capture time	1.3 ps
τ_{GS}^{ES}	ES to GS relaxation time	1.2 ps
τ_{ES}^{GS}	GS to ES escape time	0.12 ns
τ_{RS}^{ES}	ES to RS escape time	5.35 ns
τ_{RS}^{spon}	RS spontaneous emission time	0.5 ns
τ_{ES}^{spon}	ES spontaneous emission time	0.5 ns
τ_{GS}^{spon}	GS spontaneous emission time	1.2 ns
τ_p	Photon lifetime	8.1 ps
β_{sp}	Spontaneous emission factor	1×10^{-4}
a_{RS}	RS Differential gain	$2.5 \times 10^{-15} \text{ cm}^2$
a_{ES}	ES Differential gain	$1.0 \times 10^{-14} \text{ cm}^2$
a_{GS}	GS Differential gain	$5.0 \times 10^{-15} \text{ cm}^2$
ζ	Gain compression factor	$2.0 \times 10^{-16} \text{ cm}^3$
Γ_p	Optical confinement factor	0.06
α_{GS}	GS contribution to α_H -factor	1.50
N_B	Total dot number	4.3×10^6
V_B	Active region volume	$3.75 \times 10^{-11} \text{ cm}^3$
V_{RS}	RS region volume	$3.0 \times 10^{-12} \text{ cm}^3$

Table 6.1: Paramètres matériels et optiques du laser à points quantiques InAs/GaAs

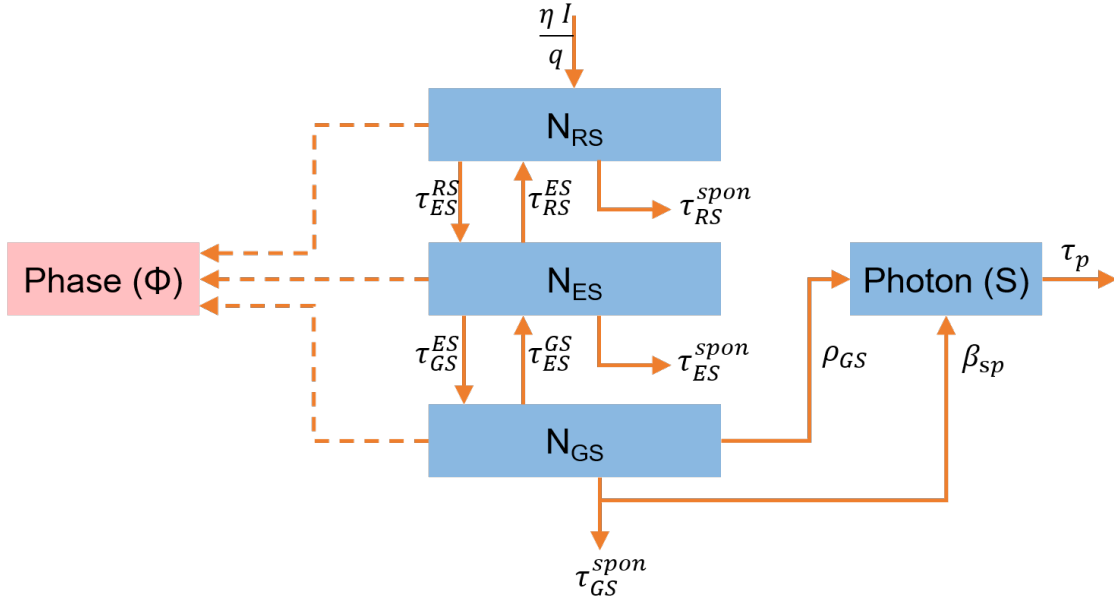


Figure 6.5: Modèle de réservoir utilisé dans l'analyse des équations de taux du laser à points quantiques. Chaque flèche pleine dans le diagramme de flux représente le nombre de particules qui circulent par unité de temps. Les lignes en pointillés représentent la relation avec la phase.

$$D_{R-R} = \frac{\eta I}{q} + \frac{N_{ES}}{\tau_{RS}^{ES}} + \frac{N_{RS}}{\tau_{ES}^{RS}}(1 - \rho_{ES}) + \frac{N_{RS}}{\tau_{RS}^{spon}} \quad (6.6)$$

$$D_{E-E} = \left(\frac{N_{RS}}{\tau_{ES}^{RS}} + \frac{N_{GS}}{\tau_{ES}^{GS}} \right) (1 - \rho_{ES}) + \frac{N_{ES}}{\tau_{GS}^{ES}} (1 - \rho_{GS}) + \frac{N_{ES}}{\tau_{RS}^{ES}} + \frac{N_{ES}}{\tau_{ES}^{spon}} \quad (6.7)$$

$$D_{G-G} = \frac{N_{ES}}{\tau_{GS}^{ES}} (1 - \rho_{GS}) + \frac{N_{GS}}{\tau_{ES}^{GS}} (1 - \rho_{ES}) + \Gamma_p \nu_g g_{GS} S_{GS} + \frac{N_{GS}}{\tau_{GS}^{spon}} \quad (6.8)$$

$$D_{S-S} = \left(\Gamma_p \nu_g g_{GS} - \frac{1}{\tau_p} \right) S_{GS} + \beta_{SP} \frac{N_{GS}}{\tau_{GS}^{spon}} \quad (6.9)$$

$$D_{\phi-\phi} = \Delta\omega_N^{GS} + \Delta\omega_N^{ES} + \Delta\omega_N^{RS} \quad (6.10)$$

$$D_{R-E} = - \left[\frac{N_{RS}}{\tau_{ES}^{RS}} (1 - \rho_{ES}) + \frac{N_{ES}}{\tau_{RS}^{ES}} \right] \quad (6.11)$$

$$D_{E-G} = - \left[\frac{N_{GS}}{\tau_{ES}^{GS}} (1 - \rho_{ES}) + \frac{N_{ES}}{\tau_{GS}^{ES}} (1 - \rho_{GS}) \right] \quad (6.12)$$

$$D_{G-S} = - \left[\beta_{SP} \frac{N_{GS}}{\tau_{GS}^{spon}} + \Gamma_p \nu_g g_{GS} S_{GS} \right] \quad (6.13)$$

$$D_{R-G} = D_{R-S} = D_{R-\phi} = D_{E-S} = D_{E-\phi} = D_{G-\phi} = D_{S-\phi} = 0 \quad (6.14)$$

Suivant la règle de Cramer et les coefficients de diffusion ci-dessus, le bruit de fréquence (FN) du laser à points quantiques peut être dérivé comme suit.

$$FN(\omega) = \langle |\delta\omega_S(\omega)|^2 \rangle = \left\langle \left| j\omega \frac{\Delta_\phi}{\Delta} \right|^2 \right\rangle \quad (6.15)$$

où $\omega = 2\pi f$, et f est la fréquence optique mesurée. Δ est le déterminant obtenu à partir du système. Puisque certaines forces de corrélation sont nulles, le $FN(\omega)$ peut être simplifié comme suit:

$$\begin{aligned} FN(\omega) &= \left\langle \frac{\omega^2}{|\Delta|^2} |D_R M_{R-\phi} - D_E M_{E-\phi} + D_G M_{G-\phi} - D_S M_{S-\phi} + D_\phi M_{\phi-\phi}|^2 \right\rangle \\ &= \frac{\omega^2}{|\Delta|^2} \left\{ \langle |D_{R-R}|^2 \rangle |M_{R-\phi}|^2 + \langle |D_{E-E}|^2 \rangle |M_{E-\phi}|^2 + \langle |D_{G-G}|^2 \rangle |M_{G-\phi}|^2 \right. \\ &\quad + \langle |D_{S-S}|^2 \rangle |M_{S-\phi}|^2 + \langle |D_{\phi-\phi}|^2 \rangle |M_{\phi-\phi}|^2 - 2 \langle D_{R-E} D_{R-E}^* \rangle \text{Re} (M_{R-\phi} M_{R-\phi}^*) \\ &\quad \left. - 2 \langle D_{E-G} D_{E-G}^* \rangle \text{Re} (M_{E-\phi} M_{G-\phi}^*) - 2 \langle D_{G-S} D_{G-S}^* \rangle \text{Re} (M_{G-\phi} M_{S-\phi}^*) \right\} \quad (6.16) \end{aligned}$$

• Comparaison des résultats numériques et expérimentaux

Le coefficient de diffusion D_{R-R} constitue notre paramètre clé pour corrélérer le bruit de fréquence et le bruit provenant de la source de courant. Lorsque l'on utilise une pompe normale pour entraîner le laser, nous considérons que le terme de bruit de courant $\eta I/q$ affecte le laser à points quantiques à travers l'état de réservoir dans le milieu actif. Lorsque la pompe silencieuse est prise en compte, nous pouvons retirer le $\eta I/q$ du D_{R-R} et donc supposer que le courant est sans bruit pour le laser à points quantiques. Selon la théorie ci-dessus, les courbes de FN sont obtenues sous différentes sources de courant comme le montre la Fig. 6.6(a-d). Avec l'augmentation du courant, le bruit de fréquence émis par les deux sources de courant se rapproche progressivement du plateau à basse fréquence. La valeur de FN à basse fréquence correspond à la largeur de raie optique ($\Delta\nu_{OL}$) du laser à points quantiques, tandis que celle du plateau à haute fréquence donne la largeur de raie de Schawlow-Townes ($\Delta\nu_{ST}$). On peut voir que la réponse de la FN à haute fréquence ne dépend pas des sources de courant. En d'autres termes, que ce soit une pompe normale ou silencieuse, cela n'affecte pas le

bruit d'émission spontanée dominé par les caractéristiques du milieu de gain. Le pic entre les deux plateaux, apparaissant au-dessus du courant de seuil, correspond à la fréquence d'oscillation de relaxation (f_{RO}) du laser à points quantiques. Ainsi, lorsque la fréquence est inférieure à f_{RO} , la FN est déterminée non seulement par l'émission spontanée mais aussi par les fluctuations des porteurs, et la largeur de raie optique peut être exprimée comme $\Delta\nu_{OL} = \Delta\nu_{ST}(1 + \alpha_H^2)$. Par conséquent, comme la largeur de raie optique est entraînée par différents bruits de porteurs, le facteur d'amplification de largeur de raie est influencé. De plus, les cartes affichées dans les Fig. 6.6(e) et 6.6(f) montrent que lorsque le laser fonctionne avec une pompe silencieuse, le laser présente une plage plus large de bas FN. Le point d'inflexion à la fréquence de résonance près de 1,8 fois le seuil est attribué au facteur d'émission spontanée ($\beta_{sp} = 1 \times 10^{-4}$). En raison de l'efficacité limitée de l'émission spontanée, la puissance de sortie du laser présente une relation non linéaire avec le courant de seuil. Dans l'ensemble, ces simulations révèlent comment le bruit de porteur provenant de la source de courant impacte le FN du laser à points quantiques en particulier près de la transition de seuil.

Dans ce qui suit, le facteur α_H a été extrait des simulations de FN et comparé aux expériences pour différentes conditions de sources de courant. Pour ce faire, le facteur α_H a été extrait autour et au-dessus du courant seuil en utilisant une méthode de modulation de phase optique décrite dans le chapitre 2. La modulation du laser à points quantiques DFB à haute fréquence (13 ~ 18 GHz) conduit à des modes secondaires distincts dans le spectre optique et les modes secondaires à différents retards optiques sont utilisés pour récupérer le facteur α_H . L'expérience est réalisée à température ambiante (20 °C). Une telle approche nous permet de retrouver la dépendance en courant de la pompe du facteur α_H avec et sans conditions de tranquillité. Les résultats expérimentaux sont représentés dans la figure 6.7(a) et comparés aux simulations (lignes pleines). Près du courant seuil, il est démontré que le facteur α_H devient beaucoup plus petit dans des conditions de pompage silencieux. Par exemple, au seuil, avec une pompe normale, le facteur α_H est d'environ 1,7 tandis qu'il est réduit à 0,5 avec un pompage silencieux. Plus le bruit du porteur est fort, plus il est facile d'être capturé par les états de défaut et d'affecter l'efficacité de l'émission stimulée. En effet, la modulation de phase optique nécessite une puissance suffisante du laser, ce qui est difficilement le cas lorsqu'il fonctionne près du seuil. Malgré cela, nous démontrons que

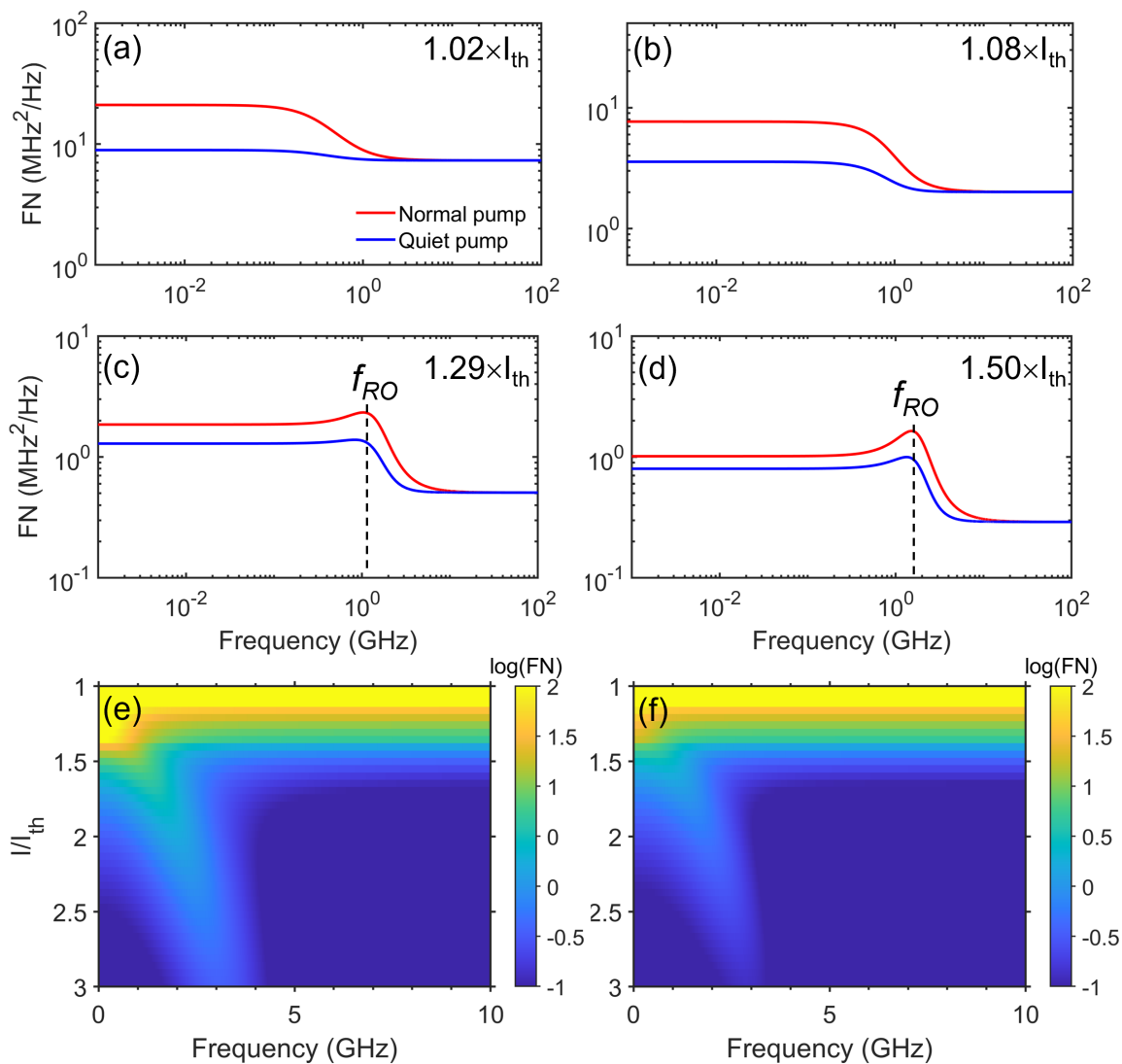


Figure 6.6: Spectres simulés du bruit de fréquence du laser à points quantiques avec pompe normale (ligne rouge) et pompe silencieuse (ligne bleue) à différents courants de polarisation (a-d). La cartographie de FN est représentée en fonction de la pompe de polarisation normalisée et de la fréquence sous (e) pompe normale et (f) pompe silencieuse.

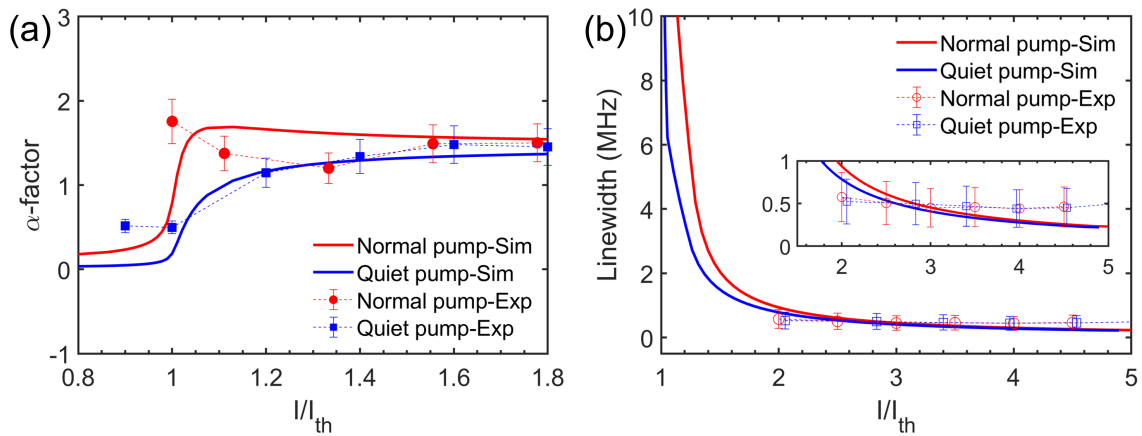


Figure 6.7: Facteur α_H expérimental (ligne en pointillés) et simulé (ligne pleine) (a) et largeur de raie optique (b) en fonction du courant de polarisation sous différentes pompes.

les facteurs α_H mesurés sont qualitativement en bon accord avec ceux des simulations. De manière intéressante, des travaux antérieurs ont également montré une augmentation du facteur α_H extrait dans un laser à points quantiques à partir de l'ASE et de la pompe normale à travers le seuil, mais les raisons exactes de ce phénomène restent obscures. Alors qu'avec les porteurs silencieux, le facteur α_H du laser à points quantiques près du courant seuil n'apparaît que comme un échelon en raison de l'inversion de population, ce qui a également été simulé dans la référence. Le facteur α_H ne tombe pas à zéro au-dessous du seuil mais s'approche d'une valeur minuscule d'environ 0,02. Même lorsque l'effet du bruit externe du porteur a été éliminé dans les simulations de pompage silencieux, les impacts de l'émission spontanée et d'autres bruits intrinsèques sur le facteur α_H sous-seuil persistent, conduisant à une valeur de facteur α_H diminuée qui n'est pas entièrement nulle. De plus, nos résultats expérimentaux et de simulation montrent que plus de différences ne sont observées à mesure que le courant augmente. Le facteur α_H devient indépendant du bruit du porteur.

Comme la largeur de raie optique est liée au facteur α_H , la mesure de la largeur de raie du laser QD DFB est également réalisée avec un interféromètre à hétérodyne à auto-décalage à 20 °C. Les résultats sont présentés par des points dans la figure 6.7(b) pour les conditions de pompage normal et silencieux. Pour extraire les largeurs de raie, un profil de lissage Voigt est utilisé. En raison de limitations techniques sur la puissance

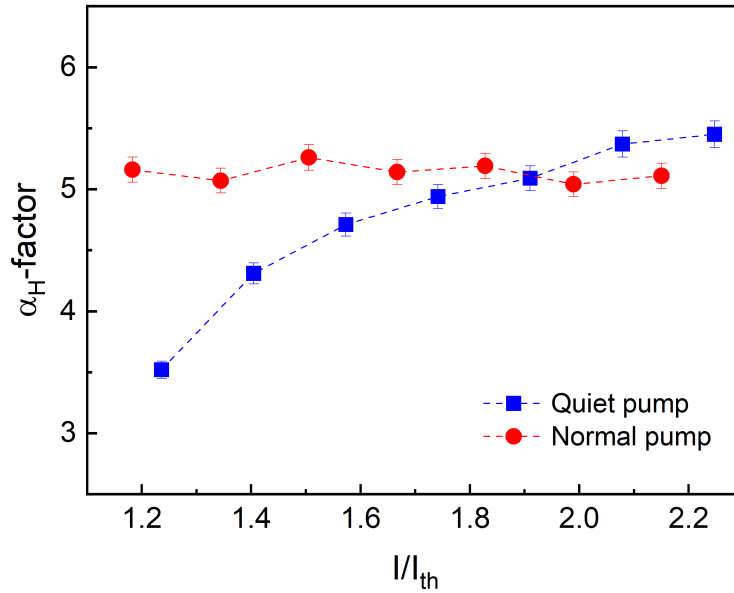


Figure 6.8: Le facteur α_H expérimental du laser QW avec des pompes normales et silencieuses.

de sortie couplée, les largeurs de raie optiques n'ont pu être extraites que au-dessus de deux fois le courant seuil. Comme prévu, nous avons constaté que la largeur de raie évolue avec le courant d'injection avec une diminution marquée au-dessus du seuil de plusieurs MHz à une valeur stable d'environ 500 kHz, ce qui est typique pour un laser à points quantiques. À fort courant de pompe, il n'y a pas de différence significative dans la largeur de raie optique lorsqu'elle est pilotée par différentes sources de courant, ce qui est également cohérent avec les résultats de simulation. Cependant, lorsque le laser est légèrement piloté au-dessus du seuil, les simulations révèlent que l'utilisation d'une pompe normale ne contribue qu'à augmenter la largeur de raie. Par exemple, à 1,5 fois le courant seuil, la largeur de raie optique est de 1,8 MHz avec la pompe silencieuse, contre 3,2 MHz pour les conditions de pompage normales. Le facteur α_H obtenu dans différentes conditions de bruit de la pompe détermine directement la tendance de la largeur de raie. La largeur de raie sera étendue de manière quadratique par le facteur α_H . Le chevauchement du facteur α_H à des courants élevés rend également la largeur de raie indépendante des différentes conditions de bruit de la pompe. Par conséquent, les impacts du bruit externe du porteur sur le bruit de fréquence s'étendent considérablement à la fois au facteur α_H et à la largeur de raie optique.

Pour comparaison, nous utilisons également différentes pompes pour piloter un laser QW DFB de référence et appliquons la méthode d'injection optique bloquée pour l'extraction du facteur α_H . Le laser QW présente également un écart près du seuil. l'écart disparaît progressivement à mesure que le courant augmente comme le montre la figure 6.8. Cela démontre également l'universalité de l'effet du bruit externe du porteur sur les lasers, indépendamment de la méthode de mesure et du matériau de la couche active.

• Conclusion

Dans cette section, l'effet des fluctuations externes des porteurs sur le bruit de fréquence et le facteur α_H des lasers à points quantiques (QD) est examiné de manière exhaustive.

Tout d'abord, les raisons causant différentes fluctuations externes des porteurs ont été analysées théoriquement. Les spectres de bruit de différentes sources de courant ont été mesurés pour visualiser les différences dans les fluctuations externes des porteurs.

L'effet des fluctuations externes des porteurs sur le facteur α_H d'un laser QD DFB a été étudié. Avec la pompe silencieuse, le facteur α_H est trouvé être beaucoup plus petit autour du seuil par rapport aux conditions de pompage normal. Les modèles numériques et les expériences confirment ensemble ce phénomène intéressant. De plus, les simulations mettent également en évidence que l'utilisation de la pompe silencieuse près du courant de seuil est bénéfique pour réduire le bruit de fréquence et par conséquent la largeur de raie optique, mais a moins d'impact à des courants élevés. Il convient de souligner que le facteur α_H du laser QW sous différentes pompes présente également un comportement similaire à celui du laser QD. Dans l'ensemble, je pense que ces résultats sont essentiels pour le développement d'oscillateurs ultra-faible bruit pouvant produire de la lumière en dessous ou à proximité du niveau du bruit de photon.

Titre : Exploration de la dynamique non-linéaire et de la compression d'amplitude des lasers à îlots quantiques

Mots clés : lasers à îlot quantiques, circuits intégré photoniques, dynamique non-linéaire, états comprimés

Résumé : Les circuits photoniques intégrés (PIC) utilisant la technologie de la photonique sur silicium présentent un potentiel significatif dans les systèmes de communication à haute vitesse, le calcul optique et la technologie quantique. Les lasers à îlot quantiques (QD), en particulier ceux qui sont cultivés épitaxialement sur silicium, affichent des caractéristiques remarquables telles qu'une forte tolérance aux défauts, un faible courant de seuil et une bonne stabilité thermique. De ce fait, ils émergent progressivement comme des sources laser prometteuses sur puce pour les PIC. Cette thèse vise à explorer la dynamique non linéaire et les propriétés d'état quantique des lasers QD, jetant ainsi les bases de diverses applications potentielles. La première section de la thèse se penche sur le rôle du facteur d'élargissement de la largeur de raie (α_H -facteur) dans les lasers QD. J'ai utilisé une technique de modulation de phase optique pour extraire le α_H -facteur des lasers QD au-dessus du seuil. Le petit α_H -facteur des lasers QD a fortement amélioré la tolérance au feedback optique. Cela facilite le développement de transmissions optiques à haute vitesse sur puce sans isolateur optique et augmente la densité d'intégration. La deuxième section explore les caractéristiques dynamiques des lasers QD sous feedback optoélectronique (OEF). Contrairement au feedback optique, j'ai démontré que les lasers QD présentent une sensibilité accrue à l'OEF, conduisant à diverses dynamiques complexes. Cette sensibilité extrême est

cruciale pour l'avancement du calcul optique basé sur le silicium sur puce et des applications des machines d'Ising, un phénomène non observé dans les lasers à puits quantiques (QW). Dans la troisième section, j'ai analysé la dépendance du bruit de fréquence au bruit porteur externe. La recherche a révélé qu'un pompage silencieux est très avantageux pour minimiser le α_H -facteur, réduire le bruit de fréquence et, par conséquent, rétrécir la largeur de raie optique des lasers QD. La dernière section met en évidence la génération de lumière comprimée en amplitude directement à partir d'un laser QD à semi-conducteurs entraîné par un courant constant. Avec le pompage silencieux, j'ai atteint une large bande passante de compression de plusieurs gigahertz à température ambiante avec un rapport de compression de 3,5 dB. L'insensibilité extrême à la réflexion du générateur QD comprimé sous feedback optique, en contraste avec un laser de référence utilisant la technologie QW standard, est également démontrée avec un rapport de compression amélioré à 5,1 dB. Trois mesures distinctes, incluant le spectre radiofréquentiel sous le bruit de grenaille, les statistiques photoniques sub-Poissonniennes et la fonction de corrélation d'ordre deux à retard zéro, valident mes conclusions. Cette recherche établit un cadre fondamental pour des circuits quantiques photoniques intégrés compacts et hautement efficaces, démontrant le potentiel d'application immense des lasers QD dans les domaines de la photonique classique et quantique.

Title : Exploring the nonlinear dynamics and amplitude-squeezing of quantum dot lasers

Keywords : quantum dot lasers, photonic integrated circuits, nonlinear dynamics, squeezed states

Abstract : Photonic integrated circuits (PICs) utilizing silicon photonics technology show significant potential in high-speed communication systems, optical computing, and quantum technology. Quantum dot (QD) lasers, particularly those epitaxially grown on silicon, exhibit notable characteristics such as strong defect tolerance, low threshold current, and good temperature stability. As a result, they are gradually emerging as promising on-chip laser sources for PICs. This thesis aims to explore the nonlinear dynamics and quantum state properties of QD lasers, laying the foundation for various potential applications. The first section of the thesis delves into the role of the linewidth enhancement factor (α_H -factor) in QD lasers. I employed an optical phase modulation technique to extract the above-threshold α_H -factor of QD lasers. The small α_H -factor of QD lasers strongly improved optical feedback tolerance. This facilitates the development of high-speed optical transmission on chips without an optical isolator and increases integration density. The second section explores the dynamic characteristics of QD lasers under optoelectronic feedback (OEF). Unlike optical feedback, I demonstrated that QD lasers exhibit enhanced sensitivity to OEF, leading to various complex dynamics. This extreme sensitivity is crucial for the advancement of on-chip silicon-based

optical computing and Ising machine applications, a phenomenon not observed in quantum well (QW) lasers. In the third section, I analyzed the dependency of frequency noise on external carrier noise. The research revealed that quiet pumping is highly advantageous for minimizing the α_H -factor, reducing frequency noise, and consequently narrowing the optical linewidth of QD lasers. The last section highlights the generation of amplitude-squeezed light directly from a constant-current-driven semiconductor QD laser. With the quiet pump, I achieved a substantial gigahertz squeezing bandwidth at room temperature with a squeezing ratio of 3.5 dB. The extreme reflection insensitivity of the squeezed QD generator under optical feedback, in contrast to a reference laser using standard QW technology, is also demonstrated with a squeezing ratio further improved to 5.1 dB. Three distinct measurements, including the sub-shot-noise radiofrequency spectrum, sub-Poissonian photon statistics, and second-order correlation function at zero delay, validate my findings. This research establishes a foundational framework for compact and highly efficient photonic quantum integrated circuits, showcasing the immense application potential of QD lasers in both classical and quantum photonics fields.